Tuning the photocatalytic activity of layered double hydroxides with loading of certain transition metals-metal oxides nanocomposites

Thesis submitted for the award of degree of

Doctor of Philosophy

Submitted by:

Jemini

(Reg. No: 902009022)

THAPAR INSTITUTE
OF ENGINEERING & TECHNOLOGY
(Deemed to be University)

Under the Supervision of

Dr. Bonamali Pal
(Professor)

Dr. Satnam Singh
(Professor)

DEPARTMENT OF CHEMISTRY AND BIOCHEMISTRY
THAPAR INSTITUTE OF ENGINEERING AND TECHNOLOGY PATIALA-147004,
INDIA APRIL-2025

Certificate

This is to certify that thesis entitled **"Tuning the photocatalytic activity of layered double hydroxides with loading of certain transition metals-metal oxides nanocomposites"** being submitted by Jemini, in the fulfillment of the requirement for the award of the Degree of Philosophy to the Department of Chemistry and Biochemistry, Thapar Institute of Engineering and Technology, Patiala, in an authentic record of candidate's own work carried out by her under my supervision and guidance. The matter presented in this thesis has not been submitted in part or full for the award of any degree in any other university of institute.

(Head)

Dr. Bonamali Pal

Professor and supervisor

Department of Chemistry and Biochemistry

Thapar Institute of Engineering and Technology

Patiala-147004

Dr. Satnam Singh

Professor and supervisor

Department of chemistry and Biochemistry

Thapar Institute of Engineering and Technology

Patiala -147004

Dr. Manmohan Chhibber

Professor and Head

Department of Chemistry and Biochemistry

Thapar Institute of Engineering and Technology Patiala-147004, India

Candidate's Declaration

I hereby declare that the work presented in the thesis entitled **"Tuning the photocatalytic activity of layered double hydroxides with loading of certain transition metals-metal oxides nanocomposites "** in the fulfillment of the award of the degree of Philosophy to the Department of Chemistry and Biochemistry , Thapar Institute of Engineering and Technology , Patiala is an authentic record of my own work carried out under the supervision of Dr. Bonamali Pal (Professor) and Dr. Satnam Singh (Professor), Department of Chemistry and Biochemistry, Thapar Institute of Engineering and Technology, Patiala, India. The matter embodied in this thesis has not been submitted in part or full to any other university or institute for the award of any degree in India or Abroad.

Jemini

Dr. Bonamali Pal

Professor and supervisor

Department of Chemistry and Biochemistry

Thapar Institute of Engineering and Technology

Patiala-147004

Dr. Satnam Singh

Professor and supervisor

Department of chemistry and Biochemistry

Thapar Institute of Engineering and Technology

Patiala -147004

Dedicated

To

My Parents

Mrs. Sunita Sharma & Mr. Raj Kumar Dogra

Acknowledgement

First and foremost, I want to express my deep gratitude to Almighty God for granting me the courage, patience, vision, and endurance necessary to complete this research.

I would like to extend my heartfelt gratitude and profound indebtedness to my doctorate advisors, **Dr. Bonamali Pal,** Professor, and **Dr. Satnam Singh**, Professor. Their unwavering support, expert guidance, and encouragement were crucial in navigating various research challenges and bringing this work to fruition.

I sincerely acknowledge **Dr. Padamakumar Nair**, Honourable Director, **Dr. N. Tejo Prakash**, Dean of Research and Development Centre (DRDC), T.I.E.T, Patiala, for providing all the necessary facilities that have been immensely helpful in carrying out this research. I extend my sincere appreciation to **Dr. Manmohan Chhibber**, Professor and Head of the Department of Chemistry and Biochemistry at Thapar Institute of Engineering and Technology, Patiala, for his constant support and encouragement. I offer my sincere thanks to my doctoral committee members, **Dr. Soumen Basu, Dr. Amjad Ali**, and **Dr. Bhaskar Chandra Mohanty**, for their crucial role in validating this research project. Their insightful feedback and scholarly discussions greatly enhanced the presentation and quality of my work.

I am deeply grateful for the support provided by the entire faculty of the Department of Chemistry and Biochemistry at TIET, Patiala. I also want to express my sincere appreciation to all the administrative, technical, and office staff in the department, especially **Mr. Chander Thakur**, **Mr. Hemant** and **Mr. Mayank Sharma**, for their cooperation and assistance throughout the duration of my research.

I would like to express my sincere gratitude for the support provided by various institutes and laboratories, including SAI Lab, SPMS and Avantha Lab TIET Patiala, and Sprint Testing Solutions in Mumbai.

I would like to express my sincere gratitude to my fellow lab colleagues and friends **Ms. Sukhandeep Kaur**, **Ms. Shreya Sharma**, **Mrs. Palak Soni**, **Ms. Mehak Bansal**, **Ms. Davinder Kaur**, **Ms. Ridhima Sharma, Ms. Puneet, Mrs. Shikha** for their unwavering support and

guidance during hard times. This entire journey would not have been possible without their indispensable contributions, rendering it an unforgettable and remarkable experience.

A very special thanks to my dearest friends **Ms. Akanksha Katoch** and **Ms. Priya Kamboj** who have been my unwavering pillars of support throughout the journey of my PhD. Their presence, encouragement and belief in me have been invaluable, not just during the highs, but in every challenging phase along the way. Both of them not only shared in my successes but also stood by me during the struggles, making this journey all the more meaningful. I am truly blessed to have friends like them, and I will forever cherish the memories of this incredible journey together. I would also like to express my thanks to my friends and Hostelmates **Ms. Parmjeet Kaur**, **Ms. Pooja Soam**, **Mrs. Monika Barak**, **Ms. Anshika Khandwal**, **Ms. Azra Showkat** for their unwavering support, consistent communication and efforts to ensure my welfare and cheering me up.

I can't put my thoughts or feelings into words to show my heartfelt appreciation to my respected parents, **Mrs. Sunita Sharma** and **Mr. Raj Kumar Dogra**. Their unwavering blessings, steadfast beliefs, and constant encouragement have guided me toward achieving my goals. They have been the driving force behind my growth into the person I am today. Whether near or far during this research journey, their insightful advice and support have been a constant presence, profoundly influencing the progress of my work. Special thanks to my loving younger brother **Mr. Jatin Dogra** for his pure love, care and unwavering support. I am truly grateful to have him by my side. I would also like to thank my sister **Ms. Arisha Sharma** pursuing her doctorate from Indian Institute of Engineering and Technology Roorkee for always being there to offer help and guidance.

I express my gratitude to all the individuals who, despite not being acknowledged here, have provided assistance, whether consciously or unconsciously, in the successful completion of my thesis.

Jemini

Table of Contents

Chapter-2

Effective performance of monoclinic WO_3/ZnCr layered double hydroxide composites towards the degradation of tetracycline under visible light irradiation

Chapter-3

Enhanced adsorption and photocatalytic activity of MgAl layered double hydroxide for degradation of ciprofloxacin under visible light irradiation

Chapter-4

Construction of ternary Ag@α-Fe_2O_3/NiCo LDH composites for efficient degradation of malachite green dye under visible light and sunlight irradiation

List of Abbreviations

a. u.	Arbitrary unit
BET	Brunauer Emmett Teller
CB	Conduction band
CIP	Ciprofloxacin
DI	Deionized water
DRS	Diffuse reflectance spectroscopy
EDX	Energy dispersive X-ray spectroscopy
E_{CB}	Conduction band edge position
E_{VB}	Valence band edge position
E_g	Band gap
FESEM	Field emission scanning electron microscopy
HRTEM	High resolution transmission electron microscopy
HRMS	High resolution mass spectroscopy
IPA	Isopropyl alcohol
JCPDS	Joint committee on powder diffraction standards
LDH	Layered double hydroxides
MG	Malachite green
MO	Metal oxide
nm	Nanometer
NPs	Nanoparticles
PL	Photoluminesence
PPM	Parts per million

RPM	Rotations per minute
SAED	Selected area electron diffraction
SPR	Surface Plasmon resonance
TC	Tetracycline hydrochloride
TOC	Total organic carbon
UV	Ultraviolet
VB	Valance band
wt%	Weight percentage
XPS	X-ray photoelectron spectroscopy
XRD	X-ray diffraction spectroscopy
λ_{max}	Wavelength of maximum absorption

List of symbols

e^-	Electron
h^+	Hole
$O_2^{\bullet-}$	Superoxide radical
·OH	Hydroxyl radical
Å	Angstrom
α	Absorption coefficient
A	Absorbance
°	Degree
λ	Wavelength
%	Percentage
µ	Micro
θ	Theta
h	Hour
E_o	Electrode potential
m	Meter
g	Gram
mg	Milligram
V	Volt
d	Distance
C	Concentration
v	Frequency

mol	Mole
µmol	Micromol
µl	Microlitre
mL	Millilitre
mM	Millimolar
L	Litre
2D	Two-dimensional
h	Planck constant
k	Pseudo first order rate constant (min^{-1})

Abstracts

Chapter-1

The structural and chemical composition, adsorption, and photocatalytic properties of 2-D nanostructured layered double hydroxides (LDH) are covered in this chapter. LDH behaviour and alterations have been explored in relation to adsorption and photocatalysis. This chapter also includes descriptions of the literature evaluation, research gaps, objectives, experimental procedures, and characterization approaches.

Chapter-2

Recently, the efficient removal of antibiotics like Tetracycline (TC) from wastewater is emerging as a crucial problem. However, low adsorption capacity and high cost of photocatalysts limit their utility. In this context, monoclinic tungsten trioxide (WO_3) loaded ZnCr layered double hydroxide (LDH) composites (ZnCr-xWO_3 x= 10 and 20%) were prepared by co-precipitation method and characterized by several techniques viz. X-ray diffraction (XRD), Fourier Transform Infrared Spectroscopy (FTIR), Raman, Photoluminescence (PL), Field-Emission Scanning Electron Microscopy (FE-SEM), Brunauer Emmett Teller (BET), Diffuse Reflectance Spectroscopy (DRS) and Dynamic Light Scattering (DLS). The XRD pattern confirms the formation of ZnCr LDH and its composites with monoclinic-WO_3. Bond vibrations and phase transitions were explored with the help of FTIR and Raman spectra. The BET analysis for ZnCr LDH and ZnCr-10WO_3 composite shows the surface area as 27.439 m^2/g and 47.691m^2/g. The higher photocatalytic performance of the composites formed is due to enhanced specific surface area and better separation efficiency of photo-generated electrons and holes through conventional class II hetero junction between ZnCr LDH and monoclinic-WO_3. The kinetics studies performed show a better fit for pseudo-first-order reaction with maximum degradation efficiency and rate constant for ZnCr-10WO_3 (i.e., 86.7% and 1.5×10^{-2} min^{-1}).

Chapter-3

An environmental friendly approach was utilized to remove pharmaceutical drugs from wastewater, employing adsorption and photocatalysis. The emphasis centered on synthesizing ternary composites comprising silver-deposited tungsten trioxide (Ag@WO_3; 2, 4 wt.%), and

MgAl layered double hydroxide (LDH) for the remediation of wastewater from the pharmaceutical industry. Combining silver-loaded WO_3 nanoparticles with MgAl LDH resulted in the enhancement of the adsorption and photocatalytic properties of MgAl LDH. The studies demonstrated that by incorporating $Ag@WO_3$ into MgAl LDH, the formed ternary composites exhibited superior performance, achieving 88% tetracycline (TC) adsorption in 90 minutes, providing the best fit for the Langmuir model, suggesting monolayer adsorption following second-order kinetics and 77.9% of ciprofloxacin (CIP) degradation under visible light irradiation in 160 minutes with rate constant of 0.96×10^{-2} min^{-1} for pseudo-first-order kinetics. The enhancement was attributed to the increased surface area and electron-accepting ability of silver NPs (surface plasmonic effect). Additionally, the $Ag_2@WO_3$-LDH heterostructure exhibited high stability and recyclability for up to 5 cycles with little loss in performance. High- resolution mass spectrometry (HRMS) studies and free radical trapping experiments were conducted to reveal the intermediates generated during the degradation process, leading to the proposed mechanism via two degradation pathways.

Chapter-4

The study aimed to enhance the photocatalytic efficiency of NiCo layered double hydroxide by forming composites with Fe_2O_3 and further improving its responsiveness to visible light by Ag loading. In comparison to bare NiCo LDH and its binary composites, the optimized ternary composite: $NCF10A_3$ LDH ($Ag_3@10Fe_2O_3$/NiCo LDH), showed significantly improved photoactivity in degrading malachite green, achieving degradation rates and rate constant of 81.2% ($k = 1.25 \times 10^{-2}$ min^{-1}) and 98.6% ($k = 3.33 \times 10^{-2}$ min^{-1}) under visible light and sunlight, respectively. This is caused by the active visible light response from Fe_2O_3 NPs and Ag NPs' SPR effect. The band gap of material decreased from 2.40 eV to 1.74 eV. The noteworthy enhancement in visible-light response and faster transfer of photoinduced carriers are attributed to the collaborative effect of NiCo LDH, Fe_2O_3, and Ag NPs in the ternary composite. Furthermore, malachite green was partially mineralized, as indicated by TOC analysis and corroborated by HR-MS chromatograms, with mineralization efficiencies of 41.3% and 49.4% under visible light and sunlight, respectively. Through examination of the fragments found at different m/z ratios, the degradation routes were proposed. In comparison to samples exposed to visible light, the HRMS spectra of the degraded product under sunlight exhibit fewer fragments,

which could be due to the accelerated rate of a reaction under high-intensity and high- temperature reaction conditions. The catalyst's durability was assessed by reusability and recyclability tests, which showed that the catalyst stayed stable and reusable for up to five cycles.

CHAPTER-1

Introduction and literature review

1.1. Introduction

1.1.1. Layered double hydroxides

Layered double hydroxides (LDHs) belong to a class of anionic clays, commonly referred to as hydrotalcite-like compounds. Hydrotalcite, a natural mineral with the formula $Mg_6Al_2(OH)_{16}CO_3.4H_2O$, exhibits structural similarities to brucite $Mg(OH)_2$ which is the basic unit of these layered structures in which each of these units combine to form layers of LDHs, therefore referred as hydrotalcite compounds [1]. LDHs are characterized by a general formula $[M(II)_{1-x}M(III)_x(OH)_2]^{x+}[A_{x/n}]^{n-}.m\ H_2O$, where A is an intercalated anion and M(II, III) are metal cations, x is the layer charge density, which is defined as the molar ratio of trivalent metal cation to the sum of molar ratio of divalent and trivalent metal cation ranging from 0.2 to 0.4, m is the number of H_2O molecules within the brucite layers along with the intercalated anions [2,3]. Different combinations of metal cations (divalent like Cu^{2+}, Co^{2+}, Zn^{2+}, etc.; trivalent like Al^{3+}, Fe^{3+}, Co^{3+}, etc.; tetravalent like Ti^{4+}, etc.) and anions CO_3^{2-}, SO_4^{2-}, NO_3^- have been used to synthesize a variety of LDH material [4]. Their structure remains electroneutral due to the intercalated anions, which are negatively charged and situated between the brucite layers, counterbalancing the positive charge of the layers [5]. The even dispersion of divalent and trivalent metal cations within the layers, the electrostatic attraction between these layers and intercalated anions, and hydrogen bonding make the layered structure stable [6,7]. The octahedral unit and structure of LDH are shown in **Fig.1.**

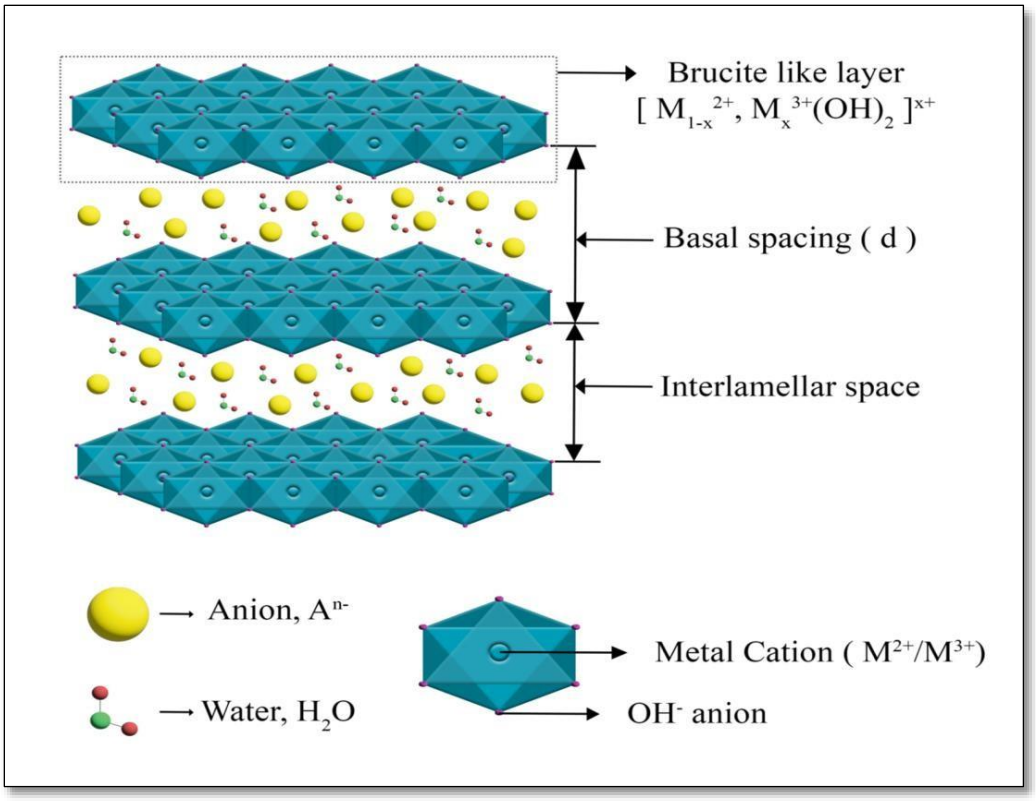

Fig.1. Structure of layered double hydroxides

LDHs can interact with anionic molecules easily as they have cationic layers. Furthermore, the anion exchange parameter is a valuable factor that influences the LDH adsorption capacity which allows toxic anionic molecules to interchange with LDH interlayer molecules because of the adjustable properties of the layers [8]. Moreover, hydroxyl groups and organic species present in modified LDH are the additional factors that enhance LDH interactions with pollutants [9]. The electrostatic coupling present between the exchangeable intercalated anions and the brucite sheets is the main source of anion exchange in LDHs [10]. The high anion exchange capacity of LDHs is an appropriate characteristic that is dependent on several factors, including the molecular mass of cations and anions, cationic metals ratio, and the applied anion's ability to stabilize layer formation. According to one study, it has been found that LDHs possess an anion exchange capacity ranging from 200–450 $cmol_c$ kg^{-1} [11]. Various synthetic methods can be employed to control the Composition, particle dimensions, structure, surface imperfections, and electronic characteristics, of LDHs [12–14]. These methods are essential for improving the capabilities of heterogeneous catalysis. Several studies have considered LDHs as a catalyst or as

a catalyst supporter. Sahoo and Parida employed Pd (II) LDH as a heterogeneous catalyst to oxidize primary alcohol within six hours, they observed successful primary alcohol oxidation and its increasing conversion rate. The catalyst was recycled multiple times with good activity and selectivity, and it was very simple to separate. [15]

In LDHs, the metal octahedra are interconnected through metal–oxygen–metal oxo bridging linkages. In photocatalytic reactions, these oxo-bridged binuclear connections function as redox centers activated by visible light, exhibiting metal-to-metal charge transfer (MMCT), which entails electronic excitation between metal ions [16]. The photocatalytic efficiencies of several doped semiconductors and their metal oxo-bridging structures have been studied [17–19]. These materials have several impressive qualities, such as high surface area, low toxicity, excellent thermal and chemical endurance, and tunable electrical and structural characteristics [20–22] which enable LDHs to find applications in catalysis, adsorption, photocatalysis, electrochemistry, and more [23–27].

Recently, calcination of layered double hydroxide (LDH) has been suggested as an alternative way to prepare mixed metal oxides (MMO). When LDHs are heated to temperatures between 450 and 500 °C, they transform into MMOs, which are noted for their evenly distributed metal cations and significant surface area. For example, $Mg_6Al_2(OH)_{16}(CO_3)\cdot 4H_2O$ (hydrotalcite) stoichiometrically alters to $Mg_3AlO_{4.5}$ (MMO) when they are calcined at an appropriate temperature, between 300 °C and 600 °C. These MMOs have high thermal stability and relatively large specific surface area [28]. A fascinating aspect of LDHs is their 'memory effect,' which means these calcined anionic clays that collapse during calcination can regenerate their original layered structure [29]. Ahmed *et al*. synthesized extremely crystalline ZnO from calcined Zn/Al-LDHs. [30]. Similar to this, Seftel *et al.* used the co-precipitation approach to prepare both calcined and uncalcined ZnAl LDHs with different cationic ratios [31]. Their findings revealed that Zn/Al-LDH, calcined at 500° C, achieved a remarkable 93% degradation of methyl orange dye within 4 hours under UV light irradiation. The noteworthy ZnO phase development was credited with this improvement. In another study, Morimoto *et al.* investigated the photocatalytic degradation of colored dyes using calcined LDHs. They found that MgAl- LDH, with its smaller particle size, exhibited superior adsorption capacity and photocatalytic activity, demonstrating its dual function in adsorption and degradation [32]. The memory effect

shown by LDHs is depicted in **Fig. 2.** Water contamination is now a major public health concern that is producing several diseases. The discharge of organic contaminants into water sources as industrial effluents is a primary cause. Adsorption and photocatalytic degradation are widely used around the world as quick, simple, inexpensive, and remarkably effective ways to remove organic contaminants from water.

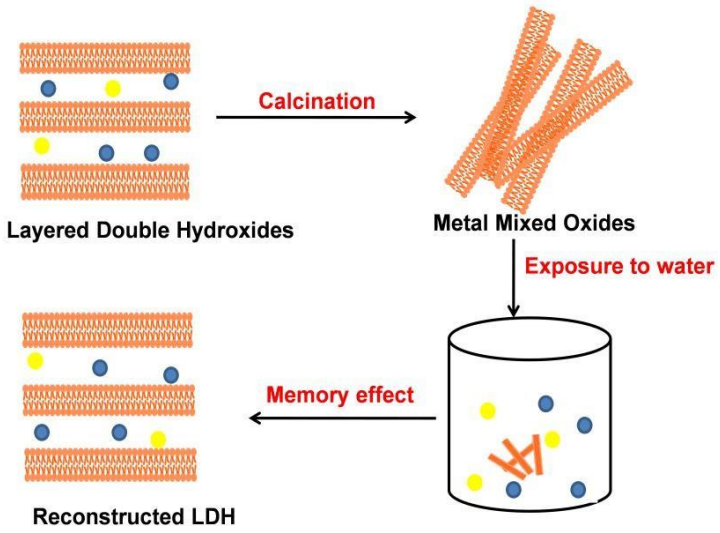

Fig.2. Layered double hydroxides showing memory effect

1.1.2. Layered double hydroxides as adsorbent

It is well recognized that a variety of dyes and pigments used in the paper, paint, leather, textile, and plastics sectors are harmful to the environment when they spill into it. Approximately 15% of industrial dyes directly affect water used for drinking. [33] Many methods, including adsorption, chemical oxidation, coagulation, and photocatalytic degradation, have been extensively documented in the literature to eliminate harmful colorants, and adsorption is considered to be an effective approach for doing so [34–36]. LDHs are favoured as effective adsorbents because of their low cost and toxicity, high stability, reusability, and facile synthesis. These adsorbents are dual-electronic, with an anionic intercalation and a positively charged surface. Strong electrostatic interaction between the cationic surface and anionic dyes facilitates the adsorption process. Various research groups have extensively investigated the removal of cationic and anionic dyes, attributing their interaction with LDH surfaces to electrostatic forces

[37]. Furthermore, hydrogen bonding between the dyes and the LDH is facilitated by hydroxyl groups on its surface. For this instance, Leite de Sa *et al.* synthesized magnetic MgAl LDH for the removal of MG dye showing 100% removal efficiency [38]. Magnetic composites also act as good adsorbents Lu *et al*. examined the impact of adding Fe_3O_4 nanoparticles to the surface of LDH and explored its potential for use in wastewater treatment applications. The adsorption capacity of congo red dye was 813 mg/g which is the highest value for magnetic adsorbents [39]. Additionally, calcination significantly enhances adsorption capacity. For instance, calcined MgAl LDH demonstrates superior effectiveness in adsorbing and removing As(V) and Cr(VI) compared to its non-calcined counterpart [40]. The surface properties and adsorption efficiency are also greatly enhanced when LDH is combined with carbon nanostructures, anions, surfactants, iron nanoparticles, and polymers. The adsorption mechanism of carbon-containing nanostructures graphene/LDH was demonstrated by the exchange of interlayer anions [41]. Calcination imparts a positive effect on the adsorption phenomenon. Calcined and noncalcined LDH nanocomposites were prepared and a very low dosage of the calcined sample (1.0g/L) showed the highest adsorption of Cr(VI) i.e. (172.55mg/g). The enhanced adsorption was attributed to the synergic effect and memory effect of calcined samples [42]. Adsorption, electrical coagulation, chemical precipitation, and ion exchange are a few techniques used to extract heavy metal anions from water. Due to its cost-effectiveness and simplicity, the use of LDH for adsorption has become a preferred method for treating water contaminated with heavy metals. Studies have documented that intercalating EDTA into LDH enhances adsorption efficiency [43]. Similarly, incorporating specific ions into layered double hydroxide structures improves their effectiveness in removing water pollutants. Intercalated MoS_4^{2-} into Mg-Al LDH was studied for the removal of heavy metal ions. Following adsorption, X-ray patterns of the samples show how coordination and intercalated structures depend on the concentration of metal ions [44].

1.1.3. Layered double hydroxides as photocatalyst

The vast pollution emissions from the pharmaceutical, textile, and other manufacturing industries are a threat to human society's long-term survival. To address these problems, photocatalytic technology has lately gained attention due to its predicted practical uses and its ability to directly convert solar energy into chemical energy; these characteristics include low energy consumption,

gentle reaction conditions, and low operating costs. Advanced oxidation processes (AOPs) are recognized for their effectiveness in generating reactive oxygen species like hydroxyl radicals (˙OH). Consequently, they find extensive use in organic pollutant degradation and energy conversion [45].

During photocatalysis, the catalyst surface gets excited by light radiation, generating electron- hole pairs. Electrons move to the CB, while holes form in the VB. These holes start the oxidation producing hydroxyl radicals, while electrons reduce dissolved O_2 to form superoxide radicals which can then be protonated to generate hydroperoxyl radicals ($HO_2^{\cdot}$) and further decompose into H_2O_2. The $OH^{\cdot}$ radicals formed oxidize organic molecules into intermediates, ultimately yielding H_2O and other smaller molecules as end products as shown in **Fig. 3**. Among AOPs, visible-light photocatalysis, in particular, is gaining attention from all around the world since it can use solar energy to catalyze reactions and because of their high adsorption capacity and adjustable band gap, LDH-based photocatalysts offer a prospective substitute for conventionally based photocatalysts [46]. This significantly influences charge transfer and separation efficiency, thereby defining the overall effectiveness of photocatalytic degradation. The optical characteristics of a photocatalyst and the position of redox potentials within the semiconductor both affect the effectiveness of the catalyst. Semiconducting metal oxides are the most widely utilized photocatalysts; nevertheless, due to their low surface area and broad, untunable band gap, mono-metal oxides have limited practical applicability [29]. The even distribution of metal cations within brucite-like layers, achieved through the edge-sharing of MO_6 octahedra, results in enhanced photocatalytic performance relative to metal oxides or hydroxides. The main cause of this effective photoactivity is the widely distributed MO_6 octahedra, which speeds up charge transfer and lessens charge carrier recombination. Zhao *et al.* demonstrated this phenomenon by incorporating visible-responsive CrO_6 octahedra into the M-Cr LDH (M = Cu, Ni, Zn) matrix. However, because of its high rate of electron-hole pair recombination and poor electron transport, chromium hydroxide exhibits negligible photoactivity. On the other hand, because of their high dispersion within the layered structure, LDHs containing scattered CrO_6 octahedral units demonstrate effective photoactivity. The Cr_{3d} orbitals (A_{2g}) serve as the valence band, while the Cr_{3d} orbitals (T_{2g}+T_{1g}) act as the conduction band, undergoing band gap transitions responsible for their photocatalytic properties [47].

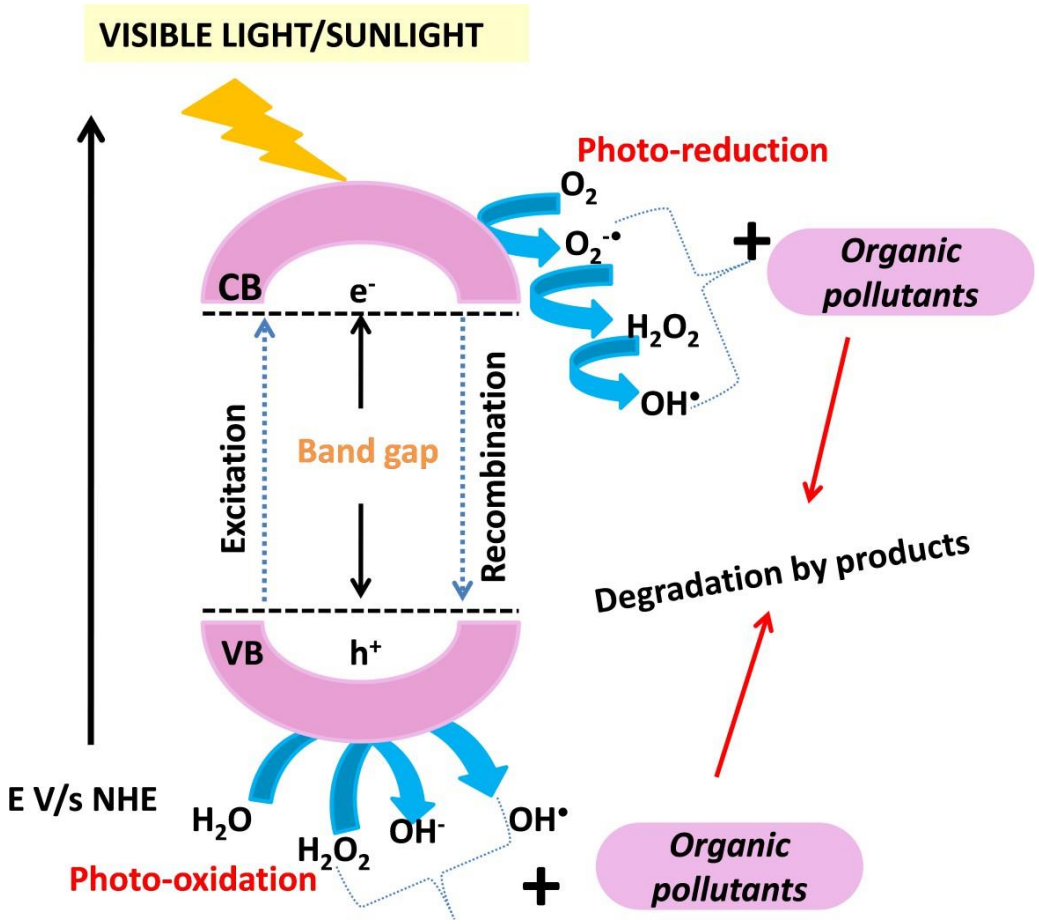

Fig.3. Photocatalytic mechanism of degradation of organic pollutants by photocatalyst

The photocatalytic performance of LDHs is influenced by various factors, including interlayer spacing, volume, electron density, band structures, size, and strength of the interlayer hydrogen bond network. The Pt/ZnTi LDH was successfully synthesized by Chen *et al.* Pt was integrated into LDHs with organic ligands, boosting the LDHs' pore volume and specific surface area from 0.317 cm^3/g to 0.081 cm^3/g and from 29.05 m^2/g to 111.46 m^2/g, respectively. [48]. Furthermore, a few LDHs have limitations with low photocatalytic efficiency caused by rapid recombination of reactive holes and electron pairs, a high band gap, and a low percentage of visible light or sunlight. Multiple methods, such as ion doping, noble metal loading, and morphological changes, have been developed to improve electron-hole separation and visible light adsorption. Moreover, connecting another semiconductor to form a heterojunction efficiently increases LDH's visible

light activity. Various modifications have been reported in the literature for effective and high photocatalytic generation of oxygen and hydrogen under visible light.[49] Similar work was done by Sahoo *et al.* they provide a deep investigation of the mechanism that $Co(OH)_2$ loaded ZnCr LDH composite releases more H_2 and O_2 in comparison to bare LDH via the construction of n-p heterojunction [50]. Doped semiconductors heterojunction also showed effective phenol degradation. Hasija *et al.* fabricated sulfur-doped C_3N_4 upon NiFe LDH and investigated the 2,4 nitrophenol photocatalytic degradation, which was almost two times greater than that of C_3N_4 and bare LDH [51].

1.1.4. Strategies for enhancing LDH photocatalytic performance

(i) Metal oxide/LDH composites

LDH known for their distinctive band structures and semiconducting properties, offers significant potential for integration with other metals or metal oxides to create advanced photocatalysts. The formation of heterojunctions between metal oxides and LDHs alters the spatial charge distribution. This alteration improves the effectiveness of electron and hole separation, overcoming typical drawbacks of unmodified LDH-based photocatalysts, such as restricted light absorption ranges, low quantum efficiency, and insufficient coverage of active catalytic sites [52]. Some metal oxide-based semiconductor photocatalysts have low visible light conversion efficiencies, which restricts their practical use. For example, TiO_2 uses more of the spectrum's ultraviolet light due to its wider band gap, yet during reactions, rapid electron-hole recombination reduces both its activity and stability. Ruijuan Lu *et al.* improved the photocatalytic activity of TiO_2 nanoparticles with the help of MgAl LDH and it was observed that TiO_2/MgAl (1:1) composite was more photo catalytically active for phenol degradation than TiO_2 [53]. Dou *et al*. also synthesized core-shell nanospheres of TiO_2/CoAl LDH which exhibited the highest photocatalytic activity towards oxygen generation i.e. 2.34 mmol $h^{-1}g^{-1}$,
2.24 mmol $h^{-1}g^{-1}$ under the influence of visible light and sunlight, respectively [54]. Similarly, certain visible light active metal oxides improved the catalytic efficiency of LDHs as Cai *et al.* synthesized CoAl/CdS LDH and examined their catalytic activities in the degradation of Rhodamine B (RhB) when exposed to visible light. In Comparison to LDHs alone, the composites' photocatalytic activity was noticeably higher. [55]

LDHs are often altered by incorporating metal elements (such as Fe, Ti, Al, and Mg e.t.c.) or metal oxides (like Fe_2O_3, TiO_2, and Cr_2O_3 etc.) to reduce the band gap and consequently enhance catalytic performance. Fe_2O_3/ZnTi-LDH and ZnO/ZnCr-LDH were synthesized and the findings showed that the metal oxide-metal element-LDH material's band gap significantly reduced as compared to the doped metal elements or metal oxides, and a high organic decomposition efficiency was demonstrated [56,57].

Currently, magnetic Fe_3O_4/LDH nanocomposites are of significant interest due to their applications in environmental remediation and photocatalysis. Several studies have documented the synthesis of Fe_3O_4/LDH nanocomposites and their applications in photocatalysis. Fe_3O_4/ZnCr LDH composites' photocatalytic potential was investigated by Chen *et al*. utilizing a two-step micro-hydrothermal method. By putting a magnet close by, they were able to demonstrate the magnetic separation of these materials in aqueous solutions and validate their magnetic characteristics. Because of this, the MO/ZnCr LDH nanohybrids can be separated effectively, which makes them perfect for environmental cleanup [58]. Lu *et al.* also investigated the degradation of organic dyes and spectral properties by integrating magnetic Fe_3O_4 nanoparticles with layered double hydroxides through a co-precipitation synthesis method. The resulting Fe_3O_4/MgAl-LDH nanocomposite had a distinctive shape and was remarkably effective for breaking down Congo red dyes in aqueous solutions because of the LDH heterojunction created with Fe_3O_4 nanoparticles [59]. Numerous studies have investigated magnetic Fe_3O_4/LDH composites for their ability to adsorb toxic metals from aqueous solutions. Yan *et al.* reported on the effectiveness of ZnAl LDHs and Fe_3O_4/ZnAl LDHs in adsorbing Cr (VI) from contaminated water [60].

(ii) Plasmonic metal loading

Photocatalysis involving various nanoparticles NPs, like Au and Ag significantly affects the optical and catalytic properties of semiconductors. Metallic silver nanoparticles (Ag NPs) absorb visible light through a process known as Surface Plasmon Resonance (SPR). In this phenomenon, the free electrons within the Ag NPs undergo a collective oscillation in response to the fluctuating electric field of the incident light. A notable study by Tonda *et al.* explores the Ag/NiAlLDH/g-C_3N_4 composite, which effectively removes organic pollutants under visible light through photocatalysis. Specifically, the LDH/C_3N_4 composites were created via this

hydrothermal process. Subsequently, a range of Ag/NiLDH/C_3N_4 composites was produced with 1 wt.% Ag and varying LDH concentrations. The interaction between Ag NPs and LDH/C_3N_4 significantly reduced the photoluminescence (PL) intensity, indicating a synergistic effect among the electronic states of the components. This interaction enhances charge separation and transfer within the three-component heterojunction, leading to a lower probability of recombination for the photogenerated electrons and holes [61]. Akbarzadeh *et al.* in their work also decorated Ag NPs on ternary Zn-Cu-Cr LDH/C_3N_5 composites and studied the photodegradation of tartrazine. The removal efficiency of tartrazine by these composites from aqueous solution under visible light exposure was higher in comparison to pure graphitic carbon nitride, LDH, and C_3N_5/LDH composite. The highly efficient photoactivity of C_3N_5/LDH/Ag photocatalyst was due to the high surface area achieved due to the hybridization of LDH and C_3N_5, the presence of silver NPs on catalyst surface improves the photocatalytic properties and effectiveness of charge transfer hence limiting the electron-hole recombination [62]. **Fig 4.** Shows the photocatalytic mechanism of pollutant degradation for MO and metal-loaded/MO-LDH composites.

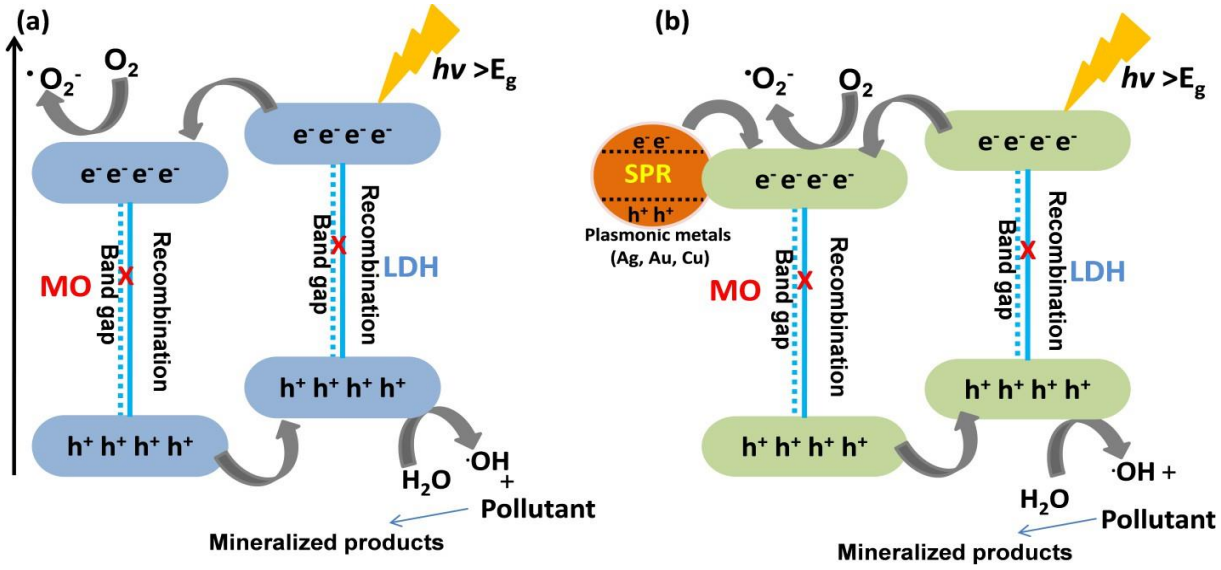

Fig.4. Photocatalytic mechanism of (a) MO/LDH and (b) metal-loaded MO/LDH composites

1.2. Methodology

1.2.1. Synthesis of LDHs

(i) Co-precipitation method

The co-precipitation method is widely favored for LDH synthesis due to its simplicity and cost-effectiveness. It involves the slow addition of mixed divalent and trivalent salt solutions to an alkaline solution in a fixed ratio. The mechanism involves the condensation of hexa-aqua metal complexes, leading to the formation of brucite-like layers. A base was used to maintain the solution at the appropriate pH, facilitating the precipitation of metal hydroxides. The resulting precipitates were stirred for a specified period, washed with distilled water and ethanol, and then dried.

(ii) Hydrothermal method

The hydrothermal method involves the thermal treatment of aqueous suspensions of oxides of divalent and trivalent metal ions kept for several hours or days in a teflon-lined autoclave under autogenous pressure. It involves transferring the prepared suspension into a teflon-lined stainless steel autoclave reactor and heating it to the desired temperature. After cooling the autoclave, the resultant was washed and dried to obtain the final product. This synthesis process offers advantages such as enhanced LDH crystallinity, larger crystallite size, and improved sample purity.

1.2.2. Synthesis of Metal oxides (MO)

(i) Synthesis of monoclinic-WO_3

Monoclinic WO_3 was synthesized using the co-precipitation method. To 0.5 M sodium tungstate solution concentrated hydrochloric acid (35%, 4 mL) was added dropwise, resulting in light yellow precipitates. The mixture was stirred at 80°C for 2 hours, then cooled to room temperature. The precipitates were washed with ethanol and DI water multiple times to remove impurities. After drying at 60°C to remove moisture, the sample was annealed at 600°C for one hour.

(ii) Synthesis of α-Fe_2O_3

Iron oxide nanoparticles were synthesized via hydrothermal treatment. Initially, 1.8 g of Fe $(NO_3)_3$•$9H_2O$ was dissolved in 20 mL of distilled water. NH_3•H_2O was gradually added to adjust the pH of the solution to approximately 9 under continuous stirring for 20 minutes. The solution was then transferred into a 100 mL Teflon-lined stainless steel autoclave and subjected to hydrothermal treatment at 120°C for 10 hours. Finally, the product was filtered, washed with distilled water and absolute ethanol, and dried at 80°C for 12 hours.

1.2.3. Synthesis of MO/LDH composites

(i) In-situ coprecipitation method

The process involves the dispersion known amount of MO in DI water followed by the drop wise addition of metal salt solutions. Further, the optimum pH of the solution was achieved by the addition of x M of NaOH and Na_2CO_3. The reaction mixture was stirred for about 24 hours and the resultant precipitates were washed with DI water several times for the removal of unwanted ions and were dried at 60°C for few hours.

(ii) Electrostatic assembly

MO/LDH composites were prepared using the electrostatic self-assembly method. LDH and MO were dispersed in a specific solvent in known amounts, mixed, and stirred for approximately 24 hours. The electrostatic interaction between oppositely charged catalysts facilitated the formation of their composites.

1.2.4. Synthesis of metal-loaded MO/LDH composites

Plasmonic metals were deposited on LDH, MO, and MO/LDH composites using the photo-reduction method. 100 mg of the catalyst was dispersed in a 50% IPA solution (10 mL). A specific amount of metal salt solution was added and kept for argon purging for few minutes to remove present oxygen and prevent oxidation. The mixture was then exposed to UV radiation (125 W Hg arc, 10.4 mW /cm ^{2}), filtered after illumination, washed with DI water, and dried.

1.3. Characterization Techniques

Various modified synthetic procedures were employed to synthesize LDHs, MO, and M@MO-LDH composites (detailed experimental protocols are outlined in their respective sections). The synthesized catalysts underwent comprehensive characterization using diverse techniques to study their surface, structural, and physicochemical properties.

1.3.1. X ray powder diffraction (XRD)

The crystallographic diffraction patterns were identified on an X-ray diffractometer (Xpert pro) equipped with Cu - K α radiation (1.5 4 Å), operating at 45 kV over a diffraction angle in the range of $5° \leq 2\,\theta \leq 80°$ (slit width: 10 mm; step scan size: 0.01; count time: 7.5 min with 10°/ min). The preparation of the sample involved placing a 0.2 mm-sized powder sample into a holder and subsequently creating a uniform surface by pressing it with glass.

1.3.2. Dynamic light scattering (DLS) and Zeta potential

Dynamic light scattering (DLS) and zeta analysis were used to measure the average hydrodynamic size, and the charge was analyzed upon Zetasizer (ZEN 3600, Malvern, U.K.). In this analysis, 2-5 mg of the catalyst was dispersed in the required amount of deionized (DI) water.

1.3.3. Fourier transform infrared spectroscopy (FTIR) and Raman spectroscopy

FTIR spectra were recorded by SHIMADZU IRTracer-100 (scan range: 4000- 500 cm^{-1}; resolution: 16 cm^{-1}; scans: 60; detector: MCT) sample in powder form was directly placed on the diamond of ATR IR. Raman spectroscopic measurements were performed on a Labram HR, Horiba micro Raman spectrometer with an excitation laser of 532 nm.

1.3.4. Surface area and porosity analysis (BET)

The surface area and pore size distribution of samples were analyzed with BET Autosorb iQ (Quantachrome Instruments version 3.01, U.S.A) for that 100-150 mg of sample was kept for

degassing using Helium gas at 150-200°C for 2 h to remove the moisture of the sample after that liquid nitrogen adsorption and desorption was performed with liquid nitrogen.

1.3.5. HRMS analysis

HRMS analysis of photodegraded samples was performed by QTOF mass spectrometer with UPLC (XEVO G2 XS), Waters (PDA detector 190-800 nm; resolution: > 40,000 FWMH).

1.3.6. Optical studies

The UV-visible diffuse reflectance spectra were obtained on a diffuse reflectance spectrophotometer (JASCO, V-750) using $BaSO_4$ as a reference in the 200-800 nm range. Photoluminescence (PL) spectra of each sample were measured using a Shimadzu RF-6000 spectrophotometer at room temperature PL for that about 2 mg of the sample was dispersed in 25 mL of distilled water (10 mm Quartz cell, scan range from 300 nm to 900 nm and slit width: Excitation and emission = 10 nm).

1.3.7. Morphological analysis

The morphologies and microstructures were observed using FESEM (Carl-Zeiss Sigma 500 FEG-SEM). The sample was prepared using the drop-casting method, dispersing 2 mg sample in 5 mL of deionized water. From this dispersion, drops were added onto copper tape, dried, and utilized for FESEM analysis (1 μm-500 nm; Magnification: 2.5-10 K X). Elemental composition and distribution were determined through Energy Dispersive Spectroscopy (Bruker EDS). High-resolution Transmission Electron Microscopy (HRTEM) images were captured using a JEOL JEM-2100 PLUS microscope.

1.3.8. X-ray photoelectron spectroscopy (XPS)

The elemental composition and oxidation state of the catalysts were determined by the XPS technique using Omicron ESCA made by Oxford Instrument Germany. X-rays with photon energy of 1486.7 eV were produced using Al K-alpha.

1.4. Adsorption and photocatalytic studies

1.4.1. Adsorption studies

The adsorption studies of adsorbents were examined using tetracycline as a model pollutant. The effect of various parameters (including pollutant concentration, adsorbent dosage, and contact time) was investigated. During adsorption studies, a set of test tubes containing 5mL of the pollutant of specific concentration and a required amount of catalyst was added and kept on stirring at (800 rpm) under dark. After a fixed interval, the test tube was removed, the solution was centrifuged, and the concentration was determined using a UV-Vis spectrophotometer SHIMADZU, UV-2600 and JASCO, V-750. To understand the adsorption mechanism on the catalyst surface Langmuir and Freundlich models were studied. Additionally, pseudo-first and second-order kinetic models were examined to predict reaction kinetics in adsorption and photodegradation. Detailed procedures and equations are elaborated in their respective chapters.

1.4.2. Photocatalytic degradation of water pollutants (pharmaceutical drugs and dyes)

Photodegradation studies of various adsorbents were conducted using different model pollutants. Test tubes containing a specified volume of pollutant at a specific concentration and a known amount of catalyst were stirred in the dark to achieve adsorption and desorption equilibrium between catalyst and pollutant molecules followed by the exposure of test tube under visible light irradiation (50W lamp; intensity:100W/m^2; λ >350 nm). At regular intervals, the test tubes were removed, the solutions were centrifuged, and the concentrations were measured using a UV-Vis spectrophotometer (SHIMADZU, UV-2600). The reaction kinetics and degradation efficiency were also estimated (Detailed procedures and equations are elaborated in their respective chapters). The mineralization efficiency of the pollutant was calculated with the help of total organic carbon (TOC) analysis. The intermediates and final products formed during the degradation were investigated using HR-MS analysis performed by QTOF mass spectrometer with UPLC (XEVO G2 XS), Waters (PDA detector 190-800 nm; resolution: > 40,000 FWMH). The setup for photocatalytic degradation of pollutants is shown in **Fig. 4.**

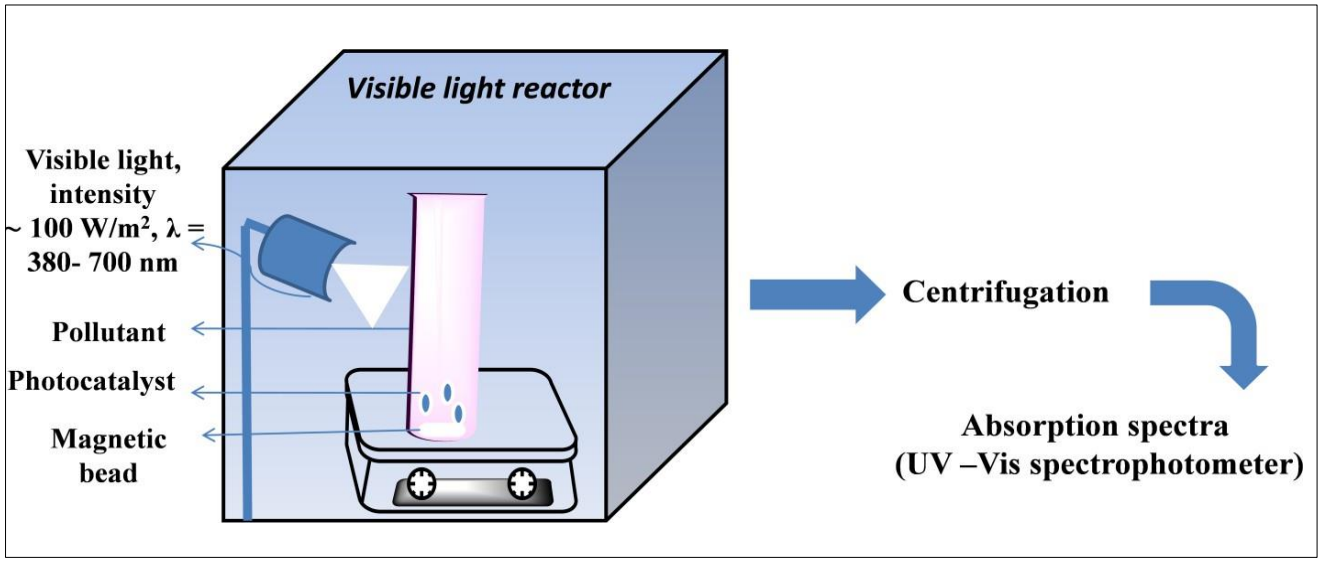

Fig.4. Schematic depiction of reaction setup for photocatalytic degradation of pollutants

Table 1.1: Model pollutants chosen for degradation using prepare photocatalysts

S.No.	Pollutant	Chemical formula	Lambda max	Structure
1.	Tetracycline	$C_{22}H_{24}N_2O_8$	360 nm	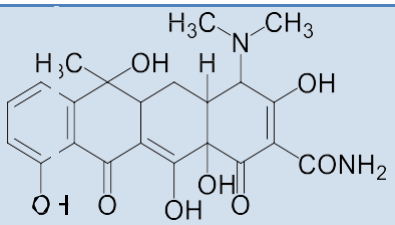
2.	Ciprofloxacin	$C_{17}H_{18}FN_3O_3$	274 nm	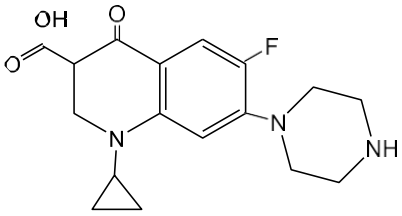
3.	Malachite green	$C_{23}H_{25}N_2Cl$	617 nm	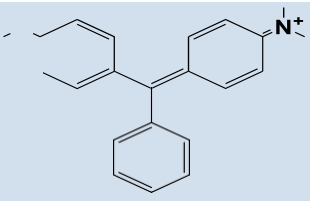

1.5. Research gaps

LDHs are a type of photocatalysts that can break down organic pollutants, including pharmaceutical and industrial waste, under visible light. Surface modifications, such as forming composites with metal oxides and incorporating plasmonic metal loadings, enhance their adsorption capacity and improve their efficiency in photocatalytic degradation. In the scientific literature, various catalysts have been studied. Among these, metal oxides have been widely used as photocatalysts for many decades. This is because they are biocompatible, stable in different conditions, and can produce charge carriers when exposed to light. The favorable combination of their electronic structure, ability to absorb light, transport charges, and maintain excited states makes metal oxides suitable for photocatalytic applications.

WO_3 is a highly promising n-type semiconductor material that shows substantial absorption in the visible range with a band gap between 2.4 and 2.8 eV. Its intrinsic properties make it a remarkable semiconductor with significant photocatalytic applications. Notably, WO_3 demonstrates excellent adsorption capabilities and efficient photocatalytic performance under visible light, effectively removing various contaminants. Coupling LDHs with the optimum amount of WO_3 can further improve their photocatalytic efficiency towards pollutant degradation. The study of optimum WO_3 amount loading upon ZnCr LDH towards pharmaceutical waste degradation under visible light irradiation has not been studied.

The combination of plasmonic metal-loaded metal oxides with LDHs effectively enhances the visible light responsiveness of layered double hydroxides via heterojunction formation. The visible light response of the LDHs with band gap > 3eV can be improved by plasmonic metal loading along with MO loadings. MgAl LDHs are valued for their stability, ease of synthesis, and cost-effectiveness as catalysts. Nonetheless, their broad band gap restricts their photocatalytic effectiveness under visible light with only a few reports in the literature demonstrating pollutant degradation under visible light. Its applications in photocatalysis can be explored by forming heterostructure WO_3 and Ag@WO_3 composites.

Similarly, hematite (α-Fe_2O_3), possessing a rhombohedral-hexagonal structure, stands out as the most stable form of iron oxide. It holds tremendous potential in the photocatalytic degradation of

diverse organic pollutants due to its antiferromagnetic property, cost-effectiveness, non-toxic nature, exceptional stability, high reliability, corrosion resistance, and appropriate band gap, enabling the absorption of a broad spectrum of solar radiation. No reports have been reported on the coupling of NiCo LDH with Fe_2O_3 towards the degradation of organic dyes. Iron oxide nanoparticles have been extensively studied for their role in photodegradation, particularly with metal loading. However, the synthesis of LDH/Fe_2O_3 composites using a novel approach remains unexplored. Hematite (α-Fe_2O_3) itself is a visible-active metal oxide semiconductor and serves as an efficient photocatalyst under visible light. Incorporating hematite into LDHs can enhance their light absorption capacity. Moreover, additional metal loadings on these composites can further improve their ability to absorb visible sunlight, leveraging the surface plasmon resonance (SPR) effect from surface electrons. This enhances the photocatalyst's responsiveness to visible light, thus utilizing solar energy effectively, a renewable energy source.

1.6. Objectives

1. Preparation and characterization of Zn-Fe, Zn-Cr, Co-Ni etc. layered double hydroxides (LDHs).

2. Influence of metal (Ag, Cu, Fe etc.) loaded MO (TiO_2, ZnO, WO_3 etc.) loading onto these LDHs and their physicochemical properties.

3. Study of adsorption property and photocatalytic activity of these M /MO-LDH. heterocomposites for degradation of organic pollutants (phenols, nitro aromatics, pesticides etc.).

References

[1] A.A. Sharwani, K.B. Narayanan, M.E. Khan, S.S. Han, Photocatalytic degradation activity of goji berry extract synthesized silver-loaded mesoporous zinc oxide (Ag@ZnO) nanocomposites under simulated solar light irradiation, Sci. Rep. 12 (2022) 1–18. https://doi.org/10.1038/s41598-022-14117-w.

[2] G. Mishra, B. Dash, S. Pandey, Layered double hydroxides: A brief review from fundamentals to application as evolving biomaterials, Appl. Clay Sci. 153 (2018) 172–

186. https://doi.org/10.1016/j.clay.2017.12.021.

[3] S. Tang, Y. Yao, T. Chen, D. Kong, W. Shen, H.K. Lee, Recent advances in the application of layered double hydroxides in analytical chemistry: A review, Anal. Chim. Acta. 1103 (2020) 32–48. https://doi.org/10.1016/j.aca.2019.12.065.

[4] S. Velu, K. Suzuki, T. Osaki, A comparative study of reactions of methanol over catalysts derived from NiAl- and CoAl-layered double hydroxides and their Sn-containing analogues, Catal. Letters. 69 (2000) 43–50. https://doi.org/10.1023/a:1019013821509.

[5] J. Kameliya, A. Verma, P. Dutta, C. Arora, S. Vyas, R.S. Varma, Layered Double Hydroxide Materials: A Review on Their Preparation, Characterization, and Applications, Inorganics. 11 (2023). https://doi.org/10.3390/inorganics11030121.

[6] S. Marappa, S. Radha, P.V. Kamath, Nitrate-intercalated layered double hydroxides - Structure model, order, and disorder, Eur. J. Inorg. Chem. (2013) 2122–2128. https://doi.org/10.1002/ejic.201201405.

[7] G. Arrabito, A. Bonasera, G. Prestopino, A. Orsini, A. Mattoccia, E. Martinelli, B. Pignataro, P.G. Medaglia, Layered double hydroxides: A toolbox for chemistry and biology, Crystals. 9 (2019). https://doi.org/10.3390/cryst9070361.

[8] L. Lv, P. Sun, Z. Gu, H. Du, X. Pang, X. Tao, R. Xu, L. Xu, Removal of chloride ion from aqueous solution by ZnAl-NO_3 layered double hydroxides as anion-exchanger, J. Hazard. Mater. 161 (2009) 1444–1449. https://doi.org/10.1016/j.jhazmat.2008.04.114.

[9] N. Ghanbari, H. Ghafuri, Design and preparation the novel polymeric layered double hydroxide nanocomposite (LDH/Polymer) as an efficient and recyclable adsorbent for the removal of methylene blue dye from water, Environ. Technol. Innov. 26 (2022) 102377. https://doi.org/10.1016/j.eti.2022.102377.

[10] N. Morel-Desrosiers, J. Pisson, Y. Israeli, C. Taviot-Guého, J.P. Besse, J.P. Morel, Intercalation of dicarboxylate anions into a Zn-Al-Cl layered double hydroxide: Microcalorimetric determination of the enthalpies of anion exchange, J. Mater. Chem. 13 (2003) 2582–2585. https://doi.org/10.1039/b303953f.

[11] L.P.F. Benício, R.A. Silva, J.A. Lopes, D. Eulálio, R.M.M. dos Santos, L.A. De Aquino, L. Vergütz, R.F. Novais, L.M. Da Costa, F.G. Pinto, J. Tronto, Layered double hydroxides: Nanomaterials for applications in agriculture | Hidróxidos duplos lamelares: Nanomateriais para aplicações na agricultura, Rev. Bras. Cienc. Do Solo. 39 (2015) 1–13.

https://doi.org/10.1590/01000683rbcs20150817.

[12] F.Z. Janani, N. Taoufik, H. Khiar, W. Boumya, A. Elhalil, M. Sadiq, A. V. Puga, N. Barka, Nanostructured layered double hydroxides based photocatalysts: Insight on synthesis methods, application in water decontamination/splitting and antibacterial activity, Surfaces and Interfaces. 25 (2021) 101263. https://doi.org/10.1016/j.surfin.2021.101263.

[13] N.N. Leont'eva, V. Drozdov, B. Bel'skaya, S. V. Cherepanova, Structural Analysis of Defects in Layered Double Hydroxides and Related Mixed Oxides, Russ. J. Gen. Chem. 90 (2020) 509–522. https://doi.org/10.1134/S1070363220030275.

[14] Y. Zhao, H. Hu, X. Yang, D. Yan, Q. Dai, Tunable Electronic Transport Properties of 2D Layered Double Hydroxide Crystalline Microsheets with Varied Chemical Compositions, Small. (2016) 4471–4476. https://doi.org/10.1002/smll.201601354.

[15] M. Sahoo, K.M. Parida, Pd(II) loaded on diamine functionalized LDH for oxidation of primary alcohol using water as solvent, Appl. Catal. A Gen. 460–461 (2013) 36–45. https://doi.org/10.1016/j.apcata.2013.04.003.

[16] W. Lin, H. Frei, Anchored metal-to-metal charge-transfer chromophores in a mesoporous silicate sieve for visible-light activation of titanium centers, J. Phys. Chem. B. 109 (2005) 4929–4935. https://doi.org/10.1021/jp040677z.

[17] Y. Lee, J.H. Choi, H.J. Jeon, K.M. Choi, J.W. Lee, J.K. Kang, Titanium-embedded layered double hydroxides as highly efficient water oxidation photocatalysts under visible light, Energy Environ. Sci. 4 (2011) 914–920. https://doi.org/10.1039/c0ee00285b.

[18] C.H. Ravikumar, M. Sakar, A. Mahto, R.T. Nanjundaiah, R. Thippeswamy, S.R. Teixeira, R.G. Balakrishna, Observation of oxo-bridged yttrium in TiO_2 nanostructures and their enhanced photocatalytic hydrogen generation under UV/Visible light irradiations, Mater. Res. Bull. 104 (2018) 212–219. https://doi.org/10.1016/j.materresbull.2018.04.014.

[19] L. Mohapatra, K. Parida, A review of solar and visible light active oxo-bridged materials for energy and environment, Catal. Sci. Technol. 7 (2017) 2153–2164. https://doi.org/10.1039/c7cy00116a.

[20] K. El Hassani, B.H. Beakou, D. Kalnina, E. Oukani, A. Anouar, Effect of morphological properties of layered double hydroxides on adsorption of azo dye Methyl Orange: A comparative study, Appl. Clay Sci. 140 (2017) 124–131.

https://doi.org/10.1016/j.clay.2017.02.010.

[21] S. Bin Lee, E.H. Ko, J.Y. Park, J.M. Oh, Mixed metal oxide by calcination of layered double hydroxide: Parameters affecting specific surface area, Nanomaterials. 11 (2021) 1–19. https://doi.org/10.3390/nano11051153.

[22] M.Q. Zhao, Q. Zhang, W. Zhang, J.Q. Huanag, Y. Zhang, D.S. Su, F. Wei, Embedded high density metal nanoparticles with extraordinary thermal stability derived from guest- host mediated layered double hydroxides, J. Am. Chem. Soc. 132 (2010) 14739–14741. https://doi.org/10.1021/ja106421g.

[23] M. Xu, M. Wei, Layered Double Hydroxide-Based Catalysts: Recent Advances in Preparation, Structure, and Applications, Adv. Funct. Mater. 28 (2018) 1–20. https://doi.org/10.1002/adfm.201802943.

[24] J. Mittal, Recent progress in the synthesis of Layered Double Hydroxides and their application for the adsorptive removal of dyes: A review, J. Environ. Manage. 295 (2021) 113017. https://doi.org/10.1016/j.jenvman.2021.113017.

[25] X. Bian, S. Zhang, Y. Zhao, R. Shi, T. Zhang, Layered double hydroxide-based photocatalytic materials toward renewable solar fuels production, InfoMat. 3 (2021) 719–738. https://doi.org/10.1002/inf2.12192.

[26] J. Hu, Y.Q. Liang, S.L. Wu, Z.Y. Li, C.S. Shi, S.Y. Luo, H.J. Sun, S.L. Zhu, Z.D. Cui, Hierarchical nickle-iron layered double hydroxide composite electrocatalyst for efficient oxygen evolution reaction, Mater. Today Nano. 17 (2022) 2–10. https://doi.org/10.1016/j.mtnano.2021.100150.

[27] K. Teramura, S. Iguchi, Y. Mizuno, T. Shishido, T. Tanaka, Photocatalytic conversion of CO 2 in water over layered double hydroxides, Angew. Chemie - Int. Ed. 51 (2012) 8008–8011. https://doi.org/10.1002/anie.201201847.

[28] L.N. Stepanova, O.B. Belskaya, A. V. Vasilevich, N.N. Leont'eva, O.N. Baklanova, V.A. Likholobov, Effect of the Composition of Initial Components and the Conditions of Activation on the Mechanochemical Synthesis of Magnesium–Aluminum Layered Double Hydroxides, Kinet. Catal. 59 (2018) 521–531. https://doi.org/10.1134/S0023158418040134.

[29] H. Ye, S. Liu, D. Yu, X. Zhou, L. Qin, C. Lai, F. Qin, M. Zhang, W. Chen, W. Chen, L. Xiang, Regeneration mechanism, modification strategy, and environment application of

layered double hydroxides: Insights based on memory effect, Coord. Chem. Rev. 450 (2022) 214253. https://doi.org/10.1016/j.ccr.2021.214253.

[30] A.A.A. Ahmed, Z.A. Talib, M.Z. Bin Hussein, A. Zakaria, Improvement of the crystallinity and photocatalytic property of zinc oxide as calcination product of Zn-Al layered double hydroxide, J. Alloys Compd. 539 (2012) 154–160. https://doi.org/10.1016/j.jallcom.2012.05.093.

[31] F.Z. Mahjoubi, A. Khalidi, M. Abdennouri, N. Barka, Zn–Al layered double hydroxides intercalated with carbonate, nitrate, chloride and sulphate ions: Synthesis, characterisation and dye removal properties, J. Taibah Univ. Sci. 11 (2017) 90–100. https://doi.org/10.1016/j.jtusci.2015.10.007.

[32] K. Morimoto, K. Tamura, N. Iyi, J. Ye, H. Yamada, Adsorption and photodegradation properties of anionic dyes by layered double hydroxides, J. Phys. Chem. Solids. 72 (2011) 1037–1045. https://doi.org/10.1016/j.jpcs.2011.05.018.

[33] M. Islam, M. Mostafa, Textile Dyeing Effluents and Environment Concerns - A Review, J. Environ. Sci. Nat. Resour. 11 (2019) 131–144. https://doi.org/10.3329/jesnr.v11i1-2.43380.

[34] A.M. Awad, S.M.R. Shaikh, R. Jalab, M.H. Gulied, M.S. Nasser, A. Benamor, S. Adham, Adsorption of organic pollutants by natural and modified clays: A comprehensive review, Sep. Purif. Technol. 228 (2019) 115719. https://doi.org/10.1016/j.seppur.2019.115719.

[35] K.C. Christoforidis, M. Louloudi, Y. Deligiannakis, Effect of humic acid on chemical oxidation of organic pollutants by iron(II) and H_2O_2: A dual mechanism, J. Environ. Chem. Eng. 3 (2015) 2991–2996. https://doi.org/10.1016/j.jece.2015.02.005.

[36] M. Pirilä, M. Saouabe, S. Ojala, B. Rathnayake, F. Drault, A. Valtanen, M. Huuhtanen, R. Brahmi, R.L. Keiski, Photocatalytic degradation of organic pollutants in wastewater, Top. Catal. 58 (2015) 1085–1099. https://doi.org/10.1007/s11244-015-0477-7.

[37] H. Starukh, S. Levytska, The simultaneous anionic and cationic dyes removal with Zn–Al layered double hydroxides, Appl. Clay Sci. 180 (2019). https://doi.org/10.1016/j.clay.2019.105183.

[38] Í.M.G.L. de Sá, I. de M. Agra, K.J. dos S. Leite, L.F.A. de M. Oliveira, E.J. da S. Fonseca, L.M.T. de M. Oliveira, C.L. de P. e S. Zanta, J.L. da S. Duarte, Magnetic MgAl-LDH for Adsorptive Removal of Malachite Green from Water, Int. J. Environ. Res. 17 (2023) 30.

https://doi.org/10.1007/s41742-023-00521-1.

[39] L. Lu, J. Li, D.H.L. Ng, P. Yang, P. Song, M. Zuo, Synthesis of novel hierarchically porous Fe_3O_4@MgAl–LDH magnetic microspheres and its superb adsorption properties of dye from water, J. Ind. Eng. Chem. 46 (2017) 315–323. https://doi.org/10.1016/j.jiec.2016.10.045.

[40] X.Y. Yu, T. Luo, Y. Jia, R.X. Xu, C. Gao, Y.X. Zhang, J.H. Liu, X.J. Huang, Three-dimensional hierarchical flower-like Mg-Al-layered double hydroxides: Highly efficient adsorbents for As(v) and Cr(vi) removal, Nanoscale. 4 (2012) 3466–3474. https://doi.org/10.1039/c2nr30457k.

[41] Y. Cao, G. Li, X. Li, Graphene/layered double hydroxide nanocomposite: Properties, synthesis, and applications, Chem. Eng. J. 292 (2016) 207–223. https://doi.org/10.1016/j.cej.2016.01.114.

[42] S. Verma, S. Verma, T. Das, B. Verma, Graphene-based nanocomposites: An efficient detoxification agent for heavy metal removal from wastewater, Indian J. Chem. Technol. 30 (2023) 411–422. https://doi.org/10.56042/ijct.v30i4.63284.

[43] J. Li, H. Yu, X. Zhang, R. Zhu, L. Yan, Crosslinking acrylamide with EDTA-intercalated layered double hydroxide for enhanced recovery of Cr(VI) and Congo red: Adsorptive and mechanistic study, Front. Environ. Sci. Eng. 14 (2020) 1–13. https://doi.org/10.1007/s11783-020-1229-x.

[44] Z. Chen, A. Jawad, Z. Liao, Z. Zhou, A. Khan, T. Wang, J. Ifthikar, A. Shahzad, Z. Chen, Fe-MoS_4: An Effective and Stable LDH-Based Adsorbent for Selective Removal of Heavy Metals, ACS Appl. Mater. Interfaces. 9 (2017) 28451–28463. https://doi.org/10.1021/acsami.7b07208.

[45] M. Cheng, G. Zeng, D. Huang, C. Lai, P. Xu, C. Zhang, Y. Liu, Hydroxyl radicals based advanced oxidation processes (AOPs) for remediation of soils contaminated with organic compounds: A review, Chem. Eng. J. 284 (2016) 582–598. https://doi.org/10.1016/j.cej.2015.09.001.

[46] L. Mohapatra, K. Parida, A review on the recent progress, challenges and perspective of layered double hydroxides as promising photocatalysts, J. Mater. Chem. A. 4 (2016) 10744–10766. https://doi.org/10.1039/c6ta01668e.

[47] Y. Zhao, S. Zhang, B. Li, H. Yan, S. He, L. Tian, W. Shi, J. Ma, M. Wei, D.G. Evans, X.

Duan, A family of visible-light responsive photocatalysts obtained by dispersing CrO_6 octahedra into a hydrotalcite matrix, Chem. - A Eur. J. 17 (2011) 13175–13181. https://doi.org/10.1002/chem.201101874.

[48] G. Chen, S. Qian, X. Tu, X. Wei, J. Zou, L. Leng, S. Luo, Enhancement photocatalytic degradation of rhodamine B on nanoPt intercalated Zn-Ti layered double hydroxides, Appl. Surf. Sci. 293 (2014) 345–351. https://doi.org/10.1016/j.apsusc.2013.12.165.

[49] H. Boumeriame, E.S. Da Silva, A.S. Cherevan, T. Chafik, J.L. Faria, D. Eder, Layered double hydroxide (LDH)-based materials: A mini-review on strategies to improve the performance for photocatalytic water splitting, J. Energy Chem. 64 (2021) 406–431. https://doi.org/10.1016/j.jechem.2021.04.050.

[50] D.P. Sahoo, S. Nayak, K.H. Reddy, S. Martha, K. Parida, Fabrication of a $Co(OH)_2$/ZnCr ldh "p-n" heterojunction photocatalyst with enhanced separation of charge carriers for efficient visible-light-driven H_2 and O_2 evolution, Inorg. Chem. 57 (2018) 3840–3854. https://doi.org/10.1021/acs.inorgchem.7b03213.

[51] V. Hasija, P. Raizada, A. Hosseini-Bandegharaei, P. Singh, V.H. Nguyen, Synthesis and Photocatalytic Activity of Ni–Fe Layered Double Hydroxide Modified Sulphur Doped Graphitic Carbon Nitride (SGCN/Ni–Fe LDH) Photocatalyst for 2,4-Dinitrophenol Degradation, Top. Catal. 63 (2020) 1030–1045. https://doi.org/10.1007/s11244-020-01359-z.

[52] P. Shandilya, R. Sharma, R.K. Arya, A. Kumar, D.V.N. Vo, G. Sharma, Recent progress and challenges in photocatalytic water splitting using layered double hydroxides (LDH) based nanocomposites, Int. J. Hydrogen Energy. 47 (2022) 37438–37475. https://doi.org/10.1016/j.ijhydene.2021.08.190.

[53] R. Lu, X. Xu, J. Chang, Y. Zhu, S. Xu, F. Zhang, Improvement of photocatalytic activity of TiO_2 nanoparticles on selectively reconstructed layered double hydroxide, Appl. Catal. B Environ. 111–112 (2012) 389–396. https://doi.org/10.1016/j.apcatb.2011.10.022.

[54] Y. Dou, S. Zhang, T. Pan, S. Xu, A. Zhou, M. Pu, H. Yan, J. Han, M. Wei, D.G. Evans, X. Duan, TiO_2@layered double hydroxide core-shell nanospheres with largely enhanced photocatalytic activity toward O_2 generation, Adv. Funct. Mater. 25 (2015) 2243–2249. https://doi.org/10.1002/adfm.201404496.

[55] P. Cai, S. Ci, N. Wu, Y. Hong, Z. Wen, Layered structured CoAl/CdS-LDHs

nanocomposites as visible light photocatalyst, Phys. Status Solidi Appl. Mater. Sci. 214 (2017). https://doi.org/10.1002/pssa.201600910.

[56] Y. Meng, X. Zhang, G. Pan, S. Xia, Z. Ni, Orthogonal synthesis of a novel hybrid layered material containing three different zincous components and its photocatalytic property investigation, J. Hazard. Mater. 350 (2018) 144–153. https://doi.org/10.1016/j.jhazmat.2018.02.021.

[57] S.J. Xia, X.B. Zhou, W. Shi, G.X. Pan, Z.M. Ni, Photocatalytic property and mechanism studies on acid red 14 by M xOy/ZnTi-layered double hydroxides (M = Fe, Sn, Ce), J. Mol. Catal. A Chem. 392 (2014) 270–277. https://doi.org/10.1016/j.molcata.2014.05.028.

[58] D. Chen, Y. Li, J. Zhang, J. Zhou, Y. Guo, H. Liu, Magnetic Fe_3O_4/ZnCr-layered double hydroxide composite with enhanced adsorption and photocatalytic activity, Chem. Eng. J. 185–186 (2012) 120–126. https://doi.org/10.1016/j.cej.2012.01.059.

[59] R.R. Shan, L.G. Yan, K. Yang, S.J. Yu, Y.F. Hao, H.Q. Yu, B. Du, Magnetic Fe_3O_4/MgAl-LDH composite for effective removal of three red dyes from aqueous solution, Chem. Eng. J. 252 (2014) 38–46. https://doi.org/10.1016/j.cej.2014.04.105.

[60] L.G. Yan, K. Yang, R.R. Shan, H.Q. Yu, B. Du, Calcined ZnAl- and Fe_3O_4/ZnAl-layered double hydroxides for efficient removal of Cr(vi) from aqueous solution, RSC Adv. 5 (2015) 96495–96503. https://doi.org/10.1039/c5ra17058c.

[61] S. Tonda, W.K. Jo, Plasmonic Ag nanoparticles decorated NiAl-layered double hydroxide/graphitic carbon nitride nanocomposites for efficient visible-light-driven photocatalytic removal of aqueous organic pollutants, Catal. Today. 315 (2018) 213–222. https://doi.org/10.1016/j.cattod.2017.12.019.

[62] A. Akbarzadeh, Y. Khazani, S.S. Khaloo, M. Ghalkhani, Highly effectual photocatalytic degradation of tartrazine by using Ag nanoparticles decorated on Zn-Cu-Cr layered double hydroxide@ 2D graphitic carbon nitride (C_3N_5), Environ. Sci. Pollut. Res. 30 (2023) 12903–12915. https://doi.org/10.1007/s11356-022-23001-z.

CHAPTER- 2

Effective performance of monoclinic WO_3/ZnCr layered double hydroxide composites towards the degradation of tetracycline under visible light irradiation

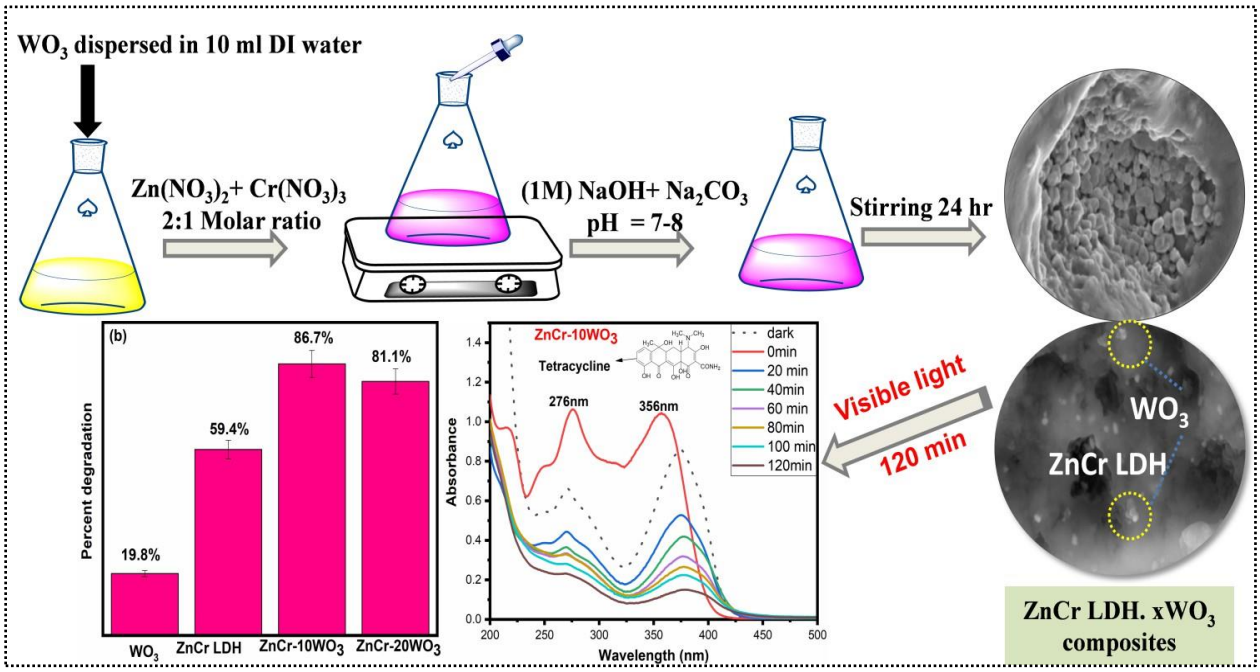

Schematic outline: The study demonstrates the superior photocatalytic efficiency of tungsten trioxide (WO_3) impregnated ZnCr LDH for the removal of tetracycline (pharmaceutical waste) under visible light irradiation. Optimal 10 wt.% WO_3-ZnCr LDH degraded TC with high effectiveness (86.7%) in 120 minutes. The enhanced performance of the binary composites results from a higher specific surface area and improved separation of photo-generated electrons and holes facilitated by a conventional class II heterojunction between ZnCr LDH and monoclinic-WO_3.

This chapter focuses on addressing the first and second objectives, which involve the preparation and characterization of LDHs (Zn-Fe, Zn-Cr, Co-Ni etc.) Additionally, the chapter examines the influence of loading materials, including TiO_2, ZnO and WO_3 etc., onto these LDHs, and investigates how these modifications affect their physicochemical properties.

2.1. Introduction

An escalating global trend of organic contaminants in water sources is evident due to increasing pollution levels and ongoing industrial and agricultural development. Recent years have seen rapid industrialization in many nations, leading to heightened pollution from heavy metals, antimicrobials, azo dyes, and other pollutants [1–4]. Among these, antibiotic-related ecological contamination poses a critical concern, primarily due to their antibiotic-resistant properties and chemical stability [5]. Presence of tetracycline in water bodies is presently a subject of incredible concern. In recent years, various techniques like adsorption, electrolysis, microbial degradation, and photodegradation have been devoted to the removal of TC and other harmful pollutants from wastewater [6–9]. Tetracycline is a broad spectrum antibiotic with molecular formula $C_{22}H_{24}N_2O_8$ that is effective against a wide range of bacterial infections. Its presence in wastewater can persist in the environment and affect aquatic organisms, potentially disrupting ecosystems. It can cause harm to humans including allergic reactions, liver and kidney damage. The wastewater containing tetracycline can contribute to the development of antibiotic-resistant bacteria, which poses a significant public health concern. Consequently, the effective removal of tetracycline residues from the environment is crucial for both ecological health and human safety. Controlling the entry of antibiotics into the environment primarily involves treating wastewater that contains these substances. Currently, photocatalysis has emerged as an eco- friendly and economical method for removing antibiotics from water sources. Additionally, this process can convert antibiotics into less harmful organic molecules and easily degradable compounds, thereby diminishing or eliminating their antibacterial properties. [10–13].

Layered double hydroxides are two-dimensional ionic clays made up of positively charged brucite-like layers and negatively charged interlayer anions are known for their great stability, low cost, flexible structure, effective support and narrow band gap semiconductor properties which make them attractive in visible light photocatalysis [14,15]. Sometimes poor visible light response and high recombination of photoinduced charge pairs of LDHs result in its low photocatalytic efficiency. Therefore several modifications have been brought to their structural and electronic composition by adopting different strategies such as cation doping, anion intercalation, calcination, heterostructure formation with semiconductors, and noble metal loading [16–23]. Which has been investigated to enhance the performances in various fields such

as photocatalytic removal of organic pollutants, photocatalytic reduction of CO_2, and other chemical transformations [24–27]. Among the various photocatalytic materials reported, layered substances such as ZnCr layered double hydroxide (LDH) stand out as highly effective photocatalysts due to their suitable redox potential and exceptional light-harvesting abilities. The capacity of ZnCr LDH to absorb visible light is linked to interelectronic excitations, such as metal-to-metal charge transfer (MMCT) facilitated by oxo-bridged bimetallic connections [28,29]. Photocatalytic systems involving WO_3 and LDH have been reported, such as efficient Z scheme WO_3/ZnS photocatalyst for complete degradation of tetracycline and high-performance Z-scheme 2D/2D WO_3@CoFe-LDH nanocomposite for the synchronic degradation of the mixture of azo dyes by sonocatalytic ozonation process [30,31].

WO_3 has been regarded as a promising n-type semiconducting material, with band gaps ranging from 2.4 and 2.8 eV and showing strong absorption in the visible region [32]. It is also found to be a semiconductor with remarkable photocatalytic applications owing to its intrinsic properties [33–35]. It demonstrates good adsorption and visible-light-driven photocatalytic capabilities for removing different contaminants. Also, the high oxidation potential of the valence band of WO_3 makes it capable of oxidizing H_2O and ^{-}OH groups to obtain $HO^{\bullet}$. Moreover, the oxygen vacancies present in WO_3 also affect the surface properties of materials upon heterojunction formation such as adsorption and improvement of optical absorption by separating photogenerated charge carriers hence, making it an efficient photocatalyst [36–39]. The composite formed by LDH and WO_3 is an effective adsorbent and photocatalyst for degrading organic pollutants due to its nontoxicity and synergic effect.

In this work positively charged ZnCr LDH was coupled with WO_3 nanoparticles via in situ coprecipitation method and the effect of percent loading of WO_3 upon LDH surface was studied towards the degradation of tetracycline. This study assessed the photocatalytic performance of ZnCr LDH and investigated how varying WO_3 loading affects its ability to degrade tetracycline antibiotics under visible light irradiation. The kinetics studies were performed for all composites 10% WO_3 loaded LDH shows better fit for pseudo first-order reaction with maximum degradation efficiency and rate constant for ZnCr-10WO_3 (i.e., 86.7% and 1.5×10^{-2} min^{-1}).

2.2. Experimental section

2.2.1. Chemicals and reagents

Zinc nitrate hexahydrate ($Zn(NO_3)_2$. $6H_2O$), Chromium nitrate nonahydrate ($Cr(NO_3)_3.9H_2O$), Sodium hydroxide (NaOH), Sodium carbonate (Na_2CO_3), Sodium tungstate ($Na_2WO_4.2H_2O$), Hydrochloric acid (HCl 35%) all were acquired from Loba Chemie (India). Tetracycline (500 mg) was purchased from CIPLA Pharmaceuticals. Double distilled water (D.I.) water used during the whole study was obtained from Milli-Q (Millipore), an ultra-filtration system (conductivity= 35mho cm^{-1} at 25º C).

2.2.2. Synthesis of ZnCr LDH

For the synthesis of ZnCr layered double hydroxide (LDH) Co-precipitation method has been adopted. Aqueous solution of $Zn(NO_3)_2.6H_2O$ and $Cr(NO_3)_3.9H_2O$ ratio (2:1) was prepared in 40 mL of DI water to this solution, 1M of NaOH and Na_2CO_3 was added to attain pH 7-8. The resultant solution was kept on stirring for about 24 hours. After the completion of the reaction, the obtained precipitates were filtered and washed several times using distilled water and ethanol to remove dissolved ions, and the product was dried at 70°C [40].

2.2.3. Synthesis of monoclinic WO_3

For the synthesis of monoclinic WO_3 Co-precipitation method was used. A solution of 0.5M of sodium tungstate was prepared in DI water to attain transparency. 4 mL of concentrated Hydrochloric acid (35%) was added dropwise and light yellow colored precipitates were observed. The mixture was stirred at 80°C for 2 h and cooled down at room temperature. The precipitates so obtained were washed with ethanol and DI water several times to remove other impurities. The precipitates were dried at 60° to remove moisture and the sample was annealed at 600°C for one hour [41].

2.2.4. Synthesis of WO_3/ZnCr LDH composites

ZnCr LDH and heterostructures ZnCr-xWO_3 (x=10 and 20%) were formed by the in situ Co-precipitation process. During synthesis, a known amount of WO_3 was dispersed in 10 mL of DI

water followed by dropwise addition of solution of 12 mM of Zn $(NO_3)_2.6H_2O$ and 6 mM of Cr $(NO_3)_3.9H_2O$ (2:1). Further, the pH of the solution was achieved to 7-8 by the addition of 1M of NaOH and Na_2CO_3. The reaction mixture was stirred for about 24 h and the resultant precipitates were washed with DI water several times for the removal of unwanted ions and were dried at 60°C for few hours. The ratio between ZnCr LDH and monoclinic-WO_3 was controlled by varying the weight ratio of monoclinic-WO_3 (10 mg and 20 mg) and keeping the amount of ZnCr LDH constant and were named ZnCr-10WO_3, ZnCr-20WO_3.

2.2.5. Photocatalytic activity

For the photocatalytic experiment, Tetracycline (TC) was taken as a model pollutant with an actual concentration of 20 ppm. From the above solution, only 5 ml of the pollutant was added to 5 mg of photocatalyst {ZnCr LDH and ZnCr-xWO_3 composites (x=10 and 20%)} before irradiation of the light source, the catalyst and pollutant solution was stirred in dark for 30 min to accomplish adsorption-desorption equilibrium. Further, to measure the photocatalytic activity of the catalyst, the solution was irradiated with a visible light source (50W lamp; intensity: 100W/m^2; λ >350 nm) for about 120 minutes and with respect to different intervals of time i.e., after every 20 min of interval the solution was filtered and UV-Vis spectra of the solution was recorded using UV-Vis spectrophotometer (Shimadzu UV-2600 spectrophotometer). The degradation efficiency was obtained using the equation:

$$\text{Degradation efficiency } (\%) = (A_0\text{-}A/A_0) \times 100 \quad \textbf{(1)}$$

Where A_0 is the absorbance of the untreated i.e., initial TC solution and A is the absorbance taken for the treated solution at a specific time interval.

2.3. Results and discussions

2.3.1. Structural and crystallographic studies

X-ray diffraction patterns for ZnCr LDH and heterostructures ZnCr-xWO_3 (x=10%) as well as for WO_3 are shown in **Fig.2.1 (a).** The strong diffraction peaks centered at 2θ of 11.6° and 23.3°, respectively are for the basal reflection planes (003) and (006) and indicate the distinctive stacking of layers. The existence of the LDH phase was further supported by the other basal

reflection planes (012), (015), (018), and (110) analogous to 2θ = 34.3º, 38.8º 47.3º, and 59.6 º respectively [42]. In the case of WO_3 **Fig.2.1 (b)** when compared to the JCPDS no. 43-1035 all diffraction peaks are comparable with those anticipated for the monoclinic WO_3 phase [43]. No other contaminants were found, demonstrating that the product only contains a monoclinic phase. Peak intensities being sharp and high indicate the crystalline structure of WO_3. Further, the diffraction peak positions of prepared heterostructures (ZnCr LDH. xWO_3) confirmed the formation of composites of LDH and WO_3 with no change in the crystal structure of ZnCr LDH. Also, on increasing the amount of WO_3 in composites, the peak intensities corresponding to WO_3 in (ZnCr LDH. xWO_3) composites increased. The stability and ordered nature of the LDH are further supported by the presence of many basal reflections, which minimize charge carrier recombination and provides efficient electron transport. Sharp and intense diffraction peaks show that WO_3 is in its highly crystalline monoclinic phase, which is necessary for effective photocatalytic activity because it guarantees low defects and good structural integrity, both of which are critical for lowering electron-hole recombination. The increase in WO_3 content in the composites improves the light absorption capacity of the composite and increases the number of active sites, thereby enhancing photocatalytic performance. The heterostructure also promotes efficient charge transfer between the ZnCr LDH and WO_3, which further reduces recombination and improves the overall photocatalytic efficiency.

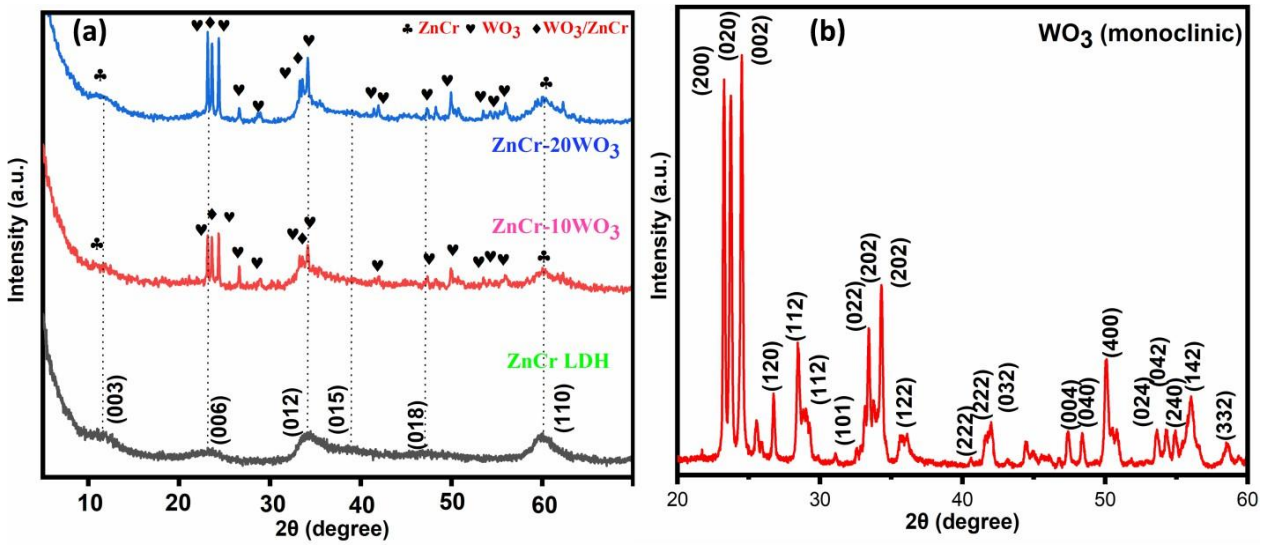

Fig. 2.1. XRD pattern of ZnCr LDH and ZnCr LDH.xWO_3 composites (a) and monoclinic WO_3 (b)

FTIR spectra were used to analyze the structures of ZnCr LDH and WO_3 and the effects of coupling between these, as shown in **Fig.2.2 (a).** Broadband was seen in the case of ZnCr LDH at wave numbers of about 3220–3600 cm^{-1} for the OH stretching vibration mode. In the inter gallery space of the LDH, the OH group was primarily attached to the metal centers of the brucite layers, whereas the symmetric and asymmetric stretching vibration modes of the intercalated CO_3^{2-}anion were concentrated at 1340 and 1470 cm^{-1}, respectively. A weaker band at about 1630 cm^{-1} is due to the bending mode of water molecules. The lattice vibration modes of the M-OH vibration and the M-O vibration in the brucite-like layers are responsible for the bands seen in the low-frequency region (800–500 cm^{-1}) [44]. For pure WO_3 absorption band at 740 cm^{-1} was observed and this band tends to decrease its intensity for (ZnCr LDH. x WO_3) composites in comparison to bare WO_3 with a slight shift of band. The broadness of the −OH stretching band also becomes more for ZnCr-10WO_3 and ZnCr-20WO_3 composites in comparison to bare ZnCr LDH due to changes brought in the chemical environment of the –OH group due to the interactions of the –OH group with WO_3 when introduced in ZnCr LDH. Therefore, FTIR provides for the composite formation of ZnCr LDH with WO_3.

Raman spectra carried out for exploring phase transition and bond vibrations in prepared catalysts are shown in **Fig.2.2 (b).** Two distinct bands observed between 430-470 cm^{-1} and a peak at 532 cm^{-1} indicate the presence of brucite sheets [45]. Additionally, a strong band at 1043 cm^{-1} corresponds to symmetric stretching modes of intercalated CO_3^{2-} anions. In contrast, Raman spectra of monoclinic WO_3 displayed four intense peaks at 273 cm^{-1}, 325 cm^{-1}, 713 cm^{-1}, and 803 cm^{-1}, attributed to O-W-O bending and stretching vibrations [46]. In heterostructures like ZnCr LDH.xWO_3, where x varies from 10% to 20%, intensities of O-W-O bond stretching and bending modes increased proportionally with higher WO_3 content, overshadowing LDH bands due to its lower concentration.

The FTIR and Raman spectra provides valuable insights into the structural and chemical interactions between ZnCr LDH and WO_3, which directly influence their photocatalytic behavior. FTIR analysis shows that ZnCr LDH contains OH groups and CO_3^{2-} anions, which play a key role in photocatalytic activity by facilitating electron and hole transfer. The shift and broadening of the OH stretching band upon WO_3 incorporation suggest interaction between the OH groups and WO_3, indicating the formation of a heterostructure that enhances charge

separation and reduces recombination, improving photocatalytic efficiency. The Raman spectra further support the composite formation, with the increasing intensity of the O-W-O stretching and bending vibrations in ZnCr LDH.xWO_3 heterostructures. This increased interaction enhances the charge transfer between the two components, promoting more efficient photocatalytic processes.

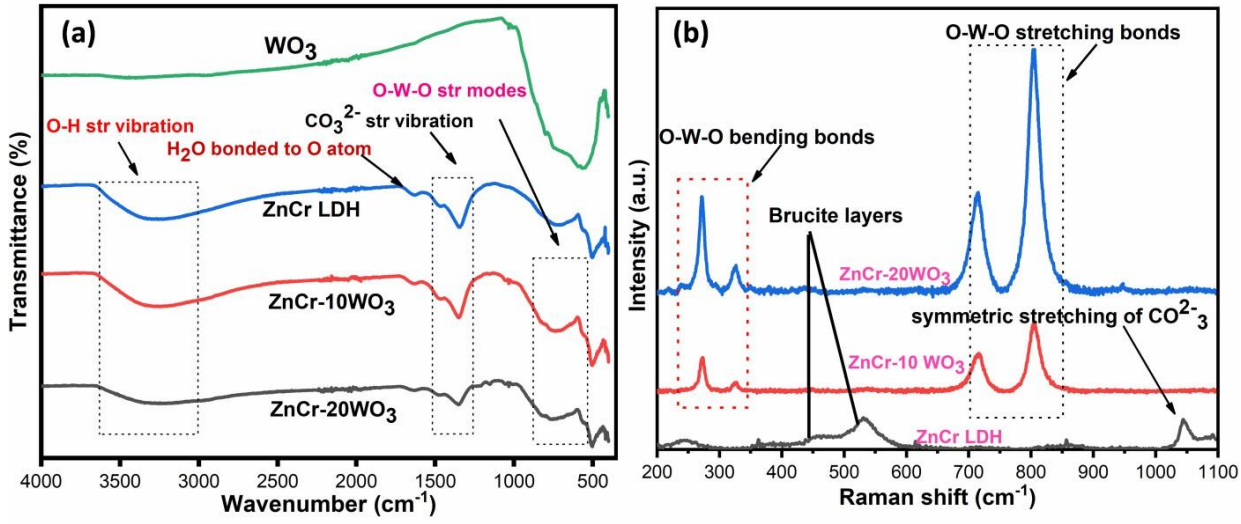

Fig.2.2. FTIR spectra (a); Raman spectra (b) of ZnCr LDH, ZnCr-10WO_3, ZnCr-20WO_3 composites

2.3.2. Optical studies

The UV-visible diffuse reflectance spectrum of ZnCr LDH is shown in **Fig.2.3 (a).** The UV- visible diffuse reflectance spectra demonstrates correlation between light absorption and photocatalytic efficiency. The ZnCr LDH absorbs in both the UV and visible regions, with strong bands at 350-470 nm and 490-700 nm due to ligand-to-metal charge transfer (LMCT) and d-d transitions of Cr^{3+}, respectively [47]. However, the absorption capability of ZnCr LDH is limited compared to WO_3. As shown in **Fig.2.3 (b)** WO_3, with its absorption onset at 480 nm, shows a narrower range of light absorption, but it is highly effective in visible light absorption. Upon composite formation the absorption range of ZnCr-10WO_3 extends significantly from 758 nm to 1038 nm, indicating an enhanced ability to absorb visible light. This extended absorption range directly correlates to improved photocatalytic efficiency, as the material can utilize a broader

spectrum of light for generating charge carriers. In contrast, the ZnCr-20WO_3 composite shows a decrease in the absorption range, which suggests that beyond a certain concentration of WO_3, the composite's ability to absorb light and drive photocatalytic reactions may decrease due to factors such as increased recombination or reduced light harvesting efficiency. Therefore, the ZnCr-10WO_3 composite exhibits the highest photocatalytic efficiency, as it is capable of harnessing more visible light and promoting more effective charge separation for photocatalytic reactions.

The optical absorption characteristics of crystalline semiconductors near their band edges can be described by the formula $\alpha h\nu = K(h\nu - E_g)^{n/2}$, where α represents the absorption coefficient, $h\nu$ is the light frequency, E_g denotes the band gap energy, and K is a constant [44]. The parameter n depends on the type of optical transition within the semiconductor.

Experimental data typically illustrate the relationship of $(\alpha h\nu)^2$ versus $h\nu$, as depicted in **Fig. 2.3 (c)**. The band gap energies calculated for ZnCr LDH and WO_3 are found to be 2.47 eV and 2.71 eV, respectively. When ZnCr LDH and WO_3 form composites (ZnCr-10WO_3 and ZnCr-20WO_3) the band gap energies decrease, i.e. 2.06 eV and 2.33 eV respectively, for the composites. This reduction in band gap energy suggests that the composites exhibit enhanced absorption of visible light compared to the bare LDH and WO_3 catalysts, as the ability to absorb a wider range of the visible spectrum facilitates more efficient generation of electron-hole pairs under light irradiation. These electron-hole pairs are essential for driving photocatalytic reactions. Consequently, the reduced band gap in the composites enhances the charge separation and transport, minimizes recombination, and improves the overall photocatalytic performance. The optimal band gap in the ZnCr-10WO_3 composite further correlates with its higher photocatalytic efficiency, as it maximizes the visible light absorption and promotes better charge carrier.

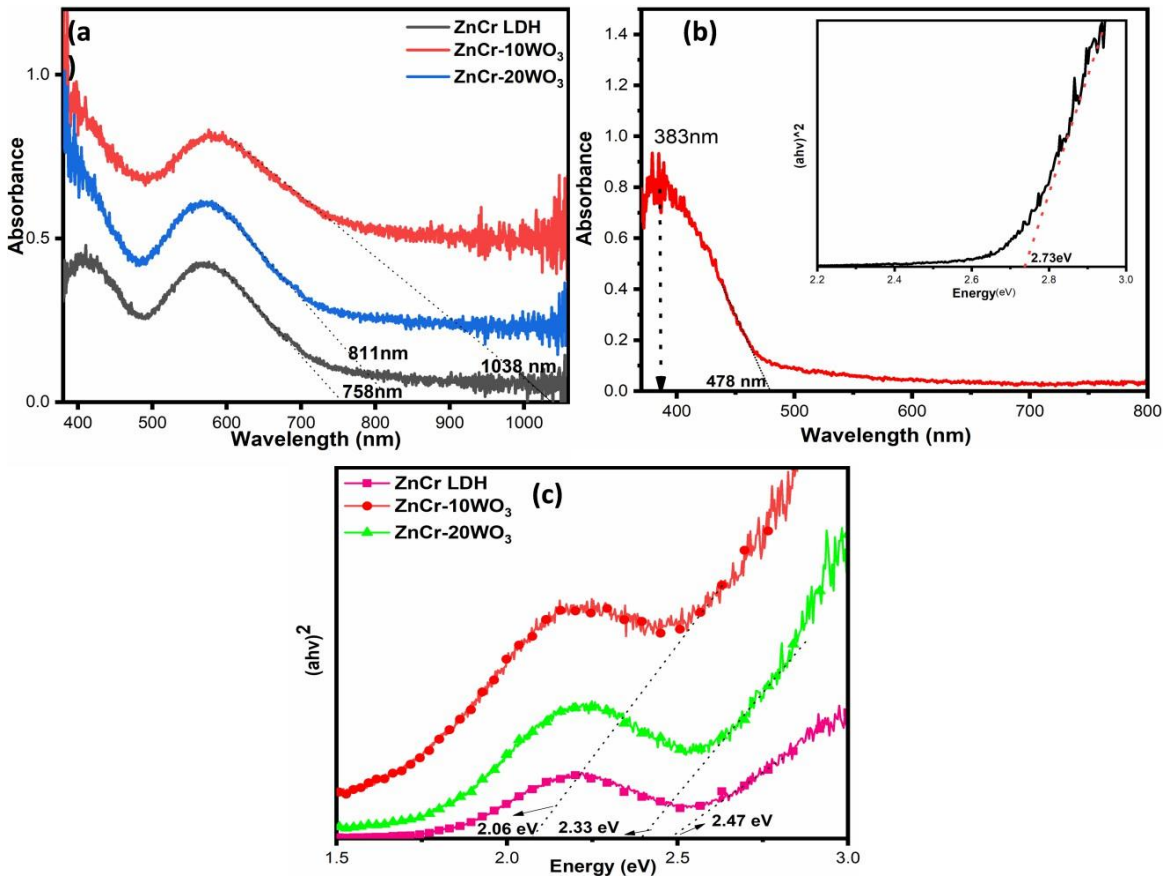

Fig. 2.3. UV-Vis diffuse-reflectance spectra of ZnCr LDH and ZnCr LDH. xWO_3 (x=10, 20%) composites (a); WO_3 (b); band gap calculated using tauc's plot (c).

PL behavior is related to the transfer of the photo-induced electrons and holes, which can reflect the separation-recombination of photo-induced charge carriers. The photocatalytic interaction can significantly influence the recombination of photo-induced charge pairs. Thus, to profoundly acquire the knowledge of recombination and separation of charge pairs in the hetero junction material, a PL study was done. **Fig. 2.4** depicts the PL emission spectra of neat ZnCr LDH and its ZnCr LDH/WO_3 composites with an excitation wavelength of 350 nm. ZnCr LDH and its composites show band spectra ranging from 365 nm to 383 nm specifying blue emission in the UV region. Emission at 468 nm was attributed to the band emission peak of LDH [48]. It was observed that upon heterostructure formation between LDH and WO_3 the PL peak intensity decreased due to decrease in radiative recombination of excitons for ZnCr/WO_3(WO_3= 10%) as compared to the parent material confirming the delayed recombination rate of photo-induced charge pairs to a certain extent whereas, rise in intensity is observed in composite (20 wt.%

WO_3) in comparison to (10 wt.% WO_3) resulting in fast recombination due to blocking of active sites of catalyst upon excess loading of WO_3. Similarly, the intensity of emission peak of heterostructures of LDH from 400-420 nm belonging to radiative recombination of localized surface trapped charge pairs are also lowered in comparison to bare LDH [49].

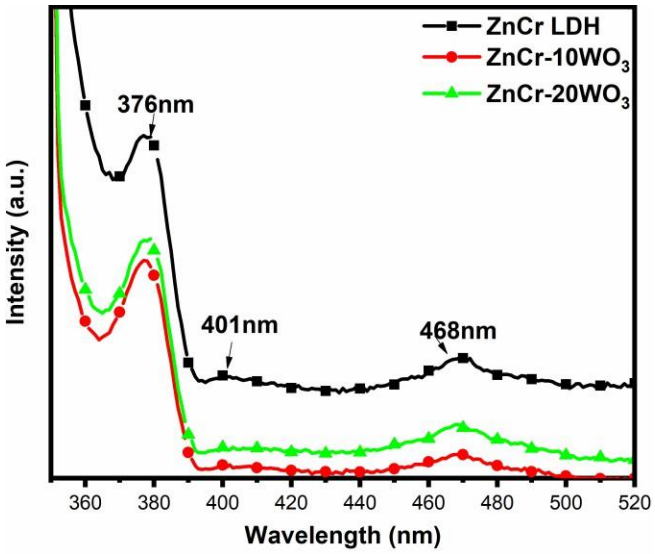

Fig.2.4. Photoluminescence spectra of ZnCr LDH and ZnCr LDH. xWO_3 (x=10, 20%) composites

2.3.3. Morphological and surface studies

The morphology of ZnCr LDH, WO_3, and its composites were determined by FESEM. **Fig. 2.5 (a)** shows the structure of ZnCr LDH forming porous surfaces. WO_3 surface in **Fig. 2.5 (b, c)** shows the growth of a large number of irregular lengths of nanoplates [41,50]. Surface of ZnCr-10WO_3 composites **Fig. 2.5 (d)** shows the same large number of irregular nanoplates of WO_3 interspersed inside as well as on the surface of ZnCr LDH which confirms the hetero-composite formation of ZnCr LDH and WO_3. The results of Energy-dispersive X-ray Spectroscopy (EDX) analysis for ZnCr LDH and ZnCr-10WO_3 are shown in **Fig.2.6 (a, b).** The spectrum shows the presence of W along with Zn, Cr, O, and C in ZnCr-10WO_3 composite.

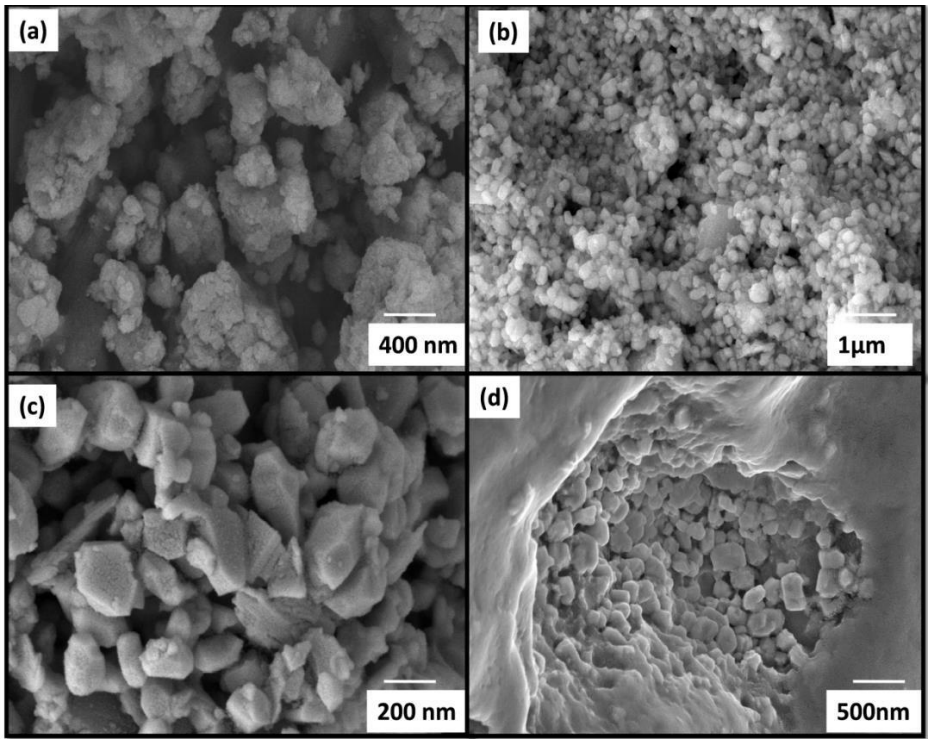

Fig.2.5. FESEM images of ZnCr LDH (a); WO_3 (b, c) and ZnCr-10WO_3 composite (d)

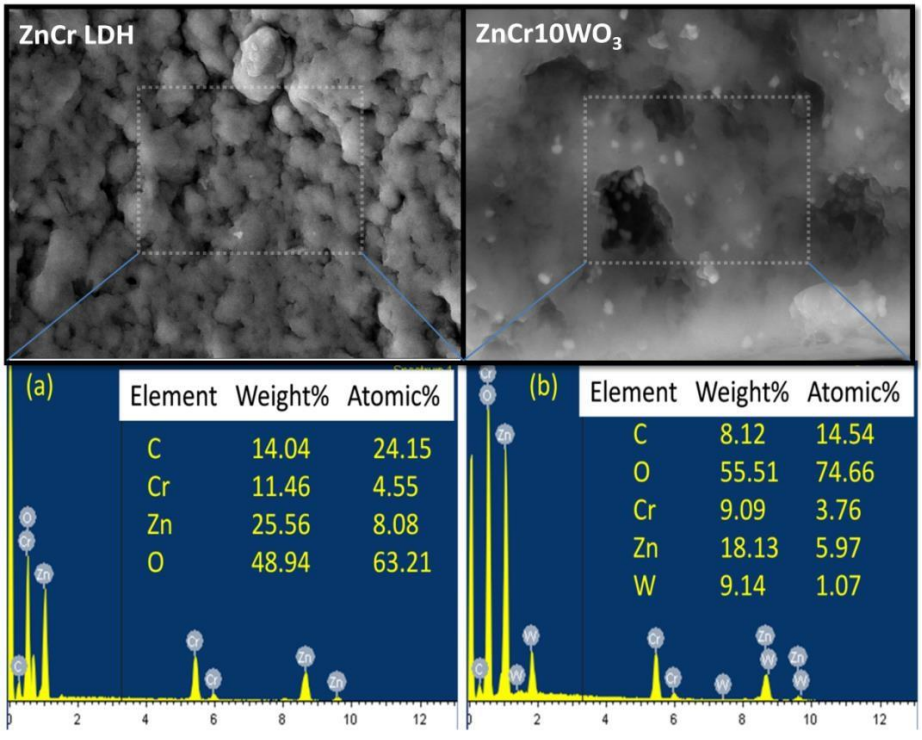

Fig.2.6. EDX spectra of ZnCr LDH (a) and ZnCr-10 WO_3 (b).

The specific surface area and pore size for prepared catalysts was analyzed by nitrogen adsorption-desorption technique. **Fig. 2.7 (a)** shows isotherms which can be classified as type IV adsorption isotherm. Presence of meso and micropores was further confirmed by pore size distribution curves in **Fig. 2.7 (b, c)** indicating the existence of pore size in a range of 0-50 nm. Specific surface area and pore size data for the catalysts estimated by the BET method was (27.43 m^2/g and 47.69 m^2/g) for ZnCr LDH, ZnCr-10WO_3 respectively [40,51]. The increase in surface area observed is due to the loading of WO_3 upon LDH surface moreover the increased pore diameter and pore volume (3.31 nm and 0.04 cm^3/g) upon composite formation suggests the fast diffusion of the reactive species hence improving the photocatalytic efficiency of the catalyst.

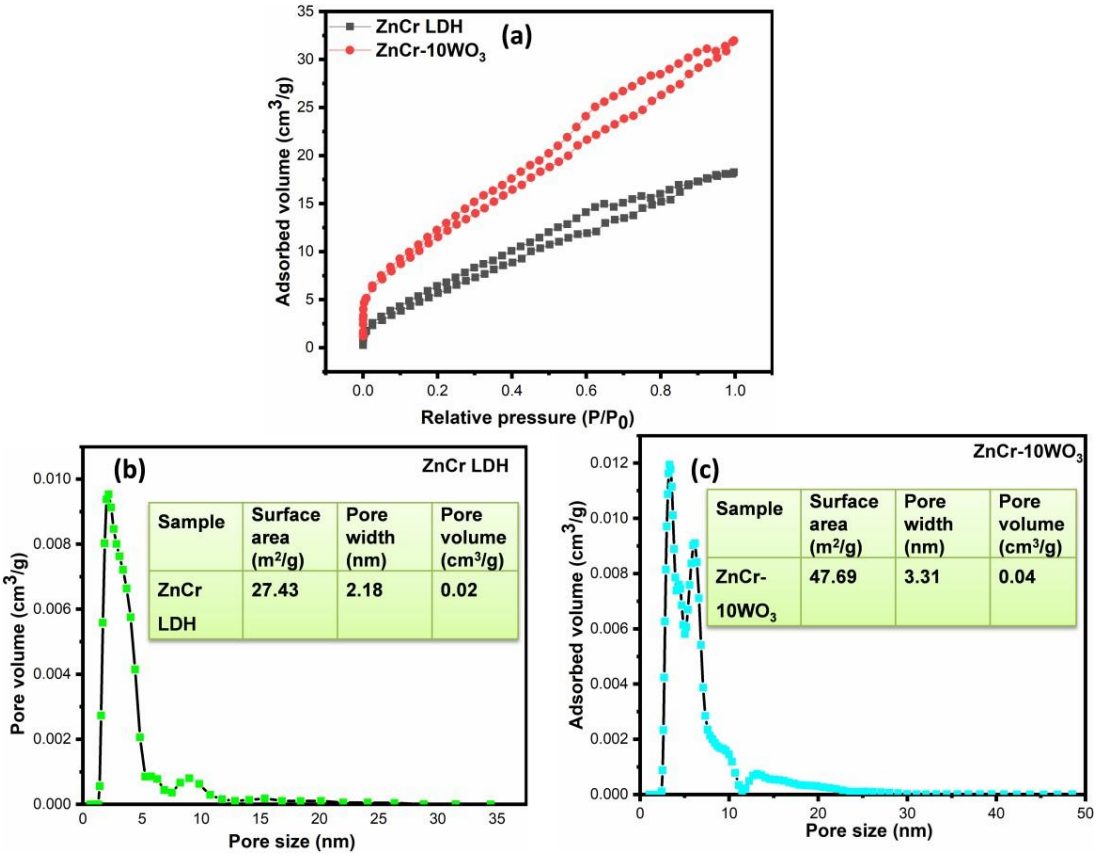

Fig.2.7. Nitrogen sorption isotherms (a) and pore size distribution curves (b, c) for ZnCr LDH and ZnCr-10WO_3

2.4. Photocatalytic activity

To evaluate the photocatalytic efficiency of the prepared catalysts, photocatalytic degradation of TC was conducted under visible light for 120 minutes. TC solution without any photocatalyst was also examined to assess the stability of the catalyst under visible light irradiation. Prior to illumination, suspensions of pollutants and catalysts were kept in the dark for 30 minutes to reach adsorption-desorption equilibrium. The characteristic absorption peak of tetracycline at 357 nm was monitored to evaluate degradation progress. After attaining adsorption desorption equilibrium the photocatalytic performance of ZnCr LDH and ZnCr/WO_3 composites was evaluated by degrading TC under visible light irradiation. **Fig. 2.8 (a,b)** shows the photocatalytic degradation of TC over various synthesized photocatalysts. The degradation efficiencies were found to be 59.4% and 19.8% for ZnCr LDH and WO_3 respectively in 120 minutes under visible light whereas, ZnCr/WO_3 photocatalyst with (WO_3 =10 and 20%) exhibited the efficiencies of 86.7% and 81.1%. The higher photocatalytic efficiencies of the ZnCr/WO_3 composites in comparison with pure ZnCr LDH and WO_3 catalysts are due to their higher surface area and synergistic effect of metal oxide and LDH.

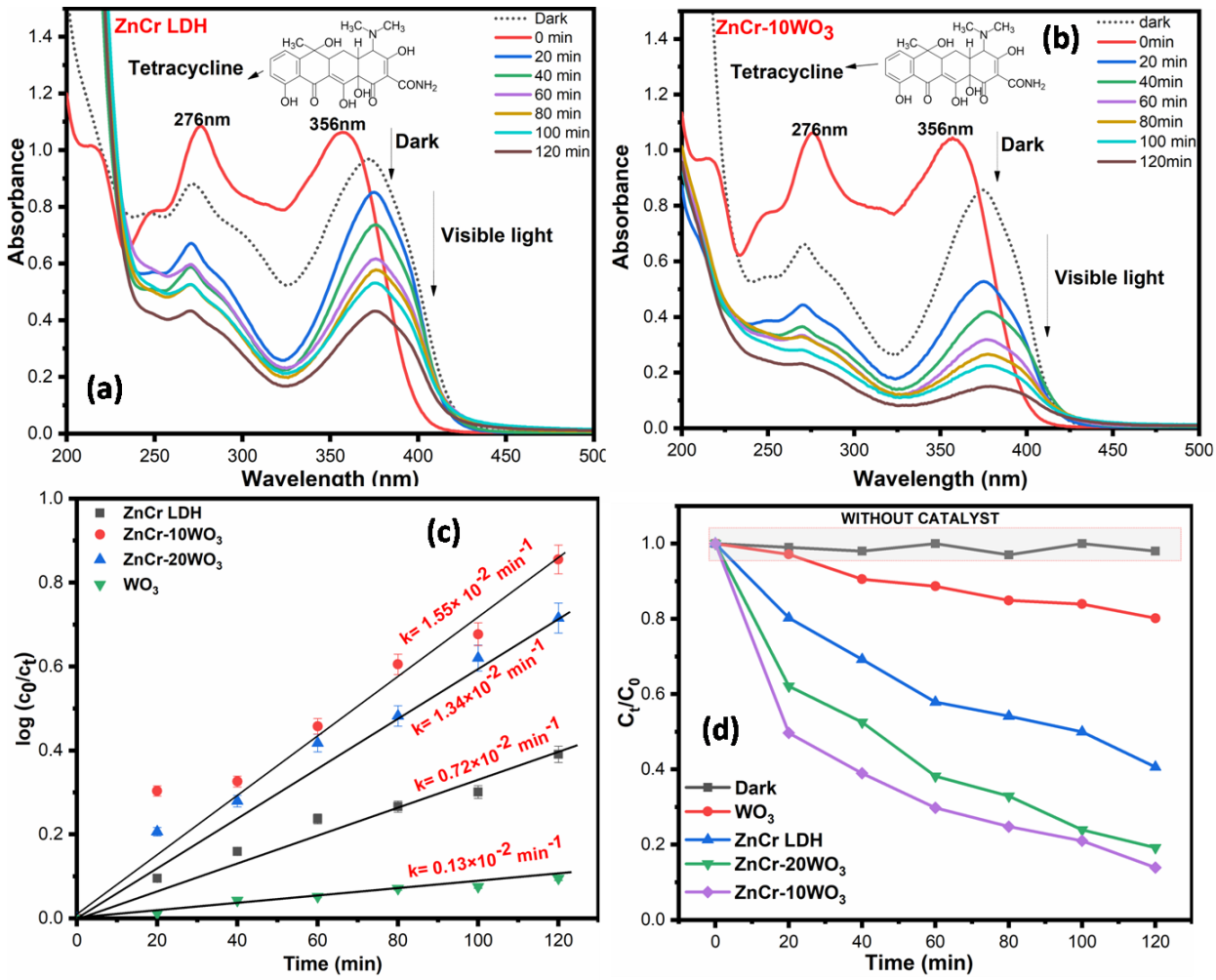

Fig.2.8. Time-dependent UV-Vis absorption spectra of TC solution using ZnCr LDH and ZnCr-10WO_3 (a, b) and time course-kinetic plot ZnCr LDH and ZnCr LDH. xWO_3 (x=10, 20%) composites (c-d)

The photocatalytic degradation of TC by ZnCr LDH and its composites obeys pseudo-first-order Kinetics. At low initial TC concentration, the simplest representation for rates of photodegradation of TC is given by:

$$\ln c_t = -kt + \ln c_0 \quad \text{.....(2)}$$

This equation can be used to demonstrate the linearity of data if the integration of Eq. (1) is given by:

$$\log (c_0/c_t) = kt/2.303 \quad \text{..... (3)}$$

Where k is the constant of the pseudo-first-order rate.

A plot of log (C_0/C_t) versus the visible irradiation time for the TC photodegradation catalyzed by ZnCr LDH, WO_3, ZnCr-10WO_3, ZnCr-20WO_3 is shown in **Fig. 2.8 (c)** A linear relation between log (C_0/C_t) and the irradiation time has been confirmed, which implies the photodegradation of TC follows the pseudo-first-order kinetics with rate constant (k) is 0.72 × 10^{-2} min^{-1}, 0.13 × 10^{-2} min^{-1}, 1.55 × 10^{-2} min^{-1} and 1.3× 10^{-2} min^{-1} and the degradation efficiency calculated was 59.4%, 19.8%, 86.7% and 81.1% for ZnCr LDH, WO_3, ZnCr-10WO_3, ZnCr-20WO_3 respectively, which is maximum for ZnCr-10WO_3 composite. **Fig. 2.9 (a, b)** shows a histogram representation of degradation efficiency rates and rate constant (k) for ZnCr LDH and its composites.

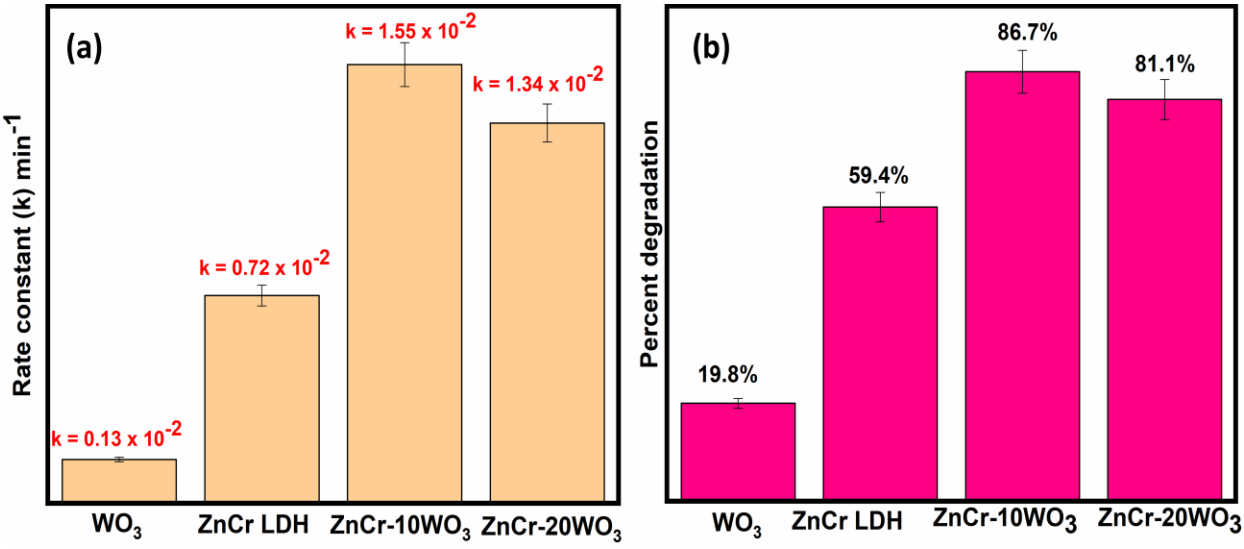

Fig.2.9. Rate constant (k) and degradation efficiency bar graph of WO_3, ZnCr LDH, ZnCr LDH. xWO_3 (x=10, 20%) composites (a, b)

Scavenging experiments were conducted to identify the active species involved in the photodegradation of TC under visible light. Methanol, IPA (isopropyl alcohol), and Ar (argon) gas were added to the TC solution under the identical reaction conditions used for the photodegradation analysis. Compared with experiments without scavengers, a decrease in percent degradation was observed. This decline in photocatalytic activity upon introducing scavengers suggests that holes, superoxide radical, and hydroxyl radicals influence the photocatalysis of TC over ZnCr-10WO_3. **Fig.2.10 (a)** shows the UV-Vis spectra of TC degradation upon adding scavangers and **Fig.2.10 (b)** depicts the bar graph showing decrease in

percent photodegradation upon adding Ar, IPA and methanol to the reaction mixture, significant decrease in photodegradation that was observed upon methanol addition, followed by IPA addition and argon purging, indicates that $O^{\bullet-}$ and $OH^{\bullet}$ are the primary species responsible for the photodegradation process. The contribution of active species during the photodegradation of TC follows the order: $O^{\bullet-} > OH^{\bullet} > h^{+}$.

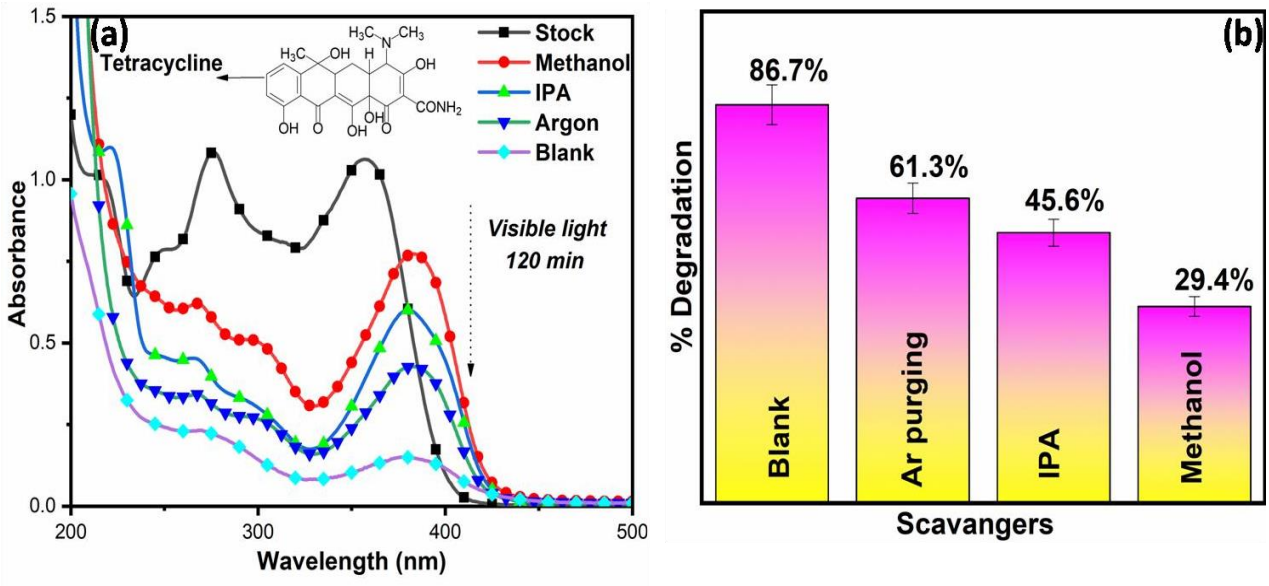

Fig.2.10. UV-Vis graph showing degradation of TC upon adding of scavangers (a) and the bar graph showing percent degradation of TC solution by ZnCr-10WO_3 catalyst (b)

2.5. HRMS analysis

HR-MS analysis was employed to identify intermediate products, which were characterized based on their mass-to-charge ratio (m/z). The possible degradation pathways of TC were proposed by analyzing the structures of these intermediate products. **Figure 2.11** illustrates the primary TC degradation pathways. Due to the higher electron density of the conjugated double bonds in the TC molecules, they are more vulnerable to attack by reactive oxygen species (ROS) [52]. In Pathway 1, ROS attacks the electron-rich conjugated double bond, forming P1, and TC undergoes demethylation to yield P2 [53]. Subsequently, P1 and P2 are converted into P3 (m/z = 274.91) through processes such as ring opening, deamination, and dealkylation [54]. P3 is further oxidized to smaller molecules, P4 (m/z = 218.01) and P5 (m/z = 167). In Pathway 2, TC is first

converted into P6 (m/z = 301.14) by hydroxylation and ring opening [55]. P6 is then transformed into P7 (m/z = 279) through an OH attack and further oxidized to the small molecule P8 (m/z = 149.02) [56]. The final degradation of P4, P5, and P8 results in the production of H_2O and CO_2.

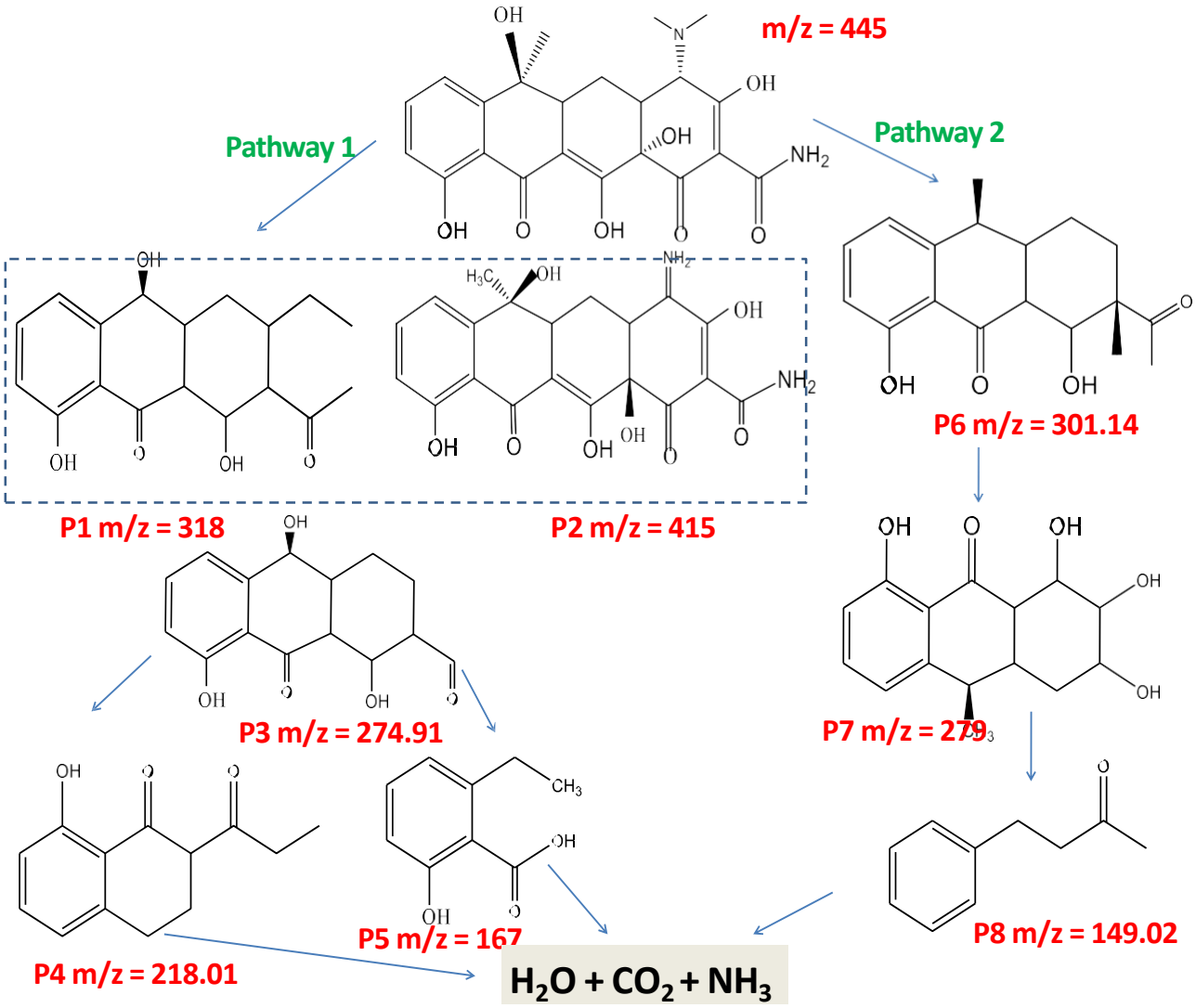

Fig.2.11. Possible TC degradation pathways under visible light irradiation

2.6. Proposed mechanism

Scheme. 1 represents the possible mechanism for the degradation of tetracycline under visible irradiation by the as-prepared catalysts. Among various strategies, the design of well-defined heterostructures is the promising approach toward the photodegradation of harmful pollutants

because of their merit in separating efficiency of photogenerated charge carriers [57–61]. ZnCr LDH, upon light illumination, absorbs visible light and excites electrons from the valence band (VB) to the conduction band (CB) with simultaneous generation of holes in VB. Then the photoexcited electrons and holes react with adsorbed oxygen and water molecules to generate reactive superoxide radical anions ($O_2^{\bullet-}$) and hydroxyl radicals ($^{\bullet}OH$). Upon hetero-composite formation of ZnCr LDH with WO_3 they belong to conventional class II hetero junction as in the mechanism shown in Scheme 1. When the light of suitable energy falls on the catalyst the ZnCr LDH would consume the visible light radiation from the source and generate electrons and holes. The electrons from the conduction band of ZnCr LDH would go to the conduction band of WO_3. To maintain electron neutrality holes jump from more positive VB (Valence band) of WO_3 to less positive VB of ZnCr LDH resulting in the accumulation of more holes in VB of ZnCr LDH. The electrons present at CB of WO_3 are not capable of reducing O_2 to $^{\bullet}O_2^-$ because of more positive conduction band potential than E_0 [(O_2/HO_2=-0.046 eV vs NHE)] whereas, the more positive valence potential of ZnCr LDH than E_0 ($OH/ ^{\bullet}OH$ = 1.99) was found suitable for generating $^{\bullet}OH$ through reaction of H_2O with oxidized hole [62]. Over time, these active species may break down the pharmaceuticals into simple degradation by-products such as CO2 and H_2O. This pathway of transfer of electrons and holes upon heterojunction formation reduces the recombination rate of charge carriers and hence, results in the improvement of photoactivity of the prepared catalyst.

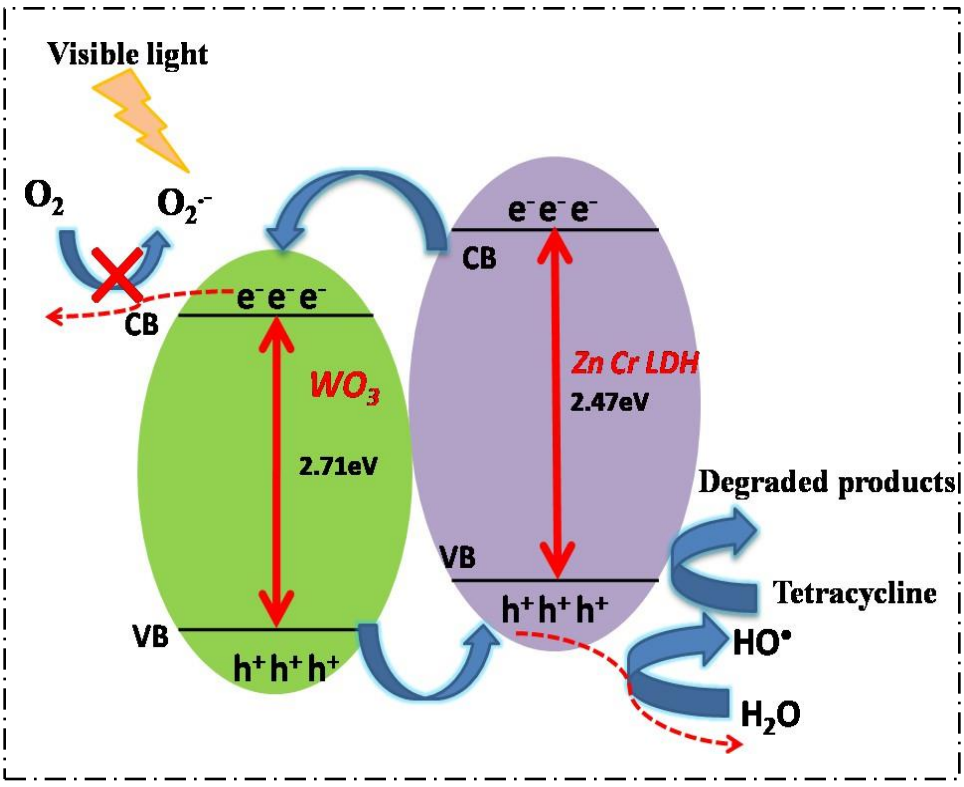

Scheme 1. Schematic representation for the photocatalytic mechanism for TC degradation using a ZnCr/ WO_3 LDH photocatalyst

Conclusion

In summary, we report a simple methodology to enhance the photocatalytic activity of ZnCr LDH-based composites. Generally, ZnCr LDH lacks excellent photoactivity because of the fast recombination of photo-generated charge carries but on the composite formation of ZnCr LDH with monoclinic-WO_3 a delay in recombination has been observed which is due to the generation of conventional class II hetero junction. The kinetic studies performed for prepared catalysts showed rate constant and degradation efficiency trend as **WO_3 < ZnCr LDH < ZnCr-20WO_3 < ZnCr-10WO_3** with maximum rate constant and degradation efficiency for ZnCr-10WO_3 composite., the introduction of monoclinic WO_3 into ZnCr LDH along with the enhancement in adsorption of tetracycline of catalyst surface (due to increase surface area) also increased charge separation efficiency of photo-induced charge carriers due to the generation of conventional class II hetero junction as compared to bare ZnCr LDH. The decreased charge separation observed for ZnCr-20WO_3 in PL spectra is due to excessive loading of monoclinic WO_3 on the LDH surface

hence making it a less effective catalyst in terms of rate constant and degradation efficiency as compared to ZnCr-10WO_3. Although this work is restricted to hetero composite synthesis further loading of metals like silver, gold, and copper could be done to form ternary (Z-scheme photocatalytic system) solar light active photocatalyst for solving various environmental issues.

References

[1] J. Briffa, E. Sinagra, R. Blundell, Heavy metal pollution in the environment and their toxicological effects on humans, Heliyon. 6 (2020) e04691. https://doi.org/10.1016/j.heliyon.2020.e04691.

[2] P. Kovalakova, L. Cizmas, T.J. McDonald, B. Marsalek, M. Feng, V.K. Sharma, Occurrence and toxicity of antibiotics in the aquatic environment: A review, Chemosphere. 251 (2020) 126351. https://doi.org/10.1016/j.chemosphere.2020.126351.

[3] P.K. Singh, R.L. Singh, Bio-removal of Azo Dyes: A Review, Int. J. Appl. Sci. Biotechnol. 5 (2017) 108–126. https://doi.org/10.3126/ijasbt.v5i2.16881.

[4] S. Sarkar, A. Banerjee, U. Halder, R. Biswas, R. Bandopadhyay, Degradation of Synthetic Azo Dyes of Textile Industry: a Sustainable Approach Using Microbial Enzymes, Water Conserv. Sci. Eng. 2 (2017) 121–131. https://doi.org/10.1007/s41101-017-0031-5.

[5] P. Gao, Y. Ding, H. Li, I. Xagoraraki, Occurrence of pharmaceuticals in a municipal wastewater treatment plant: Mass balance and removal processes, Chemosphere. 88 (2012) 17–24. https://doi.org/10.1016/j.chemosphere.2012.02.017.

[6] B. Fan, Y. Tan, J. Wang, B. Zhang, Y. Peng, C. Yuan, C. Guan, X. Gao, S. Cui, Application of magnetic composites in removal of tetracycline through adsorption and advanced oxidation processes (Aops): A review, Processes. 9 (2021). https://doi.org/10.3390/pr9091644.

[7] N. Barhoumi, H. Olvera-Vargas, N. Oturan, D. Huguenot, A. Gadri, S. Ammar, E. Brillas, M.A. Oturan, Kinetics of oxidative degradation/mineralization pathways of the antibiotic tetracycline by the novel heterogeneous electro-Fenton process with solid catalyst chalcopyrite, Appl. Catal. B Environ. 209 (2017) 637–647. https://doi.org/10.1016/j.apcatb.2017.03.034.

[8] Q. Tang, R. Niu, J. Gong, Salt-templated synthesis of 3D porous foam-like C3N4towards high-performance photodegradation of tetracyclines, New J. Chem. 44 (2020) 17405–17412. https://doi.org/10.1039/d0nj03346d.

[9] A.Q. Zhou, J.M. Yang, X.W. Zhu, X.L. Zhu, J.Y. Liu, K. Zhong, H.X. Chen, J.Y. Chu, Y.S. Du, Y.H. Song, J.C. Qian, H.M. Li, H. Xu, Self-assembly construction of NiCo LDH/ultrathin g-C3N4 nanosheets photocatalyst for enhanced CO2 reduction and charge separation mechanism study, Rare Met. 41 (2022) 2118–2128. https://doi.org/10.1007/s12598-022-01960-z.

[10] Y. Ye, Z. Zang, T. Zhou, F. Dong, S. Lu, X. Tang, W. Wei, Y. Zhang, Theoretical and experimental investigation of highly photocatalytic performance of CuInZnS nanoporous structure for removing the NO gas, J. Catal. 357 (2018) 100–107. https://doi.org/10.1016/j.jcat.2017.11.002.

[11] D. Yue, T. Zhang, T. Wang, X. Yan, C. Guo, X. Qian, Y. Zhao, Potassium stabilization of methylammonium lead bromide perovskite for robust photocatalytic H 2 generation , EcoMat. 2 (2020) 1–5. https://doi.org/10.1002/eom2.12015.

[12] X. Xu, A. Dutta, J. Khurgin, A. Wei, V.M. Shalaev, A. Boltasseva, TiN@TiO2 Core– Shell Nanoparticles as Plasmon-Enhanced Photosensitizers: The Role of Hot Electron Injection, Laser Photonics Rev. 14 (2020) 1–8. https://doi.org/10.1002/lpor.201900376.

[13] Y. Wu, Y. Wang, W. Yang, Q. Song, Q. Chen, G. Qu, J. Han, S. Xiao, Self-Cleaning Titanium Dioxide Metasurfaces with UV Irradiation, Laser Photonics Rev. 15 (2021) 1–7. https://doi.org/10.1002/lpor.202000330.

[14] H. Kaur, S. Singh, B. Pal, A brief review on modified layered double hydroxides for H2 production through photoinduced H2O splitting, Environ. Nanotechnology, Monit. Manag. 16 (2021) 100451. https://doi.org/10.1016/j.enmm.2021.100451.

[15] G. Arrabito, A. Bonasera, G. Prestopino, A. Orsini, A. Mattoccia, E. Martinelli, B. Pignataro, P.G. Medaglia, Layered double hydroxides: A toolbox for chemistry and biology, Crystals. 9 (2019). https://doi.org/10.3390/cryst9070361.

[16] M. Suárez-Quezada, G. Romero-Ortiz, V. Suárez, G. Morales-Mendoza, L. Lartundo-Rojas, E. Navarro-Cerón, F. Tzompantzi, S. Robles, R. Gómez, A. Mantilla,

Photodegradation of phenol using reconstructed Ce doped Zn/Al layered double hydroxides as photocatalysts, Catal. Today. 271 (2016) 213–219. https://doi.org/10.1016/j.cattod.2016.01.009.

[17] Y.H. Jia, Z.H. Liu, Preparation of borate anions intercalated MgAl-LDHs microsphere and its calcinated product with superior adsorption performance for Congo red, Colloids Surfaces A Physicochem. Eng. Asp. 575 (2019) 373–381. https://doi.org/10.1016/j.colsurfa.2019.05.032.

[18] G. Jácome-Acatitla, F. Tzompantzi, R. López-González, C. García-Mendoza, J.M. Alvaro, R. Gómez, Photodegradation of sodium naproxen and oxytetracycline hydrochloride in aqueous medium using as photocatalysts Mg-Al calcined hydrotalcites, J. Photochem. Photobiol. A Chem. 277 (2014) 82–89. https://doi.org/10.1016/j.jphotochem.2013.12.014.

[19] S. Nayak, G. Swain, K. Parida, Enhanced Photocatalytic Activities of RhB Degradation and H2 Evolution from in Situ Formation of the Electrostatic Heterostructure MoS2/NiFe LDH Nanocomposite through the Z-Scheme Mechanism via p-n Heterojunctions, ACS Appl. Mater. Interfaces. 11 (2019) 20923–20942. https://doi.org/10.1021/acsami.9b06511.

[20] Y. Chen, Z. Wang, Y. He, Y.J. Yoon, J. Jung, G. Zhang, Z. Lin, Light-enabled reversible self-assembly and tunable optical properties of stable hairy nanoparticles, Proc. Natl. Acad. Sci. U. S. A. 115 (2018) E1391–E1400. https://doi.org/10.1073/pnas.1714748115.

[21] Y. Chen, D. Yang, Y.J. Yoon, X. Pang, Z. Wang, J. Jung, Y. He, Y.W. Harn, M. He, S. Zhang, G. Zhang, Z. Lin, Hairy Uniform Permanently Ligated Hollow Nanoparticles with Precise Dimension Control and Tunable Optical Properties, J. Am. Chem. Soc. 139 (2017) 12956–12967. https://doi.org/10.1021/jacs.7b04545.

[22] Y. Chen, Y.J. Yoon, X. Pang, Y. He, J. Jung, C. Feng, G. Zhang, Z. Lin, Precisely Size-Tunable Monodisperse Hairy Plasmonic Nanoparticles via Amphiphilic Star-Like Block Copolymers, Small. 12 (2016) 6714–6723. https://doi.org/10.1002/smll.201602820.

[23] Y. Chen, Z. Wang, Y.W. Harn, S. Pan, Z. Li, S. Lin, J. Peng, G. Zhang, Z. Lin, Resolving Optical and Catalytic Activities in Thermoresponsive Nanoparticles by Permanent Ligation with Temperature-Sensitive Polymers, Angew. Chemie - Int. Ed. 58 (2019) 11910–11917. https://doi.org/10.1002/anie.201906329.

[24] P. Akhter, M.A. Farkhondehfal, S. Hernández, M. Hussain, A. Fina, G. Saracco, A.U. Khan, N. Russo, Environmental issues regarding CO2 and recent strategies for alternative fuels through photocatalytic reduction with titania-based materials, J. Environ. Chem. Eng. 4 (2016) 3934–3953. https://doi.org/10.1016/j.jece.2016.09.004.

[25] S. Zhang, Y. Zhao, R. Shi, C. Zhou, G.I.N. Waterhouse, L.Z. Wu, C.H. Tung, T. Zhang, Efficient Photocatalytic Nitrogen Fixation over Cuδ+-Modified Defective ZnAl-Layered Double Hydroxide Nanosheets, Adv. Energy Mater. 10 (2020) 1–10. https://doi.org/10.1002/aenm.201901973.

[26] Y. Han, Y. Chen, R. Fan, Z. Li, Z. Zou, Promotion effect of metal phosphides towards electrocatalytic and photocatalytic water splitting, EcoMat. 3 (2021) 1–32. https://doi.org/10.1002/eom2.12097.

[27] H. Zhang, K. Yu, Z. Wu, Y. Zhu, Ultrathin triphenylamine–perylene diimide polymer with D–A structure for photocatalytic oxidation of N -heterocycles using ambient air, EcoMat. 4 (2022) 2100202. https://doi.org/10.1002/eom2.12215.

[28] D.P. Sahoo, S. Nayak, K.H. Reddy, S. Martha, K. Parida, Fabrication of a co(oh)2/zncr ldh "p-n" heterojunction photocatalyst with enhanced separation of charge carriers for efficient visible-light-driven h2 and o2 evolution, Inorg. Chem. 57 (2018) 3840–3854. https://doi.org/10.1021/acs.inorgchem.7b03213.

[29] C. Prasad, H. Tang, W. Liu, Magnetic Fe3O4 based layered double hydroxides (LDHs) nanocomposites (Fe3O4/LDHs): recent review of progress in synthesis, properties and applications, J. Nanostructure Chem. 8 (2018) 393–412. https://doi.org/10.1007/s40097-018-0289-y.

[30] A. Khataee, A. Fazli, F. Zakeri, S.W. Joo, Synthesis of a high-performance Z-scheme 2D/2D WO3@CoFe-LDH nanocomposite for the synchronic degradation of the mixture azo dyes by sonocatalytic ozonation process, J. Ind. Eng. Chem. 89 (2020) 301–315. https://doi.org/10.1016/j.jiec.2020.05.026.

[31] J.C. Murillo-Sierra, A. Hernández-Ramírez, Z.Y. Zhao, A. Martínez-Hernández, M.A. Gracia-Pinilla, Construction of direct Z-scheme WO3/ZnS heterojunction to enhance the photocatalytic degradation of tetracycline antibiotic, J. Environ. Chem. Eng. 9 (2021).

https://doi.org/10.1016/j.jece.2021.105111.

[32] V. Hasija, P. Raizada, A. Sudhaik, P. Singh, V.K. Thakur, A.A.P. Khan, Fabrication of Ag/AgI/WO3 heterojunction anchored P and S co-doped graphitic carbon nitride as a dual Z scheme photocatalyst for efficient dye degradation, Solid State Sci. 100 (2020) 106095. https://doi.org/10.1016/j.solidstatesciences.2019.106095.

[33] Z. Yuan, P.C. Wu, Y.C. Chen, Optical Resonator Enhanced Photovoltaics and Photocatalysis: Fundamental and Recent Progress, Laser Photonics Rev. 16 (2022) 2100202. https://doi.org/10.1002/lpor.202100202.

[34] H. Wang, H. Li, W. Cai, P. Zhang, S. Cao, Z. Chen, Z. Zang, Challenges and strategies relating to device function layers and their integration toward high-performance inorganic perovskite solar cells, Nanoscale. 12 (2020) 14369–14404. https://doi.org/10.1039/d0nr03408h.

[35] Z. Yang, J. Du, L.I.D.J. Martin, D. Van der Heggen, D. Poelman, Highly Responsive Photochromic Ceramics for High-Contrast Rewritable Information Displays, Laser Photonics Rev. 15 (2021) 1–8. https://doi.org/10.1002/lpor.202000525.

[36] M.Y. Khan, M. Ahmad, S. Sadaf, S. Iqbal, F. Nawaz, J. Iqbal, Visible light active indigo dye/graphene/WO3 nanocomposites with excellent photocatalytic activity, J. Mater. Res. Technol. 8 (2019) 3261–3269. https://doi.org/10.1016/j.jmrt.2019.05.015.

[37] N. Tahmasebi, S. Sezari, P. Zaman, Fabrication and characterization of hydrogen-treated tungsten oxide nanofibers for cationic dyes removal from water, Solid State Sci. 100 (2020) 106073. https://doi.org/10.1016/j.solidstatesciences.2019.106073.

[38] X. Li, J. Iocozzia, Y. Chen, S. Zhao, X. Cui, W. Wang, H. Yu, S. Lin, Z. Lin, From Precision Synthesis of Block Copolymers to Properties and Applications of Nanoparticles, Angew. Chemie - Int. Ed. 57 (2018) 2046–2070. https://doi.org/10.1002/anie.201705019.

[39] B. He, Y. Wang, Q. Zhai, P. Qiu, G. Dong, X. Liu, Y. Chen, Z. Li, From polymeric carbon nitride to carbon materials: Extended application to electrochemical energy conversion and storage, Nanoscale. 12 (2020) 8636–8646. https://doi.org/10.1039/d0nr01612h.

[40] D.P. Sahoo, S. Patnaik, K. Parida, Construction of a Z-Scheme Dictated WO3-

X/Ag/ZnCr LDH Synergistically Visible Light-Induced Photocatalyst towards Tetracycline Degradation and H2 Evolution, ACS Omega. 4 (2019) 14721–14741. https://doi.org/10.1021/acsomega.9b01146.

[41] T. Thilagavathi, D. Venugopal, R. Marnadu, J. Chandrasekaran, T. Alshahrani, M. Shkir, An Investigation on Microstructural, Morphological, Optical, Photoluminescence and Photocatalytic Activity of WO3 for Photocatalysis Applications: An Effect of Annealing, J. Inorg. Organomet. Polym. Mater. 31 (2021) 1217–1230. https://doi.org/10.1007/s10904-020-01731-2.

[42] Y. Fu, F. Ning, S. Xu, H. An, M. Shao, M. Wei, Terbium doped ZnCr-layered double hydroxides with largely enhanced visible light photocatalytic performance, J. Mater. Chem. A. 4 (2016) 3907–3913. https://doi.org/10.1039/c5ta10093c.

[43] F. Peng, S. Wang, W. Yu, T. Huang, Y. Sun, C. Cheng, X. Chen, J. Hao, N. Dai, Ultrasensitive ppb-level H2S gas sensor at room temperature based on WO3/rGO hybrids, J. Mater. Sci. Mater. Electron. 31 (2020) 5008–5016. https://doi.org/10.1007/s10854-020-03067-6.

[44] N. Baliarsingh, L. Mohapatra, K. Parida, Design and development of a visible light harvesting Ni-Zn/Cr-CO 32- LDH system for hydrogen evolution, J. Mater. Chem. A. 1 (2013) 4236–4243. https://doi.org/10.1039/c2ta00933a.

[45] S. Kim, J. Fahel, P. Durand, E. André, C. Carteret, Ternary Layered Double Hydroxides (LDHs) Based on Co-, Cu-Substituted ZnAl for the Design of Efficient Photocatalysts, Eur. J. Inorg. Chem. 2017 (2017) 669–678. https://doi.org/10.1002/ejic.201601213.

[46] K. Christou, D. Louloudakis, D. Vernardou, N. Katsarakis, E. Koudoumas, One-pot synthesis of WO3 structures at 95 °C using HCl, J. Sol-Gel Sci. Technol. 73 (2015) 520–526. https://doi.org/10.1007/s10971-014-3459-5.

[47] B. Luo, R. Song, D. Jing, ZnCr LDH nanosheets modified graphitic carbon nitride for enhanced photocatalytic hydrogen production, Int. J. Hydrogen Energy. 42 (2017) 23427–23436. https://doi.org/10.1016/j.ijhydene.2017.03.001.

[48] Q. Shi, X. Zhang, Y. Yang, J. Huang, X. Fu, T. Wang, X. Liu, A. Sun, J. Ge, J. Shen, Y. Zhou, Z. Liu, 3D hierarchical architecture collaborating with 2D/2D interface interaction

in NiAl-LDH/Ti3C2 nanocomposite for efficient and selective photoconversion of CO2, J. Energy Chem. 59 (2021) 9–18. https://doi.org/10.1016/j.jechem.2020.10.038.

[49] L. Mohapatra, K. Parida, M. Satpathy, Molybdate/tungstate intercalated oxo-bridged Zn/Y LDH for solar light induced photodegradation of organic pollutants, J. Phys. Chem. C. 116 (2012) 13063–13070. https://doi.org/10.1021/jp300066g.

[50] S.I. Naya, K. Kimura, H. Tada, One-step selective aerobic oxidation of amines to imines by gold nanoparticle-loaded rutile titanium(IV) oxide plasmon photocatalyst, ACS Catal. 3 (2013) 10–13. https://doi.org/10.1021/cs300682d.

[51] A.E.A. Aboubakr, W.M.A. El Rouby, M.D. Khan, A.A. Farghali, N. Revaprasadu, ZnCr-CO3 LDH/ruptured tubular g-C3N4 composite with increased specific surface area for enhanced photoelectrochemical water splitting, Appl. Surf. Sci. 508 (2020) 145100. https://doi.org/10.1016/j.apsusc.2019.145100.

[52] L. Zhang, Y. Liu, Y. Fu, Degradation kinetics and mechanism of diclofenac by UV/peracetic acid, RSC Adv. 10 (2020) 9907–9916. https://doi.org/10.1039/d0ra00363h.

[53] T. Han, Y. Chen, H. Shi, Construction of a Bi2MoO6/CoOx/Au system with a dual- channel charge transfer path for enhanced tetracycline degradation, Catal. Sci. Technol. 12 (2022) 5565–5574. https://doi.org/10.1039/d2cy01224c.

[54] Y. Zhang, J. Zhou, X. Chen, L. Wang, W. Cai, Coupling of heterogeneous advanced oxidation processes and photocatalysis in efficient degradation of tetracycline hydrochloride by Fe-based MOFs: Synergistic effect and degradation pathway, Chem. Eng. J. 369 (2019) 745–757. https://doi.org/10.1016/j.cej.2019.03.108.

[55] S. Wang, Z. Teng, Y. Xu, M. Yuan, Y. Zhong, S. Liu, C. Wang, G. Wang, T. Ohno, Defect as the essential factor in engineering carbon-nitride-based visible-light-driven Z- scheme photocatalyst, Appl. Catal. B Environ. 260 (2020) 118145. https://doi.org/10.1016/j.apcatb.2019.118145.

[56] K. Wu, D. Chen, S. Lu, J. Fang, X. Zhu, F. Yang, T. Pan, Z. Fang, Supramolecular self-assembly synthesis of noble-metal-free (C, Ce) co-doped g-C3N4 with porous structure for highly efficient photocatalytic degradation of organic pollutants, J. Hazard. Mater. 382 (2020) 121027. https://doi.org/10.1016/j.jhazmat.2019.121027.

[57] X. Zhang, S. Pan, H. Song, W. Guo, F. Gu, C. Yan, H. Jin, L. Zhang, Y. Chen, S. Wang, Photothermal effect enables markedly enhanced oxygen reduction and evolution activities for high-performance Zn-air batteries, J. Mater. Chem. A. 9 (2021) 19734–19740. https://doi.org/10.1039/d1ta03652a.

[58] Y. Chen, T. Gan, C. Ma, L. Wang, G. Zhang, Crystallization of Polymer Chains Chemically Attached on a Surface: Lamellar Orientation from Flat-on to Edge-on, J. Phys. Chem. B. 120 (2016) 4715–4722. https://doi.org/10.1021/acs.jpcb.6b02344.

[59] M. Zhao, T. Chen, B. He, X. Hu, J. Huang, P. Yi, Y. Wang, Y. Chen, Z. Li, X. Liu, Photothermal effect-enhanced photoelectrochemical water splitting of a BiVO4photoanode modified with dual-functional polyaniline, J. Mater. Chem. A. 8 (2020) 15976–15983. https://doi.org/10.1039/d0ta03698f.

[60] X. Hu, J. Huang, F. Zhao, P. Yi, B. He, Y. Wang, T. Chen, Y. Chen, Z. Li, X. Liu, Photothermal effect of carbon quantum dots enhanced photoelectrochemical water splitting of hematite photoanodes, J. Mater. Chem. A. 8 (2020) 14915–14920. https://doi.org/10.1039/d0ta04144k.

[61] Y. Shi, X. Han, S. Pan, Y. Wu, Y. Jiang, J. Lin, Y. Chen, H. Jin, Gold Nanomaterials and Bone/Cartilage Tissue Engineering: Biomedical Applications and Molecular Mechanisms, Front. Chem. 9 (2021) 1–10. https://doi.org/10.3389/fchem.2021.724188.

[62] N. Hirata, K. Tadanaga, M. Tatsumisago, Photocatalytic O2 evolution from water over Zn-Cr layered double hydroxides intercalated with inorganic anions, Mater. Res. Bull. 62 (2015) 1–4. https://doi.org/10.1016/j.materresbull.2014.11.013.

CHAPTER-3

Enhanced adsorption and photocatalytic activity of Ag@WO_3/MgAl layered double hydroxide for degradation of ciprofloxacin under visible light irradiation

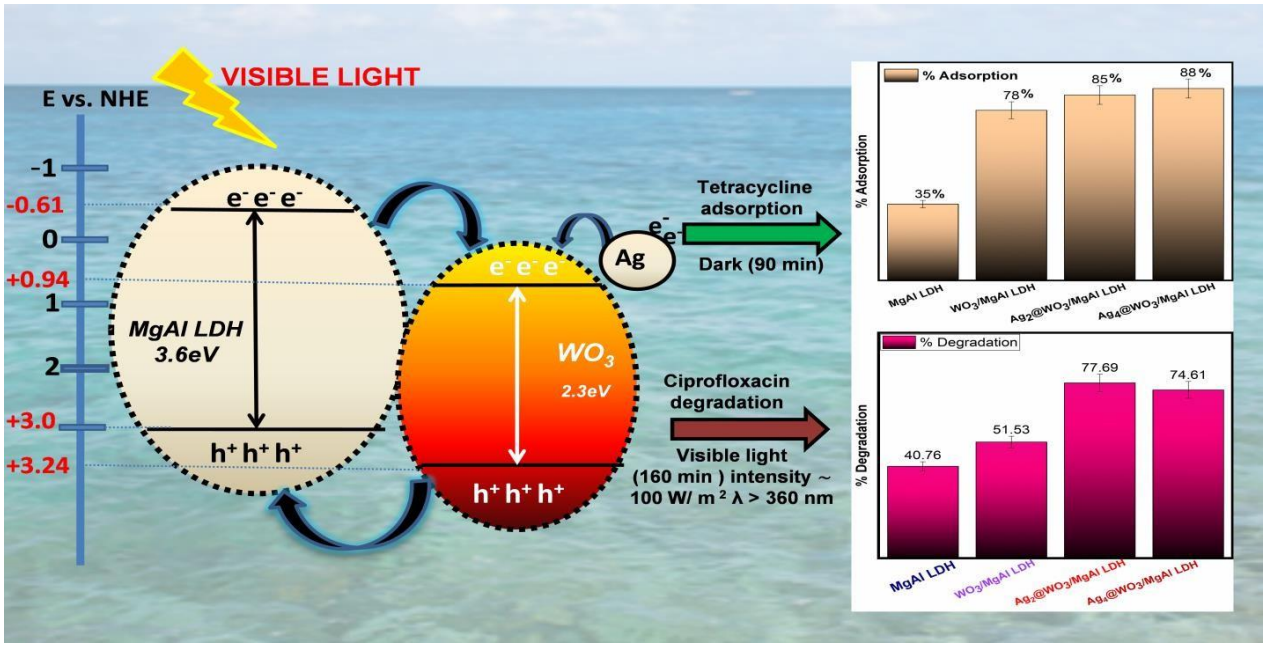

Schematic outline: Layered double hydroxides (LDHs) containing Mg and Al exhibit high surface area, stability and photoactivity with a band gap greater than 3 eV. By loading visible- light-active metal oxides like WO_3 and plasmonic metals such as Ag onto their surfaces, LDHs demonstrated enhanced responsiveness to visible light. This modification transforms LDHs into effective catalysts for degrading ciprofloxacin (77.6%) under visible light irradiation within 160 minutes. Furthermore, these modifications not only enhance the catalyst's photo activity but also improve its capability as an adsorbent for removing 85% of tetracycline.

This chapter covers second and third objective of the thesis focusing on the Influence of metal (Ag, Cu, Fe etc.) loaded MO (TiO_2, ZnO, WO_3 etc.) loading onto these LDHs and their physicochemical properties and the study of adsorption property and photocatalytic activity of these M /MO-LDH. heterocomposites for degradation of organic pollutants (phenols, nitro aromatics, pesticides etc.).

3.1. Introduction

The widespread use of antibiotics has raised concern about their impact on the ecosystem and human health. Large-scale usage of antibiotics resulted in the development of antibiotic resistance, posing a severe risk to both humans and animals [1]. Certain antibiotics, such as ciprofloxacin and tetracycline, are identified as water pollutants that can contaminate the aquatic environment [2,3]. These antibiotics are not entirely absorbed in the body their chemical stability makes them difficult to break down, and these are eliminated from the environment [4,5]. Addressing the presence of antibiotics in aquatic environments requires the development of efficient and practical techniques for their degradation. To overcome this problem, adsorption and photocatalysis using semiconductor photocatalysts have emerged as a promising, environmentally friendly, and cost-effective approach to removing organic pollutants, including antibiotics, from water [6–9].

Using effective nanosized adsorbent material is crucial in removing contaminants from wastewater, such as dyes, antibiotics, heavy metals, and various organic compounds. These materials play a vital role in adsorbing and degrading antibiotics, thereby facilitating their removal from the aquatic environment [10,11]. Recently, 2D layered double hydroxides (LDH) have attracted much interest in adsorption and photocatalysis. LDH possesses a customizable chemical composition, excellent stability, non-toxicity, low cost, ease of synthesis, high surface area, and notable light response [12,13]. These materials belong to the family of anionic clay compounds and can be represented by the general formula $[M_{1-x}^{2+}M_x^{3+}(OH)_2]^{x+}$ $[A_{x/n}]^{n-}.m\ H_2O$. LDH is composed of layers resembling brucite in which part of the divalent metal cations, such as Mg^{2+}, Fe^{2+}, Co^{2+}, Cu^{2+}, $Ni^{2+,}$ or Zn^{2+}, coordinated octahedrally by hydroxyl groups, are replaced with positively charged layers made of Al^{3+}, $Cr^{3+,}$ Ga^{3+}, In^{3+}, and Mn^{3+} [12,14].

However, specific challenges are associated with the practical application of LDH in wastewater purification. Their photocatalytic performance is limited by a few drawbacks, such as insufficient absorption of visible light, rapid recombination of photoinduced electron-hole pairs, and low specific surface area. To overcome these limitations, strategies such as heterogeneous doping, structural modification, and building heterojunctions with other semiconductors with similar band potentials have been explored to enhance the photocatalytic efficiency of LDH [15,16].

MgAl LDH is a visible light-responsive catalyst with a band gap energy of about 2-3 eV. However, the greater separation efficiency of photoinduced charge carriers limits their usefulness [17]. Tungsten oxide (WO_3) is an n-type semiconductor with band gap energy of 2.4-2.8 eV. On the other hand, it demonstrates good adsorption and visible-light-driven photocatalytic capabilities for removing different contaminants [18,19]. It possesses high adsorption capacity and good photoactivity due to its highly negatively charged surface. Combining MgAl LDH with WO_3 could result in a promising heterostructured photocatalytic material with strong adsorption and photocatalytic bifunctionality. Moreover, the use of WO_3/MgAl LDH composite for wastewater treatment has not been studied extensively. No studies have specifically investigated the synergistic effects of adsorption and photocatalysis for this composite. Plasmonic metal nanoparticles (NPs) can improve the photocatalytic performance of the catalyst by producing active electrons, encouraging the development of active species, thus enhancing the separation of photogenerated charge carriers in the system, and successfully improving the spectrum response to visible light [20–22]. For instance, scientists developed plasmonic metal (Ag, Au, Cu) loaded MgAl LDH catalysts for the degradation of tetracycline under LED light. They examined how the surface structure, optical characteristics, electrokinetics, and photocatalytic performance of LDH were affected by the loading of various plasmonic metals. Similarly, Au-Cu alloy nanoparticles supported by layered double hydroxide were found to be highly effective catalysts for the oxidative esterification of benzyl alcohol under visible light irradiation.

However, there is no report on the impact of WO_3, and plasmonic metal (Ag) loaded WO_3 upon MgAl LDH heterostructures for enhanced adsorption and degradation of pollutants under visible light irradiation. This study details the easy synthesis of MgAl LDH by the coprecipitation method and ternary plasmonic metal-loaded WO_3 heterojunction with MgAl LDH by the in situ coprecipitation method. This work appears to be the first to provide valuable insights into the influence of WO_3 and Ag loading for constructing a ternary composite comprising MgAl LDH, WO_3, and Ag. The impact of WO_3 and Ag loading on the structural, optical, and physicochemical properties of LDH in the ternary Ag@WO_3-LDH composite is described. Additionally, the study explores adsorption models and kinetic studies for tetracycline removal and a plausible mechanism for the photodegradation of ciprofloxacin over Ag@WO_3/LDH ternary

heterostructure considering the consequences of photoluminescence, scavenging, and HR-MS studies.

3.2. Experimental section

3.2.1. Materials

Aluminium nitrate nonahydrate ($Al(NO_3)_3.9H_2O$), Magnesium nitrate hexahydrate ($MgNO_3.6H_2O$, 98%), Sodium hydroxide (NaOH), Sodium carbonate (Na_2CO_3), Sodium tungstate ($Na_2WO_4.2H_2O$), Hydrochloric acid (HCl 35%), Isopropyl alcohol (C_3H_8O, 99.5%) were purchased from Loba Chemie (India). Silver nitrate was acquired from Sigma Aldrich. Ciprofloxacin: CIP ($C_{17}H_{18}FN_3O_3$), Tetracycline: TC ($C_{22}H_{24}N_2O_8$) tablets (50 mg) were purchased from the pharmacy Cipla Ltd. Organo Biotech Laboratories Pvt. Ltd. provided the triple deionized water that was used throughout the entire experiment.

3.2.2. Synthesis of MgAl LDH

MgAl LDH was synthesized by the precipitation method. Synthesis includes the addition of 50 mL of aqueous solution containing 0.0375 mol $Mg(NO_3)_2$ and 0.0125 mol $Al(NO_3)_3$ to another 50 mL 0.025 mol of Na_2CO_3 solution. The pH of the solution was maintained to 12 using 4 mol L^{-1} of NaOH solution. The resultant solution was stirred at room temperature for 12 hours. The precipitates formed were filtered and washed with distilled water, then dried at 70 °C.

3.2.3. Synthesis of WO_3

The synthesis of WO_3 is described in **section 2.2.3.**

3.2.4. Synthesis of silver-loaded WO_3

Ag-loaded WO_3 composite was synthesized by the photodeposition method. In a test tube, WO_3 powder (100 mg) was added to 10 mL of isopropanol to water (1:1) mixture along with 0.01 mM $AgNO_3$ solution corresponding to different weight percent (2%, 4%). The test tube containing the resultant mixture was purged with argon gas for 15-20 minutes and then sealed with a rubber septum to create an inert atmosphere. Further, the mixture was illuminated with UV radiation

(125 W Hg arc, 10.4 mW /cm ^{2}) for 3 h. The obtained solution was washed with distilled water and dried at 50°C.

3.2.5. Preparation of silver loaded WO_3/MgAl LDH composites

Ag@WO_3/MgAl LDH (2% and 4%) composites were prepared by in situ coprecipitation. The process involves the dispersion of a known amount of Ag@WO_3 in 10 mL of DI water, followed by the addition of 50 mL of 0.025 mol of a Na_2CO_3 solution. The resultant was stirred for 10 minutes. To the above aqueous solution, 50 mL of $Mg(NO_3)_2$(0.0375 mol) and $Al(NO_3)_3$(0.0125 mol) was added dropwise, and the pH of the reaction was maintained roughly 12 using 4 mol L^{-1} of aqueous NaOH solution. The final solution was stirred for 12 h at room temperature. Finally, precipitates were washed with distilled water and dried at 70°C. WO_3/MgAl composites were also prepared using a similar procedure whereby bare WO_3 was taken instead of Ag@WO_3. The composites were named Ag$_2$@WO_3/MgAl LDH, Ag$_4$@WO_3/MgAl LDH and WO_3/MgAl LDH.

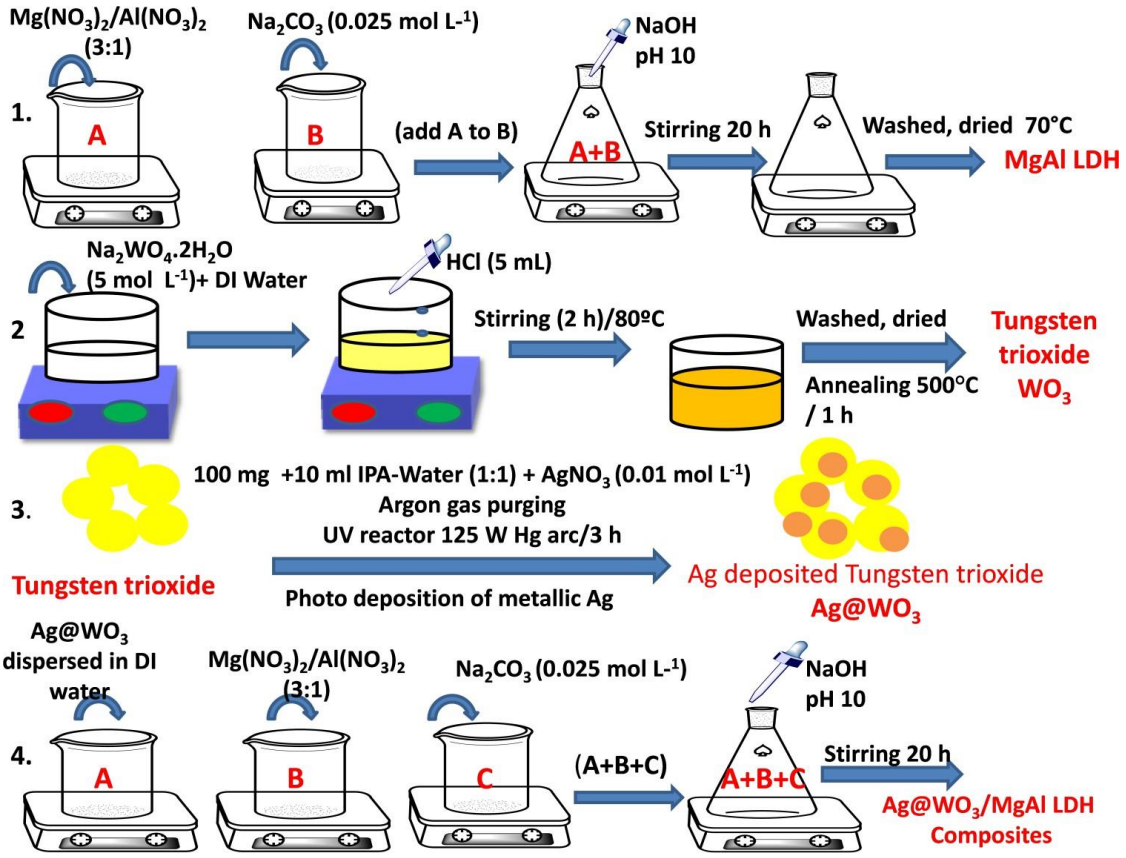

Scheme1. Schematic representation for the synthesis of ternary Ag@WO_3/MgAl LDH composites.

3.3. Results and discussions

3.3.1. Crystallographic and structural studies

X-ray diffraction patterns for MgAl LDH, WO_3, WO_3/MgAl, and Ag@WO_3/MgAl LDH are shown in **Fig. 3.1(a).** Pure MgAl LDH exhibits diffraction peaks centered at 2 theta of 11.7º, 23.4º, 34.9º, 39.4º, 46.8º, 60.9º and 62.3º for the reflection planes (003), (006), (012), (015), (018), (110) and (113) respectively according to JCPDS no. 14-0191 [23,24]. In the case of WO_3, all diffraction peaks are comparable to the monoclinic WO_3 phase when compared to the JCPDS no. 43-1035 with no other contaminants present, indicating the purity of the monoclinic phase [25]. The composite formation of MgAl LDH with WO_3 and Ag@WO_3 does not diminish the characteristic peaks of LDH at 11.7° and 23.4° suggesting the zero effect of loadings on the crystallinity of hydrotalcite material. Also, WO_3 and Ag@WO_3 loadings upon LDH crystal reduce the characteristic peaks corresponding to MgAl LDH, indicating the interaction of WO_3 with MgAl LDH. In the case of Ag@WO_3/MgAl LDH composites, no peak was observed corresponding to metallic Ag due to its low concentration, i.e. (2 - 4 wt.%). Consequently, the X- ray diffraction pattern indicates that the metallic Ag content is below the detection limit.

The FTIR spectra of MgAl LDH and its composites are depicted in **Fig. 3.1(b).** A strong, broad absorption band at 3409 cm^{-1} 3416 cm^{-1} indicates the stretching vibration of OH groups on the layer surface or interlayer water molecules. In contrast, the 1643 cm^{-1} band was due to the bending vibration of interlayer water molecules. An intense band at 1360 cm^{-1} signifies anti- symmetric stretching of carbonate ions in the interlayer region [26,27]. Metal vibrations at lower wave numbers (500-700 cm^{-1}) are present, but in the case of Ag_2@WO_3/MgAl LDH, these LDH bands were affected upon composite formation with Ag_2@WO_3. For bare WO_3, the stretching bands corresponding to O-W-O/W-O-W interbridging vibration were observed at 603 cm^{-1}, 731 cm^{-1}, and 804 cm^{-1}. Compared to bare WO_3, the stretching vibration intensity of O-W-O/W-O-W is less intense in Ag_2@WO_3/MgAl LDH composite. No vibration bands were observed for silver because of its low concentration. Additionally, the broadness of the OH stretching band was found to be decreased upon composite formation. Hence, the FTIR results are supplementary

evidence affirming the successful coupling of LDH, WO_3, and Ag NPs within the Ag_2@WO_3/MgAl LDH ternary heterostructure.

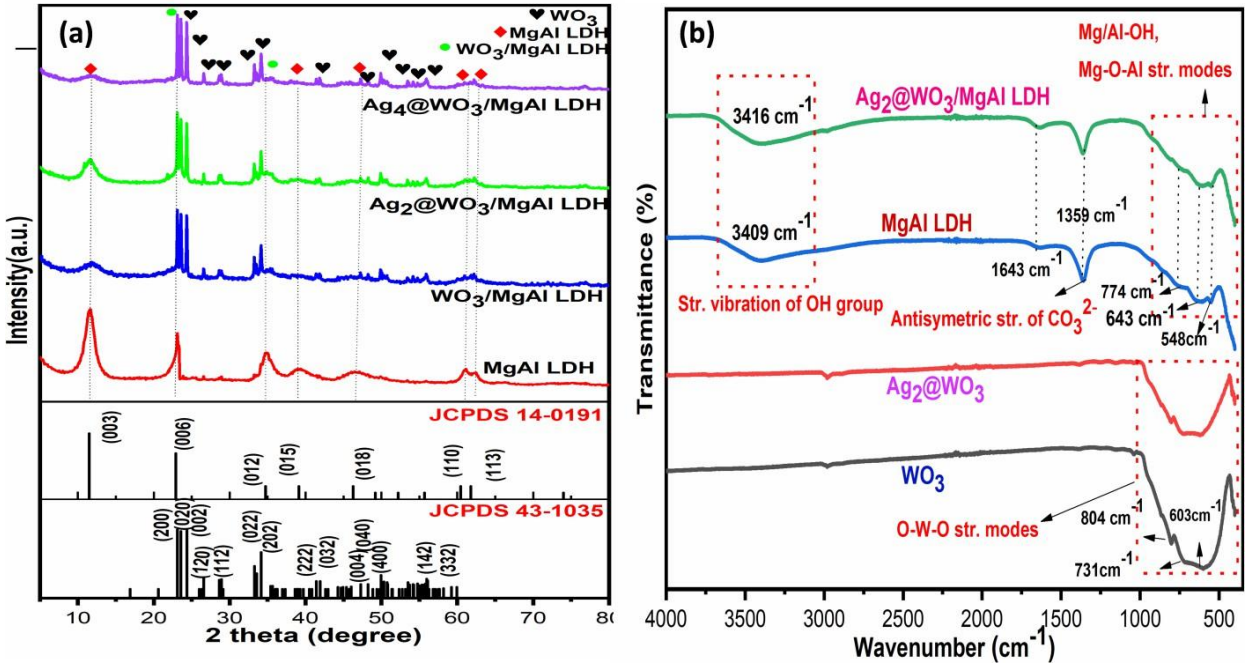

Fig. 3.1. XRD pattern (a); FTIR spectra (b) of MgAl LDH, binary WO_3/MgAl LDH, and ternary Ag@WO_3/MgAl LDH composites

Fig.3.2(a,b) illustrates the Raman spectra of MgAl LDH, WO_3/MgAl LDH, and Ag@WO_3/MgAl composites, respectively. The Raman spectra of MgAl LDH show several bands positioned at 470 cm^{-1}, 590 cm^{-1}, and 710 cm^{-1} and 1050 cm^{-1}associated with the Al-O-Al bond, Octahedral structure of brucite layers Al-O-Mg, NO_3^- ion and anion intercalated in LDH materials respectively [28]. Upon composite formation of MgAl LDH with WO_3, four highly intense bands corresponding to 273 cm^{-1}, 325 cm^{-1}, 713 cm^{-1}, and 803 cm^{-1} were observed, which are due to O-W-O stretching (713 cm^{-1} and 803 cm^{-1}) and bending modes (273 cm^{-1}, and 325 cm^{-1}) [29]. Also, the low LDH and Ag NPs concentrations result in nondetectable Raman bands for LDH in WO_3@MgAl LDH. However, in silver-loaded composites, Raman bands at 470 cm^{-1} and 1050 cm^{-1} corresponding to MgAl LDH are observed. This detection is attributed to the localized surface plasmon resonance (LSPR) effect of silver, which enables the bands to be detected. Moreover, the terminal W=O stretching band, in particular, was visible and shifted towards a lower wavenumber (935 to 895 cm^{-1}) in silver-loaded MgAl LDH composites,

demonstrating that the chemical environment of Ag NPs significantly impacted the W=O bond in Ag@WO_3/MgAl LDH composites [21].

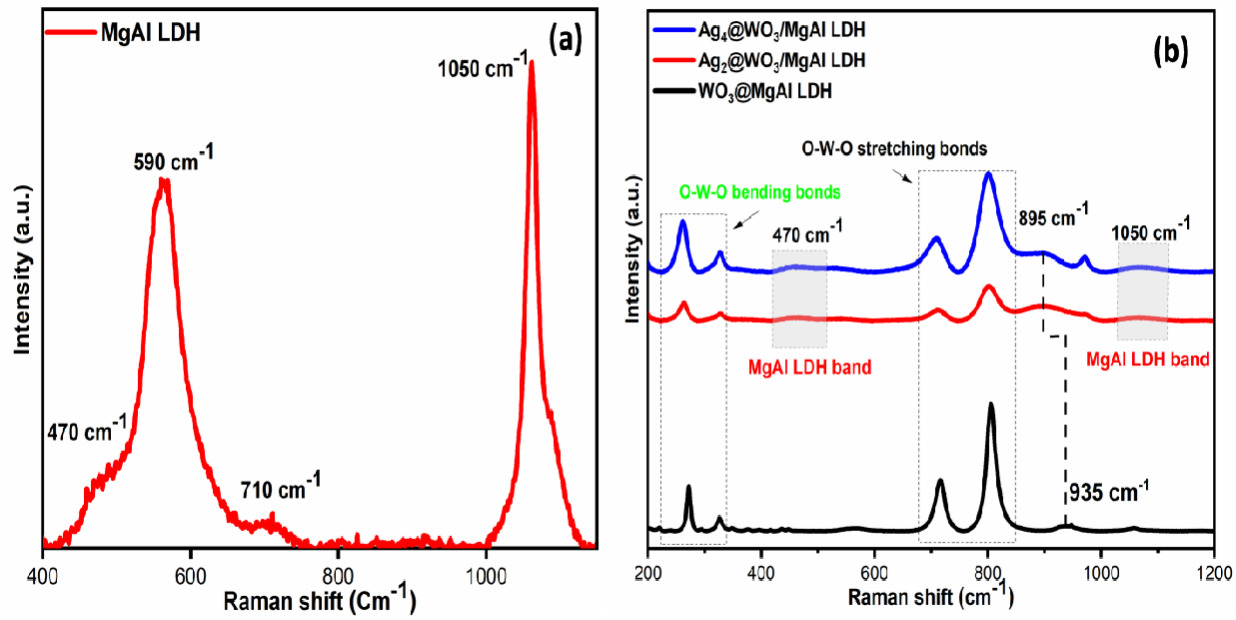

Fig.3.2. Raman spectra of bare MgAl LDH (a); WO_3@MgAl LDH, Ag_2@WO_3/MgAl LDH and Ag_4@WO_3/MgAl LDH (b)

3.3.2. Optical studies

The optical absorption properties of synthesized photocatalysts were evaluated with the help of DRS spectra. **Fig. 3.3 (a, b)** displays the absorbance spectra and colour change for the prepared catalysts. MgAl LDH shows an intense band at 260 nm and an absorption edge in the visible region (395 nm). The light absorption capacity of MgAl LDH was initially improved upon its composite formation with WO_3, resulting in a shifting of absorption onset to the more visible region (462nm). Further, the composite formation of MgAl LDH with Ag-loaded WO_3 indicates a red shift in absorption bands and a hyperchromic shift in bands, respectively. Improved light absorption was observed in the case of Ag@WO_3LDH composites due to the SPR effect [30]. Generally, the transfer of electrons between the metal d-electronic states and LDH causes the Ag nanoparticles to exhibit surface plasmon resonances at 400–500 nm. Still, the SPR band was not observed for Ag@WO_3/MgAl composites due to low silver loadings. The visible light absorbing

efficiency of prepared composites follows MgAl LDH < WO_3/MgAl LDH < Ag_2@WO_3/MgAl LDH < Ag_4@WO_3/MgAl LDH.

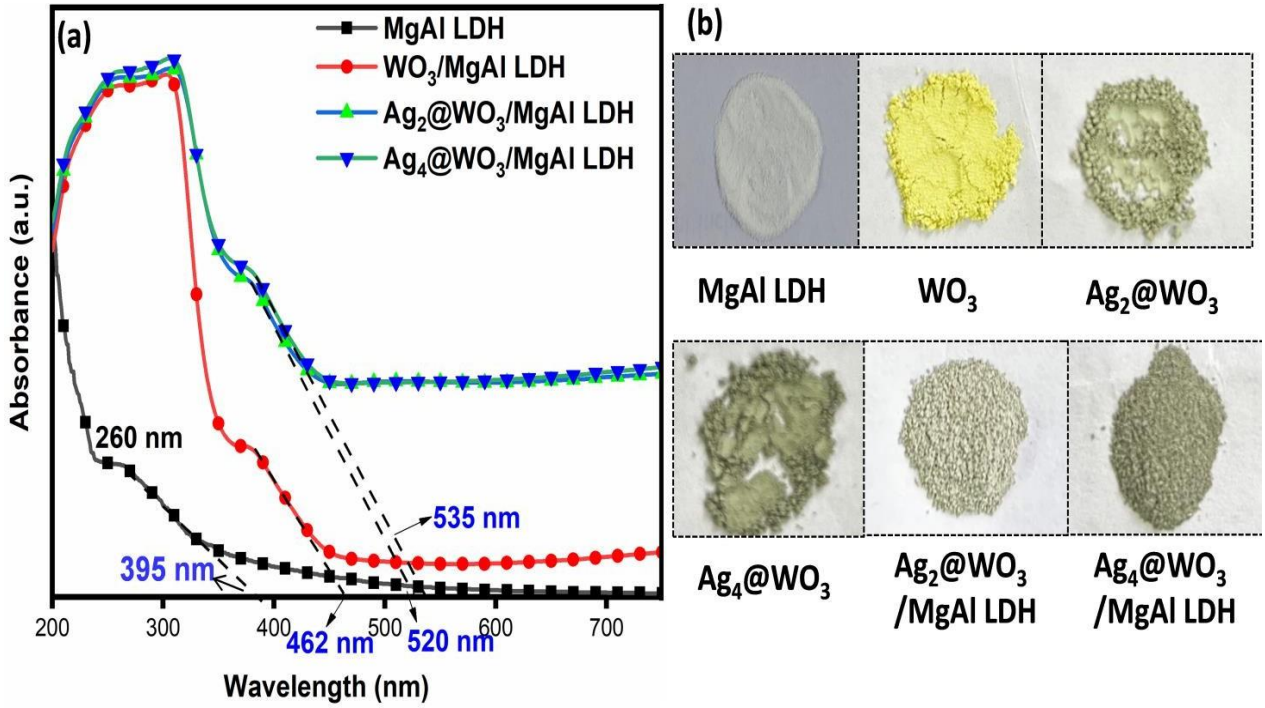

Fig.3.3. UV-Visible diffuse reflectance spectrum (a); color change (b) of MgAl LDH WO_3/MgAl LDH, Ag_2@WO_3/MgAl LDH and Ag_4@WO_3/MgAl LDH

The band gap energy was calculated using tauc's plot.

$$\alpha h\nu = K(h\nu - Eg)^{1/2} \quad \text{.....(1)}$$

Here, the absorption coefficient, light frequency, band gap energy, and a constant are represented by hν, E_g, and K. The band gap values were determined by plotting $(\alpha h\nu)^{1/2}$ v/s hν shown in **Fig. 3.4(a-d)** the respective band gap for MgAl LDH, WO_3/MgAl LDH, Ag_2@WO_3/MgAl LDH and Ag_2@WO_3/MgAl LDH was 3.6 eV, 2.54 eV, 2.46 eV and 2.28 eV.

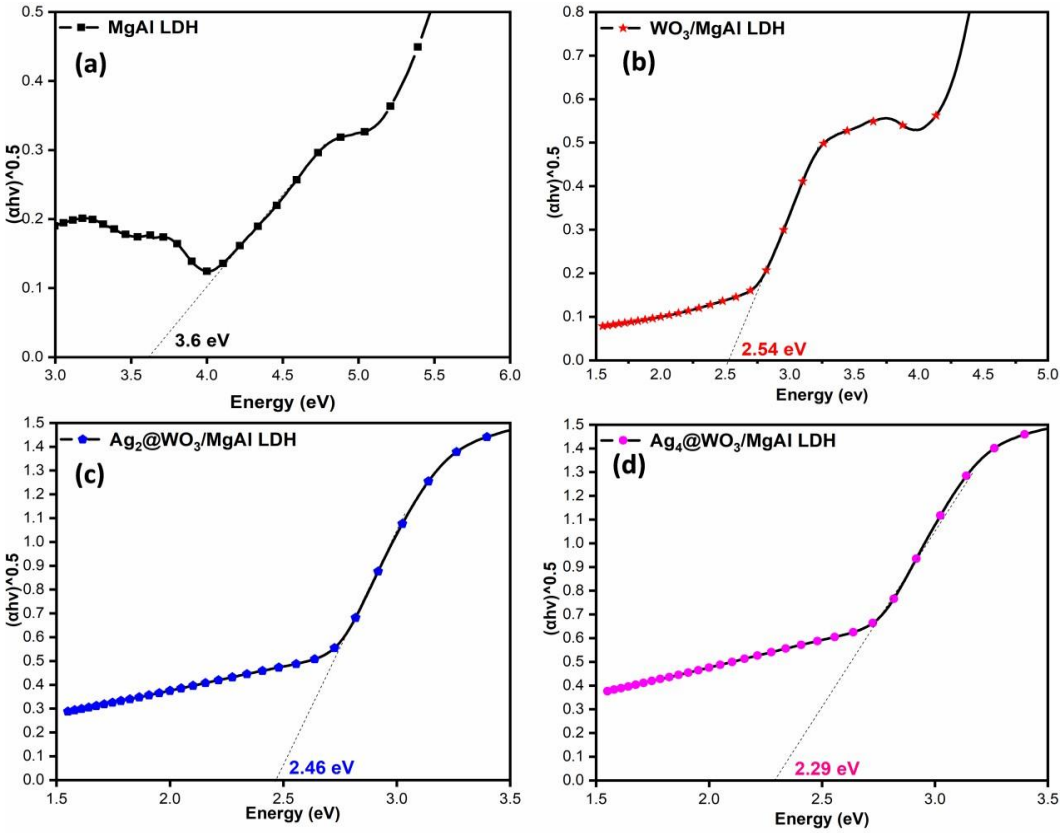

Fig.3.4. Band gap calculation using tauc's plot for MgAl LDH and its composites (a-d)

The transmission of photoinduced electrons and holes is connected to PL behavior and can represent the separation-recombination of photoinduced charge carriers. The MgAl LDH displays an intense peak at 385 nm, which was highly intense, signifying a high recombination rate of electrons and holes. Furthermore, upon composite formation of LDH with WO_3, the peak intensity decreased, signifying delayed recombination of charge carriers. The ternary composite formation of LDH with Ag-loaded WO_3 leads to the generation of a less intensified peak in comparison to bare and binary composites of LDH as the enhanced electron capturing capacity of Ag NPs decreases the recombination of photoinduced charge carriers (Corresponding to its reduction potential i.e. +0.79 eV) thus, the highest quenching was recorded for Ag loaded (2%, 4%) WO_3 LDH ternary composites followed by binary WO_3/MgAl composites and least for MgAl LDH as shown in **Fig.3.5** (Quenching order: MgAl LDH < WO_3/MgAl LDH < Ag_2@WO_3/MgAl LDH< Ag_4@WO_3/MgAl LDH) [31].

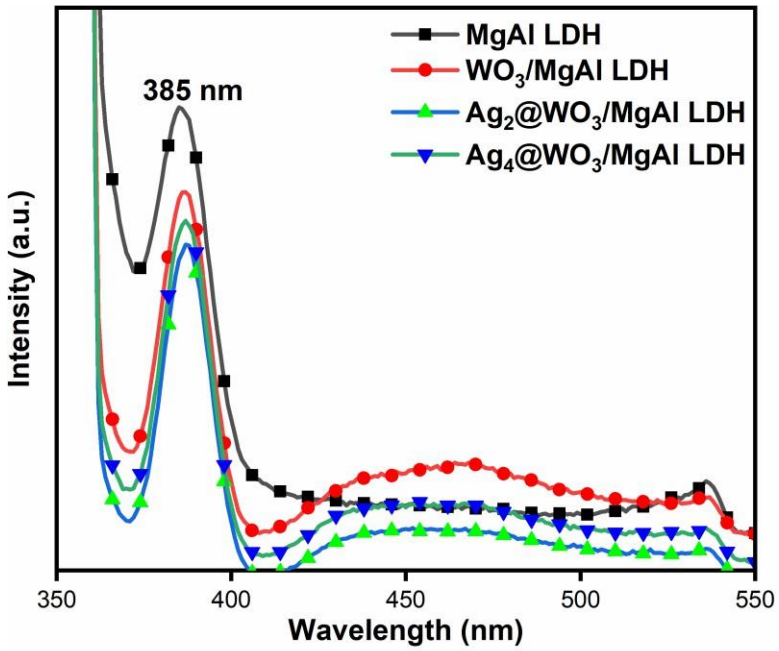

Fig.3.5. PL spectra of MgAl LDH, WO_3/MgAl LDH, Ag_2@WO_3/MgAl LDH and Ag_4@WO_3/MgAl LDH

3.3.3. Morphological and surface studies

FESEM analysis was carried out to carry out morphological studies of the prepared catalyst. **Fig.3.6 (a, b)** exhibits a porous surface of MgAl LDH with spherical morphology on the other side of the WO_3 surface in **Fig.3.6 (c, d)** depicts the development of several uneven lengths of nanoplates [32,33]. FESEM image of Ag_2@WO_3/MgAl LDH **Fig.3.6 (e, f)** reveals that Ag- loaded WO_3 nanoplates are embedded on the surface of MgAl LDH. The coexistence and uniform distribution of the elements C (Carbon), Mg (magnesium), O (oxygen), Al (aluminium), W (tungsten), and Ag (silver) in the hybrid are also confirmed by the EDX spectra and elemental coloured mapping images **Fig.3.7.**

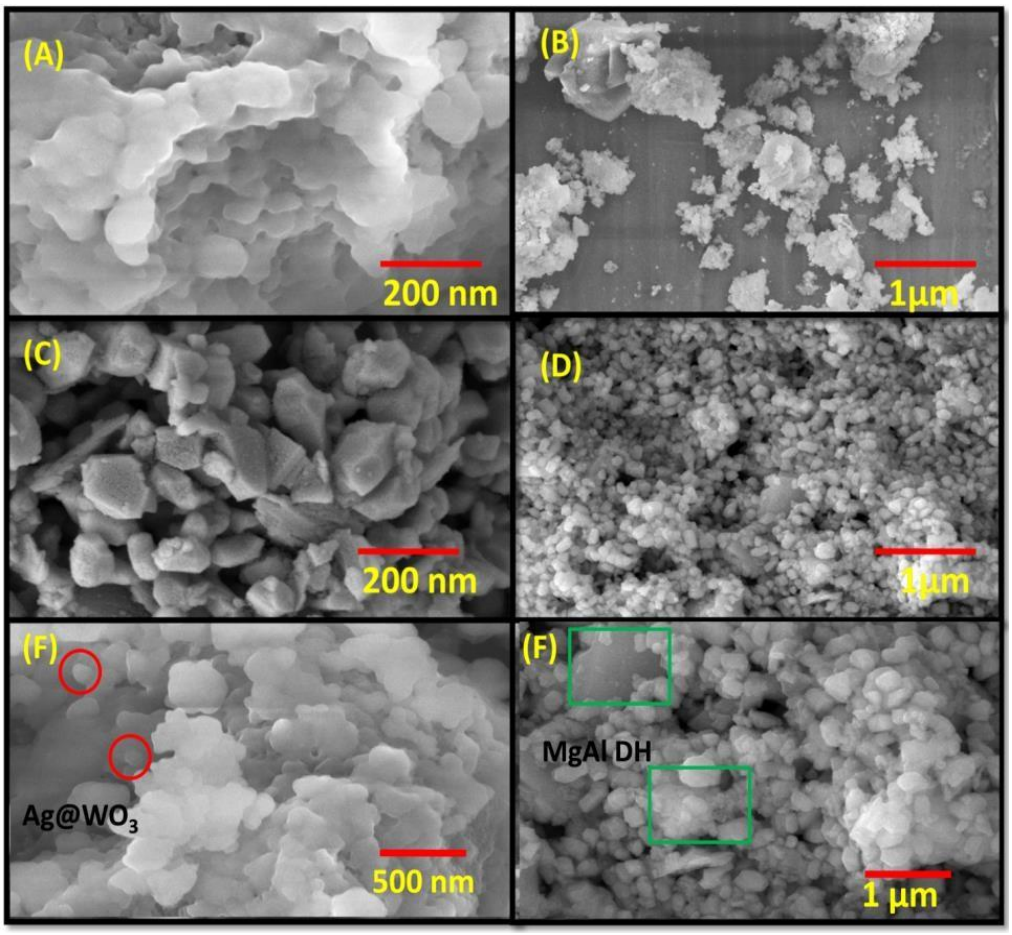

Fig.3.6. FESEM images of MgAl LDH (a,b); WO_3 (c,d) and $Ag_2@WO_3$/MgAl LDH composite (e,f)

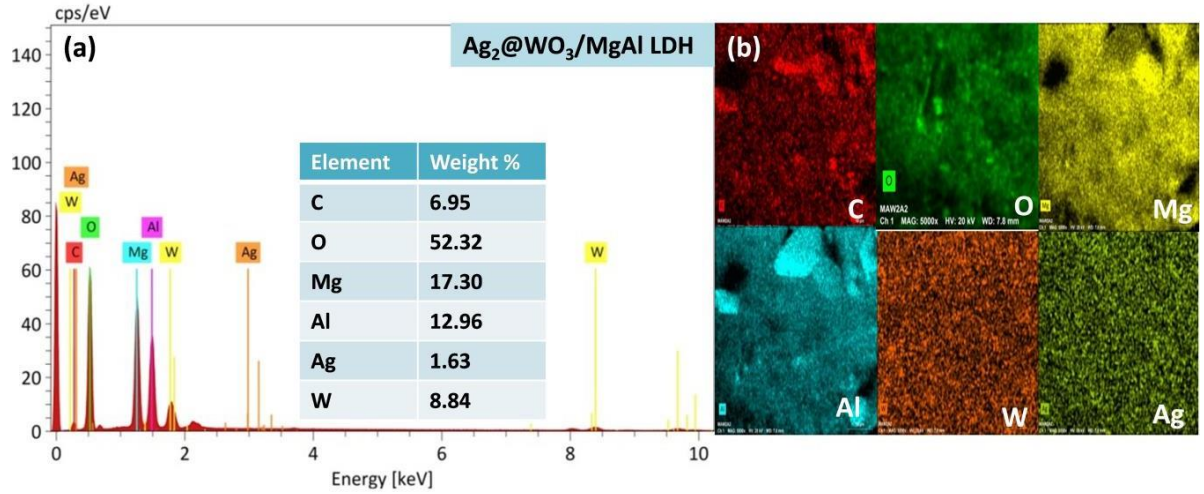

Fig.3.7. EDX spectrum (a); mapping images (b) of $Ag_2@WO_3$/MgAl LDH.

TEM analysis assessed the successful integration of MgAl LDH, WO_3, and Ag into the ternary composite. **Fig.3.8 (a, b)** presents images of the ternary composite captured at different resolutions. Specifically, **Fig. 3.8 (b)** clearly illustrates the presence of Ag nanoparticles with a size range of (20-45 nm) on the surface of WO_3. Furthermore, the HRTEM images **Fig. 3.8 (c)** revealed distinct lattice fringes spaced at 0.24 nm, 0.38 nm, and 0.48 nm, corresponding to the (111), (002), (003) diffraction planes of Ag, WO_3, and MgAl LDH, respectively [34–36]. The SAED pattern depicted in **Fig.3.8 (d)** features several concentric rings with bright spots superimposed on top, which are suggestive of the distinctive rings connected to Ag (111), WO_3 (202), and MgAl LDH (0018). This pattern provides additional evidence that Ag-deposited WO_3 is present on the surface of MgAl LDH in the composite material.

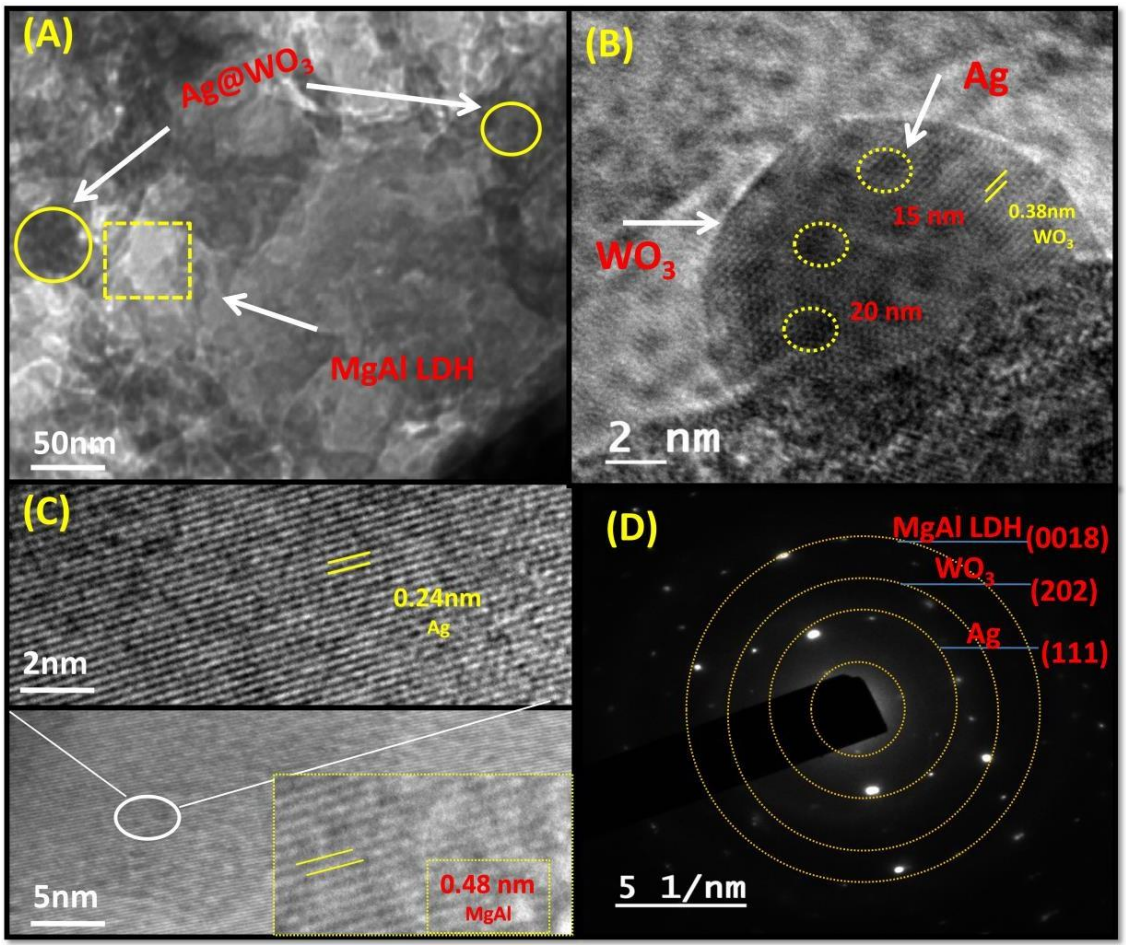

Fig. 3.8. HRTEM images (a, b); lattice fringes (c) and SAED pattern (d) of $Ag_2@WO_3$/MgAl LDH composite

Fig. 3.9(a, b) illustrates the surface area and pore size distribution curve for both MgAl LDH and the ternary composite $Ag_2@WO_3$/MgAl LDH. The N_2 adsorption-desorption isotherms for MgAl LDH and $Ag_2@WO_3$/MgAl LDH exhibit a type IV isotherm pattern, indicating a mesoporous nature with multilayer adsorption behavior. The pore size distribution analysis revealed that the pore sizes range between 1-20 nm, further confirming the mesoporous and microporous characteristic of the catalyst [37,38]. It was observed that the composite material exhibits enhanced surface area compared to the pure LDH, i.e. 52.90 m^2/g for $Ag_2@WO_3$/MgAl LDH and 39.69 m^2/g for MgAl LDH, respectively [39]. Additionally, an increase in pore size was also observed upon composite formation. These findings supported the incorporation of $Ag_2@WO_3$ into the MgAl LDH surface, leading to an increase in active sites for pollutant adsorption and improved transportation of reactants and products. Consequently, this enhancement in surface area and surface parameters contributed to the higher photoactivity of the composite material, making it beneficial for catalytic applications.

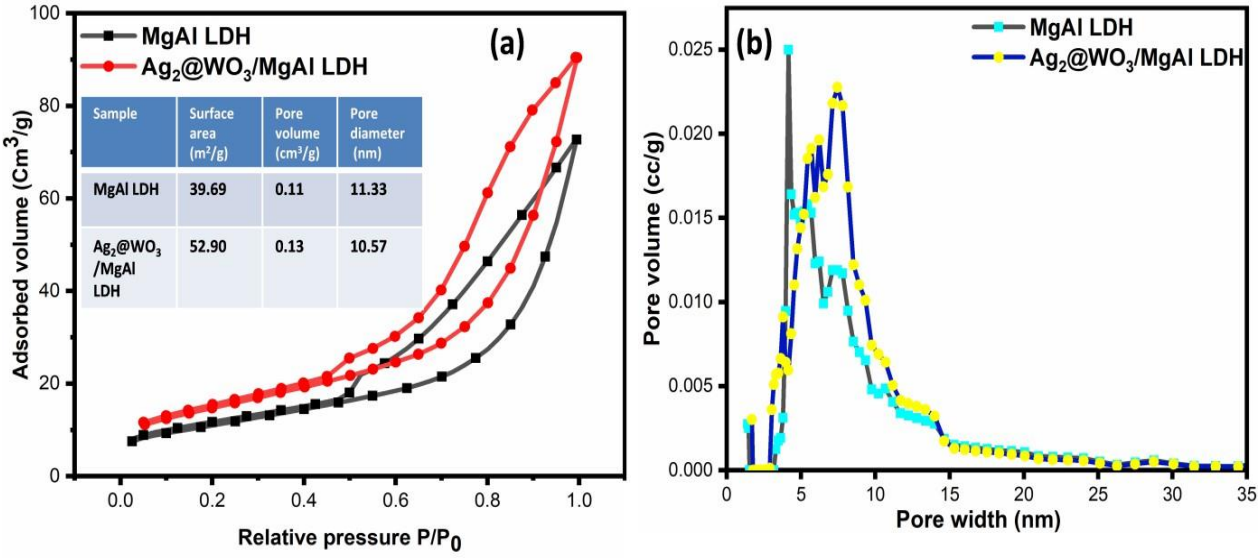

Fig.3.9. Nitrogen sorption isotherms (a) and pore size distribution curves for MgAl LDH and $Ag_2@WO_3$/MgAl LDH (b)

The electrokinetic properties of the synthesized catalysts were investigated through dynamic light scattering (DLS) and zeta potential studies. The MgAl LDH was found to have 770 nm hydrodynamic size. Upon loading of WO_3 and Ag onto the LDH surface, the hydrodynamic size increased to 1090 nm, 1296 nm, and 1460 nm for the WO_3/MgAl, $Ag_2@WO_3$/MgAl LDH, and

Ag_4@WO_3/MgAl LDH composites, respectively. This increase in hydrodynamic size **Fig.3.10 (a)** confirms the successful loading of WO_3 and Ag onto the surface of the LDH material. The zeta potential of MgAl LDH was determined to be +25 mV, indicating a positively charged surface. In contrast, the zeta potential of WO_3 was measured to be -10 mV, indicating a negatively charged surface. Upon loading WO_3 onto the LDH surface, the zeta potential decreased to 16 mV. This decrease in zeta potential can be attributed to the electrostatic interactions between the negatively charged WO_3 and the positively charged MgAl LDH surface, resulting in the neutralization of the LDH surface charge. Furthermore, upon loading silver onto the composites, the zeta potential was further reduced to +14 mV and +11 mV for the respective composites. These changes in zeta potential confirm the formation of the Ag@WO_3/MgAl LDH composites. Therefore, the variation in hydrodynamic size and changes in zeta potential shown in **Fig.3.10 (b)** provide evidence for forming the WO_3/MgAl and Ag@WO_3/MgAl composite.

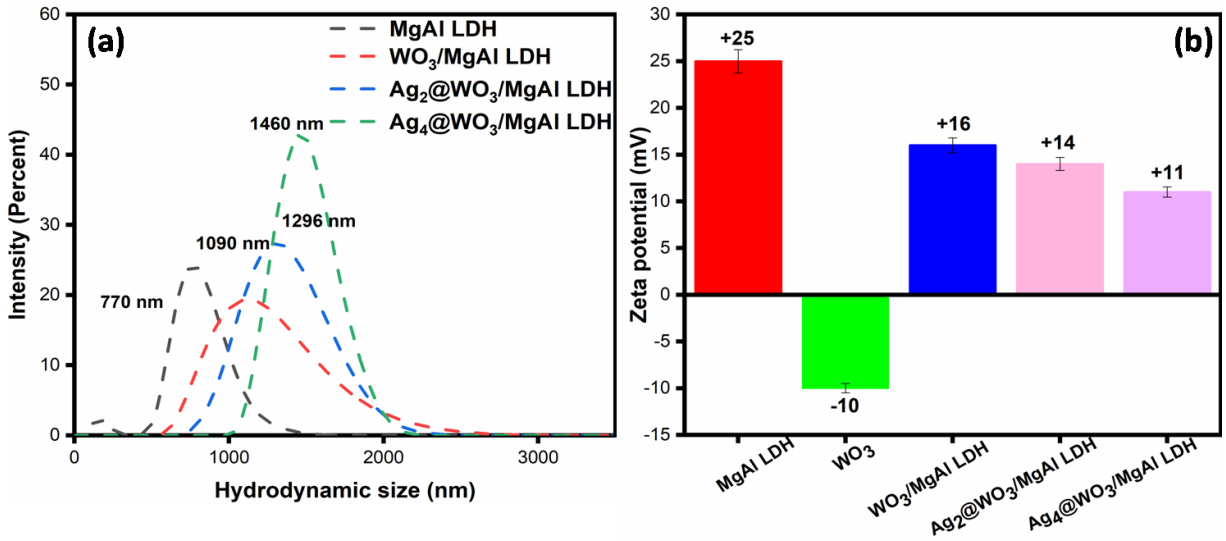

Fig.3.10. Variation of Hydrodynamic size (a); Zeta potential (b) of MgAl LDH, WO_3/MgAl, and Ag@WO_3/MgAl composites

X-ray photoelectron spectroscopy (XPS) analyses were conducted to assess the elemental composition and chemical states of synthesized heterojunction photocatalysts. In **Fig.3.11 (a)**, the survey XPS spectrum of MgAl LDH and Ag_2@WO_3/MgAl LDH indicates the presence of Mg, Al, C, and O elements in MgAl LDH, with the additional presence of W and Ag elements in its composite (Ag_2@WO_3/MgAl LDH). In **Fig.3.12(a, b)**, binding energy peaks for LDH and its composite at 50.15 eV and 50.03 eV for Mg 2p confirm the presence of $Mg(OH)_2$, while peaks at

73.94 eV and 73.70 eV for Al 2p suggest the existence of $Al(OH)_3$ within the brucite layers of MgAl LDH and $Ag_2@WO_3$/MgAl LDH, with a negative shift in energy of 0.12 eV for Mg 2p and 0.20 eV for Al 2p [40]. **Fig.3.11 (b)** displays the Mg 1s spectrum with binding energy values decreasing from 1306.06 eV to 1303.65 eV in the composite. The C 1s spectrum in **Fig.3.12 (c)** exhibits peaks at 289.91 eV, 289.38 eV, and 285.04 eV, 283.85 eV, corresponding to the binding energy of C-C and O-C=O bonds, respectively, confirming the presence of carbonate as interlayer anions [41]. In **Fig.3.12 (d)**, the O 1s spectrum reveals a peak at 532.08 eV and 531.16 eV assigned to hydroxyl groups of brucite layers at the surface of bare LDH and composite [42]. Changes in the binding energy values upon composite formation suggest alterations in the electronic structure, indicative of potential electron transfer in the composite. For the $Ag_2@WO_3$/MgAl LDH composite in **Fig.3.12 (e, f),** the W (4f) spectrum exhibits two prominent peaks at 37.12 eV and 35.03 eV, corresponding to $4f_{5/2}$ and $4f_{7/2}$. Additionally, the Ag 3d spectrum exhibits peaks at 374.15 eV and 368.11 eV, corresponding to Ag $3d_{3/2}$ and Ag $3d_{5/2}$, confirming the presence of W and metallic Ag in the composite [43].

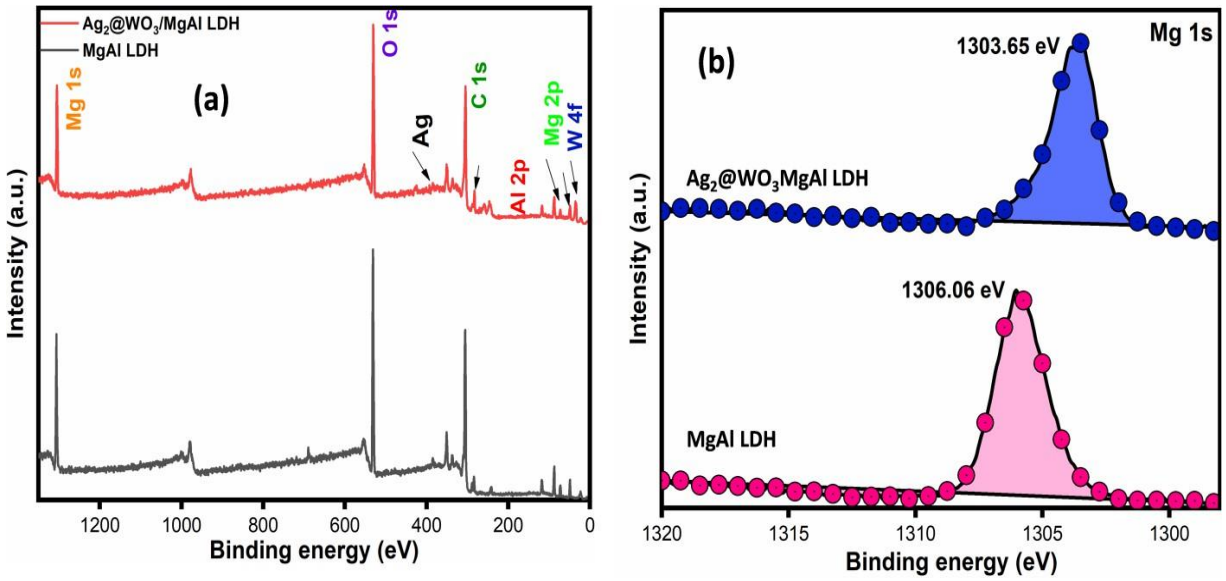

Fig.3.11. XPS survey (a); XPS spectra Mg 1s (b) of MgAl LDH and $Ag_2@WO_3$/MgAl LDH

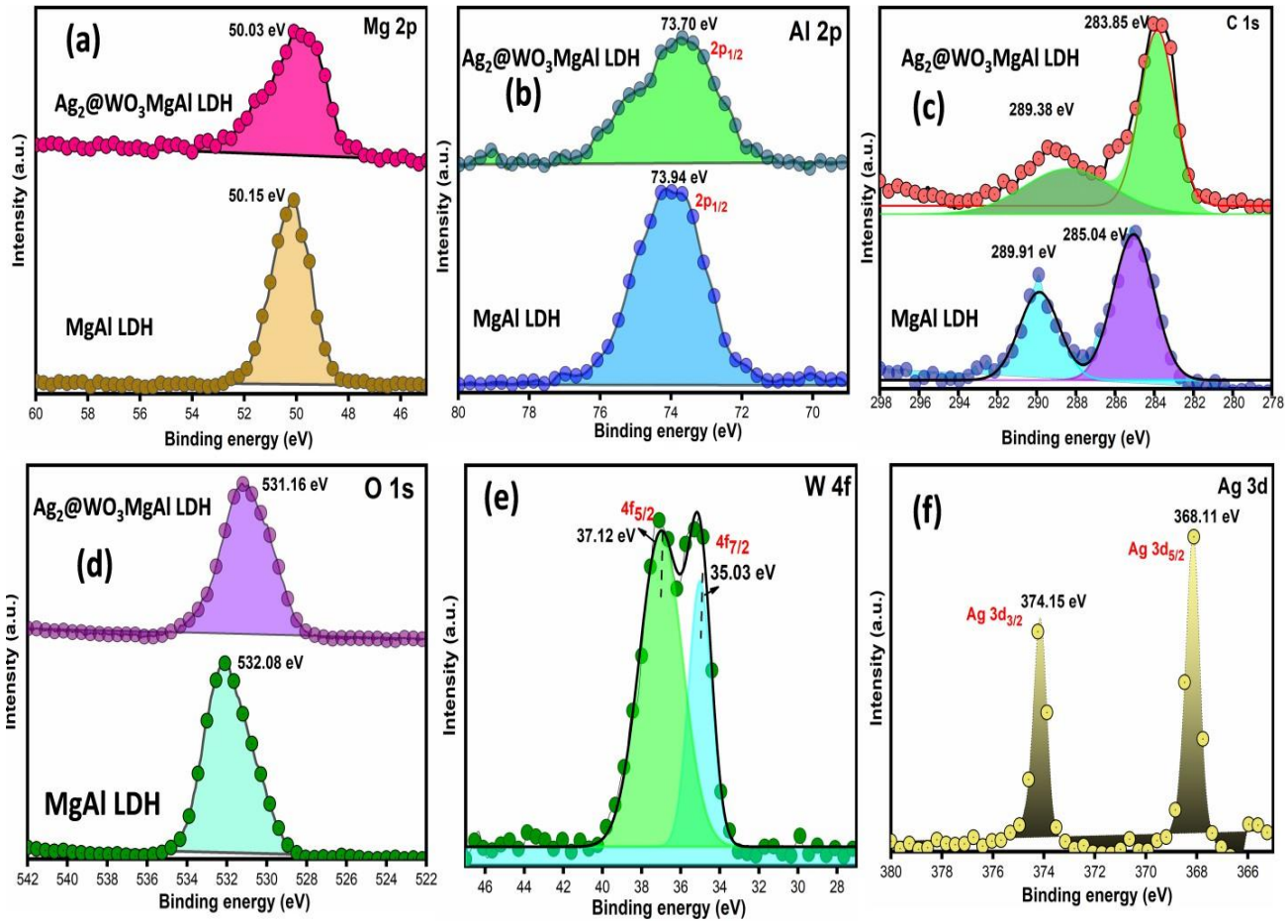

Fig.3.12. XPS spectra of MgAl LDH and $Ag_2@WO_3$/MgAl LDH (a) Mg 2p; (b) Al 2p; (c) C1s; (d) O 1s; (e) W 4f and (f) Ag 3d

3.4. Adsorption studies

The adsorption studies of adsorbents (LDH, WO_3/LDH, and Ag@WO_3/LDH composites) were examined using tetracycline (TC) as a model pollutant. The effect of various parameters, such as pollutant concentration, adsorbent dosage, and contact time, was investigated. During adsorption studies, a set of test tubes containing 5mL of the pollutant of specific concentration (10-60 mg/L) and a known amount of catalyst (0.001-0.007 g) was prepared and kept on stirring at (800 rpm) in the dark. After a fixed interval, the test tube was removed, the solution was centrifuged, and the concentration was determined using a JASCO, V-750 UV-Vis spectrophotometer in a 10 mm

Quartz cell. The adsorption capacity of the catalyst (mg/g) and percent removal efficiency were evaluated using the following equation:

Adsorption capacity (Q_e) = (C_o-C_e) V/W ..... (2)

Percent removal = (C_o-C_e)/C_e× 100 ..... (3)

Where C_o is the pollutant's initial concentration (mg/L), Ce is the pollutant's equilibrium concentration (mg/L), V is the volume of solution (L), W is the amount of adsorbent (g), and Q_e is the adsorbent's adsorption efficiency.

3.4.1. Effect of pH

The pH of a solution significantly influences the adsorption process. The adsorption capability of Ag_2@WO_3/MgAl LDH was tested using a variety of solutions generated at pH values of 3.0, 7.0, and 10.0. The purpose of these preparations was to assess how pH affects the ability of the prepared composite to adsorb substances. The TC molecules were adsorbed at maximum concentration at neutral pH (7) as the protonation and deprotonation of functional groups in the TC molecule led to changes in its chemical speciation due to varying pH levels. TC undergoes protonation of its dimethyl-ammonium group at pH values lower than 3.3, creating a cation. By shedding a proton from its phenolic diketone moiety, TC maintains its zwitterions state in the pH range of 3.3 to 7.7. The tri-carbonyl system and the phenolic diketone moiety both lose protons as the pH rises over 7.7, which causes TC to change into an anion [44]. The composite consisting of dual charge on the surface, therefore, becomes capable of adsorbing more TC molecules in a neutral pH range due to the existence of the zwitter ion. **Fig.3.13 (a)** and **(b)** depict the percent adsorption at different pH values, indicating maximum adsorption at 7 pH and UV-Vis adsorption studies of MgAl LDH and its composites adsorption at 7 pH, which was the maximum for Ag_2@WO_3/MgAl LDH. Bar graph percent adsorption and molecular structure of TC is shown in **Fig.3.13 (c) and (d),** depicting the maximum percent adsorption achieved by Ag_2@WO_3/MgAl LDH composite at neutral pH due to strong interaction between MgAl LDH composite and TC molecules due to zwitter ion formation.

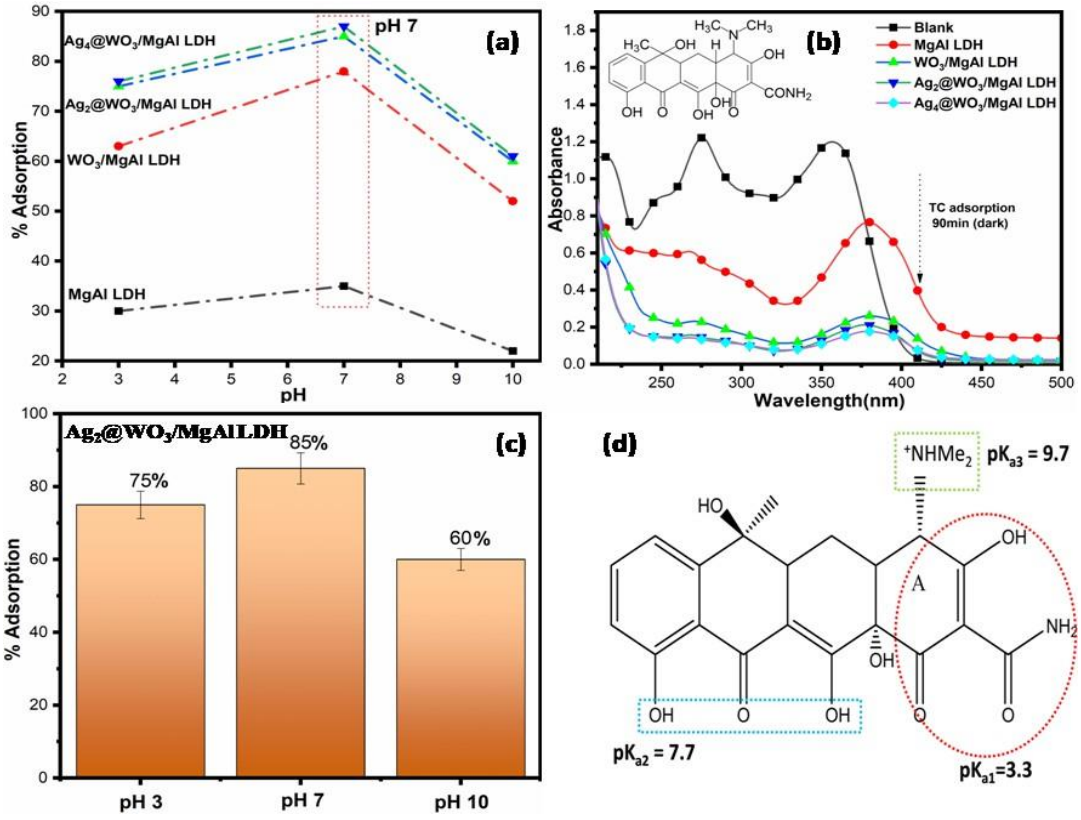

Fig.3.13. Effect of pH (a); UV-Vis adsorption spectra and percent adsorption of TC (b, c) by MgAl LDH, WO_3/LDH and Ag@WO_3/LDH composites and molecular structure of TC on a planar view (d)

3.4.2. Adsorbent dose effects

The dosage of an adsorbate directly impacts how quickly it binds to the surface of an adsorbent. This results from the fact that when the dose of the adsorbent increases, the number of accessible adsorption sites rises and eventually reaches saturation. **Fig.3.14 (a)** illustrates the impact of the dosage of unmodified LDH and its composites on the adsorption of TC antibiotic. The experimental observations indicate that a dosage of 0.005 g of LDH and its composites is adequate to achieve maximum pollutant removal (30%, 44%, 78% and 80% for MgAl LDH, WO_3/MgAl LDH, Ag_2@WO_3/MgAl LDH, Ag_4@WO_3/MgAl LDH). Upon further increasing the dosage, no significant improvement in adsorption efficiency was observed, likely due to reaching a saturation point.

3.4.3. Effect of initial concentration of adsorbate

The adsorption efficiency of LDH and its composites were examined by varying the concentrations of TC (10-60 mg/L). As shown in **Fig. 3.14 (b)** the highest adsorption efficiency of 88 mg/g was observed for Ag_4@WO_3/MgAl LDH at an initial concentration of 40 mg/L for TC, with a subsequent plateau indicating the saturation of adsorption sites.

3.4.4. Effect of contact time

The duration of contact between the adsorbate and adsorbent is a critical factor in the adsorption process, as adsorption increases with longer contact times until equilibrium is reached. From **Fig.3.14 (c and d),** it is evident that over 88% of TC adsorbs onto the surface of Ag_4@WO_3/MgAl LDH within the first 90 minutes, followed by a slower adsorption rate over time. Similarly, bare LDH, WO_3/MgAl LDH, and Ag_2@WO_3/MgAl LDH attain equilibrium in the first 90 minutes and adsorbs up to 36%, 78%, and 85% of TC. The adsorption of TC demonstrates high efficiency on the catalyst surface, which provides a large contact area and facilitates electrostatic interactions between the catalyst surface and TC molecules.

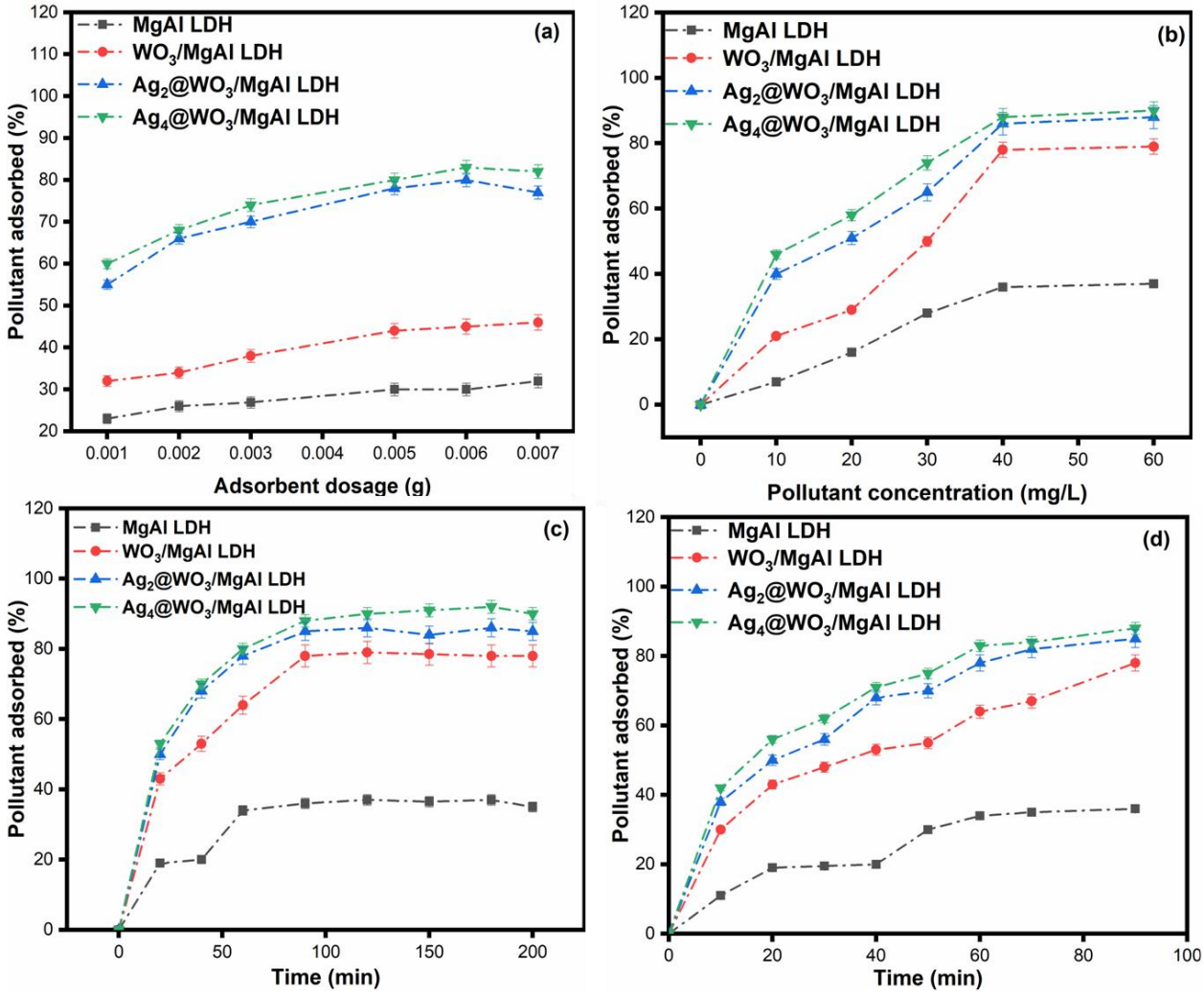

Fig.3.14. Effect of catalyst dosage (a); pollutant concentration (b); contact time (c, d) on adsorption efficiency of bare MgAl LDH, WO_3/MgAl LDH and Ag@WO_3/MgAl LDH composites towards TC removal

3.4.5. Adsorption isotherms and Kinetic studies

The adsorption process at equilibrium was characterized using two commonly employed adsorption isotherm models: Langmuir and Freundlich. The investigation involved varying the initial concentration of pollutant (10-60 mg/L for TC) added to a fixed amount (0.005 g) of the adsorbent. The Langmuir isotherm presupposes a homogeneous adsorption mechanism in which an identical adsorbate monolayer develops on the adsorbent's surface and has similar energy. As each molecule occupies a single adsorption site, it also presupposes that there are no interactions

between nearby adsorbed molecules. The mathematical representation of the Langmuir adsorption isotherm is:

$$Q_e = q_{max}\ K_L C_e / 1 + K_L C_e \quad (4)$$

The linear form of Langmuir isotherm can be represented as:

$$1/Qe = 1/K_L q_{max}.1/C_e + 1/q_{max} \quad (5)$$

$R_L = 1 / (1 + K_L \times C_o)$, where R_L is the separation factor.

In this equation, K_L stands for Langmuir's isotherm constant in (L/mg), which represents the binding affinity between TC and LDH composites, and q_{max} denotes the maximal adsorption capacity in (mg/g). C_o represents the highest initial concentration of the pollutant. The separation factor (R_L) can be determined by substituting the appropriate values. The R_L value provides insights into the nature of the adsorption process. R_L values indicate a value of $R_L = 0$ shows irreversible adsorption, favorable adsorption between 0 and 1, linear adsorption is represented by R_L=1, while non-favorable adsorption is shown by R_L values higher than 1 [45].

The Freundlich's isotherm equation is represented by Equation:

$$Qe = K_f C_e^{1/n} \quad (6)$$

The linear form is given by:

$$Log(Q_e) = Log(K_f) + (1/n) \times Log(C_e) \quad (7)$$

The adsorption capacity is measured using Freundlich's constant (K_f), and the value of 1/n provides information about the adsorption process. A favorable adsorption process occurs if the 1/n value is equal to or between 0.1-0.5. Conversely, if $1/n \geq 2$, it suggests an unfavorable adsorption process [46].

According to the study, the Langmuir and Freundlich models were used to suit the experimental results of pollutant adsorption. The corresponding parameters obtained from the slope and intercept of the graphs are presented in **Table 1**. The R^2 values for the Langmuir model ranged

from 0.946 to 0.99, which were greater than the R^2 values for the Freundlich model, which ranged from 0.728 to 0.932 for both MgAl LDH and its composites. These findings suggest that the Langmuir model better fits the data when compared to the Freundlich model. That means the adsorption of pollutants is monolayer adsorption on the surface.

Furthermore, the calculated R_L values using the Langmuir model equation fall within the range of 0 to 1, indicating favorable adsorption of TC pollutants. The value of 1/n, where n is the Freundlich parameter, indicates the favorability of the adsorption process. In this case, the range of $0.1 \leq 1/n \leq 0.5$ demonstrates favorable adsorption.

Overall, based on the analysis and results obtained, the Langmuir model provides the best fit, indicating monolayer adsorption is taking place; also, pollutant adsorption is favorable according to both the Langmuir and Freundlich models.

Table 1: Langmuir and Frendulich model parameters for TC adsorption on MgAl LDH and its composites

	Langmuir model				**Frendulich model**		
Adsorbent	Q_{max}	K_L	R^2	R_L	K_F	1/n	R^2
MgAl LDH	684	0.03	0.967	0.268	0.234	0.539	0.805
WO_3/MgAl LDH	800	0.05	0.946	0.196	0.269	0.463	0.728
WO_3@Ag_2/MgAl LDH	884	0.15	0.997	0.073	0.355	0.403	0.932
WO_3@Ag_4/MgAl LDH	980	0.18	0.978	0.0629	0.364	0.400	0.892

Kinetic study:

The kinetic studies conducted during the adsorption process involved the examination of two kinetic models, i.e., pseudo-first-order and pseudo-second-order. Their linear forms are expressed as follows:

1. Pseudo first-order kinetic model: $\log(Q_e - Q_t) = \log(Q_e) - (k_1/2.303)\times t$
2. Pseudo second-order kinetic model: $t/Q_t = 1/(k_2\ Qe^2) + t/Q_e$

These equations, k_1, and k_2, denote the first- and second-order rate constants, respectively. Q_t and Q_e are the adsorbate adsorbed per mass of the adsorbent (mg/g) at equilibrium and at a specific time (t). These kinetic models provide insights into the rate and mechanism of the adsorption process, allowing for the determination of rate constants and predicting the adsorption behavior over time [47].

Table 2: Parameters of first-order and second-order kinetics for adsorption of TC on MgAl LDH and its composites

	First order kinetics			**Second order kinetics**		
Adsorbent	Q_e	K_1	R^2	Q_e	K_2	R^2
MgAl LDH	0.284	0.054	0.933	80.64	0.00136	0.951
WO_3/MgAl LDH	0.329	0.036	0.972	147.05	0.00068	0.947
WO_3@Ag_2/MgAl LDH	0.317	0.038	0.966	163.13	0.00076	0.970
WO_3@Ag_4/MgAl LDH	0.330	0.047	0.884	172.41	0.00084	0.976

The first- and second-order kinetics parameters were calculated using the slope and intercept obtained from the graphs, and the results are presented in **Table 2**. After the study, it was found that the second-order kinetics had greater R^2 values than the first-order kinetics. Additionally, it was observed that the second-order kinetics had a greater value for Qe, which measures the quantity of adsorbate adsorbed per unit mass of the adsorbent (mg/g) at equilibrium. These findings suggest that the second-order kinetics better fit the experimental data. As a result, the findings suggest that the second-order kinetics model is superior to the first-order kinetics model for characterizing the adsorption process because it exhibits better R^2 values and a larger adsorption capacity (Q_e). The adsorption model isotherms and kinetic studies are shown in **Fig.3.15 (a-d).**

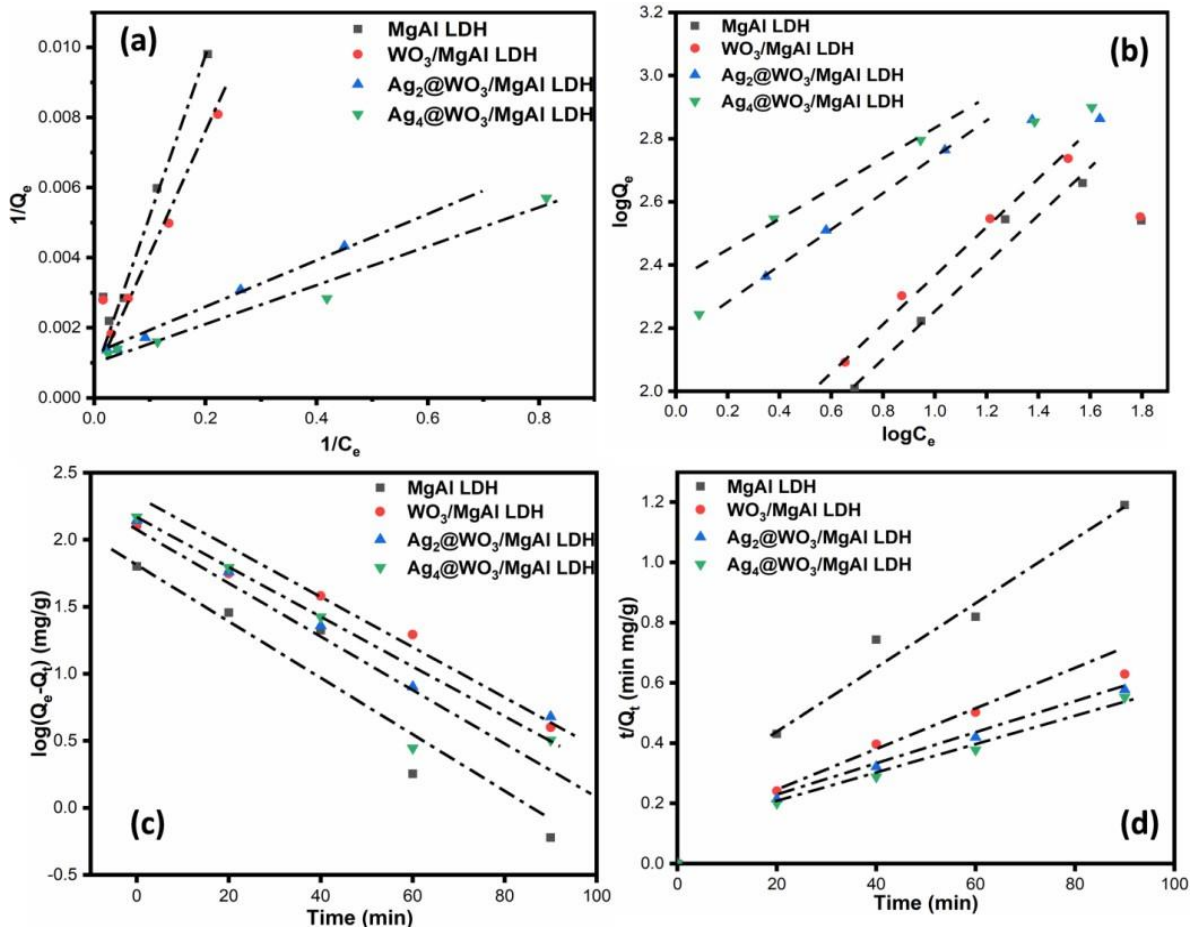

Fig.3.15. Modelling of adsorption equilibria by Langmuir and Freundlich isotherm (a, b); kinetics of adsorption of TC by MgAl LDH, WO_3/MgAl LDDH and Ag@WO_3/MgAl LDH composites according to first and second order kinetics (c, d)

3.5. Photocatalytic studies

3.5.1. Photodegradation reaction

The photocatalytic activity of MgAl LDH and Ag@WO_3/MgAl LDH composites was examined using ciprofloxacin (CIP) as a model pollutant with an initial concentration of 10 ppm, for degradation of CIP 5mg of catalyst was dispersed in a test tube containing 5 mL of CIP pollutant. The suspensions were stirred in the dark for 30 min to achieve adsorption and desorption equilibrium shown in **Fig. 3.16 (a-d)**. After that, the test tubes were irradiated with the visible light source (50W LED lamp, Wipro Garnet B22, intensity ~ 100 W/ m^2, λ = 380- 700 nm) for

140 min. At definite intervals, the catalysts were removed by centrifugation following the separation, and the absorbance spectra of CIP were examined at λ_{max} = 274 nm (JASCO V-750 spectrophotometer). Adsorption efficiencies of all the catalysts' were observed as Ag_4@WO_3/MgAl LDH > Ag_2@WO_3/MgAl LDH > WO_3/MgAl LDH >MgAl LDH, which can be explained based on enhanced surface area of binary and ternary composites giving rise to more active sites for the reaction to occur.

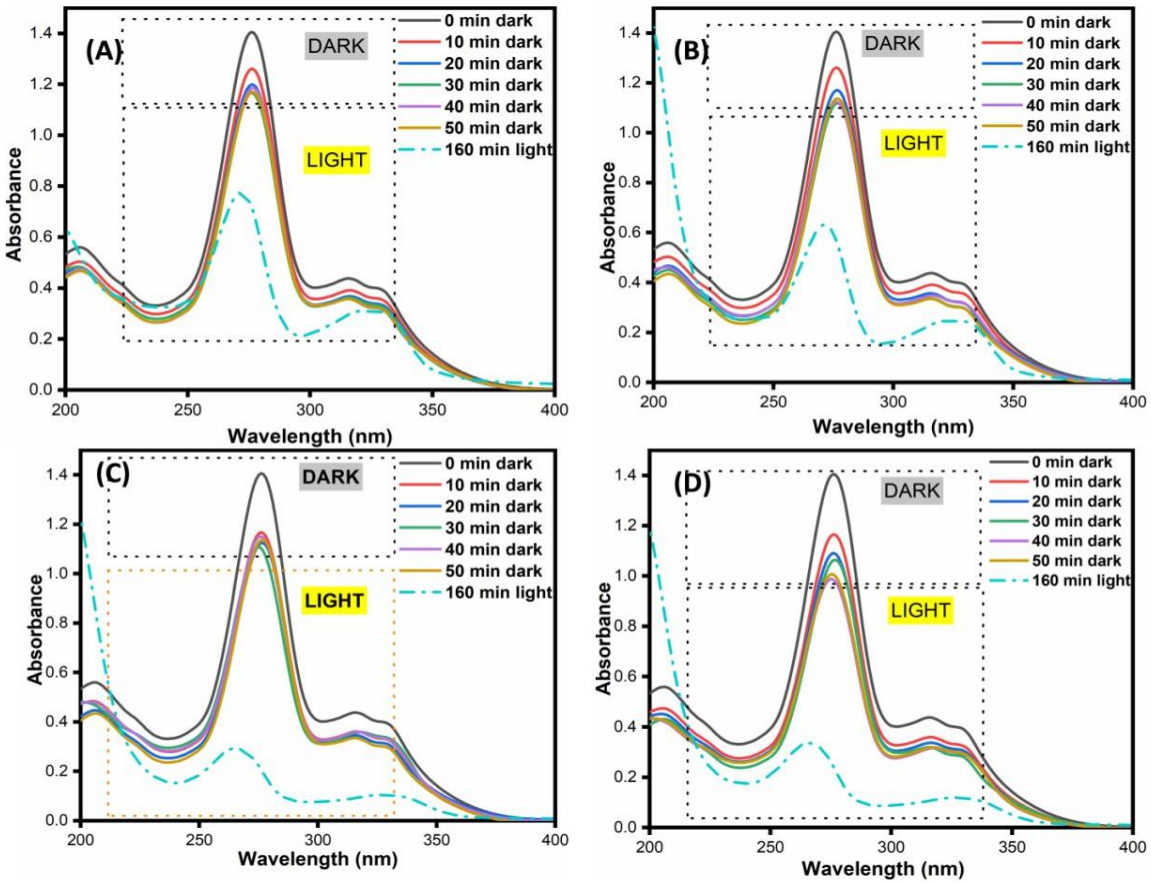

Fig.3.16. UV Visible spectrum of adsorption and degradation of CIP by MgAl LDH (a) MgAl /WO_3 (b) Ag_2@WO_3/MgAl LDH (c) Ag_4@WO_3/MgAl LDH (d) under dark and visible light

The percent degradation for CIP was calculated by using the following equation:

$$\% \text{ Degradation} = (C_o - C_t / C_o) \times 100 \quad (8)$$

C_o and C_t are the initial and final concentrations of CIP (mg/L) at time t.

The mineralization efficiency of Ag@WO_3/MgAl LDH was calculated with the help of total organic carbon (TOC) analysis.

The mineralization of the samples was calculated using the following equation:

Mineralization (%) = TOC initial- TOC final/TOC initial ×100 ..... (9)

The intermediates and final products formed during the degradation of CIP were investigated using HR-MS analysis.

During photodegradation, the MgAl LDH with a wide band gap of 3.6 eV showed minimum photoactivity under visible light. However, WO_3 and Ag_2@WO_3 loadings upon MgAl LDH shifted the band gap to 2.2 eV, enhancing the light-absorbing properties and better photocatalytic performance. The adsorption and photodegradation curves of CIP across various catalysts are shown in **Fig.3.17 (a) and Fig.3.17 (b)** illustrates the photodegradation efficiencies of the catalyst under visible light for 160 min. Bare LDH achieves a degradation efficiency of 40%, whereas binary and ternary composites showed 51% and 77% efficiency for WO_3/MgAl LDH and Ag_2@WO_3/MgAl LDH, respectively. The increased efficiency is because of the loading of metal oxides and plasmonic metal oxides upon the LDH surface, thereby enhancing the surface area and light-absorbing capacity due to the SPR effect of plasmonic metals [48]. Among different LDH composites, the Ag_2@WO_3/MgAl composite exhibited the best activity because of the smaller band gap of the loaded WO_3/LDH composite providing better visible light absorption. Additionally, the high electronegativity and electron affinity of Ag helped to improve electron trapping efficiency. Also, it was observed that the composites with more metal loading (Ag_4@WO_3/MgAl LDH) showed decreased photodegradation due to the agglomeration of metal NPs and, hence, decreasing photo efficiency.

The photocatalytic degradation of CIP by MgAl LDH and its composites follows pseudo-first-order kinetics. The rate of photodegradation at low concentrations of CIP is given by:

$\ln c_t = -kt + \ln c_o$ ..... (10)

This linear integration of Eq. (3) is given by:

$\text{Log } (c_o/c_t) = k \times t/2.303$ ..... (11)

Where C_o is the CIP solution's initial concentration before exposure, C_t is the CIP solution's concentration as a function of exposure time (t), k is the pseudo-first-order rate constant (min^{-1}), and t is the experimental duration (min). **Fig. 3.17(c and d)** demonstrates the linear fit first-order reaction kinetics for all the prepared catalysts. Silver metal loaded composites showed the enhanced photodegradation of CIP antibiotic under visible light irradiation in comparison to MgAl LDH with kinetic rate constant 0.97×10^{-2} min^{-1}, which is almost three times that of MgAl LDH rate constant i.e. 0.36×10^{-2} min^{-1}. The significant factors contributing to this enhanced degradation and highest rate constant are enhanced surface generated for catalytic reaction, optimum quenching in the PL signal, highest separation efficiency of charge carriers, and better electron capturing tendency of Ag due to higher reduction potential (+0.79 eV).

Moreover, we contrasted the photocatalytic performance of the as-fabricated $Ag_2@WO_3$/MgAl LDH photocatalyst with that of the majority of other recently reported photocatalysts for CIP degradation (as tabulated in **Table-3**)

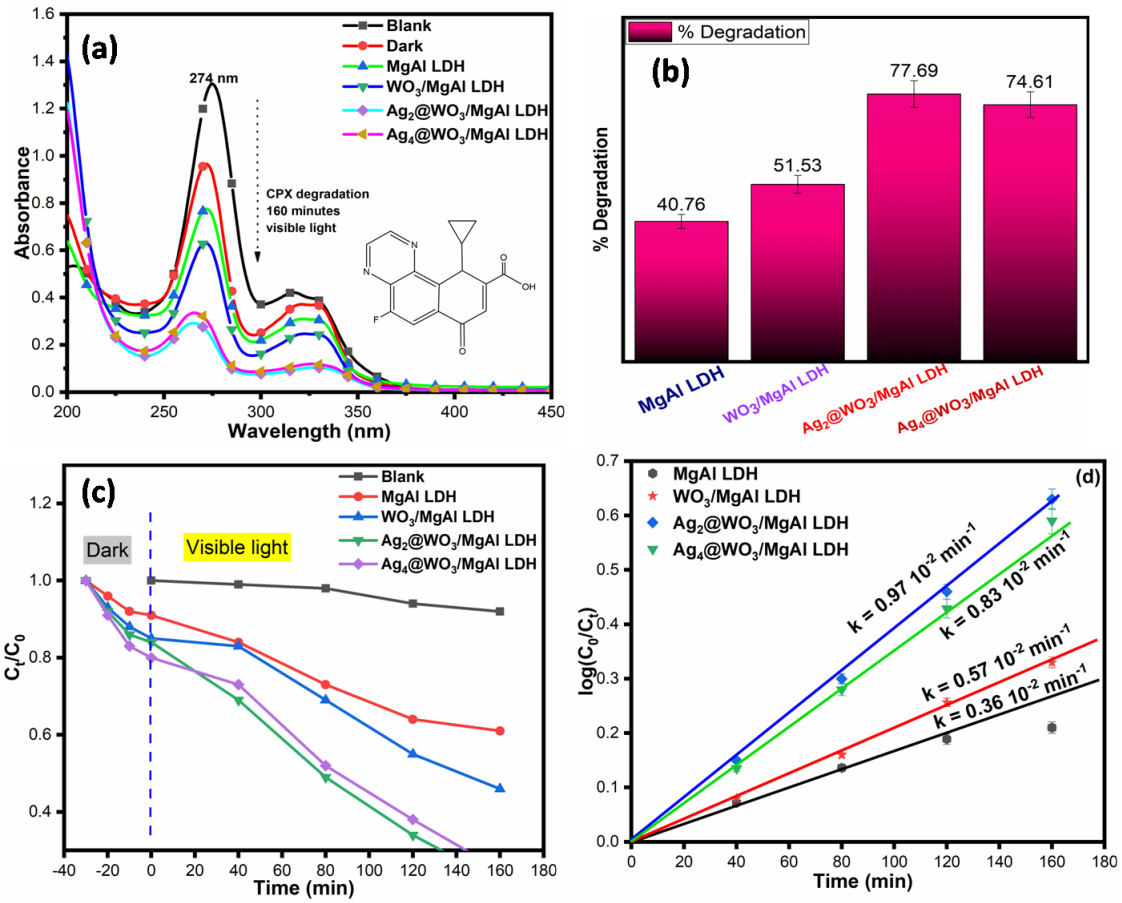

Fig.3.17. Time dependent UV-Vis spectra of CIP solution (a); Percent degradation efficiency (b-d) apparent change in rate constants and time course kinetic plots of MgAl LDH and its composites under 160 minutes visible light irradiation.

Table 3: Summary of comparison of different photocatalysts for CIP degradation

S.No.	Photocatalyst	Light source	% deg in minutes	Band gap (eV)	Rate constant (min^{-1})	Reference
1.	MgAl LDH-CT	UV light	65.73 in 120 min	4.98	0.0198	[49]
2.	MgAl LDO-CT	UV light	73.30 in 120 min	2.34	0.0230	[49]
3.	5% C_3N_4-CoAl LDH	Vis light	58.50 in 90 min	-	0.00985	[50]
4.	WRG-40	Vis light	90 in 120 min	2.32	0.2078	[51]
5.	CAB-21.26	Vis light	93 in 120 min	-	0.2011	[52]
6.	R_2-CuO	Vis light	94.6 in 240 min	2.024	0.0038	[53]
7.	Ag_2@WO_3/MgAl LDH	Vis light	77.69 in 160 min	2.46	0.97	Present work

3.5.2. HRMS analysis

The HR-MS (High-resolution mass spectroscopy) technique was employed to analyze the intermediates generated during the photodegradation of CIP using Ag_2@WO_3/MgAl LDH as the photocatalyst. In the HR-MS spectrum, the m/z value represents the molecular weight of the intermediates, where "m" denotes the molecular weight and "z" represents the charge number **.** Based on the intermediates found in the HR-MS analysis (**Fig.3.18)**, the hypothesized CIP degradation pathways are shown in **Fig. 3.19.** In the first pathway (P1), the piperazine and quinoline moieties in the CIP molecule are susceptible to attack by active species such as $O_2^{\bullet-}$,

$OH^{\bullet}$, and h^{+}. The CIP molecule initially exhibits a peak corresponding to m/z = 332. The piperazine ring breaks during the degradation process, oxidizing the secondary amine groups, and an intermediate known as P1 with m/z = 362 is produced. P1 is decarboxylated to create P2 (m/z = 334). `Further attack by holes leads to the loss of a formaldehyde group, generating P3 (m/z = 301). P3 subsequently undergoes hydroxylation to generate P4 (m/z = 291). The loss of a carbonyl group results in the generation of P5 (m/z = 263) [54].

In the second pathway, the piperazine ring is attacked by $OH^{\bullet}$, leading to the formation of P6 (m/z = 301). P6 undergoes further hydroxylation, which removes the CH-NH_2 group to form P7 (m/z = 263). An intermediate in this pathway is demethylated to produce another intermediate, which is then defluorinated to produce P8 (m/z = 245). The detected intermediate molecules eventually disintegrate into small inorganic substances such as CO_2, H_2O, and NH_4^{+}. The HR- MS analysis sheds light on the mechanism and how various radicals ($O_2^{\bullet-}$, $OH^{\bullet}$, and h^{+}) contribute to photodegradation [17,55].

Therefore, based upon HR-MS analysis, the proposed degradation pathways and the identified intermediates elucidate the involvement of $O_2^{\bullet-}$, $OH^{\bullet}$, and h^{+} radicals in the degradation of CIP using Ag_2@WO_3/MgAl LDH as a photocatalyst.

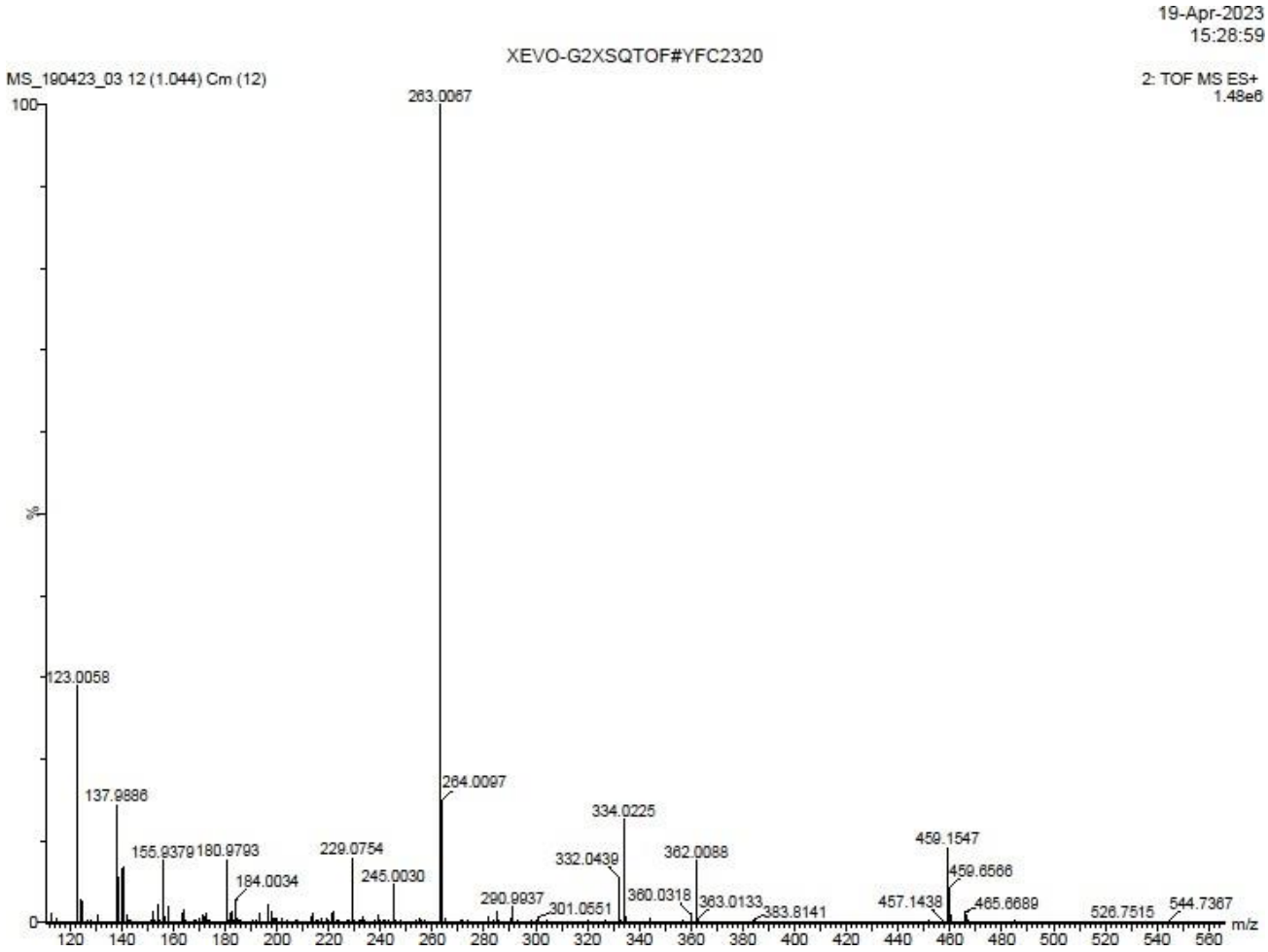

Fig.3.18. HRMS spectra of CIP degradation by $Ag_2@WO_3$/MgAl LDH under visible light irradiation

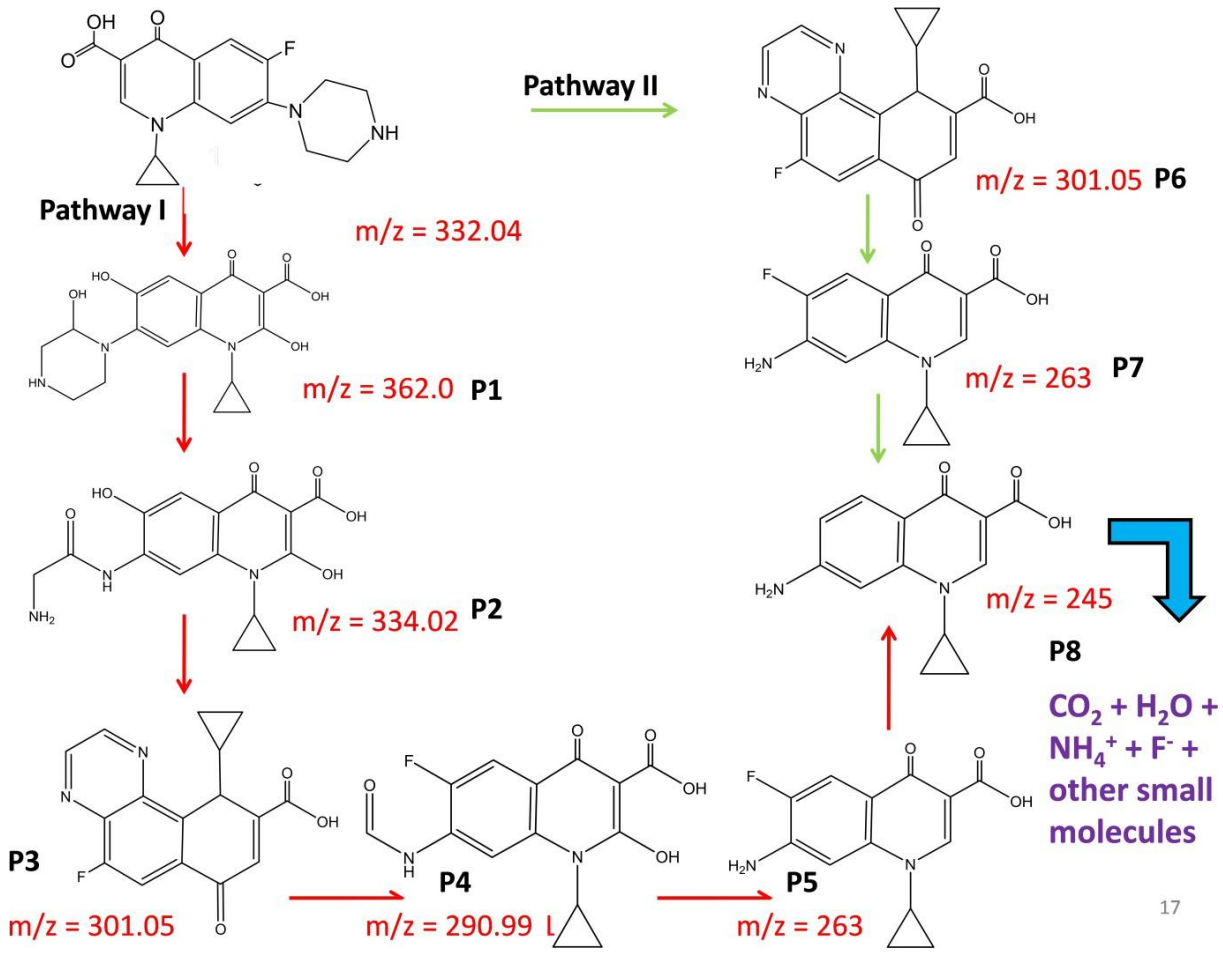

Fig.3.19. Proposed photocatalytic degradation pathway of CIP antibiotic by $Ag_2@WO_3$/MgAl LDH composite

3.5.3. Reusability and stability test

The study looked into the role of various active species in the photodegradation process, including superoxide anion radicals ($O_2^{\bullet-}$), hydroxide radicals ($OH^{\bullet}$), and holes (h^+). Scavengers were introduced into the reaction system to examine their roles. Particularly, scavengers for $O_2^{\bullet-}$, $OH^{\bullet}$, and h^+ were employed in the form of $K_2Cr_2O_7$, Ar purging, methanol, and isopropanol, respectively. Under the same experimental conditions as previously mentioned, the scavenging tests were carried out during the photodegradation of the CIP solution over the $Ag_2@WO_3$/MgAl LDH photocatalyst. The results, depicted in **Fig.3.20 (a),** revealed that the degradation performance of $Ag_2@WO_3$/MgAl LDH was maximum and decreased upon the addition of $K_2Cr_2O_7$ and Argon purging, indicating that $O_2^{\bullet-}$ species played a key role in the degradation

process. On the other hand, the degradation activity was also suppressed when isopropanol and methanol were added, suggesting that h^+ and $O\dot{H}$ were also involved in the degradation of CIP.

The TOC (total organic carbon) process is related to the amount of organic content in the solution after photodegradation. Although it is known that degradation does not mean the complete mineralization of organic pollutants into carbon dioxide, water, and other products, it is important to find the amount of mineralization occurring for harmful pollutants. The same $Ag_2@WO_3$/MgAl LDH composite with higher photodegradation efficiency was taken for TOC analysis of the CIP antibiotic. The results showed that after 160 min of exposure to visible light, the TOC values of CIP decreased by 50%, from 9.6 g/L to 4.6 g/L. The calculated TOC values confirm the mineralization of CIP pollutant and the degradation under visible light.

Recyclability and reusability are crucial considerations when evaluating a catalyst's application. In the case of the $Ag_2@WO_3$/MgAl LDH catalyst, its reusability was evaluated based on its photodegradation effectiveness, as depicted in **Fig.3.20 (b)**. The catalyst was subjected to five reuse cycles under the same experimental conditions. After each cycle, the powder catalyst was separated from the solution, washed, dried, and reused. To assess the stability of the catalyst, XRD spectra of the $Ag_2@WO_3$/MgAl LDH composite were studied before and after the photocatalytic reaction, as shown in **Fig.3.20 (c)**. The XRD analysis revealed that the crystal structure of the catalyst remained unchanged after the photocatalytic reaction. This demonstrated the stability of the catalyst throughout the degradation process.

Based on the aforementioned results, it can be concluded that the $Ag_2@WO_3$/MgAl LDH composite exhibited favorable recyclability and reusability for the degradation of ciprofloxacin. The minor decrease in photodegradation efficiency after multiple reuse cycles was primarily attributed to the physical processes involved in catalyst separation and washing. The XRD analysis further confirmed the stability of the catalyst, reinforcing its suitability for the degradation of CIP confirmed the stability of the catalyst, reinforcing its suitability for the degradation of CIP.

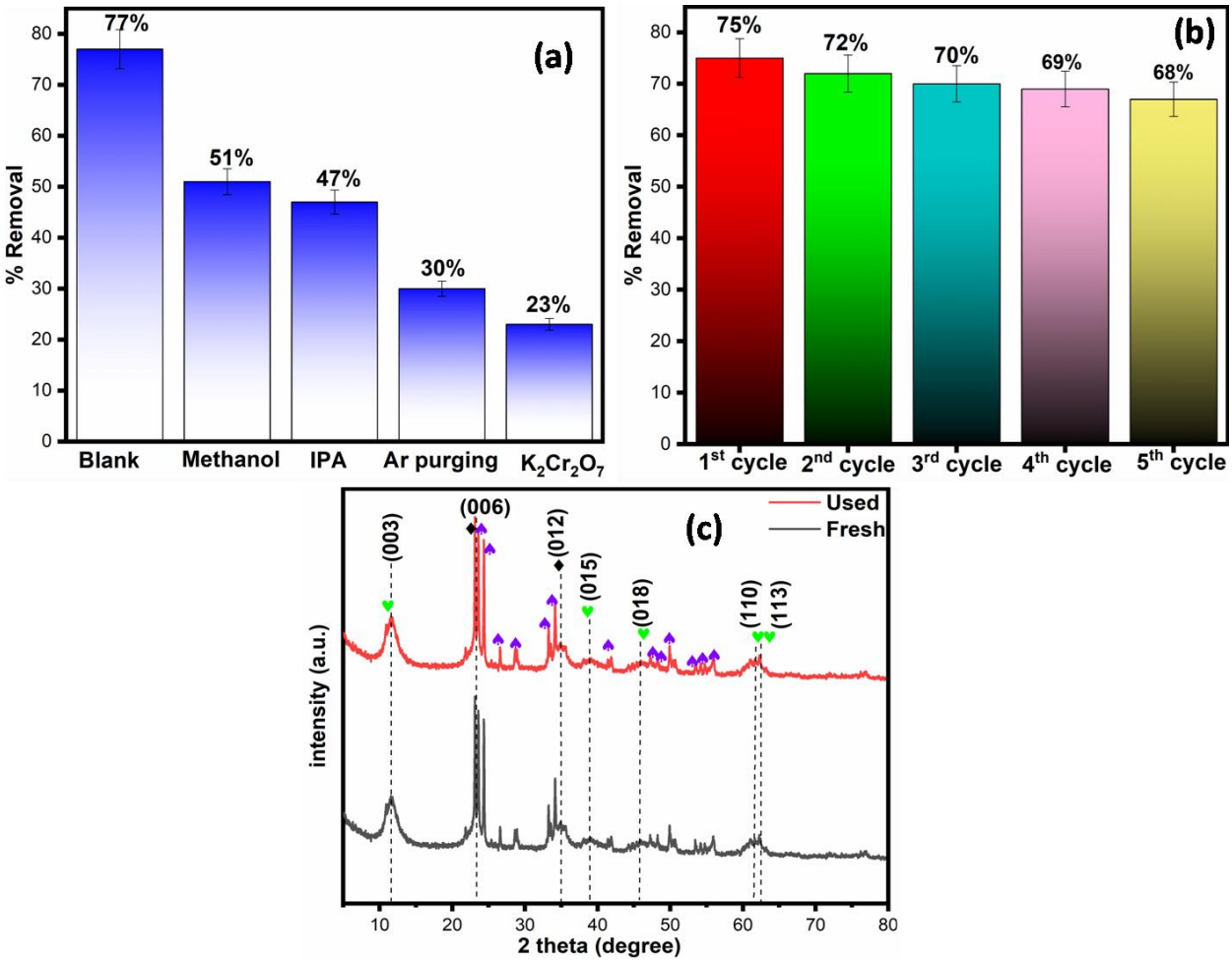

Fig.3.20. Effect of scavengers on CIP degradation with Ag_2@WO_3/MgAl LDH (a); reusability studies (b) and XRD spectra of Ag_2@WO_3/MgAl LDH composite before and after 5 cycles of CIP degradation (c)

3.5.4. Proposed mechanism

In **Scheme 2** the charge transfer mechanism in the MgAl LDH/Ag loadedWO_3 photocatalyst under simulated visible light irradiation is described. The valence band and conduction band potentials of WO_3 are measured to be +3.24 V and +0.94 V versus the NHE, respectively, and VB and CB potentials for MgAl LDH are measured to be +3.0 V and -0.61 V versus NHE. The following equations estimated the valence band and conduction band of MgAl LDH and WO_3:

$E_{VB} = \chi - E_e + 0.5E_g$ ..... (12)

$E_{CB} = E_{VB} - E_g$ ..... (13)

Ternary Ag@WO_3/MgAl LDH belongs to a type II heterojunction. When the composite was illuminated with visible light radiation, LDH and WO_3 became excited and generated electrons and holes. Electrons moved easily from MgAl LDH to WO_3 because of the CB edge potential of MgAl LDH (-0.61 eV) being more negative and higher than that of WO_3 (+0.94 eV). In contrast, the VB edge potential of WO_3 (+3.24 eV) was more positive and was lower than that of MgAl LDH (+3.00 eV), which led to the rapid transfer of holes created in the valence band of WO_3 to that of LDH [56]. The efficient migration and restriction of rejoining of electron-hole pairs across the Ag@WO_3/LDH heterojunction were made possible by the suitable band potentials of LDH and WO_3. This process led to the accumulation of electrons and holes in the CB and VB of WO_3 and MgAl LDH, respectively. The electrons in the CB of silver NPs get directly transfered on the surface of WO_3.

The presence of Ag NPs in the Ag@WO_3/MgAl LDH composite significantly enhances charge separation by leveraging the unique properties of Ag such as surface Plasmon resonance (SPR) and its efficient electron transfer capabilities. When exposed to visible light, Ag NPs undergo collective oscillations of conduction electrons, generating hot electrons that possess higher energy than the normal conduction band electrons. These hot electrons can be easily injected into the conduction band of WO_3, promoting efficient charge separation and preventing the recombination of electron-hole pairs. Additionally, the silver NPs facilitate the transfer of photogenerated electrons from MgAl LDH to WO_3 by reducing potential barriers at the interface. This enhanced electron migration, coupled with the ability of silver to trap electrons, effectively extends the charge carrier lifetime and accelerates the photocatalytic reactions. The combination of these effects ensures that the Ag@WO_3/MgAl LDH composite exhibits superior photocatalytic activity, with silver playing a crucial role in optimizing charge separation and improving overall reaction efficiency. Also, the value of E_{CB} on MgAl LDH (-0.61 V) is negative than the standard oxidation-reduction potential of $O_2/^{\bullet}O_2^-$ (-0.33 V), so O_2 stayed in the CB of MgAl LDH can be reduced to produce $^{\bullet}O_2^-$. Similarly, the E_{VB} of MgAl LDH and WO_3 (+3.0 V and 3.24 V) are more positive than that of the oxidation-reduction potential of $^{\bullet}OH/OH^-$ (+1.99 V); therefore, OH^- can be oxidized to produce •OH. The analysis of the charge transfer mechanism in the Ag@WO_3/MgAl LDH composite was consistent with the results of scavenging experiments. The photocatalytic system produces energetic species like $^{\bullet}O_2^-$ and $OH^{\bullet}$

would ultimately result in the effective breakdown of harmful pollutants into organic intermediates and, in the end, into environmentally beneficial products like H_2O and CO_2.

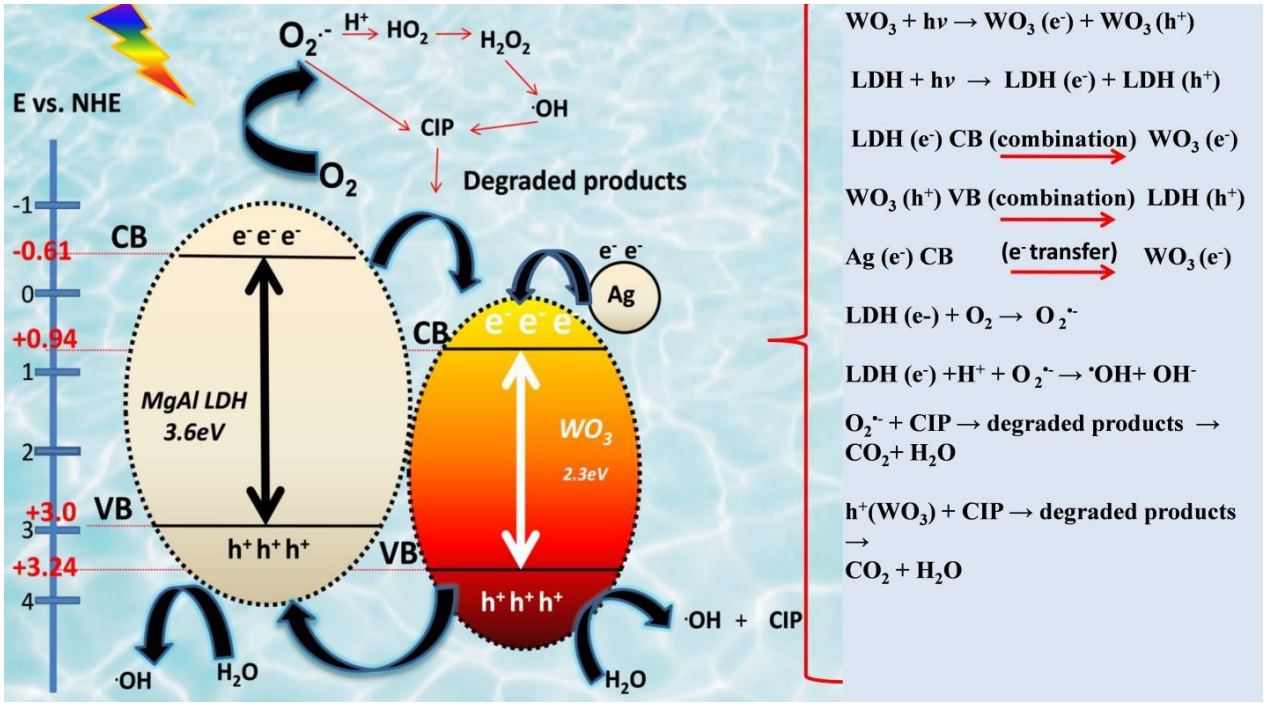

Scheme 2. Possible reaction mechanism of CIP degradation over Ag_2@WO_3/MgAl LDH composite under visible light irradiation

Conclusion

In this study, composites were formed with silver-loaded WO_3 to enhance the adsorption capacity and photocatalytic performance of broad band-gap Mg-Al LDH under visible light irradiation. The effects of these composites on the surface structural, physicochemical, and optical properties of the LDH material were extensively investigated and compared. Remarkably, the composite material designed exhibited significantly enhanced adsorption capacity for TC removal (80% in 90 min) and photocatalytic degradation towards CIP removal (77.6% in 160 min). These results outperformed the adsorption and photocatalytic activities of pristine MgAl LDH and binary hybrids such as WO_3/MgAl LDH. The observed enhancement in adsorption of TC molecules can be due to the increased surface area of the catalyst, and the composite

exhibiting better visible light response is due to the incorporation of silver, giving rise to the SPR effect and thus leading to improved photocatalytic activity.

Furthermore, after four consecutive degradation cycles, the created photocatalyst showed good stability with little performance loss. The findings of the HR-MS analysis and the trapping tests gave thorough information regarding the likely intermediate products and reaction mechanisms involved in degrading pollutants. This analysis highlighted the pivotal role of $O_2^{\bullet-}$ as an active species responsible for degradation. The mineralization efficiency of the developed photocatalyst was also assessed using the TOC test to evaluate its ability to remove organic pollutants.

References

[1] M. Ahmad, A.U. Khan, Global economic impact of antibiotic resistance: A review, J. Glob. Antimicrob. Resist. 19 (2019) 313–316. https://doi.org/10.1016/j.jgar.2019.05.024.

[2] C.A. Igwegbe, S.N. Oba, C.O. Aniagor, A.G. Adeniyi, J.O. Ighalo, Adsorption of ciprofloxacin from water: A comprehensive review, J. Ind. Eng. Chem. 93 (2021) 57–77. https://doi.org/10.1016/j.jiec.2020.09.023.

[3] S. Shurbaji, P.T. Huong, T.M. Altahtamouni, Review on the visible light photocatalysis for the decomposition of ciprofloxacin, norfloxacin, tetracyclines, and sulfonamides antibiotics in wastewater, Catalysts. 11 (2021). https://doi.org/10.3390/catal11040437.

[4] F. Saadati, N. Keramati, M.M. Ghazi, Influence of parameters on the photocatalytic degradation of tetracycline in wastewater: A review, Crit. Rev. Environ. Sci. Technol. 46 (2016) 757–782. https://doi.org/10.1080/10643389.2016.1159093.

[5] F. Ahmadijokani, H. Molavi, S. Tajahmadi, M. Rezakazemi, M. Amini, M. Kamkar, O.J. Rojas, M. Arjmand, Coordination chemistry of metal–organic frameworks: Detection, adsorption, and photodegradation of tetracycline antibiotics and beyond, Coord. Chem. Rev. 464 (2022) 214562. https://doi.org/10.1016/j.ccr.2022.214562.

[6] L. Lu, J. Li, D.H.L. Ng, P. Yang, P. Song, M. Zuo, Synthesis of novel hierarchically porous Fe3O4@MgAl–LDH magnetic microspheres and its superb adsorption properties of dye from water, J. Ind. Eng. Chem. 46 (2017) 315–323. https://doi.org/10.1016/j.jiec.2016.10.045.

[7] J. Hu, C. Sun, L. xu Wu, G. qing Zhao, H. yin Liu, F. peng Jiao, Halogen doped g-C3N4/ZnAl-LDH hybrid as a Z-scheme photocatalyst for efficient degradation for tetracycline in seawater, Sep. Purif. Technol. 309 (2023). https://doi.org/10.1016/j.seppur.2022.123047.

[8] C. Sun, L. Wu, J. Hu, S.A. Hussain, J. Yang, F. Jiao, A novel dual S-scheme heterojunction photocatalyst β-Bi2O3/NiAl-LDH/α-Bi2O3 induced by phase-transformed bismuth oxide for efficient degradation of antibiotics in full-spectrum: Degradation pathway, DFT calculation and mechanism insight, Chem. Eng. J. 474 (2023) 145616. https://doi.org/10.1016/j.cej.2023.145616.

[9] L. Wu, C. Sun, S. Jiao, J. Hu, J. Yang, F. Jiao, Internal Electric-Field-Driven CoAl-LDH Coupled N-Rich Carbon Nitride of C3N5 for Improved Photocatalytic Performance, Ind. Eng. Chem. Res. 62 (2023) 2729–2740. https://doi.org/10.1021/acs.iecr.2c04227.

[10] L. Jiang, J. Chen, D. Han, S. Chang, R. Yang, Y. An, Y. Liu, F. Chen, Potential of core-shell NiFe layered double hydroxide@Co3O4 nanostructures as cathode catalysts for oxygen reduction reaction in microbial fuel cells, J. Power Sources. 453 (2020) 227877. https://doi.org/10.1016/j.jpowsour.2020.227877.

[11] Jemini, S. Singh, B. Pal, Efficient ZnCr LDH/monoclinic-WO3 composites for Degradation of Tetracycline under Visible Light, ChemistrySelect. 7 (2022) 73825– 73848. https://doi.org/10.1002/slct.202203846.

[12] M. Xu, M. Wei, Layered Double Hydroxide-Based Catalysts: Recent Advances in Preparation, Structure, and Applications, Adv. Funct. Mater. 28 (2018) 1–20. https://doi.org/10.1002/adfm.201802943.

[13] H. Kaur, S. Singh, B. Pal, Impact of g-C3N4 loading on NiCo LDH for adsorptive removal of anionic and cationic organic pollutants from aqueous solution, Korean J. Chem. Eng. 38 (2021) 1248–1259. https://doi.org/10.1007/s11814-021-0784-6.

[14] L. Mohapatra, K. Parida, A review on the recent progress, challenges and perspective of layered double hydroxides as promising photocatalysts, J. Mater. Chem. A. 4 (2016) 10744–10766. https://doi.org/10.1039/c6ta01668e.

[15] S.G. Kumar, K.S.R.K. Rao, Comparison of modification strategies towards enhanced

charge carrier separation and photocatalytic degradation activity of metal oxide semiconductors (TiO 2 , WO 3 and ZnO), Appl. Surf. Sci. 391 (2017) 124–148. https://doi.org/10.1016/j.apsusc.2016.07.081.

[16] S. Bera, S. Ghosh, S. Shyamal, C. Bhattacharya, R.N. Basu, Photocatalytic hydrogen generation using gold decorated BiFeO 3 heterostructures as an efficient catalyst under visible light irradiation, Sol. Energy Mater. Sol. Cells. 194 (2019) 195–206. https://doi.org/10.1016/j.solmat.2019.01.042.

[17] H. Liang, M. Yu, J. Guo, R. Zhan, J. Chen, D. Li, L. Zhang, J. Niu, A novel vacancy-strengthened Z-scheme g-C3N4/Bp/MoS2 composite for super-efficient visible-light photocatalytic degradation of ciprofloxacin, Sep. Purif. Technol. 272 (2021) 118891. https://doi.org/10.1016/j.seppur.2021.118891.

[18] N.A. Mohd Razali, W.N. Wan Salleh, F. Aziz, L.W. Jye, N. Yusof, A.F. Ismail, Review on tungsten trioxide as a photocatalysts for degradation of recalcitrant pollutants, J. Clean. Prod. 309 (2021) 127438. https://doi.org/10.1016/j.jclepro.2021.127438.

[19] X. Liu, A. Jin, Y. Jia, T. Xia, C. Deng, M. Zhu, C. Chen, X. Chen, Synergy of adsorption and visible-light photocatalytic degradation of methylene blue by a bifunctional Z-scheme heterojunction of WO 3 /g-C 3 N 4, Appl. Surf. Sci. 405 (2017) 359–371. https://doi.org/10.1016/j.apsusc.2017.02.025.

[20] Y. Zhu, R. Zhu, G. Zhu, M. Wang, Y. Chen, J. Zhu, Y. Xi, H. He, Plasmonic Ag coated Zn/Ti-LDH with excellent photocatalytic activity, Appl. Surf. Sci. 433 (2018) 458–467. https://doi.org/10.1016/j.apsusc.2017.09.236.

[21] D.P. Sahoo, S. Patnaik, K. Parida, Construction of a Z-Scheme Dictated WO3- X/Ag/ZnCr LDH Synergistically Visible Light-Induced Photocatalyst towards Tetracycline Degradation and H2 Evolution, ACS Omega. 4 (2019) 14721–14741. https://doi.org/10.1021/acsomega.9b01146.

[22] X. Wang, R. Wang, J. Wang, C. Fan, Z. Zheng, The synergistic role of the support surface and Au-Cu alloys in a plasmonic Au-Cu@LDH photocatalyst for the oxidative esterification of benzyl alcohol with methanol, Phys. Chem. Chem. Phys. 22 (2020) 1655– 1664. https://doi.org/10.1039/c9cp05992j.

[23] Y. Cao, D. Zheng, S. Dong, F. Zhang, J. Lin, C. Wang, C. Lin, A Composite Corrosion Inhibitor of MgAl Layered Double Hydroxides Co-Intercalated with Hydroxide and Organic Anions for Carbon Steel in Simulated Carbonated Concrete Pore Solutions, J. Electrochem. Soc. 166 (2019) C3106–C3113. https://doi.org/10.1149/2.0141911jes.

[24] S. Naseem, B.R. Gevers, F.J.W.J. Labuschagn, A. Leuteritz, Materials-13-04384-V2.Pdf, (2020).

[25] D.J. Ham, A. Phuruangrat, S. Thongtem, J.S. Lee, Hydrothermal synthesis of monoclinic WO3 nanoplates and nanorods used as an electrocatalyst for hydrogen evolution reactions from water, Chem. Eng. J. 165 (2010) 365–369. https://doi.org/10.1016/j.cej.2010.09.003.

[26] R.R. Shan, L.G. Yan, K. Yang, S.J. Yu, Y.F. Hao, H.Q. Yu, B. Du, Magnetic Fe3O4/MgAl-LDH composite for effective removal of three red dyes from aqueous solution, Chem. Eng. J. 252 (2014) 38–46. https://doi.org/10.1016/j.cej.2014.04.105.

[27] G. Zheng, C. Wu, J. Wang, S. Mo, Y. Wang, Z. Zou, B. Zhou, F. Long, Facile synthesis of few-layer MoS2 in MgAl-LDH layers for enhanced visible-light photocatalytic activity, RSC Adv. 9 (2019) 24280–24290. https://doi.org/10.1039/c9ra03858b.

[28] L.P.F. Benício, D. Eulálio, L. de Moura Guimarães, F.G. Pinto, L.M. Da Costa, J. Tronto, Layered double hydroxides as hosting matrices for storage and slow release of phosphate analyzed by stirred-flow method, Mater. Res. 21 (2018). https://doi.org/10.1590/1980-5373-mr-2017-1004.

[29] K. Christou, D. Louloudakis, D. Vernardou, N. Katsarakis, E. Koudoumas, One-pot synthesis of WO3 structures at 95 °C using HCl, J. Sol-Gel Sci. Technol. 73 (2015) 520–526. https://doi.org/10.1007/s10971-014-3459-5.

[30] W. Shi, M. Li, X. Huang, H. Ren, F. Guo, C. Yan, Three-dimensional Z-Scheme Ag3PO4/Co3(PO4)2@Ag heterojunction for improved visible-light photocatalytic degradation activity of tetracycline, J. Alloys Compd. 818 (2020) 152883. https://doi.org/10.1016/j.jallcom.2019.152883.

[31] H.J. Kang, D. Il Won, Y. Lim, J. Kim, W.I. Lee, Remarkable variation of visible light photocatalytic activities of M/Sn0.9Sb0.1O2/TiO2 (M=Au, Ag, Pt) heterostructures depending on the loaded metals, Chemosphere. 265 (2021) 129160.

https://doi.org/10.1016/j.chemosphere.2020.129160.

[32] T. Thilagavathi, D. Venugopal, R. Marnadu, J. Chandrasekaran, T. Alshahrani, M. Shkir, An Investigation on Microstructural, Morphological, Optical, Photoluminescence and Photocatalytic Activity of WO3 for Photocatalysis Applications: An Effect of Annealing, J. Inorg. Organomet. Polym. Mater. 31 (2021) 1217–1230. https://doi.org/10.1007/s10904-020-01731-2.

[33] H. Wang, Y. Wang, Y. Liu, J. Zhao, J. Li, Q. Wang, J. Luo, Tribological behavior of layered double hydroxides with various chemical compositions and morphologies as grease additives, Friction. 9 (2021) 952–962. https://doi.org/10.1007/s40544-020-0380-5.

[34] J. Zhang, X. Xie, C. Li, H. Wang, L. Wang, The role of soft colloidal templates in the shape evolution of flower-like MgAl-LDH hierarchical microstructures, RSC Adv. 5 (2015) 29757–29765. https://doi.org/10.1039/c5ra01561h.

[35] W. Shi, X. Zhang, J. Brillet, D. Huang, M. Li, M. Wang, Y. Shen, Significant enhancement of the photoelectrochemical activity of WO3 nanoflakes by carbon quantum dots decoration, Carbon N. Y. 105 (2016) 387–393. https://doi.org/10.1016/j.carbon.2016.04.051.

[36] Y.A. Wu, L. Li, Z. Li, A. Kinaci, M.K.Y. Chan, Y. Sun, J.R. Guest, I. McNulty, T. Rajh, Y. Liu, Visualizing Redox Dynamics of a Single Ag/AgCl Heterogeneous Nanocatalyst at Atomic Resolution, ACS Nano. 10 (2016) 3738–3746. https://doi.org/10.1021/acsnano.6b00355.

[37] U. Kuila, M. Prasad, Specific surface area and pore-size distribution in clays and shales, Geophys. Prospect. 61 (2013) 341–362. https://doi.org/10.1111/1365-2478.12028.

[38] S. Ullah, A.U. Rahman, F. Ullah, A. Rashid, T. Arshad, E. Viglašová, M. Galamboš, N.M. Mahmoodi, H. Ullah, Adsorption of malachite green dye onto mesoporous natural inorganic clays: Their equilibrium isotherm and kinetics studies, Water (Switzerland). 13 (2021). https://doi.org/10.3390/w13070965.

[39] J. Xu, X. Liu, R. Li, B. Shen, Z. Zhou, L. Deng, L. Liu, X. Zhu, Production of renewable fuel from CO2 by Co3O4/Cr doped MgAl–LDH p-n heterojunction catalyst, Fuel Process. Technol. 246 (2023) 107762. https://doi.org/10.1016/j.fuproc.2023.107762.

[40] X. Li, J. Xue, S. Ma, P. Xu, C. Huang, M. Wang, Synthesis of MgAl LDH/Acidified g-C3N4 Heterojunction Photocatalyst for Improved Tetracycline Hydrochloride Degradation Activity, Nano. 14 (2019) 1–13. https://doi.org/10.1142/S1793292019500668.

[41] X. fei Tan, Y. guo Liu, Y. ling Gu, S. bo Liu, G. ming Zeng, X. Cai, X. jiang Hu, H. Wang, S. mian Liu, L. hua Jiang, Biochar pyrolyzed from MgAl-layered double hydroxides pre-coated ramie biomass (Boehmeria nivea (L.) Gaud.): Characterization and application for crystal violet removal, J. Environ. Manage. 184 (2016) 85–93. https://doi.org/10.1016/j.jenvman.2016.08.070.

[42] Y.C.G. Kwan, G.M. Ng, C.H.A. Huan, Identification of functional groups and determination of carboxyl formation temperature in graphene oxide using the XPS O 1s spectrum, Thin Solid Films. 590 (2015) 40–48. https://doi.org/10.1016/j.tsf.2015.07.051.

[43] F. He, S. Wang, H. Zhao, Y. Wang, J. Zhang, Q. Yan, P. Dong, Z. Tai, L. Chen, Y. Wang, C. Zhao, Construction of Schottky-type Ag-loaded fiber-like carbon nitride photocatalysts for tetracycline elimination and hydrogen evolution, Appl. Surf. Sci. 485 (2019) 70–80. https://doi.org/10.1016/j.apsusc.2019.04.164.

[44] M. Liu, L. an Hou, S. Yu, B. Xi, Y. Zhao, X. Xia, MCM-41 impregnated with A zeolite precursor: Synthesis, characterization and tetracycline antibiotics removal from aqueous solution, Chem. Eng. J. 223 (2013) 678–687. https://doi.org/10.1016/j.cej.2013.02.088.

[45] A. Ayub, Z.A. Raza, M.I. Majeed, M.R. Tariq, A. Irfan, Development of sustainable magnetic chitosan biosorbent beads for kinetic remediation of arsenic contaminated water, Int. J. Biol. Macromol. 163 (2020) 603–617. https://doi.org/10.1016/j.ijbiomac.2020.06.287.

[46] J. Wang, X. Guo, Adsorption isotherm models: Classification, physical meaning, application and solving method, Chemosphere. 258 (2020) 127279. https://doi.org/10.1016/j.chemosphere.2020.127279.

[47] M.A. Hubbe, S. Azizian, S. Douven, Implications of apparent pseudo-second-order adsorption kinetics onto cellulosic materials: A review, BioResources. 14 (2019) 7582–7626. https://doi.org/10.15376/biores.14.3.hubbe.

[48] Z. Chen, W. Wang, Z. Zhang, X. Fang, High-E ffi ciency Visible-Light-Driven Ag 3 PO 4 /AgI Photocatalysts: Z - Scheme Photocatalytic Mechanism for Their Enhanced Photocatalytic Activity, (2013) 3–9.

[49] Rohmatullaili, N. Ahmad, D. Savira, D. Erviana, Zultriana, R. Mohadi, A. Lesbani, A series of MgAl layer double hydroxide-based materials intercalated with Clitoria ternatea flower extract as photocatalysts in the ciprofloxacin degradation, Chem. Phys. Impact. 8 (2024) 100587. https://doi.org/10.1016/j.chphi.2024.100587.

[50] H. Kaur, S. Singh, B. Pal, Construction of Ag deposited g-C3N4 loaded Co Al LDH ternary composites mechanism for ciprofloxacin degradation, Applied Clay Science.10 (2023) 106922. https://doi.org/10.1016/j.clay.2023.106922.

[51] T. Govindaraj, C. Mahendran, V.S. Manikandan, J. Archana, M. Shkir, J. Chandrasekaran, Fabrication of WO3 nanorods/RGO hybrid nanostructures for enhanced visible-light-driven photocatalytic degradation of Ciprofloxacin and Rhodamine B in an ecosystem, J. Alloys Compd. 868 (2021) 159091. https://doi.org/10.1016/j.jallcom.2021.159091.

[52] X.J. Wen, C.G. Niu, L. Zhang, C. Liang, H. Guo, G.M. Zeng, Photocatalytic degradation of ciprofloxacin by a novel Z-scheme CeO2–Ag/AgBr photocatalyst: Influencing factors, possible degradation pathways, and mechanism insight, J. Catal. 358 (2018) 141–154. https://doi.org/10.1016/j.jcat.2017.11.029.

[53] X. Yu, J. Zhang, J. Zhang, J. Niu, J. Zhao, Y. Wei, B. Yao, Photocatalytic degradation of ciprofloxacin using Zn-doped Cu2O particles: Analysis of degradation pathways and intermediates, Chem. Eng. J. 374 (2019) 316–327. https://doi.org/10.1016/j.cej.2019.05.177.

[54] Y. Mu, C. Huang, H. Li, L. Chen, D. Zhang, Z. Yang, Electrochemical degradation of ciprofloxacin with a Sb-doped SnO2 electrode: Performance, influencing factors and degradation pathways, RSC Adv. 9 (2019) 29796–29804. https://doi.org/10.1039/c9ra04860j.

[55] B. Gupta, A.K. Gupta, Photocatalytic performance of 3D engineered chitosan hydrogels embedded with sulfur-doped C3N4/ZnO nanoparticles for Ciprofloxacin removal: Degradation and mechanistic pathways, Int. J. Biol. Macromol. 198 (2022) 87–100.

https://doi.org/10.1016/j.ijbiomac.2021.12.120.

[56] J. Xiong, H.Y. Zeng, C.F. Liu, J.F. Peng, Z.L. Yang, W.Y. Ji, Amorphous/crystalline heterophase W-Zn(Ti)O for the removal of Cr(VI) and tetracycline in single and mixed pollutant systems, Chem. Eng. J. 473 (2023) 145231. https://doi.org/10.1016/j.cej.2023.145231.

CHAPTER-4

Construction of ternary Ag@α-Fe_2O_3/NiCo LDH composites for efficient degradation of malachite green dye under visible light and sunlight irradiation

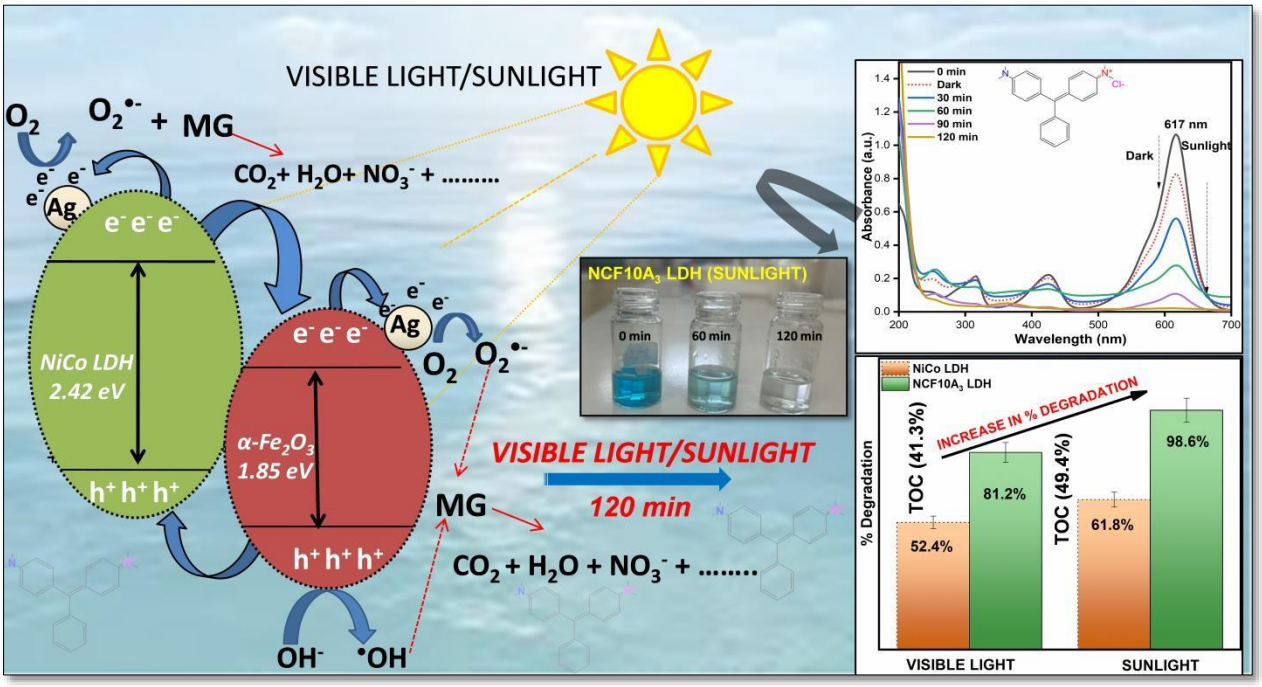

Schematic outline: The photoactivity of NiCo LDH was improved by forming a heterostructure with Fe_2O_3 and loading Ag NPs on the prepared composites. The structural and physicochemical properties of LDH and its composites were analyzed. The remarkable degradation of malachite green (MG) dye under solar light irradiation (98.6%) was achieved as compared to visible light irradiation (81.2%). This enhanced photoactivity of Ag@Fe_2O_3/NiCo LDH composites is due to the synergic effect of Fe_2O_3 and Ag which highly improved the degradation efficiency and facilitates the rapid transfer of charge on the catalyst surface.

This chapter covers second and third objective of the thesis focusing on the Influence of metal (Ag, Cu, Fe etc.) loaded MO (TiO_2, ZnO, WO_3 etc.) loading onto these LDHs and their physicochemical properties and the study of photocatalytic activity of these M /MO-LDH. heterocomposites for degradation of organic pollutants (phenols, nitro aromatics, pesticides etc.).

4.1. Introduction

Global environmental degradation has become a significant concern due to reckless urban modernization and industrial progress. There is a widespread acknowledgment that water pollution severely threatens human society and sustainable improvement. Extensive endeavors have been dedicated to mitigating water pollution by employing various methods, such as chemical oxidation, biochemical degradation, and physical adsorption [1–5]. The practical utility of these methods has been hindered by their drawbacks, including elevated energy consumption, intricate operation, and recurrent pollution. The photodegradation process has attracted considerable attention owing to its cost-effectiveness, absence of secondary pollution, and the potential utilization of solar light, a clean and renewable resource [6–11]. Consequently, developing novel sunlight/visible-light-driven materials is increasingly important to enhance the efficiency of dye photodegradation [12,13].

In recent years, scholars have progressively directed their attention towards utilizing layered double hydroxides in photocatalytic applications aimed at environmentally sustainable objectives. These applications include photocatalytic splitting of water for H_2 production, CO_2 reduction, degrading harmful and toxic organic pollutants into harmless or less toxic forms [14– 17]. LDHs are characterized by cationic layers with a structural composition represented as $[M_{1-x}^{2+}M_x^{3+}(OH)_2]^{x+}(A^{n-})_{x/n}\cdot mH_2O$, where A^{n-} denotes the interlayer anion, and M^{2+} and M^{3+} represent metal ions with charges of +2 and +3, respectively. LDHs offer promising prospects for photocatalytic applications due to their distinctive structural features, comprising a layered configuration, inherent defects, adjustable band gap, cost-effectiveness, substantial specific surface area, and accessible synthesis methods. However, despite these advantages, LDH-based photocatalysts encounter challenges such as rapid electron-hole recombination and slow mobility of charge carriers, which can hinder their overall photocatalytic efficiency [18,19].

Hematite (α-Fe_2O_3), possessing a rhombohedral-hexagonal structure, stands out as the most stable form of iron oxide. It holds tremendous potential in the photocatalytic degradation of diverse organic pollutants due to its antiferromagnetic property, cost-effectiveness, non-toxic nature, exceptional stability, high reliability, corrosion resistance, and appropriate band gap (ranging from 2.0 to 2.2 eV), enabling the absorption of a broad spectrum of solar radiation [20–

23]. According to existing literature, diverse methods are being explored to improve the photocatalytic efficiency of unmodified semiconductor nanoparticles. These strategies aim to increase surface area, create active sites, and reduce the recombination of active charge carriers, and can be achieved through elemental doping, forming composites, and designing heterojunctions [24–28]. Among these approaches, constructing heterostructures emerges as a highly efficacious method to develop high-performing photocatalysts. Heterostructures involve combining two different photocatalysts with disparate band gaps, creating hybrid conduction and valence bands. This arrangement increases surface active sites, facilitates faster charge transfer, and suppresses the recombination of holes and electrons, ultimately enhancing photocatalytic degradation performance. Plasmonic metal-loaded LDH and metal oxide/LDH composites have garnered interest in the photodegradation of pollutants under visible light. Metals like Ag, Cu, and Au enhance light absorption of catalysts at longer wavelengths through their surface electrons' SPR effect [29]. Metal loading enhances visible spectrum light absorption, boosting the generation and separation of photogenerated charge carriers [30]. Employing plasmonic metal nanoparticles within the Fe_2O_3/LDH heterostructure is a potent strategy for enhancing catalyst efficiency in absorbing visible light.

Literature studies have demonstrated the potential of LDH-based composites and metal oxide catalysts like Fe_2O_3 for photocatalytic applications, but the impact of varying Fe_2O_3 and Ag loadings on the photocatalytic efficiency and degradation mechanism has not been extensively explored. The photocatalytic activity of Ag-loaded α-Fe_2O_3 was evaluated for methylene blue (MB) mineralization under visible light. Results showed that 5.0 wt. % Ag loading enhanced the photocatalytic performance, achieving 68.6% degradation in 150 minutes [31]. Similarly, Ag@Fe_2O_3 demonstrated superior photocatalytic performance compared to Fe_2O_3 under solar light irradiation [32]. Various research have also been reported showing the limitations of LDHs, challenges often result in reduced performance under prolonged use or varying environmental conditions. To overcome these issues, modifications such as the incorporation of nanoparticles or the creation of heterojunctions are being explored. In this context, Lu et al. investigated the degradation of organic dyes and spectral properties by integrating magnetic Fe_3O_4 nanoparticles with LDHs through a co-precipitation synthesis method. The resulting Fe_3O_4/MgAl-LDH nanocomposite exhibited a unique structure and demonstrated exceptional efficiency in

degrading Congo red dyes in aqueous solutions [33]. Similarly LDHs have been modified using metal oxides for better photoactivity as Fe_2O_3/ZnTi-LDH and ZnO/ZnCr-LDH composites were synthesized, and the results indicated that the band gap of the metal oxide-metal element-LDH materials was significantly reduced compared to the individual metal oxides or doped metal elements. This reduction in band gap contributed to a notably higher efficiency in organic decomposition [34,35]. Building on the findings from previous literature, it can be hypothesized that silver-loaded Fe_2O_3 nanoparticles could significantly enhance the photocatalytic activity of LDH. However, as far as our understanding extends, no literature discusses how varying Fe_2O_3 loadings on NiCo LDH and adjusting plasmonic metal Ag loadings on Fe_2O_3/LDH heterostructures influence the degradation of toxic pollutants under visible light and sunlight.

The research aims to amplify the photoactivity of NiCo LDH by forming a heterostructure with Fe_2O_3 and subsequently enhancing its effectiveness through Ag incorporation. NiCo LDH and Fe_2O_3 NPs were synthesized via a hydrothermal technique, followed by the preparation of Fe_2O_3/LDH composites using a wet impregnation method (Fe_2O_3: 5% and 10%). Subsequently, the catalysts underwent modification with Ag loading through a photochemical reduction method. The efficacy of the photocatalysts was assessed for malachite green dye degradation under visible light and sunlight irradiation respectively. The findings indicated optimal degradation under sunlight, demonstrating a viable and sustainable approach for reducing pollutants. The impact of Fe_2O_3 and Ag loading on the LDH surface was investigated, and mineralization experiments confirmed the effectiveness of degradation under sunlight irradiation. Moreover, the degradation route was also suggested following the HRMS examination.

4.2. Experimental section

4.2.1. Chemicals and reagents

Nickel(II) nitrate hexahydrate ($Ni(NO_3)_2 \cdot 6H_2O$), Cobalt(II) nitrate hexahydrate ($Co(NO_3)_2 \cdot 6H_2O$), Iron(III) nitrate nonahydrate ($Fe(NO_3)_3 \cdot 9H_2O$), $NH_3 \cdot H_2O$, cetyltrimethylammonium bromide (CTAB), Methanol, Isopropyl alcohol (C_3H_8O 99.5%) and malachite green ($C_{23}H_{25}N_2Cl$) were obtained from Loba Chemie (India). Silver nitrate was purchased from Sigma Aldrich (India). All these chemicals were used without further

purification. Triple distilled deionized (DI) water was purchased from Organo Biotech Laboratories Pvt. Ltd., India.

4.2.2. Synthesis of NiCo LDH

The NiCo LDH was synthesized using the hydrothermal method. 0.524 g of $Ni(NO_3)_2 \cdot 6H_2O$, 0.349 g of $Co(NO_3)_2 \cdot 6H_2O$, and 1 g of CTAB were dispersed in a mixed solvent of 60 mL methanol and 12 mL ultrapure water. The mixture was then stirred magnetically at room temperature for an hour. Subsequently, the mixture was transferred into a teflon-lined autoclave (100 mL) and subjected to hydrothermal reaction at 180°C for 24 h [36]. Followed by cooling to room temperature, the resulting precipitates were filtered, washed with distilled water, and subsequently dried at 70 °C.

4.2.3. Synthesis of Fe_2O_3

Iron oxide NPs were synthesized in hydrothermal treatment. Initially, 1.8 g of Fe $(NO_3)_3 \cdot 9H_2O$ was dissolved in 20 mL of distilled water. $NH_3 \cdot H_2O$ was then added gradually to adjust the pH of the solution to around 9 with continuous stirring for 20 min. The solution was transferred into a 100 mL teflon-lined stainless steel autoclave and subjected to hydrothermal treatment at 120°C for 10 h. Finally, the product was filtered and washed with distilled water, absolute ethanol and dried at 80°C for 12 h [37].

4.2.4. Synthesis of Fe_2O_3 loaded NiCo LDH composite

Fe_2O_3/NiCo LDH was synthesized by the wet impregnation method, which involves the dispersion of an appropriate amount of NiCo LDH and Fe_2O_3 in DI water. The aqueous dispersion of Fe_2O_3 was added dropwise to NiCo LDH suspension and sonicated for another 1h. The resultant suspension was stirred for 24 h, and the solid was isolated by centrifugation and dried at 70°C to reddish brown colored powder with 5 and 10 wt.% Fe_2O_3, abbreviated as NCF5, NCF10 LDH.

4.2.5. Preparation of Ag deposited Fe_2O_3/NiCo LDH composites

Silver-loaded Fe_2O_3/NiCo LDH composites were prepared by photodeposition method 100 mg of the prepared NCF10 composite was dispersed to 10 mL of 50% by volume IPA solution, along with a 0.01 mM solution of $AgNO_3$ corresponding to different weight percentages (3% and 5%). The resultant was sealed and kept for argon purging for about 15-20 min to maintain an inert atmosphere. Subsequently, the mixture was exposed to UV radiation (125 W Hg arc, 10.4 mW/cm^2) for 2 h. The solution obtained after illumination was filtered, washed with DI water, and dried at 70°C. The 3, 5 wt % silver-loaded NCF10 composites were abbreviated as $NCF10A_3$ and $NCF10A_5$ LDH.

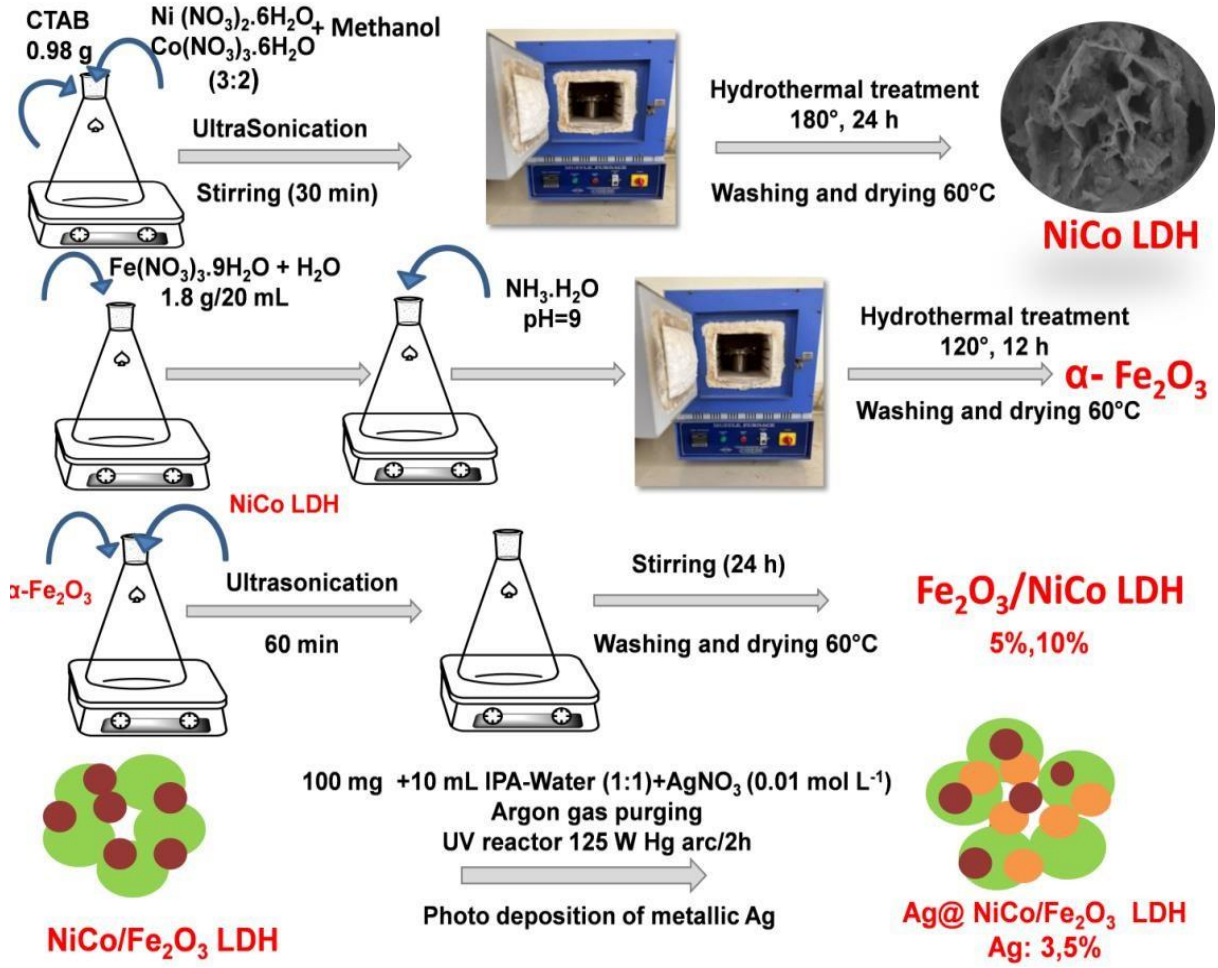

Scheme 4.1. Schematic illustration of the synthesis of ternary Ag@Fe_2O_3/NiCo LDH composites

4.3. Results and discussion

4.3.1. Crystallographic and structural studies

X-ray diffraction (XRD) patterns depicted peaks for NiCo LDH, Fe_2O_3, NCF LDH (Fe_2O_3 = 5%, 10%) and NCF10A LDH (Ag = 3%, 5%) **Fig.4.1 (a)**. In the crystalline NiCo LDH pattern, peaks were observed at 2θ values of 11.29°, 22.14°, 34.15°, 38.50°, 43.58°, 60.85°, and 61.54°, corresponding to the (003), (006), (012), (015), (107), (110) and (113) planes, respectively [38]. Upon composite formation, additional peaks corresponding to α-Fe_2O_3 nanoparticles emerged in the LDH pattern, indexed at (104), (110), (202), (024), and (116) planes which confirms the loading of Fe_2O_3 on LDH structure [39]. Furthermore, new peaks at 2θ = 44.5°, 64.8°corresponding to the (200) and (220) planes were observed upon silver loading on Fe_2O_3/NiCo LDH [$NCF10A_3$ and $NCF10A_5$ LDH] [40]. The amplification in intensity of silver peaks correlated with the rise in wt.% of Ag (3, 5%). The loading of Fe_2O_3 and Ag onto NiCo LDH did not result in a shift of 2θ values in the LDH peaks, suggesting successful surface loading without penetration into the crystal structure.

The crystallite size of NiCo LDH and its composites were calculated using the Debye -Scherrer equation:

$$D = K \lambda / \beta \cos \theta \quad \text{.....(1)}$$

In the given equation, D represents the crystallite size, K is the Scherrer constant (0.9), β denotes the full width at half maximum (FWHM), λ (1.54 Å) stands for the wavelength of X-rays used and θ represents the Bragg's diffraction angle. **Fig.4.1 (b)** depicts no shift in the 2θ value for the (003) and (006) plane peaks. The calculated crystallite sizes from the (003) peak are 12.87 nm, 14.00 nm, 14.51 nm, 14.77 nm, and 15.34 nm for NiCo LDH and its composites. The alteration in crystallite structure may result from phase transformation or changes in LDH surface energy upon Fe_2O_3 and Ag NPs loading. These observed changes, coupled with structural modifications, indicate successful composite formation.

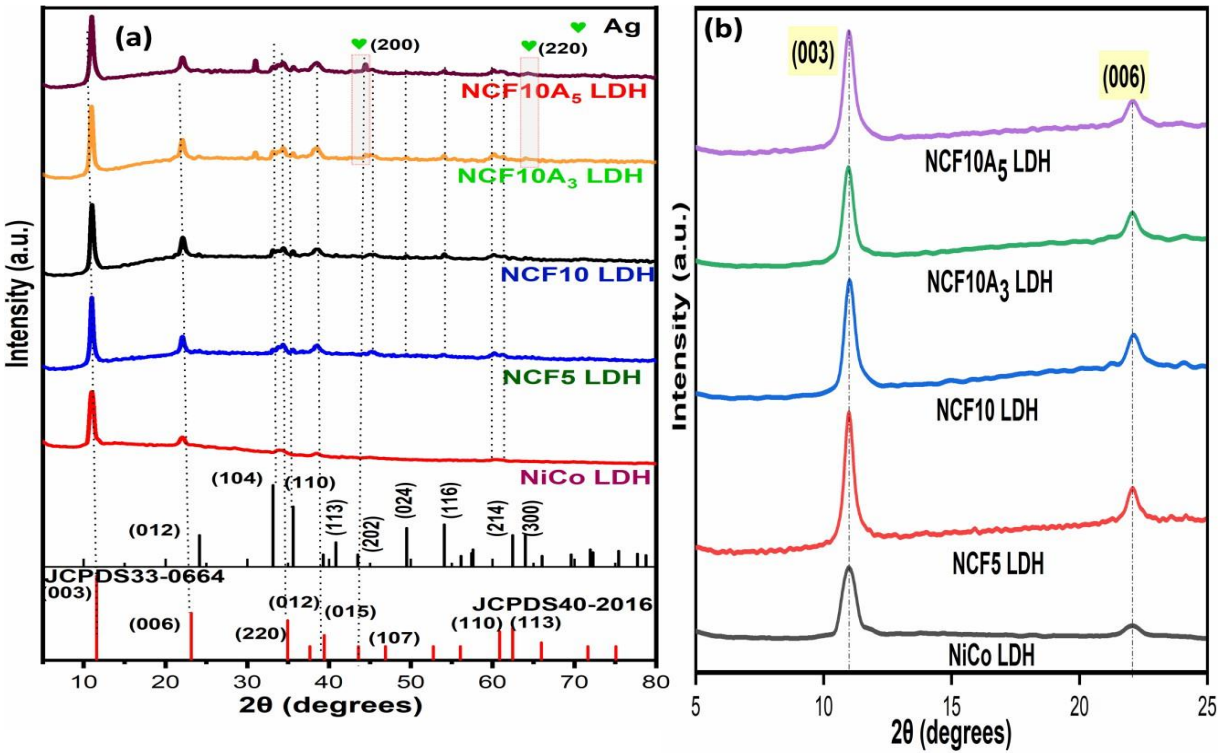

Fig. 4.1. X-ray diffraction pattern of bare NiCo LDH, binary {NCF5LDH, NCF10LDH}, ternary {NCF10A_3, NCF10A_5 LDH} composites (a) and enlarged view of peak corresponding to (006) and (003) planes (b)

The structural and morphological properties of the materials were examined using Raman spectroscopy **Fig.4.2 (a)**. NiCo LDH exhibited two prominent bands at 462 cm^{-1} and 516 cm^{-1}, attributed to the Ni-O and Co-O vibrational modes, respectively[41]. In NCF5 LDH and NCF10 LDH composites, additional bands at 225 cm^{-1}, 243 cm^{-1}, 293 cm^{-1}, and 412 cm^{-1}, corresponding to A_{1g}, E_g, E_g, and E_g, were detected, aligning with the characteristic bands of α-Fe_2O_3. Moreover, in silver-loaded Fe_2O_3/NiCo LDH composites, supplementary bands at 657 cm^{-1} and 829 cm^{-1} emerged, likely originating from the vibrational modes of NiCo and α-Fe_2O_3 [42]. These bands could be attributed to the localized surface Plasmon resonance (LSPR) effect of the Ag present within the composites.

The FTIR spectra of NiCo LDH and its composites are depicted in **Fig.4.2 (b)**. A prominent absorption band at 3452 cm^{-1} was ascribed to the stretching vibration of OH groups on the layered surface or interlayer water molecules. Another band at 1640 cm^{-1} corresponded to the

bending vibration of interlayer water molecules [43]. Upon composite formation, a reduction in the intensities of bands at 1059 cm^{-1} and 500-700 cm^{-1}, corresponding to Metal-Oxygen (Ni/Co-O) stretching and bending vibration bands, was observed, indicating alterations in the LDH surroundings [44]. Additionally, a band at 884 cm^{-1}, attributed to Ni/Co-OH bending vibration, displayed decreased intensity upon Fe_2O_3 loading. No bands corresponding to Fe and Ag were detected in the NCF10A (3-5%) LDH composites, possibly due to the low loading levels. Furthermore, the spectra showed no substantial variances in the spectra compared to NiCo LDH, suggesting that the loading of Fe_2O_3 and Ag did not alter the chemical structure of LDH.

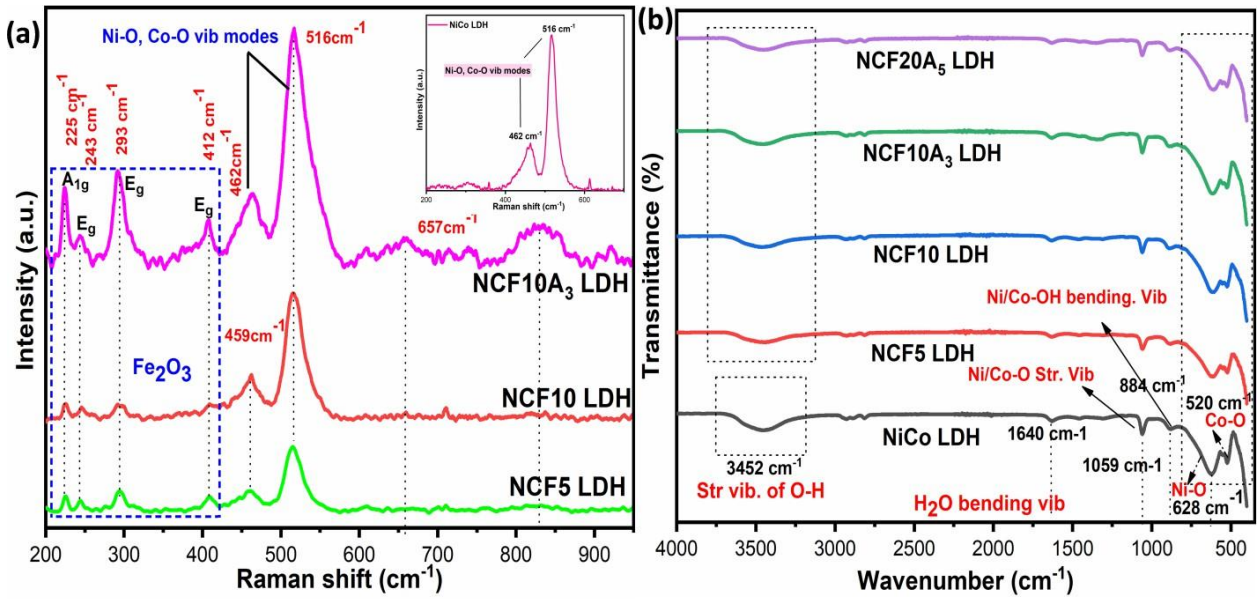

Fig. 4.2. Raman spectra of NiCo LDH, NCF (5, 10%) and $NCF10A_3$ LDH (a); FTIR spectra of NiCo LDH and its binary (NCF5, NCF10 LDH) and ternary ($NCF10A_3$, $NCF10A_5$ LDH) composites (b)

4.3.2. Optical studies

Photoluminescence (PL) investigations were conducted to examine the defects and the recombination efficiency of electron-hole pairs within the composites. **Fig.4.3 (a)** depicts the PL emission spectra of both pristine NiCo LDH and its composites. These experiments were carried out at ambient temperature at an excitation wavelength of 390 nm. Two distinct bands observed in the visible region correspond to Near Band Edge (NBE) emission and deep-level emission

respectively, attributed to oxygen vacancies, surface defects, and OH defects [45,46]. NiCo LDH exhibited a strong PL signal, indicating maximum charge recombination. Upon composite formation, the intensity of bands at the same wavelengths (483 nm and 530 nm) decreased, suggesting suppression in the rate of recombination of charge carriers [47]. The comparable intensity of the spectra in both the 3% and 5% silver-loaded Fe_2O_3/LDH composites suggests that 3 wt.% is the optimal concentration for suppressing electron-hole recombination. Subsequent increases in silver concentration do not significantly impact the recombination rate. Therefore, the PL spectra reveal the role of co-catalysts (Fe_2O_3, Ag) in achieving an efficient charge carrier system with a lower recombination rate, thereby enhancing photoactivity. The increasing quenching order is as follows: NiCo LDH < NCF5 LDH < NCF10 LDH < $NCF10A_5$ < $NCF10A_3$.

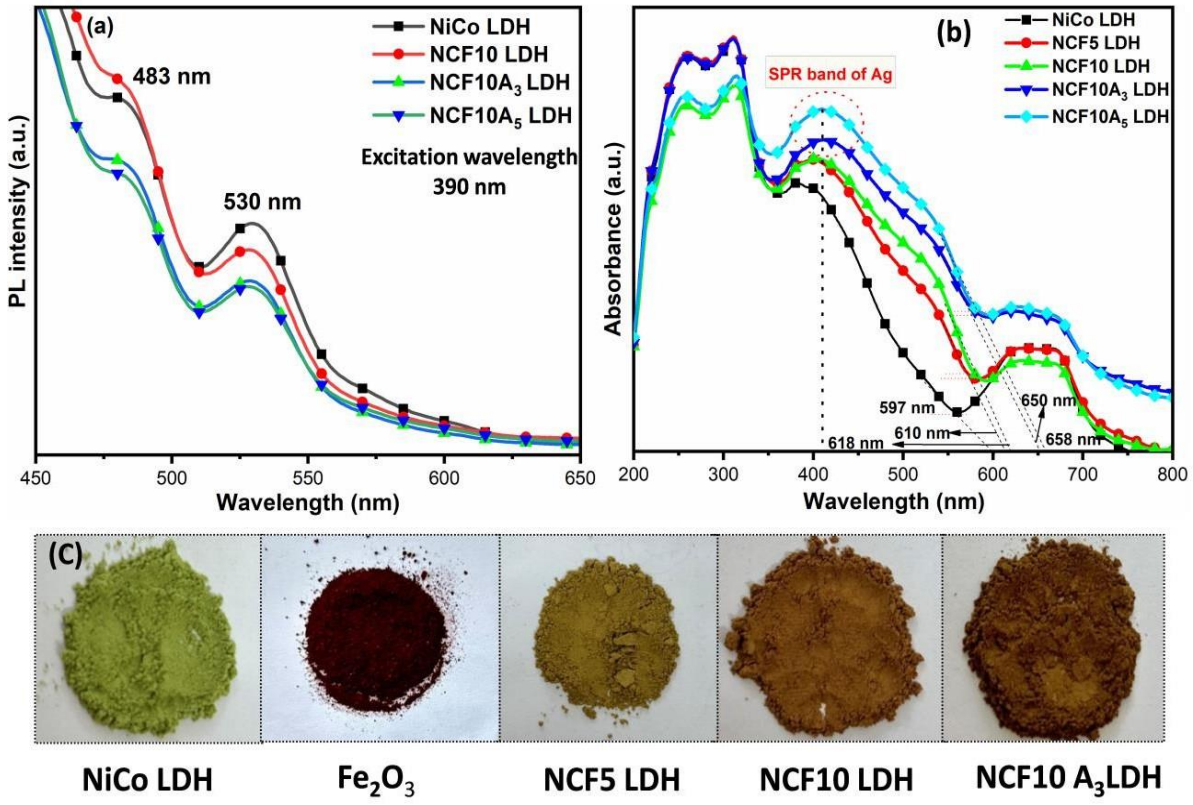

Fig.4.3. Photoluminescence (a); UV-Vis DRS spectra (b) and colour change (c) of pristine NiCo LDH, Fe_2O_3/NiCo LDH, Ag@Fe_2O_3/NiCo LDH composites

The optical absorption properties of the LDH and its composites were evaluated with the help of DRS spectra **Fig.4.3 (b).** NiCo LDH exhibited absorption in the visible region, with an absorption onset at 597 nm [48]. The α-Fe_2O_3/NiCo LDH composites displayed an extended absorption spectrum, extending to 618 nm, attributable to the integration of Fe_2O_3 nanoparticles onto the LDH surface, thereby enhancing the LDH's light absorption capability in the visible spectrum [49]. Additionally, the Ag@Fe_2O_3/LDH composites displayed even greater light absorption capability, with a shift towards longer wavelengths, from 597 nm to 658 nm. The shift observed is due to the combined effects of the visible light absorption by Fe_2O_3 nanoparticles and the surface plasmon resonance (SPR) effect induced by Ag [50]. The surface plasmon band, emerging in the 400–500 nm range, arises from electron transfer between the d-electronic states of the metal and LDH. The powered samples also demonstrate a color shift upon composite formation. Initially, LDH appeared green, but upon combining with α-Fe_2O_3 and Ag, the catalyst shifted to greenish-brown and dark brown **Fig.4.3 (c).** The band gap energies (E_g) of each photocatalyst were determined using the equation [51]:

$$ahv = A(h\nu - E_g)^{1/2} \quad \text{.....(2)}$$

Here, α, h, ν, and A represent the absorption coefficient, Planck's constant, frequency of incident light, and proportionality constant, respectively, while E_g denotes the band gap energies.

As shown in **Fig.4.4 (a-f)** the band gap calculated for NiCo LDH, Fe_2O_3, NCF5 LDH, NCF10 LDH, NCF10A_3 LDH, and NCF10A_5 LDH was 2.40 eV, 1.85 eV, 2.0 eV, 1.95 eV, 1.87 eV and 1.89 eV respectively. The increase in the band gap observed in the NCF10A_5 LDH composite in comparison to NCF10A_3 LDH may be due to the excessive loading of Ag on the catalyst surface, thus affecting the efficiency of charge carriers. The analysis of DRS spectra and calculated band gaps indicates that integrating NiCo LDH with α-Fe_2O_3 and Ag significantly reduces its band gap thereby enhancing visible light activity.

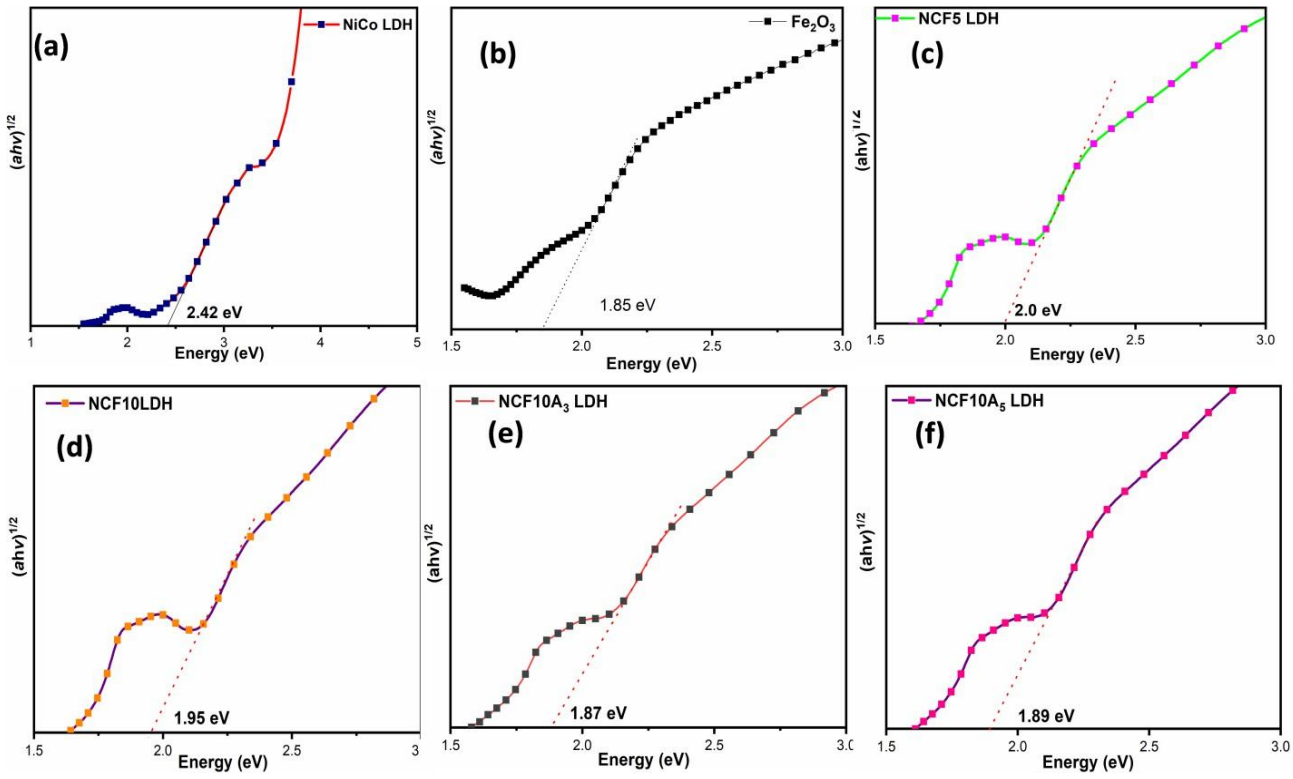

Fig.4.4. Calculated band gap of NiCo LDH, Fe_2O_3, NCF5 LDH, NCF10 LDH, $NCF10A_3$ LDH and $NCF10A_5$ LDH (a-f)

4.3.3. Structural morphological and surface studies

The morphological and microstructural characteristics of NiCo LDH and $NCF10A_3$ LDH composites were analyzed using the FESEM technique, illustrated in **Fig.4.5 (a, b)**. NiCo LDH displayed layered nanoflower morphology with a smooth surface [52]. Further, small spherical nanoparticles of α-Fe_2O_3 were detected on the NiCo LDH surface upon composite formation **Fig. 4.5 (c, d)** [53]**.** The presence of Ag in the composite was not evident from FESEM imaging because of its extremely small size. Elemental composition and FESEM images of nanogranual α-Fe_2O_3 NPs are shown in **Fig.4.6** and $NCF10A_3$ LDH and NiCo LDH, are shown in **Fig.4.7 (a- d).** The presence of Ni, Co, O, Fe, and Ag elements in the composite confirms the presence of silver and Fe_2O_3 in Ag-loaded Fe_2O_3/NiCo LDH with their uniform distribution on the LDH surface. Therefore, FESEM imaging and EDX spectra confirm the successful formation of the $NCF10A_3$ LDH composite.

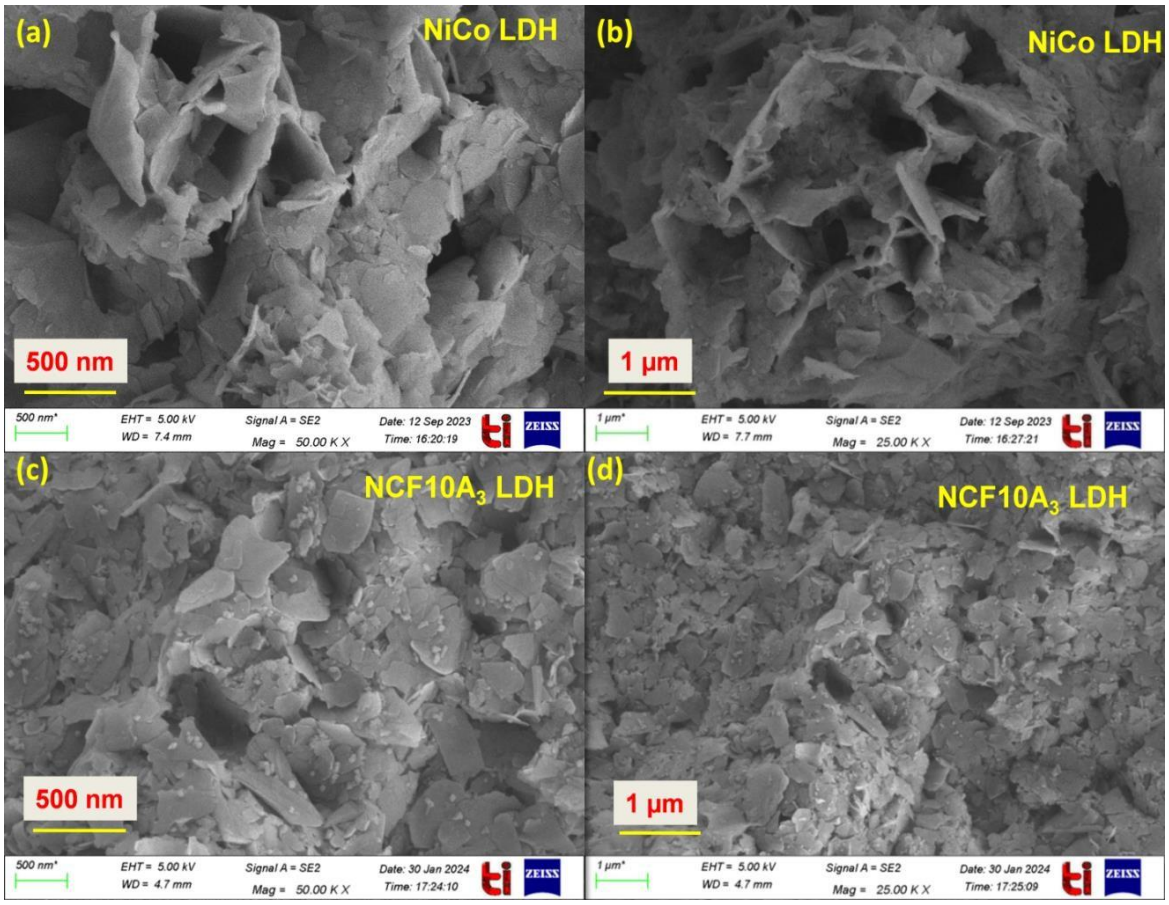

Fig.4.5. FESEM images of NiCo LDH (a, b) and NCF10A$_3$ LDH (c, d)

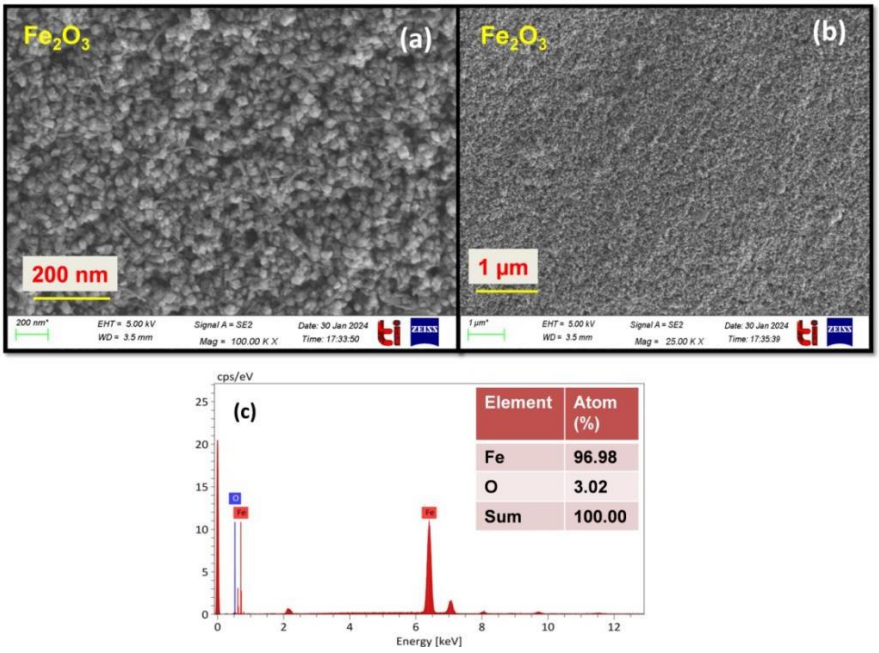

Fig.4.6. FESEM images (a, b) and EDX spectra of Fe_2O_3 NPs (c).

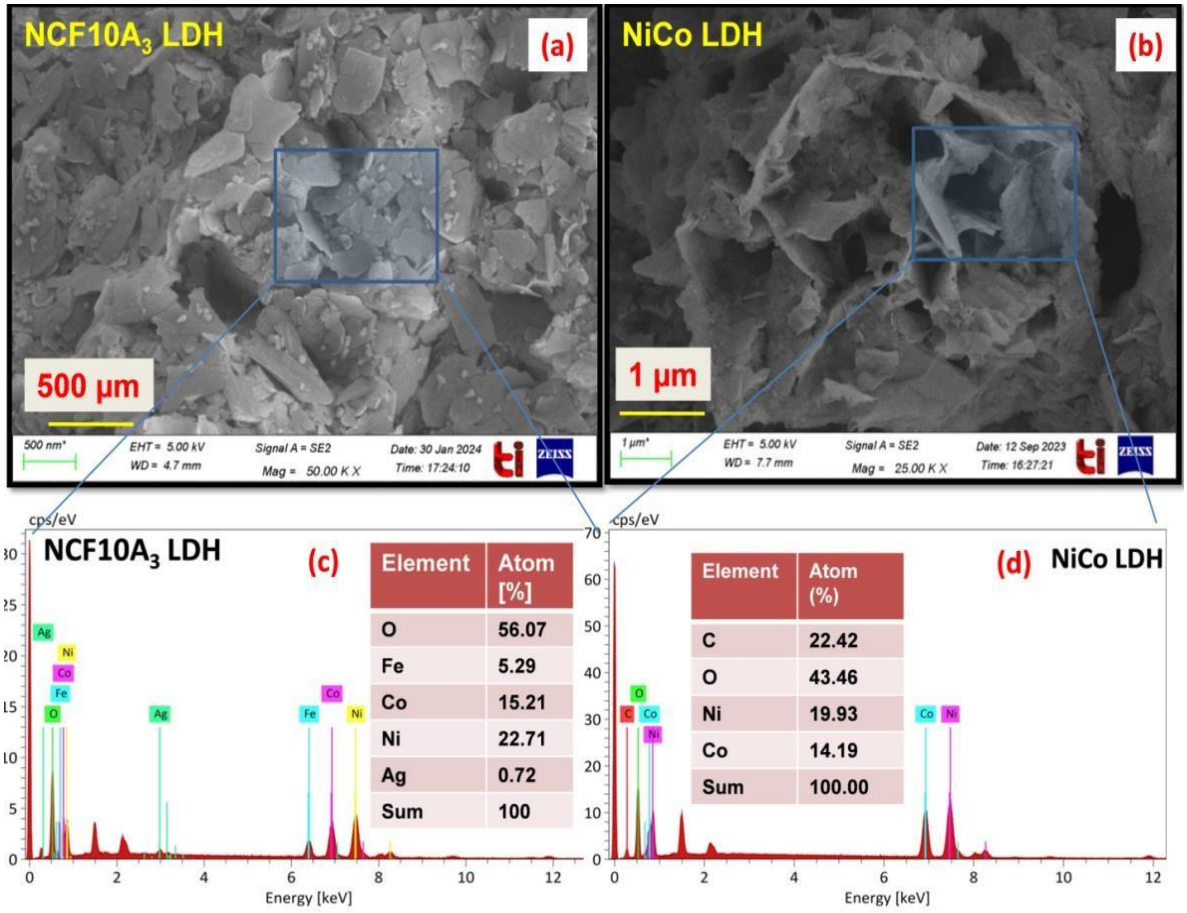

Fig.4.7. FESEM images (a, b) and EDS spectra (c, d) of NCF10A3 LDH and NiCo LDH HRTEM

analysis of NCF10A3 LDH revealed the presence of spherical Ag nanoparticles and nanosized α-Fe_2O_3 (spherical and hexagonal shaped) embedded within the flowered-shaped nanosheets of NiCo LDH (**Fig.4.8 a and b**). Silver nanoparticles (Ag NPs) were evenly dispersed on the surfaces of the LDH and Fe_2O_3. The lattice fringes with distances of 0.40 nm, 0.37 nm and 0.23 nm were observed and indexed for NiCo LDH, Fe_2O_3, and Ag NPs in **Fig.4.8 (c)** [54,55]. The SAED pattern **Fig.4.8 (d)** revealed the (111) plane aligned with the 0.236 nm d-spacing of Ag nanoparticles, the (440) plane for α-Fe_2O_3, and the (015) and (110) planes for NiCo LDH, confirming the formation of the Ag-deposited α-Fe_2O_3/NiCo LDH composite [36,56,57].

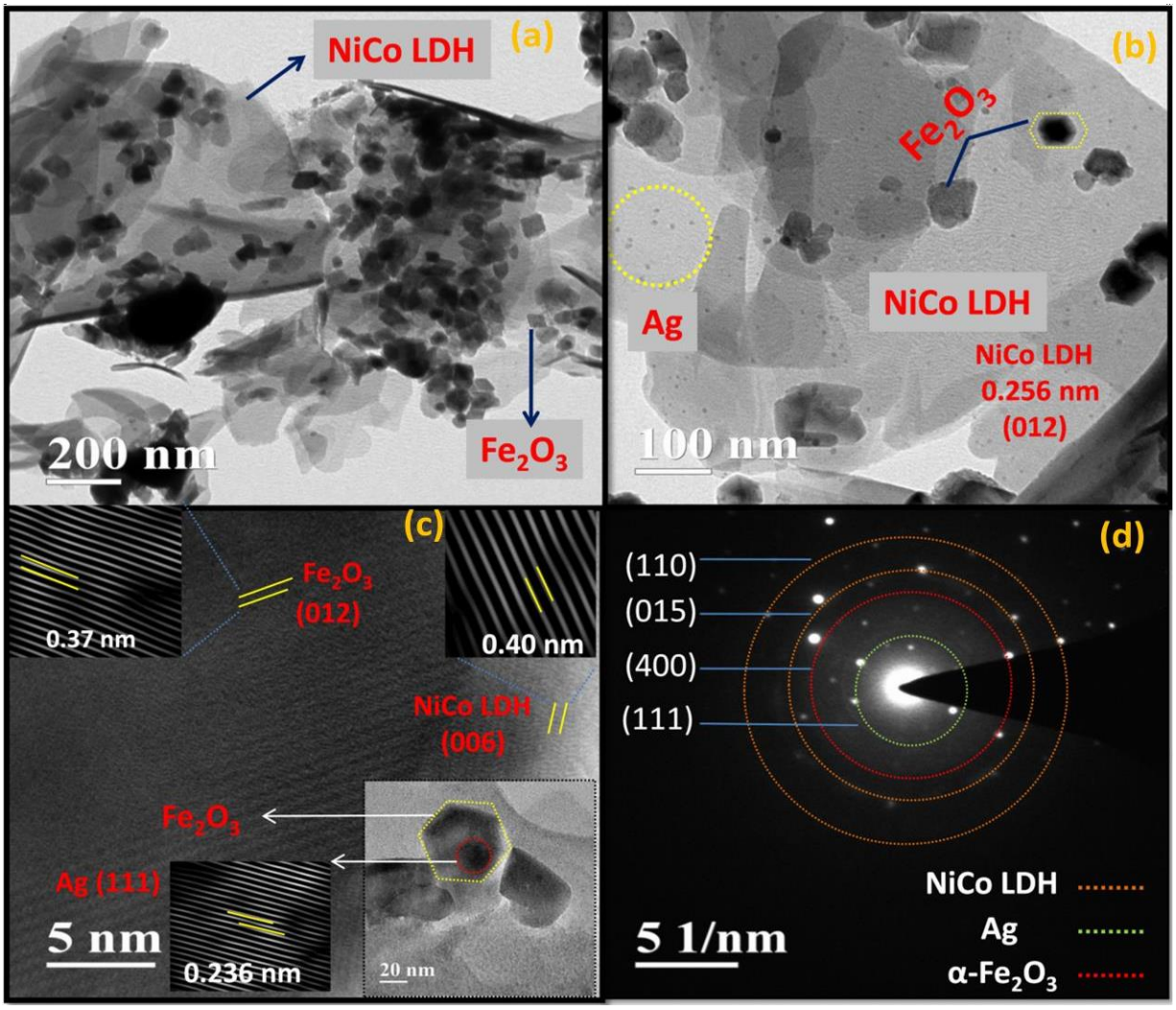

Fig.4.8. HRTEM images (a-b); lattice fringes (c); SAED pattern (d) of NCF10A$_3$ LDH composite

The electrokinetic characteristics of the synthesized catalysts were examined using dynamic light scattering (DLS) and zeta potential analysis. The NiCo LDH exhibited a hydrodynamic size of 292 nm. Following the deposition of α-Fe_2O_3 onto the LDH surface, the hydrodynamic size increased to 616 nm for NCF5 LDH and 756 nm for NCF10 LDH composite, indicating a rise in hydrodynamic size with the addition of Fe_2O_3 amount. Significantly, the hydrodynamic sizes of Ag (3%, 5%)@NCF10 LDH composites were observed to be 830 nm and 1140 nm, respectively **Fig. 4.9 (a).** The zeta potential analysis of NiCo LDH indicated a positive surface charge of +20 mV. Conversely, α-Fe_2O_3 exhibited a negative zeta potential of -12 mV. Upon Fe_2O_3 loading

onto the LDH surface, the zeta potential decreased to +12 mV, indicating a neutralization of the LDH surface charge due to electrostatic interactions with the negatively charged α-Fe_2O_3. Subsequently, upon silver loading onto the composites, the zeta potential decreased further to +8 mV, +6 mV, and +5 mV for the respective composites. These alterations in zeta potential validate the formation of the Ag@Fe_2O_3/NiCo LDH composites **Fig.4.9 (b)**. Thus, the observed variations in hydrodynamic size and zeta potential changes provide substantial evidence for forming the NCF10A_5 LDH composite.

Fig.4.9 (c, d) depict the surface area and pore size distribution curves for both NiCo LDH and the ternary composite Ag_3@Fe_2O_3/NiCo LDH adsorption-desorption isotherms for NiCo LDH and the composite exhibit a type 1V isotherm pattern, indicating a mesoporous nature. Pore size distribution analysis revealed pore sizes ranging between 1-20 nm for both catalysts. The calculated surface area for pure NiCo LDH and NCF10A_3 LDH was 29.881 m^2/g and 34.027 m^2/g respectively. The slight increase in surface area may be attributed to the deposition of Fe_2O_3 and Ag NPs on the LDH surface. Additionally, the composite showed increased pore volume and pore diameter i.e. 0.078 cc/g and 0.102 cc/g respectively, potentially facilitating rapid diffusion of reactants and active species, thereby enhancing the photocatalytic efficiency of the catalyst.

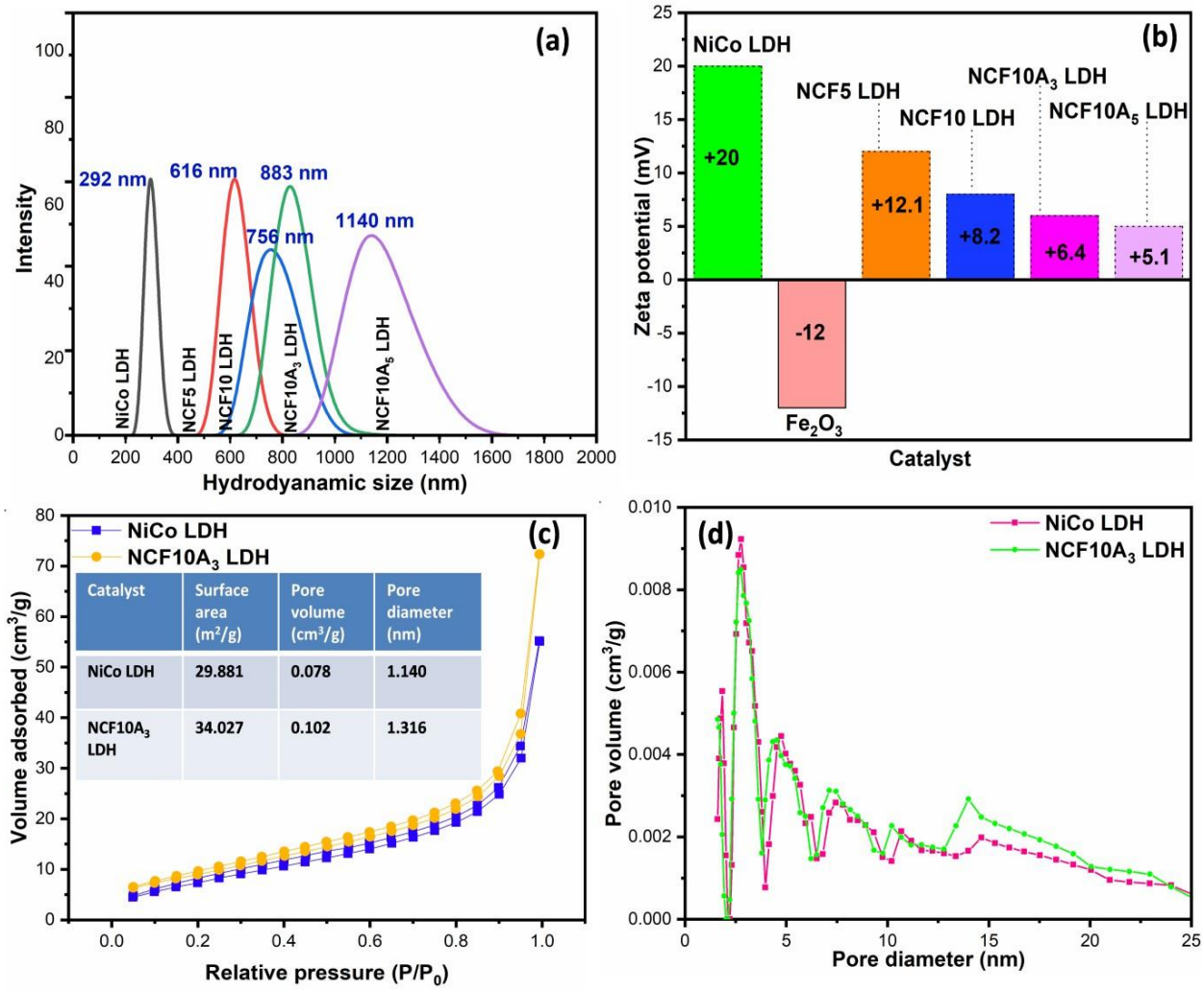

Fig.4.9. Variation of Hydrodynamic size (a); Zeta potential (b); N_2 adsorption isotherm and pore size distribution curves (c, d) of NiCo LDH and its composites

4.4. Photocatalytic studies

During photocatalytic studies, malachite green (MG) was chosen as a representative toxic pollutant to investigate the photocatalytic properties of NiCo LDH and its composites. The experiments were carried out at room temperature in test tubes containing 5 mg of photocatalyst and 5 ml of MG solution (20 ppm). Before initiating the reactions, the suspensions were equilibrated under dark conditions for 30 minutes. Subsequently, the test tubes were exposed to visible light irradiation (50W LED lamp, Wipro Garnet B22, intensity ~ 100 W /m ^{2}, λ = 380- 700 nm) for 120 min and sunlight experiments were conducted under the same reaction

conditions on April 25 (11 am to 1 pm), the intensity of light was around 112 W /m^2, temp 41°C. Following irradiation, the catalysts were separated via centrifugation, and the concentration of MG remaining in the solutions was determined using a UV-VIS spectrophotometer (solution temp visible light: 37°C; solution temp sunlight: 42°C). The efficiency of MG photodegradation was optimized using the following formula:

$$\eta\ (\%) = (C_0-C_t)/C_0 \times 100 \quad \text{.....(3)}$$

Where η is the photocatalytic degradation efficiency (%), C_0 and C_t are the pollutant concentration at the initial time (t = 0 min) and at a specific time interval. Scavenging experiments were conducted similarly to the photocatalytic degradation process, including scavengers such as Argon purging, methanol, and isopropyl alcohol (IPA). The mineralization efficiency (TOC) and the intermediates formed during the degradation process were determined by HRMS analysis. The stability of the catalyst was also assisted by recovering the catalyst after degradation, followed by drying and using the sample for consecutive different runs under the same reaction conditions.

4.4.1. Factors affecting photocatalytic degradation of MG dye

(i) Effect of catalyst dosage

To investigate the correlation between photocatalytic degradation efficiency and the adsorbate amount, tests were conducted by altering the dosage of the catalyst **Fig.4.10 (a)**. The catalyst amount was fixed from 0.001-0.008 g. The least degradation efficiency was observed for the low amount of catalyst due to the adsorption of lesser molecules of MG on the catalyst surface. Hence, less degradation was observed, further increasing the amount up to 0.005 g, its efficiency tends to increase, but after the optimum amount, the degradation started decreasing as excessive catalyst concentration might reduce solution transparency, impede light penetration and deactivate catalyst surface area that aids the degradation process**. Fig.4.10 (c and d)** shows the degradation spectra and percent degradation of MG at optimized amount of catalyst.

(ii) Effect of pollutant concentration

The impact of MG concentration on the removal rate was investigated within the range of 5–35 ppm **Fig. 4.10 (b).** High photodegradation activity was observed at lower drug concentrations (20 ppm), diminishing efficiency as MG concentrations increased to 35 ppm. At higher MG concentrations, photocatalytic activity decreased primarily due to increased coverage of active sites on the catalyst surface by MG molecules, limiting the generation of active radicals. Additionally, high MG concentrations obstruct light transmission, impeding catalyst light absorption and thus affecting photodegradation efficiency.

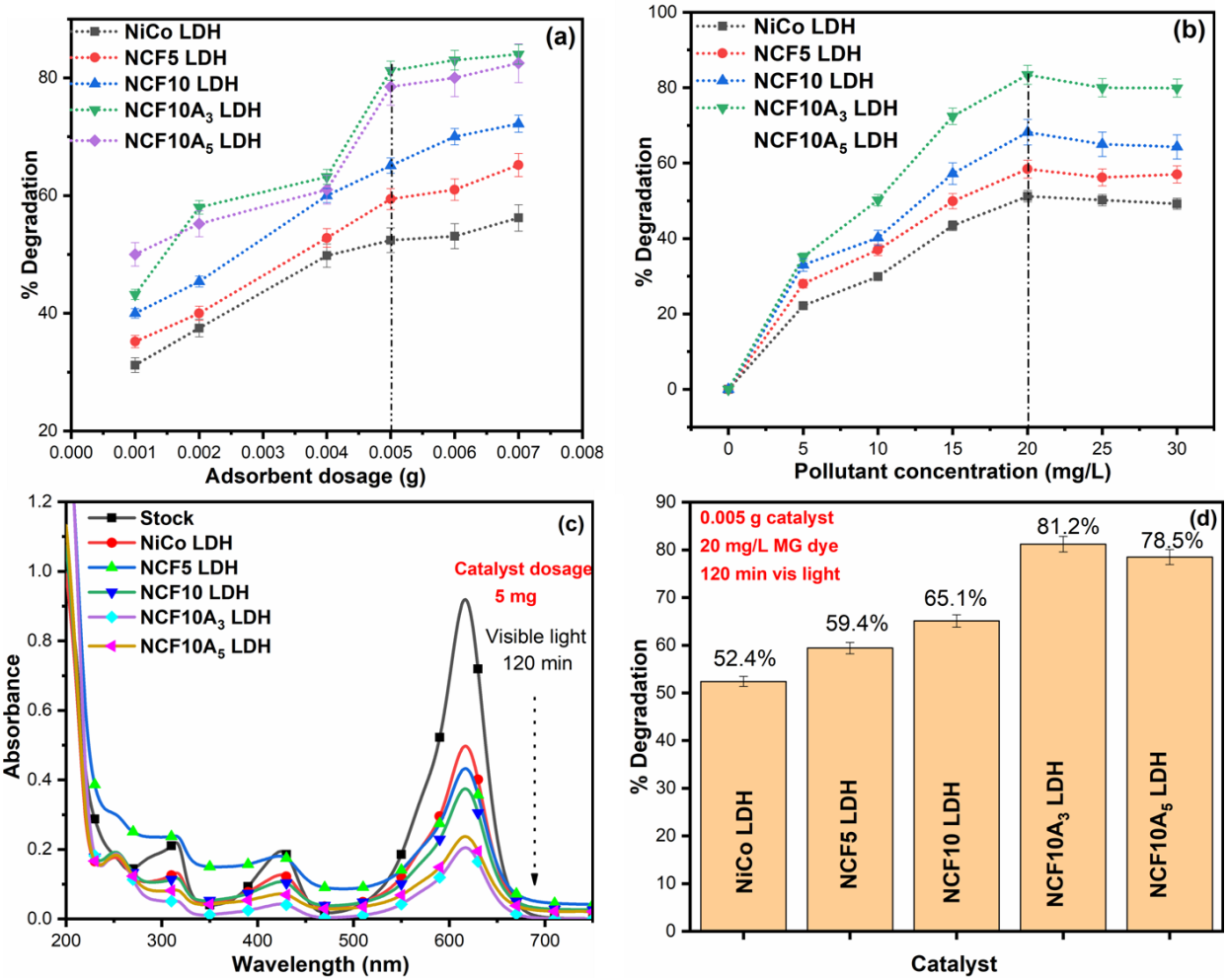

Fig.4.10. Effect of catalyst dosage (a); pollutant concentration (b); UV-Vis spectra of degradation of MG dye (c) and bar graph showing percent degradation (d) of MG dye by NiCo LDH, its binary Fe_2O_3 loaded and ternary Ag loaded NiCo LDH composites

4.4.2. Photocatalytic reaction

The photocatalytic efficiency of each catalyst was assessed through the degradation of MG dye under visible light and sunlight **Fig.4.11 (a-d)**. Initially, a 5 mL MG solution containing 5 mg of catalyst was stirred in darkness for 30 minutes to achieve adsorption-desorption equilibrium. Afterward, the aforementioned was exposed to both visible light and sunlight for photodegradation studies. **Fig.4.12 (a, b)** illustrates the kinetics of adsorption and photodegradation of MG across various catalysts. Notably, without any catalyst, the MG solution under light irradiation exhibited negligible degradation, highlighting the ineffectiveness of light alone in pollutant removal. Subsequent experiments utilized synthesized photocatalysts, namely NiCo LDH, NCF5 LDH, NCF10 LDH, NCF10A_3 LDH, and NCF10A_5 LDH, revealing a degradation efficiency: NiCo LDH (52.8%, 61.8%) < NCF5 LDH (59.4%, 68.4%) < NCF10 LDH (66.9%, 73.5%) < NCF10A_3 LDH (82.2%, 98.6%) < NCF10A_5 LDH (76.4%, 96.4%) visible light and sunlight irradiation respectively. The limited degradation efficiency of bare LDH was attributed to its broader band gap compared to binary (NCF5, NCF10 LDH) and ternary (NCF10A_3, NCF10A_5 LDH) composites. The degradation extent correlates strongly with the quantity of loaded Fe_2O_3. As the Fe_2O_3 content in the composites increases, their removal efficiencies gradually rise before eventually declining. Among all the Fe_2O_3/LDH composites, NCF10 LDH (Fe_2O_3:10 wt %) showed the highest efficiency in MG removal. Further increasing the Fe_2O_3 content to 15 wt.% slightly reduced the removal efficiency of MG. Excessive Fe_2O_3 loading may partially obstruct the active sites, impeding incident illumination from reaching the catalyst surface and thereby diminishing the photocatalytic capacity. Hence, loading an appropriate amount of cocatalyst is essential to achieve optimum synergy between the catalyst and cocatalyst.

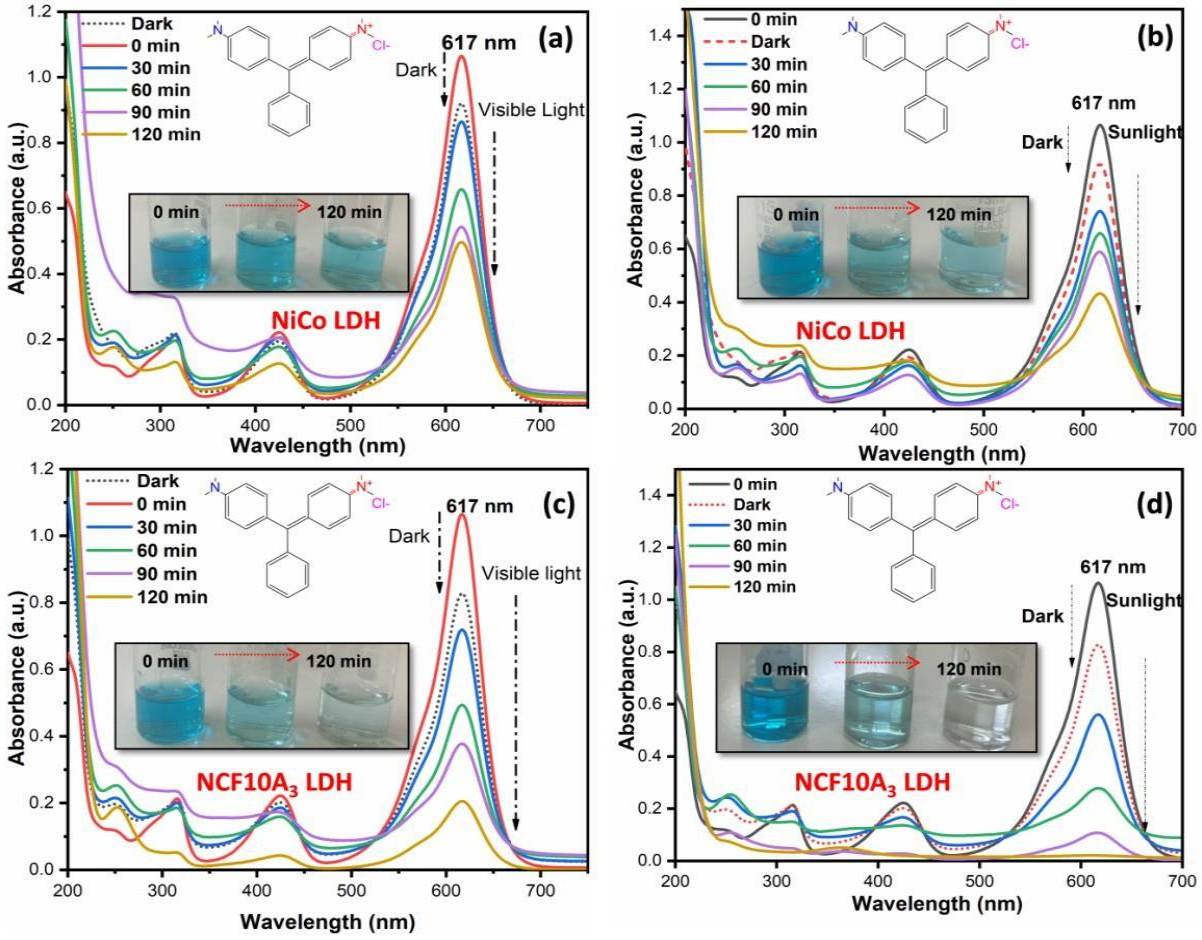

Fig.4.11. UV-Vis spectra of time course study of degradation of MG by NiCo LDH (a, b) and NCF10A$_3$ LDH (c, d) under visible light and sunlight irradiation

Moreover, depositing plasmonic metals positively boosted photocatalytic activity, because of the Surface Plasmon resonance phenomenon exhibited by the metal NPs, which are activated by photons. This effect minimized the recombination rate of electron-hole pairs, among the composites tested the best photoactivity was attained with the NCF10A$_3$ LDH composite. The optimal weight percentage of metal NPs improved active sites and electron transfer, but higher content caused nanoparticle agglomeration, decreasing photo-efficiency. Therefore, the optimal weight percentage of metal nanoparticles was found to be 3 wt.%, as further loading reduced activity.

The degradation of MG by NiCo LDH and its composites follows pseudo-first-order kinetics. The rate of photodegradation at low MG concentrations is expressed as:

$\ln(C_t) = -kt + \ln(C_o)$ ..... (4)

The linear integration of equation (3) can be written as:

$\log(C_o/Ct) = k * t / 2.303$ .....(5)

Here, C_o signifies the initial concentration of the MG solution, C_t stands for the concentration of the MG solution at a given time (t), k denotes the pseudo-first-order rate constant (min^{-1}), and t indicates the experimental duration in minutes. **Fig.4.12 (c, d)** illustrates the linear fit first-order reaction kinetics for all the catalysts prepared with rate constant value (0.88×10^{-2} min^{-1}, 0.76×10^{-2} min^{-1}): NiCo LDH ; (0.92×10^{-2} min^{-1}, 0.94×10^{-2} min^{-1}): NCF5 LDH ; (0.93×10^{-2} min^{-1}, 1.0×10^{-2} min^{-1}): NCF10 LDH ; (1.25×10^{-2} min^{-1}, 3.33×10^{-2} min^{-1}): $NCF10A_3$ LDH ; (1.57×10^{-2} min^{-1} 2.0×10^{-2} min^{-1}): $NCF10A_5$ LDH under illumination of visible light and sunlight, respectively.

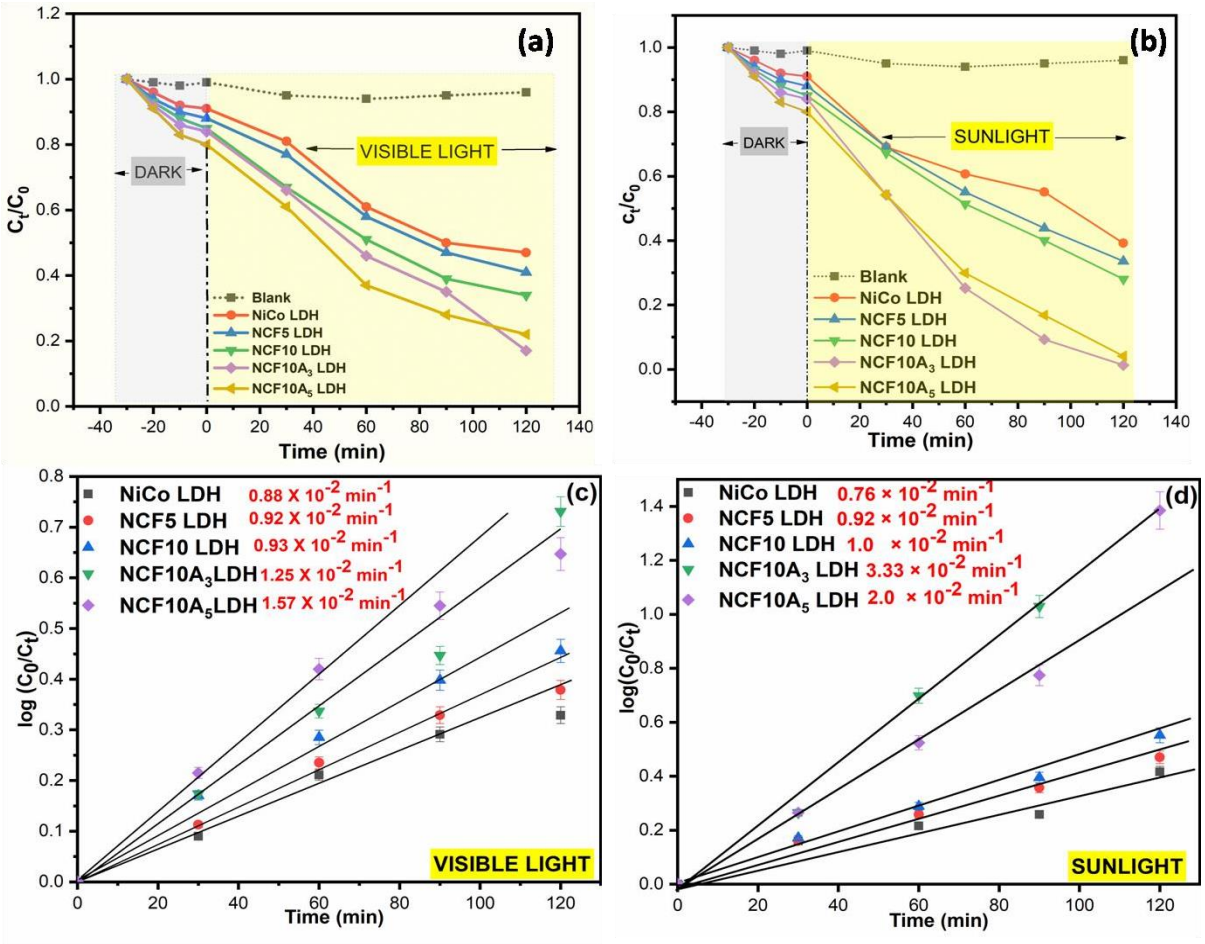

Fig.4.12. Time course-kinetic plots (a, b); variations in apparent reaction rate constants values obtained for the degradation of MG using different photocatalysts under visible light and sunlight (c, d)

4.4.3. Mineralization efficiency and scavenging experiments

Photocatalytic processes aim to mineralize organic pollutants, with TOC analysis utilized to measure the mineralization extent by measuring dissolved organic carbon in the solution. TOC values represent the quantity of organic carbon present, and a decrease in TOC concentration indicates greater organic content mineralization post-reaction [58]. This method is pivotal in assessing the efficiency of photocatalytic treatments for environmental remediation. TOC measurements were conducted before and after degradation to determine the extent of MG mineralization by the synthesized NCF10A_3 LDH. The findings showed a mineralization efficiency of 41.3% when exposed to visible light and 49.4% under sunlight for 120 minutes with the NCF10A_3 photocatalyst **Fig.4.13 (a).** The relatively modest TOC removal percentage compared to degradation efficiency might be due to the enhanced stability of the MG molecule owing to its substantial aromatic ring structure. Moreover, the formation of numerous intermediate products during degradation could elevate the overall TOC levels in the solution, thereby impacting the outcomes. The % mineralization was calculated using the equation given:

Mineralization (%) = {TOC (final) - TOC (initial)}/ TOC (initial)* 100….....(6)

Scavenging experiments were conducted to identify the active species involved in the photodegradation of MG under visible light. Methanol, IPA, and argon purging were added to the MG solution under the identical reaction conditions used for the photodegradation analysis. Compared with experiments without scavengers, a decrease in percent degradation was observed. This decline in photocatalytic activity upon introducing scavengers suggests that holes, superoxides, and hydroxyl radicals influence the photocatalysis of MG over NCF10A_3 LDH. **Fig.4.13 (b)** shows the significant decrease that occurred with methanol addition, followed by argon purging and IPA addition, indicating that $OH^{\bullet}$ and $O_2^{\bullet-}$ are the primary species responsible for the photodegradation process. The contribution of active species during the photodegradation of MG follows the order: $OH^{\bullet} > O_2^{\bullet-} > h^+$.

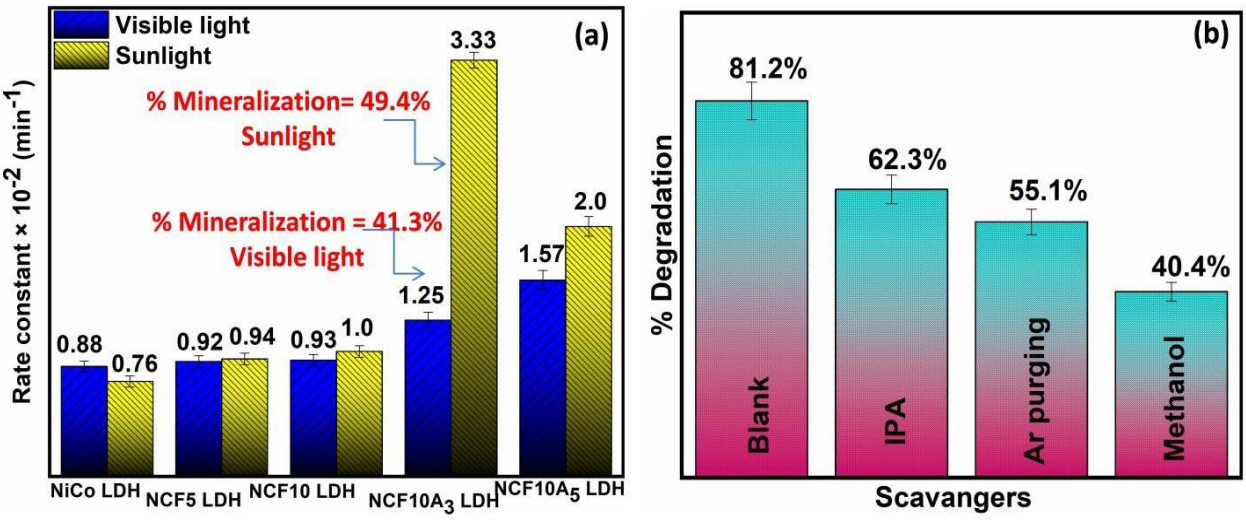

Fig.4.13. Percent degradation (a); the role of scavengers on degradation on MG with NCF10A$_3$ photocatalyst (b)

4.4.4. HRMS studies

The analysis of intermediates formed during the photodegradation of MG was conducted using High-resolution mass spectrometry (HR-MS), with NCF10A$_3$ LDH serving as the photocatalyst. The HRMS spectra of malachite green degraded under visible light and sunlight are shown in (**Fig.4.14** and **Fig.4.15**). The hypothesized pathways for MG degradation under visible light irradiation are illustrated based on the intermediates identified in the HR-MS analysis **Fig.4.16 (a)**. MG (m/z = 329.20) can degrade either through a gradual demethylation and hydroxylation process or via an initial oxidative breakdown reaction followed by a stepwise demethylation process. The degradation of MG begins with the hydroxylation of leucomalachite green (LMG) m/z = 330.20, which is generated through the oxidation of MG. In the first pathway, LMG is hydroxylated to form malachite green carbinol (MG, m/z = 347.21), which is subsequently reduced by hydroxyl radicals to produce 4-(dimethylamino) benzophenone with m/z = 226.12. Two successive demethylations and hydroxylation intermediates with m/z = 198 and 227.12 were formed, which can further oxidize into oxalic acid and eventually mineralize to CO_2 and H_2O. In an alternative degradation pathway, MG undergoes three successive demethylations, resulting in the formation of three metabolic products: desmethyl malachite green (m/z = 315.18), didesmethyl malachite green (m/z = 301.17), and tri desmethyl malachite green (m/z =

287). This process occurs without undergoing any ring cleavage reaction [59]. Hence, the degradation pathways proposed, along with the intermediates identified through HR-MS analysis, provide evidence of radical involvement in the degradation of MG when utilizing NCF10A$_3$ LDH as a photocatalyst. Also, the intermediates were detected for the sunlight- degraded MG sample, but fewer were observed than the visible light-degraded sample. This could be attributed to the faster reaction under sunlight and the increased temperature, accelerating the conversion of intermediates into degraded products. The mechanism shown in **Fig.4.16 (b)** involves the N-demethylation of the MG cation, which forms an intermediate (m/z = 273.1), followed by hydroxyl radical species formation with m/z = 291.1 and finally fragmentation into a molecule with m/z 213.1. Further successive breakdown leads to the formation of hydroquinone. Hydroquinone is further fragmented into benzoquinone and then into maleic acid. Finally, all intermediate molecules could be further fragmented and mineralized into CO_2 and H_2O [60].

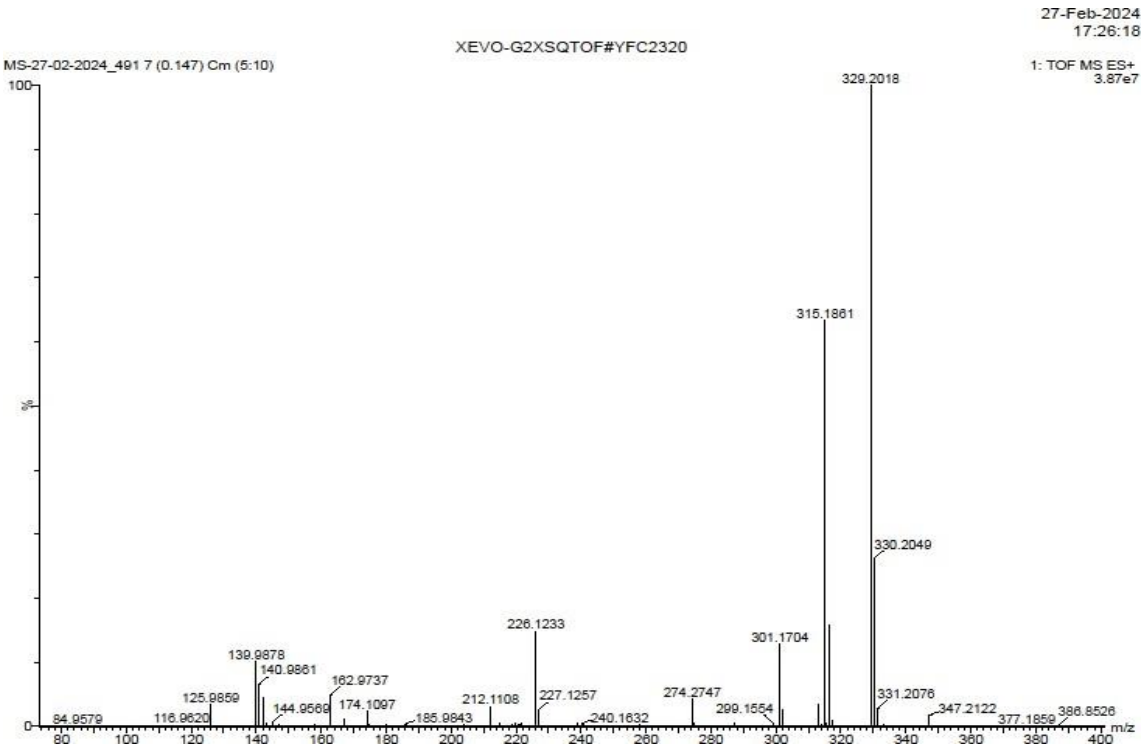

Fig.4.14. The HR-MS spectrum of malachite green solution after degradation under visible light irradiation

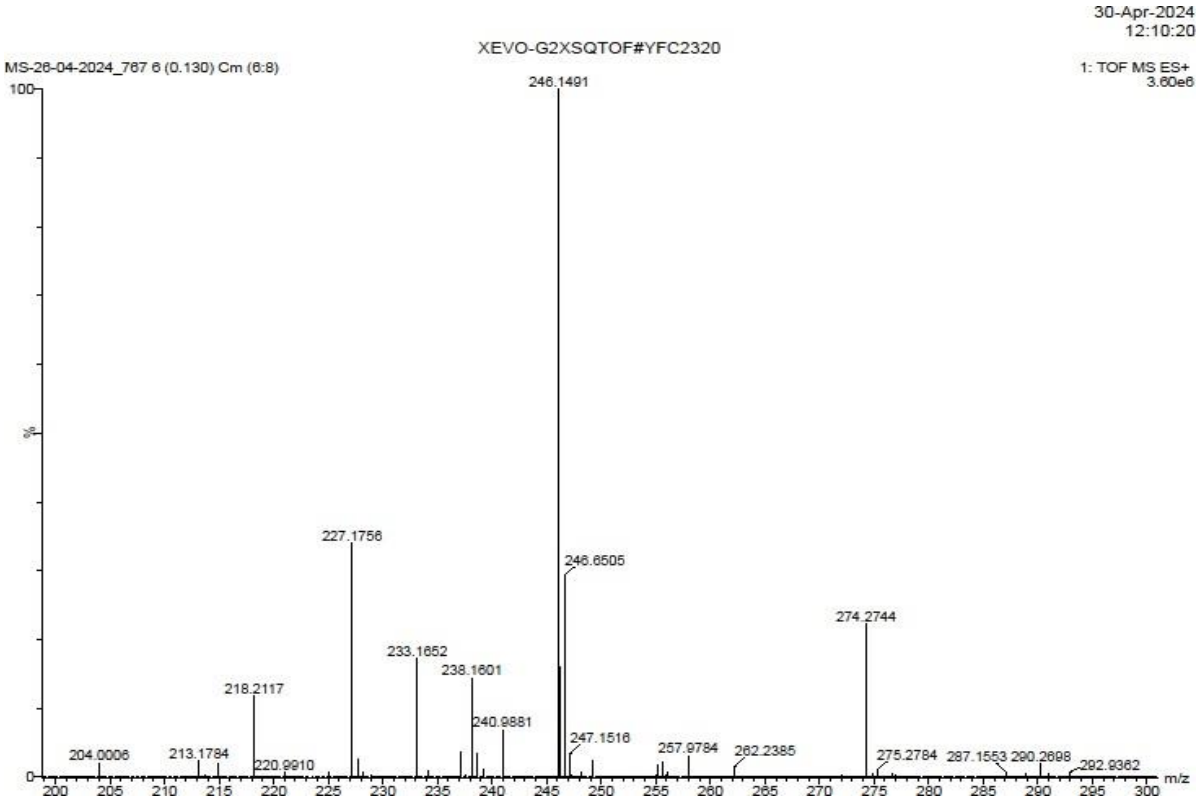

Fig.4.15. The HR-MS spectrum of malachite green solution after degradation under sunlight irradiation

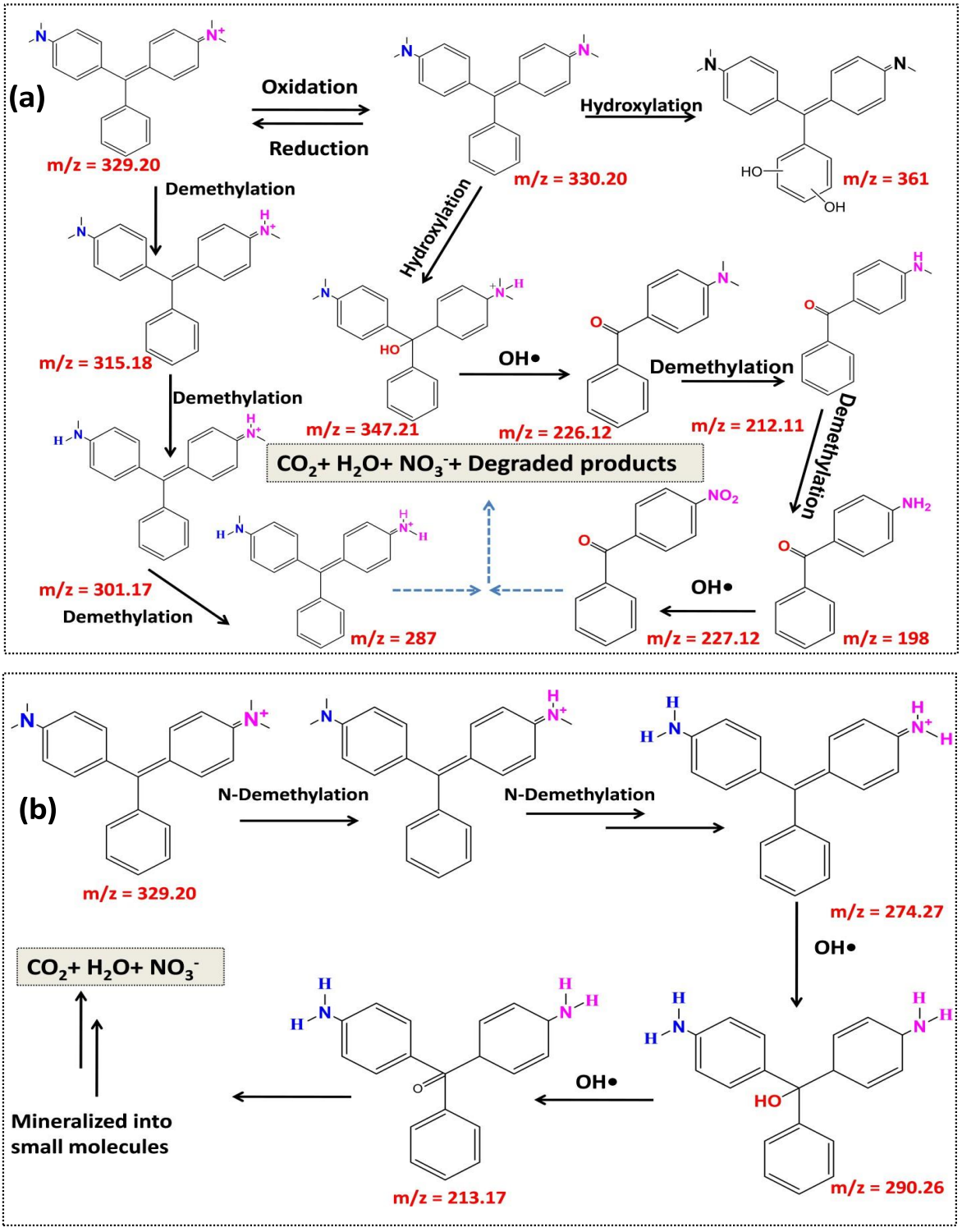

Fig.4.16. Proposed photocatalytic degradation pathway of MG by NCF10A$_3$ LDH composite under visible light (a) and sunlight (b)

4.4.5. Reusability and stability of the catalyst

Stability and reusability tests were conducted on NCF10A$_3$ LDH to degrade MG. Recycling experiments revealed a decrease in the degradation efficiencies of the catalyst after five runs i.e. from 81.2% to 76.5% **Fig.4.17 (a)**. Additionally, FESEM, XRD and DRS spectra were obtained after recycling tests to assess any alterations in the photocatalyst's structure after multiple uses as shown in **Fig.4.17 (b, c and d)**. The characteristic XRD peaks in the NCF10A$_3$ LDH composite remained consistent after five cycles. Furthermore, the DRS spectra of the photocatalyst after five photocatalytic runs displayed a negligible change in the absorption spectra. FESEM image further evidence of the photocatalyst's remarkable stability, showing that its morphology remains unchanged and unaffected even after multiple cycles of use. The decrease in degradation efficiency could be due to either blockage of active sites of the catalyst or loss of the catalyst amount during separation.

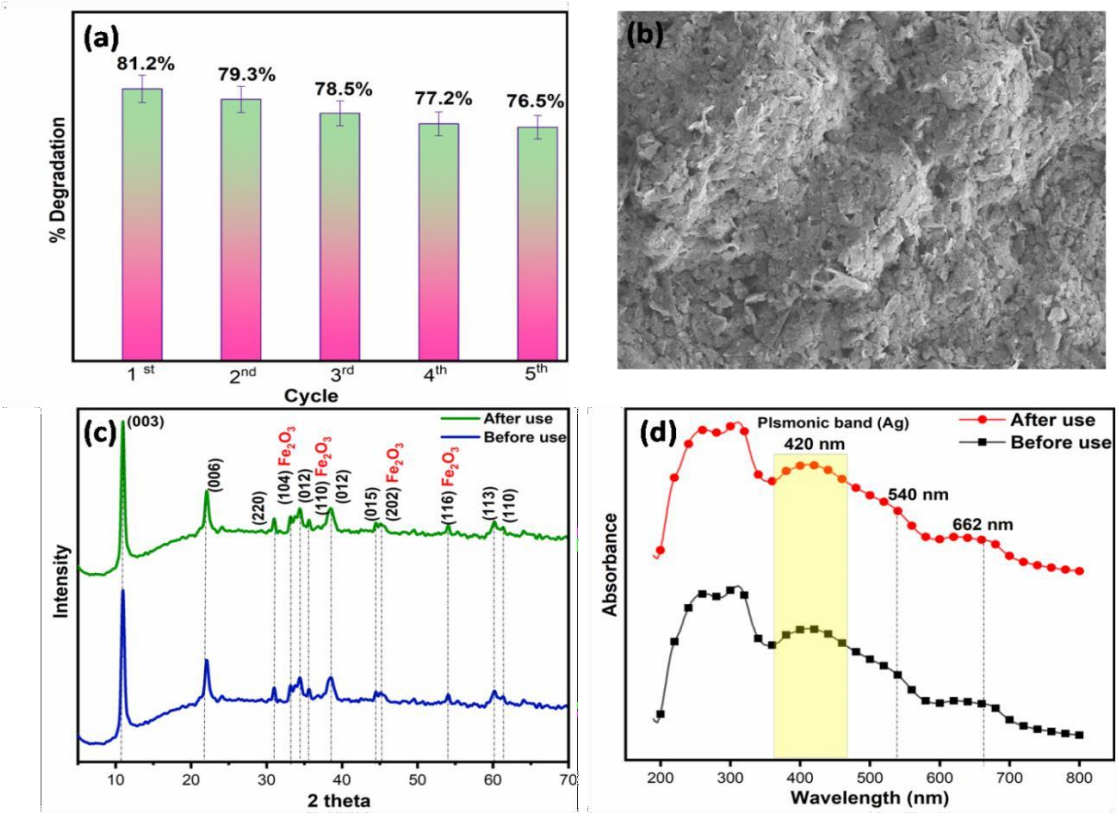

Fig. 4.17. Reusability studies (a); FESEM, XRD and DRS spectra of NCF10A$_3$ LDH before and after 5 cycles of MG degradation (b-d)

4.4.6. Proposed degradation mechanism

The suggested mechanism for the photocatalytic degradation of MG using NCF10A3 LDH is illustrated in **Scheme 4.2**. Upon visible light/sunlight illumination, electrons in the valence band of LDH and Fe_2O_3 become excited, creating holes in the valence band. The conduction band edge potential of NiCo LDH (-0.44 eV) is more negative than that of Fe_2O_3 (+0.40 eV), facilitating the migration of electrons from the LDH conduction band to the Fe_2O_3 conduction band. Conversely, the valence band potential of Fe_2O_3 (+2.25 eV) is more positive than that of LDH (+1.98 eV), promoting the rapid transfer of holes produced in Fe_2O_3 to the LDH valence band. The efficient migration and prevention of recombination of electron-hole pairs across the Ag@Fe_2O_3/LDH heterojunction are enabled by the appropriate band potentials of LDH and Fe_2O_3. Furthermore, electrons from LDH and Fe_2O_3 conduction bands are captured by silver nanoparticles on the Ag@Fe_2O_3/LDH (NCF10A$_3$) composite surface. This enhances the separation efficiency of photogenerated charge carriers due to silver NPs surface plasmon resonance (SPR), generating hot electrons upon exposure to light. This collective oscillation of conduction electrons further boosts the photocatalytic reaction on the surface.

Ag nanoparticles capture electrons, initiating a reaction with dissolved oxygen (O_2) to yield superoxide anion radicals ($O_2^{\bullet-}$) ($EO_2/EO_2^{\bullet-} = -0.046$ eV) [61]. The generated $O_2^{\bullet-}$ is then protonated to produce the hydro-peroxyl radical (HOO$^\bullet$) first and then H_2O_2, which dissociates into a highly active $^\bullet$OH species. Due to the larger positive VB potential value (EVB) than the E_0 (OH^-/ $^\bullet$OH) (+1.99 eV vs. NHE) photo-induced holes left on the VB of Fe_2O_3 can react with surface OH^- ions to generate another powerful oxidant, the OH$^\bullet$ radical [62]. Alternatively, some radicals directly target MG in aqueous solutions, leading to their oxidation and degradation into smaller molecules. Ultimately, numerous reactive species (h^+, $^\bullet$OH, and $^\bullet O_2^-$) work together in mineralizing the MG molecules into less harmful intermediates and products such as H_2O and CO_2.

The synergistic role of Ag and Fe_2O_3 in enhancing the photocatalytic performance can be expanded by further emphasizing how the combination of these materials facilitates not only efficient charge separation and transfer but also optimizes the production of reactive oxygen species. Ag nanoparticles contribute to the generation of hot electrons through surface plasmon

resonance (SPR), which enhances the electron transfer from the conduction band of LDH and Fe_2O_3 to the Ag surface, leading to a significant increase in electron density at the Ag surface. This enhancement allows for a more efficient reduction of oxygen to produce superoxide anion radicals ($O^{\bullet-}$), which are crucial for initiating oxidative reactions. In parallel, the Fe_2O_3 component facilitates the generation of hydroxyl radicals ($^{\bullet}OH$) via both hole transfer to the LDH and direct interaction with surface hydroxyl groups, creating a powerful oxidative environment. Together, the Ag and Fe_2O_3 components create a dynamic electron flow system that not only boosts the separation and migration of charge carriers but also enhances the formation of ROS like $O_2^{\bullet-}$ and $^{\bullet}OH$, which are highly effective in decomposing pollutants. The cooperation between these two materials effectively accelerates the degradation of MG into less toxic by- products, improving the overall photocatalytic efficiency and stability of the composite.

The mechanism includes the steps as follows:

$Fe_2O_3 + h\nu \rightarrow Fe_2O_3 (e^-) + Fe_2O_3 (h^+)$.....(7)

$LDH + h\nu \rightarrow LDH (e^-) + LDH (h^+)$ .....(8)

$LDH (e^-)$ CB $\rightarrow Fe_2O_3 (e^-)$ Combination .....(9)

$Fe_2O_3 (h^+)$ CB $\rightarrow$LDH (h^+) Combination.....(10)

$Fe_2O_3 (e^-)$/LDH (e^-) CB $\rightarrow$ Ag (e^-) Electron transport ..... (11)

$LDH/Fe_2O_3 (e^-) + O_2 \rightarrow {}^{\bullet}O_2$.....(12)

$O_2^{-\bullet} + H^+ \rightarrow {}^{\bullet}OOH$.....(13)

$2{}^{\bullet}OOH \rightarrow O_2 + H_2O_2$ .....(14)

$H_2O_2 + (e^-) \rightarrow {}^{\bullet}OH + OH$ .....(15)

$LDH (h^+) + OH^- \rightarrow {}^{\bullet}OH$.....(16)

$O_2^{\bullet-}/{}^{\bullet}OH/h^+ + MG \rightarrow CO_2 + H_2O + NO_3^- +$ degraded products.....(17)

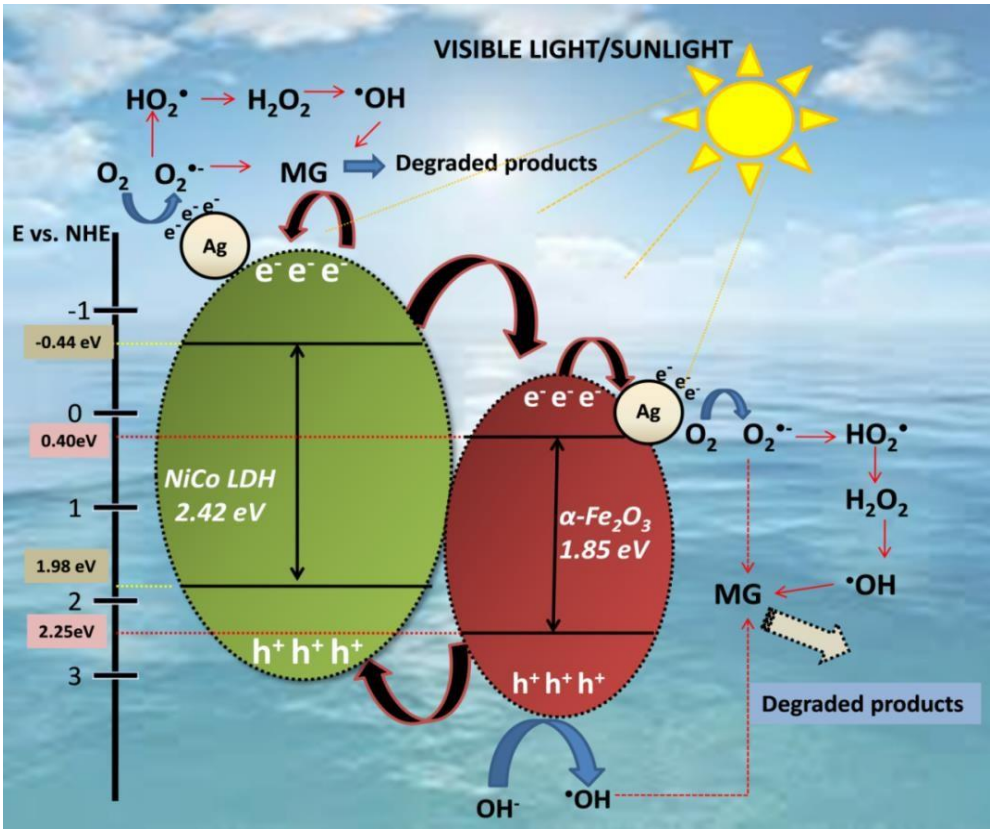

Scheme 4.2. Possible reaction mechanism of MG degradation over NCF10A$_3$ LDH under visible light-sunlight

Conclusion

This study achieved notable enhancements in the visible-light photocatalytic efficiency of NiCo LDH upon its composite formation with α-Fe_2O_3 and optimizing the appropriate loading of Fe_2O_3 to increase its activity. The study investigated the degradation activity of NCF10 LDH (65%), which was highest among different compositions of Fe_2O_3/LDH composites. Silver nanoparticles (Ag NPs) ranging from 3 to 5 wt.% were deposited onto NCF10 LDH composite via photochemical reduction and the Ag$_3$@NCF10 LDH composite exhibited superior degradation rates (81.2%, 98.6 %) under visible light irradiation and sunlight respectively. This optimized composite also showed altered physicochemical and structural properties. Furthermore, after multiple consecutive degradation cycles, the photocatalyst showed robust stability with little performance loss. This analysis of scavenging experiments highlighted the pivotal role of OH$^•$ as a primary species, with significant contributions of holes and O_2^{-}• in the

degradation process. The mineralization efficiency of the developed photocatalyst was also assessed using the TOC test to evaluate its ability to remove organic pollutants. TOC detection indicated 41.3% and 49.3% mineralization efficiencies for the visible light and sunlight irradiated respectively. In HRMS analysis fewer intermediates were detected for the sunlight- degraded sample, possibly due to the fast reaction facilitated by the high temperature during sunlight optimization.

References

[1] M.S. Nawaz, M. Ahsan, Comparison of physico-chemical, advanced oxidation and biological techniques for the textile wastewater treatment, Alexandria Eng. J. 53 (2014) 717–722. https://doi.org/10.1016/j.aej.2014.06.007.

[2] T. Shindhal, P. Rakholiya, S. Varjani, A. Pandey, H.H. Ngo, W. Guo, H.Y. Ng, M.J. Taherzadeh, A critical review on advances in the practices and perspectives for the treatment of dye industry wastewater, Bioengineered. 12 (2021) 70–87. https://doi.org/10.1080/21655979.2020.1863034.

[3] P. Falås, A. Wick, S. Castronovo, J. Habermacher, T.A. Ternes, A. Joss, Tracing the limits of organic micropollutant removal in biological wastewater treatment, Water Res. 95 (2016) 240–249. https://doi.org/10.1016/j.watres.2016.03.009.

[4] M. Xia, Z. Chen, Y. Li, C. Li, N.M. Ahmad, W.A. Cheema, S. Zhu, Removal of Hg(ii) in aqueous solutions through physical and chemical adsorption principles, RSC Adv. 9 (2019) 20941–20953. https://doi.org/10.1039/c9ra01924c.

[5] M. Ince, O. Kaplan Ince, Makale gönderme tarihi, Int. J. Pure Appl. Sci. 3 (2017) 10–19.

[6] N. Venkatesh, K. Sabarish, G. Murugadoss, R. Thangamuthu, P. Sakthivel, Visible light–driven photocatalytic dye degradation under natural sunlight using Sn-doped CdS nanoparticles, Environ. Sci. Pollut. Res. 27 (2020) 43212–43222. https://doi.org/10.1007/s11356-020-10268-3.

[7] V. Archana, J. Joseph Prince, S. Kalainathan, Simple One-Step Leaf Extract-Assisted Preparation of α -Fe2O3Nanoparticles, Physicochemical Properties, and Its Sunlight-Driven Photocatalytic Activity on Methylene Blue Dye Degradation, J. Nanomater. 2021

(2021). https://doi.org/10.1155/2021/8570351.

[8] Jemini, S. Singh, B. Pal, Efficient ZnCr LDH/monoclinic-WO3 composites for Degradation of Tetracycline under Visible Light, ChemistrySelect. 7 (2022) 73825– 73848. https://doi.org/10.1002/slct.202203846.

[9] L. Mohapatra, K. Parida, A review on the recent progress, challenges and perspective of layered double hydroxides as promising photocatalysts, J. Mater. Chem. A. 4 (2016) 10744–10766. https://doi.org/10.1039/c6ta01668e.

[10] P. Bansal, D. Sud, Photocatalytic degradation of commercial dye, CI Reactive Red 35 in aqueous suspension: Degradation pathway and identification of intermediates by LC/MS, J. Mol. Catal. A Chem. 374–375 (2013) 66–72. https://doi.org/10.1016/j.molcata.2013.03.018.

[11] P. Kaur, P. Bansal, D. Sud, Heterostructured nanophotocatalysts for degradation of organophosphate pesticides from aqueous streams, J. Korean Chem. Soc. 57 (2013) 382–388. https://doi.org/10.5012/jkcs.2013.57.3.382.

[12] Jemini, S. Singh, B. Pal, Ag2@WO3/MgAl Layered double hydroxide displayed superior adsorption and photocatalytic activity under visible light, Appl. Clay Sci. 250 (2024) 107281. https://doi.org/10.1016/j.clay.2024.107281.

[13] A. Rajeswari, S. Vismaiya, A. Pius, Preparation, characterization of nano ZnO-blended cellulose acetate-polyurethane membrane for photocatalytic degradation of dyes from water, Elsevier B.V., 2017. https://doi.org/10.1016/j.cej.2016.10.124.

[14] M. Suárez-Quezada, G. Romero-Ortiz, V. Suárez, G. Morales-Mendoza, L. Lartundo-Rojas, E. Navarro-Cerón, F. Tzompantzi, S. Robles, R. Gómez, A. Mantilla, Photodegradation of phenol using reconstructed Ce doped Zn/Al layered double hydroxides as photocatalysts, Catal. Today. 271 (2016) 213–219. https://doi.org/10.1016/j.cattod.2016.01.009.

[15] P. Shandilya, R. Sharma, R.K. Arya, A. Kumar, D.V.N. Vo, G. Sharma, Recent progress and challenges in photocatalytic water splitting using layered double hydroxides (LDH) based nanocomposites, Int. J. Hydrogen Energy. 47 (2022) 37438–37475. https://doi.org/10.1016/j.ijhydene.2021.08.190.

[16] Z. zhu Yang, J. jing Wei, G. ming Zeng, H. qing Zhang, X. fei Tan, C. Ma, X. cheng Li, Z. hao Li, C. Zhang, A review on strategies to LDH-based materials to improve adsorption capacity and photoreduction efficiency for CO 2, Coord. Chem. Rev. 386 (2019) 154–182. https://doi.org/10.1016/j.ccr.2019.01.018.

[17] S. Tonda, S. Kumar, M. Bhardwaj, P. Yadav, S. Ogale, G-C3N4/NiAl-LDH 2D/2D Hybrid Heterojunction for High-Performance Photocatalytic Reduction of CO2 into Renewable Fuels, ACS Appl. Mater. Interfaces. 10 (2018) 2667–2678. https://doi.org/10.1021/acsami.7b18835.

[18] H. Kaur, S. Singh, B. Pal, Impact of g-C3N4 loading on NiCo LDH for adsorptive removal of anionic and cationic organic pollutants from aqueous solution, Korean J. Chem. Eng. 38 (2021) 1248–1259. https://doi.org/10.1007/s11814-021-0784-6.

[19] M. Daud, A. Hai, F. Banat, M.B. Wazir, M. Habib, G. Bharath, M.A. Al-Harthi, A review on the recent advances, challenges and future aspect of layered double hydroxides (LDH)–Containing hybrids as promising adsorbents for dyes removal, J. Mol. Liq. 288 (2019) 110989. https://doi.org/10.1016/j.molliq.2019.110989.

[20] R. Lebrun, A. Ross, S.A. Bender, A. Qaiumzadeh, L. Baldrati, J. Cramer, A. Brataas, R.A. Duine, M. Kläui, Tunable long-distance spin transport in a crystalline antiferromagnetic iron oxide, Nature. 561 (2018) 222–225. https://doi.org/10.1038/s41586-018-0490-7.

[21] X. Pan, Counter electrode for dye-sensitized solar cells, Dye. Sol. Cells. (2022) 269–298. https://doi.org/10.1515/9783110344363-005.

[22] A. Boudjemaa, A. Rebahi, B. Terfassa, R. Chebout, T. Mokrani, K. Bachari, N.J. Coville, Fe2O3/carbon spheres for efficient photo-catalytic hydrogen production from water and under visible light irradiation, Sol. Energy Mater. Sol. Cells. 140 (2015) 405–411. https://doi.org/10.1016/j.solmat.2015.04.036.

[23] M. Pourmadadi, E. Rahmani, A. Shamsabadipour, S. Mahtabian, M. Ahmadi, A. Rahdar, A.M. Díez-Pascual, Role of Iron Oxide (Fe2O3) Nanocomposites in Advanced Biomedical Applications: A State-of-the-Art Review, Nanomaterials. 12 (2022). https://doi.org/10.3390/nano12213873.

[24] X. Wang, F. Liang, H. Gu, S. Wu, Y. Cao, G. Lv, H. Zhang, Q. Jia, S. Zhang, In situ

synthesized α-Fe2O3/BCN heterojunction for promoting photocatalytic CO2 reduction performance, J. Colloid Interface Sci. 621 (2022) 311–320. https://doi.org/10.1016/j.jcis.2022.04.003.

[25] E. Fernandes, J. Gomes, R.C. Martins, Semiconductors Application Forms and Doping Benefits to Wastewater Treatment: A Comparison of TiO2, WO3, and g-C3N4, Catalysts. 12 (2022). https://doi.org/10.3390/catal12101218.

[26] P.R. Lestari, T. Takei, N. Kumada, Novel ZnTi/C3N4/Ag LDH heterojunction composite for efficient photocatalytic phenol degradation, J. Solid State Chem. 294 (2021) 121858. https://doi.org/10.1016/j.jssc.2020.121858.

[27] D. Gilea, R.G. Ciocarlan, E.M. Seftel, P. Cool, G. Carja, Engineering Heterostructures of Layered Double Hydroxides and Metal Nanoparticles for Plasmon-Enhanced Catalysis, Catalysts. 12 (2022) 1–28. https://doi.org/10.3390/catal12101210.

[28] S. Singh, P. Kaur, Abhivyakti, V. Kumar, K. Tikoo, S. Singhal, Facile integration of a novel Sm-doped CoFe2O4@ g-CN heterostructure to expedite PMS and H2O2 assisted degradation of pharmaceutical pollutants, Appl. Surf. Sci. 580 (2022) 152254. https://doi.org/10.1016/j.apsusc.2021.152254.

[29] H. Kaur, S. Singh, B. Pal, Effect of plasmonic metal (Cu, Ag, and Au) loading over the physicochemical and photocatalytic properties of Mg-Al LDH towards degradation of tetracycline under LED light, Appl. Surf. Sci. 609 (2023) 155455. https://doi.org/10.1016/j.apsusc.2022.155455.

[30] S. Kaur, B. Pal, Superior visible-light absorbing Ag@ZnO nanorods hybrid photocatalyst for efficient decomposition of commercial pharmaceuticals tetracycline and amoxicillin, J. Water Process Eng. 58 (2024) 104765. https://doi.org/10.1016/j.jwpe.2023.104765.

[31] W. Chomkitichai, P. Jansanthea, D. Channei, Photocatalytic Activity Enhancement in Methylene Blue Degradation by Loading Ag Nanoparticles onto α-Fe2O3, Russ. J. Inorg. Chem. 66 (2021) 1995–2003. https://doi.org/10.1134/S0036023621130027.

[32] S. Rajamohan, V. Kumaravel, A. Abdel-Wahab, S. Ayyadurai, R. Muthuramalingam, Exploration of Ag decoration and Bi doping on the photocatalytic activity α-Fe2O3 under simulated solar light irradiation, Can. J. Chem. Eng. 96 (2018) 1713–1722.

https://doi.org/10.1002/cjce.23122.

[33] R.R. Shan, L.G. Yan, K. Yang, S.J. Yu, Y.F. Hao, H.Q. Yu, B. Du, Magnetic Fe3O4/MgAl-LDH composite for effective removal of three red dyes from aqueous solution, Chem. Eng. J. 252 (2014) 38–46. https://doi.org/10.1016/j.cej.2014.04.105.

[34] Y. Meng, X. Zhang, G. Pan, S. Xia, Z. Ni, Orthogonal synthesis of a novel hybrid layered material containing three different zincous components and its photocatalytic property investigation, J. Hazard. Mater. 350 (2018) 144–153. https://doi.org/10.1016/j.jhazmat.2018.02.021.

[35] S.J. Xia, X.B. Zhou, W. Shi, G.X. Pan, Z.M. Ni, Photocatalytic property and mechanism studies on acid red 14 by M xOy/ZnTi-layered double hydroxides (M = Fe, Sn, Ce), J. Mol. Catal. A Chem. 392 (2014) 270–277. https://doi.org/10.1016/j.molcata.2014.05.028.

[36] M. Li, L. Fang, H. Zhou, F. Wu, Y. Lu, H. Luo, Y. Zhang, B. Hu, Three-dimensional porous MXene/NiCo-LDH composite for high performance non-enzymatic glucose sensor, Appl. Surf. Sci. 495 (2019). https://doi.org/10.1016/j.apsusc.2019.143554.

[37] F. Wang, X.F. Qin, Y.F. Meng, Z.L. Guo, L.X. Yang, Y.F. Ming, Hydrothermal synthesis and characterization of α-Fe2O 3 nanoparticles, Mater. Sci. Semicond. Process. 16 (2013) 802–806. https://doi.org/10.1016/j.mssp.2012.12.029.

[38] P.K. Ray, R. Mohanty, K. Parida, Recent advancements of NiCo LDH and graphene based nanohybrids for supercapacitor application, J. Energy Storage. 72 (2023) 108335. https://doi.org/10.1016/j.est.2023.108335.

[39] D.E. Fouad, C. Zhang, H. El-Didamony, L. Yingnan, T.D. Mekuria, A.H. Shah, Improved size, morphology and crystallinity of hematite (α-Fe2O3) nanoparticles synthesized via the precipitation route using ferric sulfate precursor, Results Phys. 12 (2019) 1253–1261. https://doi.org/10.1016/j.rinp.2019.01.005.

[40] S. Latha, M. Shilpa, N. Parushuram, Y. Sangappa, Green synthesis of silver nanoparticles and their characterization, AIP Conf. Proc. 2220 (2020). https://doi.org/10.1063/5.0001143.

[41] G. Lei, D. Chen, Q. Li, H. Liu, Q. Shi, C. Li, NiCo-layered double hydroxide with cation vacancy defects for high-performance supercapacitors, Electrochim. Acta. 413 (2022)

140143. https://doi.org/10.1016/j.electacta.2022.140143.

[42] M. Qayoom, K.A. Shah, A.H. Pandit, A. Firdous, G.N. Dar, Dielectric and electrical studies on iron oxide (α-Fe2O3) nanoparticles synthesized by modified solution combustion reaction for microwave applications, J. Electroceramics. 45 (2020) 7–14. https://doi.org/10.1007/s10832-020-00219-2.

[43] D. Du, X. Wu, S. Li, Y. Zhang, W. Xing, L. Li, Q. Xue, P. Bai, Z. Yan, Remarkable supercapacitor performance of petal-like LDHs vertically grown on graphene/polypyrrole nanoflakes, J. Mater. Chem. A. 5 (2017) 8964–8971. https://doi.org/10.1039/c7ta00624a.

[44] M. Shamloofard, S. Shahrokhian, M.K. Amini, Mesoporous nanostructures of NiCo-LDH/ZnCo2O4 as an efficient electrocatalyst for oxygen evolution reaction, J. Colloid Interface Sci. 604 (2021) 832–843. https://doi.org/10.1016/j.jcis.2021.07.059.

[45] Y. Wang, S. Guo, X. Xin, Y. Zhang, B. Wang, S. Tang, X. Li, Effective interface contact on the hierarchical 1D/2D CoO/NiCo-LDH heterojunction for boosting photocatalytic hydrogen evolution, Appl. Surf. Sci. 549 (2021) 149108. https://doi.org/10.1016/j.apsusc.2021.149108.

[46] S. Seong, I.S. Park, Y.C. Jung, T. Lee, S.Y. Kim, J.S. Park, J.H. Ko, J. Ahn, Synthesis of Ag-ZnO core-shell nanoparticles with enhanced photocatalytic activity through atomic layer deposition, Mater. Des. 177 (2019) 107831. https://doi.org/10.1016/j.matdes.2019.107831.

[47] G. Jiang, C. Zheng, Z. Jin, Hexagonal CdS assembled with lamellar NiCo LDH form S-scheme heterojunction for photocatalytic hydrogen evolution, Mater. Sci. Semicond. Process. 135 (2021) 106128. https://doi.org/10.1016/j.mssp.2021.106128.

[48] A.Q. Zhou, J.M. Yang, X.W. Zhu, X.L. Zhu, J.Y. Liu, K. Zhong, H.X. Chen, J.Y. Chu, Y.S. Du, Y.H. Song, J.C. Qian, H.M. Li, H. Xu, Self-assembly construction of NiCo LDH/ultrathin g-C3N4 nanosheets photocatalyst for enhanced CO2 reduction and charge separation mechanism study, Rare Met. 41 (2022) 2118–2128. https://doi.org/10.1007/s12598-022-01960-z.

[49] M.R. Shenoy, S. Ayyasamy, V. Bhojan, R. Swaminathan, N. Raju, P. Senthil Kumar, M. Sasikumar, G. Kadarkarai, S. Tamilarasan, S. Thangavelu, S. J, M. V. Reddy, Visible light

sensitive hexagonal boron nitride (hBN) decorated Fe2O3 photocatalyst for the degradation of methylene blue, J. Mater. Sci. Mater. Electron. 32 (2021) 4766–4783. https://doi.org/10.1007/s10854-020-05215-4.

[50] S. Nayak, K.M. Parida, Dynamics of Charge-Transfer Behavior in a Plasmon-Induced Quasi-Type-II p-n/n-n Dual Heterojunction in Ag@Ag3PO4/g-C3N4/NiFe LDH Nanocomposites for Photocatalytic Cr(VI) Reduction and Phenol Oxidation, ACS Omega. 3 (2018) 7324–7343. https://doi.org/10.1021/acsomega.8b00847.

[51] Z. Hu, D. Chen, X. Zhan, F. Wang, L. Qin, Y. Huang, Synthesis of Ag-loaded SrTiO3/TiO2 heterostructure nanotube arrays for enhanced photocatalytic performances, Appl. Phys. A Mater. Sci. Process. 123 (2017). https://doi.org/10.1007/s00339-017-1014- 2.

[52] X. Dai, Y. Dai, J. Lu, L. Pu, W. Wang, J. Jin, F. Ma, N. Tie, Cobalt oxide nanocomposites modified by NiCo-layered double hydroxide nanosheets as advanced electrodes for supercapacitors, Ionics (Kiel). 26 (2020) 2501–2511. https://doi.org/10.1007/s11581-019-03333-6.

[53] S. Sagadevan, R.P. Sivasankaran, J.A. Lett, I. Fatimah, G.K. Weldegebrieal, E. Léonard, M.V. Le, T. Soga, Evaluation of Photocatalytic Activity and Electrochemical Properties of Hematite Nanoparticles, Symmetry (Basel). 15 (2023). https://doi.org/10.3390/sym15061139.

[54] X. Wang, X. Li, X. Du, X. Ma, X. Hao, C. Xue, H. Zhu, S. Li, Controllable Synthesis of NiCo LDH Nanosheets for Fabrication of High-Performance Supercapacitor Electrodes, Electroanalysis. 29 (2017) 1286–1293. https://doi.org/10.1002/elan.201600602.

[55] M. Zhou, F. Xu, S. Zhang, B. Liu, Y. Yang, K. Chen, J. Qi, Low consumption design of hollow NiCo-LDH nanoflakes derived from MOFs for high-capacity electrode materials, J. Mater. Sci. Mater. Electron. 31 (2020) 3281–3288. https://doi.org/10.1007/s10854-020-02876-z.

[56] D. Cao, H. Li, L. Pan, J. Li, X. Wang, P. Jing, X. Cheng, W. Wang, J. Wang, Q. Liu, High saturation magnetization of γ 3-Fe2 O3 nano-particles by a facile one-step synthesis approach, Sci. Rep. 6 (2016) 1–9. https://doi.org/10.1038/srep32360.

[57] S. Some, O. Bulut, K. Biswas, A. Kumar, A. Roy, I.K. Sen, A. Mandal, O.L. Franco, İ.A. İnce, K. Neog, S. Das, S. Pradhan, S. Dutta, D. Bhattacharjya, S. Saha, P.K. Das Mohapatra, A. Bhuimali, B.G. Unni, A. Kati, A.K. Mandal, M.D. Yilmaz, I. Ocsoy, Effect of feed supplementation with biosynthesized silver nanoparticles using leaf extract of Morus indica L. V1 on Bombyx mori L. (Lepidoptera: Bombycidae), Sci. Rep. 9 (2019) 1–14. https://doi.org/10.1038/s41598-019-50906-6.

[58] M. Kus, S. Ribbens, V. Meynen, P. Cool, Microvolume TOC analysis as useful tool in the evaluation of lab scale photocatalytic processes, Catalysts. 3 (2013) 74–87. https://doi.org/10.3390/catal3010074.

[59] A. Barapatre, K.R. Aadil, H. Jha, Biodegradation of Malachite Green by the Ligninolytic Fungus Aspergillus flavus, Clean - Soil, Air, Water. 45 (2017) 1–12. https://doi.org/10.1002/clen.201600045.

[60] N.K. Shee, H.J. Kim, Sn(IV) Porphyrin-Based Ionic Self-Assembled Nanostructures and Their Application in Visible Light Photo-Degradation of Malachite Green, Catalysts. 12 (2022). https://doi.org/10.3390/catal12070799.

[61] T. Wang, X. Liu, C. Ma, Y. Liu, H. Dong, W. Ma, Z. Liu, M. Wei, C. Li, Y. Yan, 3D Ag/NiCo-layered double hydroxide with adsorptive and photocatalytic performance, J. Taiwan Inst. Chem. Eng. 93 (2018) 298–305. https://doi.org/10.1016/j.jtice.2018.07.031.

[62] M. Sohrabian, V. Mahdikhah, E. Alimohammadi, S. Sheibani, Improved photocatalytic performance of SrTiO3 through a Z-scheme polymeric-perovskite heterojunction with g-C3N4 and plasmonic resonance of Ag mediator, Appl. Surf. Sci. 618 (2023) 156682. https://doi.org/10.1016/j.apsusc.2023.156682.

Conclusion and Future Outlook

To solve the various environmental-related issues layered double hydroxides and its composites have been synthesized to remove the pharmaceutical and industrial waste by photodegradation phenomenon. Various visible light responsive LDHs (ZnCr LDH, MgAl LDH, and NiCo LDH) were synthesized and their binary (MO-LDH, MO = WO_3, Fe_2O_3) and ternary (M@MO-LDH; M = Ag) loaded composites showed enhanced degradation in comparison to bare LDH under visible light/sunlight irradiation. Creating heterojunctions between metal oxides and LDHs changes the spatial distribution of charge, enhancing the separation of electrons and holes. This modification addresses common limitations of unmodified LDH-based photocatalysts, including narrow light absorption ranges, low quantum efficiency, and inadequate coverage of active catalytic sites. This study highlighted the incorporation of plasmonic metal Ag nanoparticles onto LDH and MO-LDH composites. The results demonstrated that these plasmonic nanocomposites achieved superior photocatalytic performance for degrading organic pollutants (tetracycline, ciprofloxacin, and malachite green dye). The findings from each chapter contribute significantly to the advancement of photocatalysis for water treatment applications, particularly in the degradation of TC, CIP and MG dye. The ZnCr LDH with monoclinic WO_3 effectively improved photocatalytic performance due to the creation of a Class II heterojunction, which facilitates enhanced charge separation and delays charge recombination and hence, the composite exhibited the highest rate constant and degradation efficiency, outperforming pure ZnCr LDH and other composites. The overloading WO_3 in ZnCr-20WO_3 resulted in decreased photocatalytic activity, indicating the importance of optimizing the ratio of components for maximum performance.

In Silver-Loaded WO_3/MgAl LDH the incorporation of silver into WO_3/MgAl LDH composites significantly enhanced both the adsorption and photocatalytic performance, particularly under visible light irradiation. The silver-induced surface plasmon resonance (SPR) effect improved the visible light absorption of the composite, leading to higher adsorption and photocatalytic degradation rates of TC and CIP, compared to pristine MgAl LDH and binary hybrids. This approach demonstrated a promising strategy to enhance the broad-band gap MgAl LDH photocatalyst, offering a more efficient method for removing pollutants under visible light.

Further, the combination of NiCo LDH with α-Fe_2O_3 and the optimization of Fe_2O_3 loading led to significant enhancements in photocatalytic degradation of MG dye, with the NCF10 composite exhibiting the highest degradation rate as compare to bare LDH. The introduction of silver nanoparticles further improved the photocatalytic activity of Fe_2O_3/LDH composite, with the Ag_3@NCF10 LDH composite achieving near-total degradation under sunlight (98.6%). The studies across all these chapters underscore the potential of composite materials to significantly enhance photocatalytic activity, especially under visible light. The heterojunction formation, surface modification (such as silver loading), and optimization of component ratios are key strategies that lead to improved charge separation, enhanced adsorption and superior photocatalytic performance. The findings from this study open up several avenues for future research as

(i) Future work could explore the formation of ternary composites for ZnCr-10WO_3, by incorporating additional metals like gold, silver, or copper, for further enhancing the photocatalytic activity and broadening the light absorption spectrum.

(ii) Scaling up the synthesis of these composites and testing them in real-world water treatment scenarios, including the degradation of other environmental pollutants (e.g., dyes, industrial chemicals), would be essential to assess their effectiveness and viability.

(iii) Further investigation into the detailed reaction mechanisms, degradation pathways and the interaction between pollutants and catalysts could be analyzed through computational studies which would provide deeper insights into optimizing photocatalytic processes.

In extension to this work, MO/LDH composites formed after the modification of LDH surface charge can improve the adsorption efficiency of oppositely charged pollutants on the surface and M/MO-LDH nanocomposites could be employed for demonstrating hydrogen production through water splitting and dehydrogenation of waste alcohols under light radiations.

List of Publications

1. **Jemini**, Satnam Singh, Bonamali Pal **"**Efficient ZnCr LDH/monoclinic-WO_3 composites for Degradation of Tetracycline under Visible Light". **ChemistrySelect, 7, (2022), 73825-73848. (I.F. 2.1)** https://doi.org/10.1002/slct.202203846.

2. **Jemini**, Satnam Singh, Bonamali Pal **"**Ag_2@WO_3/MgAl Layered double hydroxide displayed superior adsorption and photocatalytic activity under visible light". **Applied Clay Science, 250, (2024), 107281. (I.F. 5.3)** https://doi.org/10.1016/j.clay.2024.107281.

3. **Jemini**, Satnam Singh, Bonamali Pal " Construction of ternary Ag@α-Fe_2O_3/NiCo LDH hetrocomposite for efficient degradation of malachite green dye under visible light/sunlight irradiation" **(Accepted in Journal of Taiwan Institute of Chemical Engineers)**

Other Publications

1. Amandeep kaur, Bonamali Pal, **Jemini*** Photocatalytic activity of Ag@TiO_2 modified Co-Al layered double hydroxide for degradation of dye under visible and sunlight" **(Manuscript under review in Journal of Alloys and Compounds).**

2. **Jemini,** Satnam Singh, Bonamali Pal, A short review on layered double hydroxides as catalysts, phtotocatalysts and adsorbents **(Manuscript under preparation).**

Conferences and Workshops

1. Volunteered in **SCI-FEST** 2022, held at Thapar Institute of Engineering and Technology, Patiala, on 7th June, 2022.

2. Attended 7 days, Hands on training program on insights into the application of high-end instrument in chemical sciences, under the **DST-STUTI** scheme held at Thapar Institute of Engineering and Technology, Patiala. 21th- 27th February, 2023.

3. Volunteered in **SCI-FEST** 2023, held at Thapar Institute of Engineering and Technology, Patiala, on 18th March, 2023.

4. Volunteered in **workshop on "Advanced instrumental techniques in Chemical analysis"** organized by Department of Chemistry and Biochemistry held at Thapar Institute of Engineering and Technology, Patiala. 4-5 October, 2023.

5. Attended "**International conference on emerging trends in science and technology**" organized by Department of Applied Sciences, Punjab Engineering College, Chandigarh from 10-11 June, 2022.

6. Poster presentation at **National conference** on the theme "**Environment, food security and health with respect to climate change**" organized by SGGS World University Fatehgarh Shahib from 7-9Feb, 2023. (WON BEST POSTER AWARD)

7. Participated in poster presentation at **International conference** on "**Advances in chemical and applied sciences for sustainable development**" (ACASSD-2024) organized by JECRC University ,Jiapur from March 29-30,2024.

Thesis plag (JEMINI)

ORIGINALITY REPORT

14%	6%	12%	2%
SIMILARITY INDEX	INTERNET SOURCES	PUBLICATIONS	STUDENT PAPERS

PRIMARY SOURCES

1	Shikha Rani, Satnam Singh, Bonamali Pal. "Core-shell structure of reduced graphene oxide@Ag–TiO2 for photocatalytic H2O splitting and CH3OH dehydrogenation under UV light irradiation", International Journal of Hydrogen Energy, 2024 Publication	1%
2	Xinyao Li, Jinjuan Xue, Shuaishuai Ma, Peng Xu, Chengjuan Huang, Mingxin Wang. " Synthesis of MgAl LDH/Acidified g-C N Heterojunction Photocatalyst for Improved Tetracycline Hydrochloride Degradation Activity ", Nano, 2019 Publication	<1%
3	Guanhua Zhang, Xueqiang Zhang, Yue Meng, Guoxiang Pan, Zheming Ni, Shengjie Xia. "Layered double hydroxides-based photocatalysts and visible-light driven photodegradation of organic pollutants: A review", Chemical Engineering Journal, 2020 Publication	<1%

ChemistrySelect

Research Article
doi.org/10.1002/slct.202203846

Chemistry Europe
European Chemical Societies Publishing

www.chemistryselect.org

Efficient ZnCr LDH/monoclinic-WO_3 composites for Degradation of Tetracycline under Visible Light

■■ Jemini, Satnam Singh, and Bonamali Pal*[a]

Recently, efficient removal of antibiotics like Tetracycline (TC) from wastewater is emerging as a crucial problem. However, low adsorption capacity and high cost of photocatalysts limit their utility. In this context, monoclinic tungsten trioxide (WO_3) loaded ZnCr layered double hydroxide (LDH) composites [ZnCr-xWO_3, x = 10 and 20%) are prepared by co-precipitation method and characterized by several techniques viz. X-Ray diffraction (XRD), Fourier Transform Infrared Spectroscopy (FTIR), Raman, Photoluminescence (PL), Field-Emission Scanning Electron Microscopy (FE-SEM), Brunauer Emmett Teller (BET), Diffuse Reflectance Spectroscopy (DRS) and Dynamic Light Scattering (DLS). The XRD pattern confirms the formation of ZnCr LDH and its composites with monoclinic-WO_3. Bond vibrations and phase transitions were explored with the help of FTIR and Raman spectra. The BET analysis for ZnCr LDH and ZnCr-10WO_3 composite shows surface area as 27.459 m^2/g and 47.691 m^2/g. The higher photocatalytic performance of the composites formed is due to enhanced specific surface area and better separation efficiency of photo-generated electrons and holes through conventional class II hetero junction between ZnCr LDH and monoclinic-WO_3. The kinetics studies performed shows better fit for pseudo first order reaction with maximum degradation efficiency and rate constant for ZnCr-10WO_3 (i.e., 86.7% and 1.5×10^{-2} min^{-1}).

Address for correspondence

Introduction

An increasing trend of organic contaminants in water sources has been observed throughout the world due to the increase in world pollution and continuous industrial and agricultural development. It has been found that in recent years, the industrialization of different nations has grown quickly bringing about an expansion in pollutants from heavy metals, antimicrobials, azo colors, etc.[1-4]

Ecological contamination related to antibiotics is possibly the most critical issue to be addressed. The most risky impact of the anti-infection agents is their multi-resistant antibacterial properties and chemical stability.[5] Tetracycline (TC) is one of the generally utilized anti-infection agent being frequently used in therapeutic medicine and feed supplements because of its low absorptivity, so it enters the environment as unmetabolized compound which is viewed as a likely danger to the biological system and human wellbeing because of the ecotoxicity and antimicrobial opposition.[6,7] Presence of TC in water bodies is presently a subject of incredible concern. In recent years, various techniques like adsorption, electrolysis, microbial degradation, and photodegradation have been devoted for the removal of TC and other harmful pollutants from wastewater.[8-11] Among these methods, photocatalysis is one of the most encouraging advancements because of its great effectiveness, eco-friendly nature, and easy operation.[12-14] Layered double hydroxides (LDH), belong to the group of anionic clays which are known as hydrotalcite as most of the naturally occuring LDHs contain Mg^{2+} and Al^{3+} minerals (talc) with the chemical formula Mg_6Al_2 $(OH)_{16}CO_3.4H_2O$ hydrotalcite being one of the most representative mineral of this group, therefore, LDHs are known as 'Hydrotalcite-like compounds' with the general formula $[M(II)_{1-x}M(III)_x(OH)_2]^{x+}$ $[A^{n-}_{x/n}]^{x-}.mH_2O$ where M(II)and M(III) are metal cations and A is an intercalate anion (CO_3^{2-}, SO_4^{2-}, NO_3^-, F^-, Cl^-). Generally, these two-dimensional ionic clays made up of positively charged brucite-like layers and negatively charged interlayer anions are known for their great stability, low cost, flexible structure, effective support, and narrow band gap semiconductor properties which made them attractive in visible light photocatalysis.[15-17]

In this regard, among the different detailed photocatalytic materials, layered materials like ZnCr layered two fold hydroxide (LDH) are viewed as one of the effective photocatalysts due to their appropriate redox potential and huge light-accumulation capacities.[18] The capacity of ZnCr LDH to absorb visible spectrum is related with inter electronic excitation like metal-to-metal charge transition (MMCT) through oxo-connected bimetallic linkage. However, the poor visible light response and high recombination of photoinduced electron-hole pairs generally result in low photocatalytic efficiency of bare LDH.[19] Several modifications have been brought to their structural and electronic composition by adopting different strategies such as cation doping, anion intercalation, calcination, heterostructure formation with semiconductors, and noble metal loading.[20-29] Which has been investigated to enhance the performances in various fields such as photocatalytic removal of organic pollutants, photo-

[a] ■■ Jemini, Prof. S. Singh, Prof. Dr. B. Pal
School of Chemistry and Biochemistry
Thapar Institute of Engineering and Technology
Patiala 147004, Punjab, India
Tel: 91-175-2393443
Fax: 91-175-2364498
E-mail: bpal@thapar.edu

Applied Clay Science 250 (2024) 107281

Contents lists available at ScienceDirect

Applied Clay Science

journal homepage: www.elsevier.com/locate/clay

Research Paper

$Ag_2@WO_3$/MgAl Layered double hydroxide displayed superior adsorption and photocatalytic activity under visible light

Jemini, Satnam Singh, Bonamali Pal *

Department of Chemistry and Biochemistry, Thapar Institute of Engineering and Technology, Patiala, Punjab 147004, India

ARTICLE INFO

Keywords:
Layered double hydroxides
$Ag@WO_3$/MgAl LDH
Adsorption
Photocatalysis
Degradation pathways
Antibiotics

ABSTRACT

An environmental friendly approach was utilized to remove pharmaceutical drugs from wastewater, employing adsorption and photocatalysis. The emphasis centered on synthesizing ternary composites comprising silver-deposited tungsten trioxide ($Ag@WO_3$ 2%), and MgAl layered double hydroxide (LDH) for the remediation of wastewater from pharmaceutical industry. Combining silver-loaded WO_3 nanoparticles with MgAl LDH resulted in enhancement of adsorption and photocatalytic properties of MgAl LDH. The studies demonstrated that by incorporating $Ag@WO_3$ into MgAl LDH, the ternary composites exhibited superior performance, achieving 88% tetracycline (TC) adsorption in 90 min, providing the best fit for the Langmuir model, suggesting monolayer adsorption following second-order kinetics and 77.9% of ciprofloxacin (CIP) degradation under visible light in 160 min with rate constant of 0.96×10^{-2} min^{-1} for pseudo-first-order kinetics. The enhancement was attributed to the increased surface area and electron-accepting ability of silver NPs (surface plasmonic effect). Additionally, the $Ag_2@WO_3$-LDH heterostructure exhibited high stability and recyclability for up to 5 cycles with little loss in performance. High-resolution mass spectrometry (HRMS) studies and free radical trapping experiments were conducted to reveal the intermediates generated during the degradation process, leading to the proposed mechanism via two degradation pathways.

1. Introduction

The widespread use of antibiotics has raised concern about their impact on the ecosystem and human health. Large-scale usage of antibiotics resulted in the development of antibiotic resistance, posing a severe risk to both humans and animals (Ahmad and Khan, 2019). Certain antibiotics, such as ciprofloxacin and tetracycline, are identified as water pollutants that can contaminate the aquatic environment (Igwegbe et al., 2021; Sharbaji et al., 2021). These antibiotics are not entirely absorbed in the body; their chemical stability makes them difficult to break down, and these are eliminated from the environment (Saadati et al., 2016; Ahmadijokani et al., 2022). Addressing the presence of antibiotics in aquatic environments requires the development of efficient and practical techniques for their degradation. To overcome this problem, adsorption and photocatalysis using semiconductor photocatalysts has emerged as a promising, environmental friendly, and cost-effective approach to remove organic pollutants, including antibiotics, from water. (Lu et al., 2017; Hu et al., 2022; Sun et al., 2023; Wu et al., 2023).

Using effective nanosized adsorbent material is crucial in removing contaminants from wastewater, such as dyes, antibiotics, heavy metals, and various organic compounds. These materials play a vital role in adsorbing and degrading antibiotics, thereby facilitating their removal from the aquatic environment (Jiang et al., 2020; Jemini et al., 2022). Recently, 2D layered double hydroxides (LDH) have attracted much interest in adsorption and photocatalysis. LDH possesses a customizable chemical composition, excellent stability, non-toxicity, low cost, ease of synthesis, high surface area, and notable light response (Xu and Wei, 2018; Kour et al., 2021). These materials belong to the family of anionic clay compounds and can be represented by the general formula $[M^{2+}_{1-x}M^{3+}_{x}(OH)_2]^{x+}\ [A_{x/y}]^{y-}.m\ H_2O$. LDH is composed of layers resembling brucite in which part of the divalent metal cations, such as Mg^{2+}, Fe^{2+}, Co^{2+}, Cu^{2+}, Ni^{2+} or Zn^{2+}, coordinated octahedrally by hydroxyl groups, are replaced with positively charged layers made of Al^{3+}, Cr^{3+}, Ga^{3+}, In^{3+}, and Mn^{3+} (Mohapatra and Parida, 2016; Xu and Wei, 2018).

However, specific challenges are associated with the practical application of LDH in wastewater purification. Their photocatalytic performance is limited by a few drawbacks, such as insufficient

* Corresponding author.
E-mail address: bpal@thapar.edu (B. Pal).

https://doi.org/10.1016/j.clay.2024.107281
Received 21 August 2023; Received in revised form 10 January 2024; Accepted 28 January 2024